Masterarbeit

Study of CP Properties of the Higgs Boson produced in Gluon Fusion with two Jets in Proton - Proton Collisions at $\sqrt{s} = 8$ TeV with the ATLAS Experiment

Alena Lösle

Fakultät für Mathematik und Physik
Albert-Ludwigs-Universität Freiburg

Study of CP Properties of the Higgs Boson produced in Gluon Fusion with two Jets in Proton - Proton Collisions at $\sqrt{s} = 8\,\text{TeV}$ with the ATLAS Experiment

Masterarbeit

vorgelegt von

Alena Lösle

4. November 2015

Prof. Dr. Markus Schumacher
Fakultät für Mathematik und Physik der
Albert-Ludwigs-Universität
Freiburg im Breisgau

Abstract

Measurements of the CP properties of the Higgs boson detected in 2012 are an important aspect in order to confirm the predictions of the Standard Model of particle physics. In the Standard Model, the Higgs boson is a scalar particle with $J^{CP} = 0^+$. Any violation of CP invariance in the Higgs sector would directly lead to the need for new physics beyond the Standard Model. In this thesis, the CP properties of the Higgs boson are studied by investigating its coupling structure to gluons. This is done in the Higgs boson production channel in gluon fusion in association with two jets. The subsequent decay of the Higgs boson into a pair of τ-leptons in the full-leptonic final state is considered. In the gluon fusion production, the Higgs boson couples to the gluons via a heavy quark loop, which is dominated by top-quarks. However, for the infinite top-quark mass limit this loop can be approximated by an effective point-like Higgs-gluon coupling. This coupling vertex can be parametrized in terms of a mixing angle $\cos(\alpha)$ between CP even and CP odd contributions, which is measured in this thesis. Here, CP sensitive variables are used in order to investigate the underlying coupling structure. In this analysis, the Optimal Observable, taking into account matrix elements for SM and CP odd couplings, and the signed azimuthal angle difference between the outgoing jets $\Delta\Phi_{jj}^{sign}$ are used. The analysis is based on data taken with the ATLAS detector in 2012 in proton-proton collisions at a center of mass energy of 8 TeV. This dataset corresponds to an integrated luminosity of $20.3\,\text{fb}^{-1}$.

Zusammenfassung

Die Bestimmung der CP-Quantenzahlen des im Juli 2012 entdeckten Higgs-Bosons stellen eine wichtige Aufgabe da, um die Vorhersagen des Standardmodells der Teilchenphysik bestätigen zu können. Das Standardmodell beinhaltet ein skalares Higgs-Boson mit Spin- und CP-Quantenzahlen $J^{CP} = 0^+$. Jegliche Art von CP-Verletzung im Higgs-Sektor würde ein direktes Anzeichen für Physik jenseits des Standardmodells darstellen. In dieser Arbeit werden die CP-Quantenzahlen des Higgs-Bosons durch die Untersuchung seiner effektiven Kopplung and Gluonen gemessen. Hierbei wird die Higgs-Boson Produktion in der Gluonfusion in Assoziation mit zwei Jets verwendet. Des Weiteren wird der Zerfall des Higgs-Bosons in zwei τ-Leptonen im voll leptonischen Endzustand betrachtet. In der Gluonfusion koppelt das Higgs-Boson an die masselosen Gluonen über eine umlaufende Schleife von schweren Quarks, wobei hier das Top-Quark den dominierenden Beitrag liefert. Für die Näherung einer unendlichen Top-Quark Masse kann diese Schleife jedoch mit einer effektiven Higgs-Gluon Wechselwirkung beschrieben werden. Die Struktur dieser Wechselwirkung kann dann mit Hilfe eines Mischungswinkels $\cos(\alpha)$ parametrisiert werden, der die Beiträge von CP-gerader und CP-ungerader Kopplung beschreibt. Die Form der zugrundeliegenden Wechselwirkungsstruktur kann experimentell mit Hilfe von CP-sensitiven Observablen untersucht werden. In dieser Arbeit werden hierfür die Optimal Observable, welche sich aus den Matrixelementen für CP-gerade und CP-ungerade Wechselwirkungen zusammensetzt, und die vorzeichenbehaftete Azimuthwinkeldifferenz zwischen den auslaufenden Jets, $\Delta\Phi_{jj}^{sign}$, betrachtet. Die Analyse basiert auf Daten, die mit dem ATLAS-Detektor im Jahr 2012 in Proton-Proton-Kollisionen bei einer Schwerpunktsenergie von 8 TeV aufgenommen wurden. Der vollständige Datensatz entspricht hierbei einer integrierten Luminosität von $20.3\,\text{fb}^{-1}$.

Contents

1 Introduction

Research in elementary particle physics is dedicated to studying the smallest constituents of matter and their interactions. A precise description of all elementary particles as known today and their fundamental interactions is provided by the Standard Model (SM) of particle physics developed in the 1960s. It predicts the existence of half-integer spin particles, *fermions*, which make up the matter around us, and integer spin particles, *bosons*, mediating the fundamental interactions. The SM is based on relativistic quantum field theories, which allow to describe three out of the four known interactions: the electromagnetic, the weak and the strong interaction. Only gravity is not included in the SM, but plays a minor role for the energy scales considered in particle physics. The SM does not only provide an accurate description of most of the observed phenomena in particle physics, but also predicted the existence of several previously unknown particles, which were subsequently experimentally discovered.

In its early formulation, the relativistic quantum field theories describing the SM did not contain any mass terms for bosons or fermions, as this would violate the principle of local gauge invariance. This is in contradiction with experimentally observed massive fermions and bosons, as the $W^{\pm}$-bosons and the Z^0-boson with $m_{W^{\pm}} = 82.1\,\text{GeV}$ and $m_{Z^0} = 93.0\,\text{GeV}$[1] [1–3]. This conflict was solved by the introduction of the Brout-Englert-Higgs (BEH) Mechanism[2] [4–8] based on the principle of spontaneous symmetry breaking. Within the BEH Mechanism fermions and bosons obtain mass by their interaction with the vacuum expectation value of an additional scalar field, the Higgs field. As a consequence the existence of a new particle, the Higgs boson, is predicted. Great effort has been put on the experimental side over the last decades in order to achieve discovery of this new boson.

In 2012 the ATLAS[3] and CMS[4] experiments at CERN[5] announced the observation of a new boson with a mass of around 125 GeV [9, 10]. Several subsequent measurements, such as the coupling strength in various production and decay modes and its spin, confirmed that the observed boson is consistent with the predicitions for the Higgs boson in the SM. The combination of measurements from the ATLAS and CMS experiments result in a Higgs-boson mass of $m_H = 125.09 \pm 0.21(\text{stat}) \pm 0.11(\text{syt})$ [11]. The Higgs-boson discovery at CERN was followed in 2013 by the Nobel Prize awarded to Peter Higgs and Francois Englert for the theoretical formulation of the BEH Mechanism.

Although no deviation from the SM predictions has been observed so far, detailed measurements of the Higgs-boson properties are an important aspect in order to exclude alternative theories. In the SM the Higgs boson is a CP even particle with a spin J of zero: $J^{\text{CP}} = 0^+$. In general, the CP nature describes the particle's behaviour under Charge conjugation and Parity transformation. If all fundamental interactions of the particle are invariant under such a transformation, this is called CP conservation. The particle is then an eigenstate of the

[1] in natural units with $\hbar \equiv c \equiv 1$

[2] more precise: Englert-Brout-Higgs-Guralnik-Hagen-Kibble Mechanism

[3] **A** **T**oroidal **L**HC **A**pparatu**S**

[4] **C**ompact **M**uon **S**olenoid

[5] **C**onseil **E**uropéen pour la **R**echerche **N**ucléaire

CP operator with even (+1) or odd (-1) eigenvalue. On the other hand, if the particle is not found to be an CP eigenstates this results in a violation of CP invariance and would be direct evidence for beyond SM physics (BSM). In particular, the observation of a CP violation in the Higgs-boson couplings would reveal great implications for explaining the measured baryon asymmetry in our universe via the mechanism of *baryogenesis* [12]. In the SM, the only source of CP violation is obtained by the complex phase in the mixing between the quark mass eigenstates parametrized in terms of the CKM matrix [13, 14]. However, the observed magnitude of CP violation might not be sufficient to explain the observed value of the baryon asymmetry, but additional sources of CP violation need to exist.
Recent results by the ATLAS experiment in the $H \to ZZ^* \to 4l$, $H \to WW^* \to 2l2\nu$ and $H \to \gamma\gamma$ final states indicate that the Higgs boson indeed carries $J^{CP} = 0^+$ while other non-SM J^{CP}-configurations are excluded at more than 99.9% confidence level [15]. However, an important study is to investigate if a mixing between CP even and CP odd eigenstate is present, which would result in the violation of CP invariance.
Various measurements of CP properties mostly relying on the coupling of the Higgs boson to weak vector bosons [15, 16]. However, here the CP odd coupling is suppressed. Instead it is promising to study possible CP violation in the coupling of the Higgs boson to quarks and leptons, where both CP even and odd contributions can enter at the same level.
In this thesis, the CP properties of the Higgs boson are studied by investigating its coupling structure to gluons. This is done in the Higgs boson production channel in gluon fusion with two jets H+2jets. The subsequent decay of the Higgs boson into a pair of τ-leptons in the full leptonic final state is considered. In the gluon fusion production, the Higgs-boson couples to the gluons via a heavy quark loop, which is dominated by top-quarks. However, for the infinite top-quark mass limit $m_{top} \to \infty$, this loop can be approximated by an effective point-like Higgs-gluon coupling. This coupling vertex can be parametrized in terms of a mixing angle $\cos(\alpha)$ between CP even and CP odd contributions. The nature of the coupling can be experimentally probed by exploiting CP sensitive variables. In this analysis, the Optimal Observable, taking into account matrix elements for SM and CP odd couplings, and the signed azimuthal angle difference between the outgoing jets $\Delta\Phi_{jj}^{sign}$ are used. These observables are odd under CP-transformation, therefore allow to investigate anomalous coupling contributions. The analysis is based on data taken with the ATLAS detector in proton-proton collisions in 2012 at $\sqrt{s} = 8\,\mathrm{TeV}$ corresponding to an integrated luminosity of $20.3\,\mathrm{fb}^{-1}$.

The structure of the thesis is as follows: The first chapter gives a brief theoretical introduction into the Standard Model with the incorporated BEH Mechanism and discusses the current status of Higgs-boson property measurements. Moreover, the description of Higgs-gluon couplings in the context of an effective field theory is given and the observables, which are used in this analysis to investigate anomalous Higgs-gluon couplings, are introduced. In Chapter 3 the signal process and relevant background contributions are discussed. This chapter also describes the reweighting procedure to simulate Higgs-boson production with anomalous couplings. In Chapter 4 an investigation of the signal sensitivity to anomalous couplings at generator level is described. In Chapter 5 and Chapter 6 the LHC and the ATLAS experiment are described and an overview of reconstruction of physics objects is given. Chapter 7 presents the analysis strategy to separate signal from background events. The estimation of specific background processes is described in Chapter 8 followed by a discussion of systematic uncertainties in Chapter 9. In Chapter 10 the statistical procedure is introduced and the results are presented. Finally, the thesis concludes in Chapter 11 with a summary of the obtained results and an outlook for further studies.

2 Theoretical Background

This chapter gives an overview of the theoretical background, on which the analysis in this thesis is based. The first section introduces the Standard model (SM) of particle physics, which describes the elementary particles and their fundamental interactions. Afterwards, the Higgs-boson phenomenology and its production and decay channels in proton-proton collisions are discussed. This is followed by a brief overview of the Higgs-boson discovery at the LHC and the current experimental status of its property measurements. Then, the theoretical description of Higgs-gluon couplings in the context of effective field theories and the parametrization for describing anomalous coupling contributions is given. The chapter closes with the description of the CP-sensitive observables, which are used in this thesis to investigate anomalous contributions to the Higgs-gluon coupling structure.

2.1. The Standard Model

The Standard Model of particle physics, developed in the 1960s and 1970s, describes the so far known elementary particles and their fundamental interactions with great precision. Its prediction of several previously unknown particles, such as the $W^{\pm}/Z^0$- bosons and the top-quark, were subsequently experimentally discovered [1, 17, 18]. The SM consists of combined quantum field theories assuring the invariance under local phase transformations, which is called gauge invariance. It is able to describe three out of the four known fundamental interactions: the electromagnetic force, the weak force and the strong force. Only gravity is not included in the SM framework, but plays a minor role for energy scales accessible at current collider experiments and can be neglected.
The descriptions in the following sections are based to a large extend on Ref. [19–21] and other references given in the text.

2.1.1. Elementary Particles

The elementary particle content of the SM consists of fermions with half integer spin and bosons carrying integer spin. Fermions can be further grouped into leptons participating in the electroweak interaction only, and quarks, which interact via electroweak and strong force. Experimental measurements show that both leptons and quarks appear in three generations. The second and third generations are copies of the first generation with identical quantum numbers, but different lepton flavour and increasing mass. Table 2.1 gives an overview of the generation content for leptons and quarks with their electric charge and approximate mass. Each generation of quarks contains one up - type quark with fractional electric charge $Q = \frac{2}{3}$ and one down - type quark carrying $Q = -\frac{1}{3}$[1]. This gives six different quark flavors (up, down, charm, strange, top, bottom) in total. For leptons the three generations consist of electrons e, muons μ and τ-leptons with electric charge $Q = -1$ including uncharged neutrinos of same

[1] The electric charge Q is usually given in units of the elementary electric charge $e = 1.6 \times 10^{-19}$ C carried by a single electron

lepton flavor: the electron neutrino ν_e, the muon neutrino ν_μ and the τ-neutrino ν_τ.
The matter around us only consists of first generation fermions: up-quarks and down-quarks forming protons and neutrons, and the electron. Fermions of the second and third generations only appear in cosmic rays or collider experiments.
In the SM, fundamental interactions are mediated by gauge bosons with spin one. Table 2.2 summarizes the gauge bosons with corresponding interaction type and properties.
The electromagnetic interaction is transmitted by the photon γ, which couples to particles carrying electric charge Q. Since the photon is massless and stable, the electromagnetic interaction has infinite range.
The massive $W^{\pm}/Z^0$-bosons are the mediators of the weak interaction and couple to the so called weak isospin I_w. Due to their heavy masses of $m_{W^\pm} = 80.4\,\text{GeV}$ and $m_{Z^0} = 91.2\,\text{GeV}$ [22] the weak interaction appears to couple weakly at low energies and is limited in its interaction range.
The strong force is mediated by massless gluons, which couple to colour-charged particles. As the gluon itself carries colour and anti-colour charge, it exists in eight different flavor states.
In addition to the spin-1 gauge-bosons the SM also contains a scalar spin-0 particle, the Higgs boson, which has been detected in 2012 with the ATLAS and CMS experiments at CERN [9, 10]. Section 2.2 gives a detailed description of its observation and the status of current Higgs-boson property measurements.

	Generation	Fermion	Q [e]	Mass [GeV]
Leptons	1^{st}	e	-1	$\approx 0.5 \times 10^{-3}$
		ν_e	0	$< 2 \times 10^{-9}$
	2^{nd}	μ	-1	$\approx 105 \times 10^{-3}$
		ν_μ	0	$< 0.19 \times 10^{-3}$
	3^{rd}	τ	-1	≈ 1.7
		ν_τ	0	$< 18 \times 10^{-3}$
Quarks	1^{st}	u	$\frac{2}{3}$	$\approx 2.49 \times 10^{-3}$
		d	$-\frac{1}{3}$	$\approx 5.05 \times 10^{-3}$
	2^{nd}	c	$\frac{2}{3}$	≈ 1.27
		s	$-\frac{1}{3}$	≈ 0.10
	3^{rd}	t	$\frac{2}{3}$	≈ 172.0
		b	$-\frac{1}{3}$	≈ 4.19

Table 2.1.: Leptons and quarks in the SM grouped in three generations with their electric charge Q and approximate mass [22].

2.1.2. Fundamental Interactions and Gauge Theories

Quantum Electrodynamics

The electromagnetic interaction is described by a relativistic quantum field theory, called Quantum Electrodynamics (QED), with an underlying U(1) symmetry. It is mediated by the massless photon γ, which couples to the electric charge q. The Lagrangian density of a free

Gauge boson	Force	Q [e]	Mass [GeV]
Photon γ	electromagnetic	0	0
W-boson $W^{\pm}$	weak	± 1	80.385
Z-boson Z^0	weak	0	91.188
Gluon g	strong	0	0

Table 2.2.: Gauge bosons in the SM with corresponding fundamental interactions, electric charge Q and approximate mass [22].

fermion with mass m is given by

$$\mathcal{L} = \bar{\psi} \left(i\gamma^{\mu} \partial_{\mu} - m \right) \psi \tag{2.1}$$

with the Dirac spinor ψ, the Dirac matrices γ^{μ} and the partial derivative $\partial_{\mu} = \frac{\partial}{\partial x^{\mu}}$. The corresponding equation of motion, called Dirac equation, is obtained by applying the Euler-Lagrange equation:

$$(i\gamma^{\mu} \partial_{\mu} - m)\psi = 0 \tag{2.2}$$

Any gauge theory has to be locally invariant under all transformations of the symmetry group. Therefore, the Lagrangian density in Eq. 2.1 is required to be invariant under local U(1)-transformations of the form

$$\psi(x) \mapsto \exp\left(-iq\alpha(x)\right)\psi(x) \tag{2.3}$$

Here, q denotes the electric charge and the local phase $\alpha(x)$ dependents on space and time. However, one finds that the first term in Eq. 2.1 is not invariant under this transformation

$$\partial_{\mu}\psi \mapsto \partial_{\mu} \left(\exp\left(-iq\alpha(x)\right)\psi \right) \tag{2.4}$$

but acquires an additional term. To achieve a U(1)-invariant Lagrangian density an additional coupling between the fermion and a new vector field A_{μ}, which transforms as

$$A_{\mu} \mapsto A_{\mu} + \partial_{\mu}\alpha(x) \tag{2.5}$$

has to be introduced. By defining the covariant derivative

$$D_{\mu} = \partial_{\mu} + iqA_{\mu} \tag{2.6}$$

the gauge-invariant Lagrangian density of QED reads

$$\mathcal{L} = \bar{\psi} \left(i\gamma^{\mu} D_{\mu} - m \right) \psi \tag{2.7}$$

The new vector field A_{μ} ensures local phase invariance and couples to fermions with the coupling strength e. This so called gauge field can be identified with the physical photon γ when adding a kinematic term to the Lagrangian density in Eq. 2.7 and defining the field strength tensor $F_{\mu\nu} = \partial_{\mu}A_{\nu} - \partial_{\nu}A_{\mu}$:

$$\mathcal{L}_{QED} = \bar{\psi} \left(i\gamma^{\mu} \left(\partial_{\mu} - ieA_{\mu} \right) - m \right) \psi - \frac{1}{4} F^{\mu\nu} F_{\mu\nu} \tag{2.8}$$

As the introduction of any mass term of the form $(-\frac{1}{2}m^2 A^{\mu} A_{\mu})$ would violate gauge invariance, the formalism of QED requires a massless gauge boson. This is in agreement with experimental measurements, where upper limits on the photon mass of $m_{\gamma} < 3 \times 19^{-27}\,\mathrm{eV}$ can be set [23].

Quantum Chromodynamics

Quantum Chromodynamics (QCD) is the gauge theory of a local SU(3) invariance describing the strong interaction of quarks and gluons. The charge corresponding to the strong interaction is the colour charge, which is experimentally found to exist in three different flavor states: red, blue and green [24]. Therefore, the four component Dirac spinor ψ is replaced by a vector of three spinors referring to the colour degrees of freedom:

$$\psi = \begin{pmatrix} \psi_{\text{red}} \\ \psi_{\text{blue}} \\ \psi_{\text{green}} \end{pmatrix} \tag{2.9}$$

A free quark field $\psi(x)$ transforms under local SU(3) transformation as

$$\psi(x) \mapsto \exp\left(i\frac{g_s}{2} \sum_{a=1}^{8} \lambda_a \beta_a(x) \right) \psi(x) \tag{2.10}$$

with the coupling strength g_s, the eight Gell-Man matrices λ_a and the eight-component transformation functions $\vec{\beta}(x)$ [25]. In contrast to QED, the generators of the fundamental SU(3) representation do not commute. In general, groups with this feature are called *non-abelian*. As a consequence, the field strength tensors $G^a_{\mu\nu}$ for the gluon fields G^a_μ $(a = 1, .., 8)$ acquire an additional term:

$$G^a_{\mu\nu} = \partial_\mu G^a_\nu - \partial_\nu G^a_\mu - g_s f^{abc} G^b_\mu G^c_\nu \tag{2.11}$$

As gluons carry colour and anti-colour charge, eight gluon fields exist. By introducing the covariant derivative

$$D_\mu = \partial_\mu + i g_s \frac{\lambda_a}{2} G^a_\mu \tag{2.12}$$

the Lagrangian density of QCD for a single quark state reads:

$$\mathcal{L}_{QCD} = \bar{\psi} \left(i\gamma^\mu \partial_\mu - m \right) \psi - g_s \left(\bar{\psi} \gamma^\mu T_a \psi \right) G^a_\mu - \frac{1}{4} G^a_{\mu\nu} G^{a,\mu\nu} \tag{2.13}$$

Due to the non-abelian structure of SU(3) the last term in Eq. 2.13 describes the gluon self-interaction, which has no equivalent in QED. Furthermore, the gauge invariance requires the gluons as force carriers to be massless, which is in agreement with all experimental measurements. In contrast to QED, this does not result in an infinite interaction range of QCD, but provides a completely different energy scaling behaviour. The interaction potential of the strong force increases with higher spatial separation between colour-charged particles. Thus, quarks do not exist in free states, but are bound in mesons (quark and anti-quark) and baryons (three (anti-)quarks), which is called *confinement*. Therefore, all experimentally observed particles will be color-neutral. On the other hand, at high energy scales, which corresponds to small spatial separations, QCD becomes weakly coupled. This is referred to as *asymptotic freedom* [26, 27]. In contrast to mass terms for gluons, quark masses do not break the SU(3) invariance. Although the quark flavours are found to have different masses, the mass for a given flavour state does not depend on the colour charge.

Electroweak Unification

The weak interaction couples to the weak isospin I_w and is mediated by the charged $W^\pm$-bosons and the neutral Z^0-boson. While the exchange of a $W^\pm$-boson leads to a flavour

modification for quarks, called *charged currents*, no flavour transition is observed for *neutral currents* represented by a Z^0-boson exchange. Experiments show that the charged current weak interaction violates parity maximally as it only couples to left-handed particles [28,29]. Glashow, Salam and Weinberg proposed a theory of electroweak interaction [30–32], which is able to describe the weak and electromagnetic force within an underlying $\mathrm{SU}(2)_{L,I_w} \times \mathrm{U}(1)_Y$ symmetry. Here, Y is called hypercharge and L refers to the coupling of the weak interaction to left-handed fermions. The relation between the electric charge Q, the hypercharge Y and the third component of the weak isospin I_w^3 is given by the Gell-Mann-Nishijima relation [33,34]:

$$Q = I_w^3 + \frac{Y}{2} \tag{2.14}$$

Left-handed fermions are assigned to $SU(2)_{L,I_w}$ doublets with $I_3 = \pm\frac{1}{2}$ and same hypercharge, while fermions in right-handed states can be described by $SU(2)$ singlets with I=0. Table 2.3 gives an overview of the fermions and their quantum numbers. Right-handed massless neutrinos are not listed as they would not interact within the SM. However, recent results from neutrino oscillations indicate that at least two neutrinos have nonzero mass [35–37]. Quarks exist in weak eigenstates (d', s', b') with $I_3 = -\frac{1}{2}$ as mixtures of their mass eigenstates (d, s, b) described by the Cabbibo-Kobayashi-Mascawa (CKM) matrix [13,14]:

$$\begin{pmatrix} d' \\ s' \\ b' \end{pmatrix} = \begin{pmatrix} V_{ud} & V_{us} & V_{ub} \\ V_{cd} & V_{cs} & V_{cb} \\ V_{td} & V_{ts} & V_{tb} \end{pmatrix} \begin{pmatrix} d \\ s \\ b \end{pmatrix} \tag{2.15}$$

Here, $|V_{ij}|^2$ gives the probability for a quark flavor transition $i \to j$ by the interaction with a $W^{\pm}$-boson. The complex phase in the CKM matrix results in a violation of CP invariance. Left-handed isospin doublets are transformed under $SU(2)_{L,I_w}$ as

$$\psi_L(x) \mapsto \exp\left(i\frac{g}{2}\sum_{a=1}^{3}\tau_a\alpha_a(x)\right)\psi_L(x) \tag{2.16}$$

where τ_a (a=1,2,3) are the generators of the $SU(2)_{L,I_w}$ group given by the (2×2) Pauli matrices. The coupling strength is given by g and $\alpha_a(x)$ refers to the local phase. Under $U(1)_Y$ symmetry the transformations of left-handed isospin doublets and right-handed singlets are

$$\begin{aligned} \psi_L(x) &\mapsto \exp\left(i\frac{g'}{2}Y\beta(x)\right)\psi_L(x) \\ \psi_R(x) &\mapsto \exp\left(i\frac{g'}{2}Y\beta(x)\right)\psi_R(x) \end{aligned} \tag{2.17}$$

with another coupling strength g', the local phase $\beta(x)$ and the hypercharge generator Y. The requirement of local phase invariance results in the introduction of three vector fields W^a(a=1,2,3) for $SU(2)_{L,I_w}$ and one gauge field B for $U(1)_Y$. By introducing the covariant derivatives for left-handed and right-handed fermion fields

$$\begin{aligned} D_\mu^L &= \partial_\mu + i\frac{g}{2}\tau_a W_\mu^a + i\frac{g'}{2}YB_\mu \\ D_\mu^R &= \partial_\mu + i\frac{g'}{2}YB_\mu \end{aligned} \tag{2.18}$$

the electroweak Lagrangian density including kinematic terms reads

$$\mathcal{L}_{EW} = \bar{\psi}_L i\gamma^\mu D_\mu^L\psi_L + \bar{\psi}_R i\gamma^\mu D_\mu^R\psi_R - \frac{1}{4}W_{\mu\nu}^a W^{a,\mu\nu} - \frac{1}{4}B_{\mu\nu}B^{\mu\nu} \tag{2.19}$$

where the field strength tensors are defined as

$$\begin{aligned} W^a_{\mu\nu} &= \partial_\mu W^a_\nu - \partial_\nu W^a_\mu - g\varepsilon^{abc} W^b_\mu W^c_\nu \\ B_{\mu\nu} &= \partial_\mu B_\nu - \partial_\nu B_\mu \end{aligned} \tag{2.20}$$

with the structure constant ε^{abc} of $\mathrm{SU}(2)_L$. Thus, the gauge fields W^a_μ $(a = 1, 2, 3)$ are able to interact with themselves, whereas B_μ only couples to fermions. However, since W^3_μ and B_μ both interact with neutrinos, non of this gauge fields can be identified with the physical photon-field A_μ. Instead, A_μ needs to be a linear combination of these gauge fields satisfying the requirement to couple both to left- and right-handed fermions with the same coupling strength and to not interact with neutrinos. As it also has to be orthogonal to the Z^0-boson, a mixing angle θ_w is introduced:

$$\cos(\theta_w) = \frac{g}{\sqrt{g^2 + g'^2}} \tag{2.21}$$

Then, the photon and Z^0-boson fields can be parametrized in terms of a mixing between the neutral gauge fields of $SU(2)_{L,I_w} \times U(1)_Y$:

$$\begin{pmatrix} Z_\mu \\ A_\mu \end{pmatrix} = \begin{pmatrix} \cos(\theta_w) & -\sin(\theta_w) \\ \sin(\theta_w) & \cos(\theta_w) \end{pmatrix} \begin{pmatrix} W^3_\mu \\ B_\mu \end{pmatrix} \tag{2.22}$$

Considering the isospin transformations of the matrices $\tau^- = \frac{1}{2}(\tau_1 - i\tau_2)$ and $\tau^+ = \frac{1}{2}(\tau_1 + i\tau_2)$ the charged eigenstates for the $W^\pm$-bosons are expressed as:

$$W^\pm_\mu = \frac{1}{\sqrt{2}} \left(W^1_\mu \mp i W^2_\mu \right) \tag{2.23}$$

Moreover, the coupling strength of the electromagnetic interaction q can be written in terms of the coupling strength of the $U(1)_Y$ and $SU(2)_{L,I_w}$ transformations:

$$q = \frac{g g'}{\sqrt{g^2 + g'^2}} = g' \cos(\theta_w) = g \sin(\theta_w) \tag{2.24}$$

This theory, however, only holds for massless fermions and electroweak gauge bosons, as any mass term in Eq. 2.19 violates gauge invariance. While the demand for massless gauge bosons in the electromagnetic and strong interactions agree with experimental measurements, the prediction in the electroweak model is in contrast to the experimentally observed $W^\pm/Z^0$-boson masses. In addition, the underlying $SU(2)_{L,I_w}$ symmetry results in the prohibition of massive fermions, which is in conflict with experimental observations.
To account for this contradiction, an additional scalar field in the context of spontaneous symmetry breaking [4–8] is introduced. The so called *Higgs-mechanism*[2] and its consequences are further described in the next section.

2.1.3. Spontaneous Symmetry Breaking

The general idea of spontaneous symmetry is, that a symmetric system can be located in a state of minimum energy, the so called *vacuum state*, which is not symmetric with respect to the gauge group of the theory. In the SM, spontaneous symmetry breaking is introduced to resolve the conflict of massless gauge bosons and fermions following the request of local phase

[2] More precise: Englert-Brout-Higgs-Guralnik-Hagen-Kibble mechanism

	Generation			Quantum numbers			
	1st	2nd	3rd	I_w	I_w^3	Y	Q [e]
Leptons	$\begin{pmatrix} \nu_e \\ e \end{pmatrix}_L$	$\begin{pmatrix} \nu_\mu \\ \mu \end{pmatrix}_L$	$\begin{pmatrix} \nu_\tau \\ \tau \end{pmatrix}_L$	$\frac{1}{2}$ $\frac{1}{2}$	$\frac{1}{2}$ $-\frac{1}{2}$	-1 -1	0 -1
	e_R	μ_R	τ_R	0	0	-2	-1
Quarks	$\begin{pmatrix} u \\ d' \end{pmatrix}_L$	$\begin{pmatrix} c \\ s' \end{pmatrix}_L$	$\begin{pmatrix} t \\ b' \end{pmatrix}_L$	$\frac{1}{2}$ $\frac{1}{2}$	$\frac{1}{2}$ $-\frac{1}{2}$	$\frac{1}{3}$ $\frac{1}{3}$	$\frac{2}{3}$ $-\frac{1}{3}$
	u_R	c_R	t_R	0	0	$\frac{4}{3}$	$\frac{2}{3}$
	d_R	s_R	b_R	0	0	$-\frac{2}{3}$	$-\frac{1}{3}$

Table 2.3.: Summary of fermions in the electroweak model grouped in three generations with their quantum numbers.

invariance under $SU(2)_{L,I_w} \times U(1)_Y$. Therefore, an additional complex scalar $SU(2)$-doublet with quantum numbers $Y = 1$ and $I_w = \frac{1}{2}$ is introduced [25]:

$$\Phi = \begin{pmatrix} \Phi^+ \\ \Phi^0 \end{pmatrix} = \begin{pmatrix} \Phi_1 + i\Phi_2 \\ \Phi_3 + i\Phi_4 \end{pmatrix} \tag{2.25}$$

This so called *Higgs field* is described by the Lagrangian density:

$$\mathcal{L} = (\partial_\mu \Phi)^\dagger (\partial^\mu \Phi) + V(\Phi) \tag{2.26}$$

As this Lagrangian density has to be invariant under local $SU(2)_{L,I_w} \times U(1)_Y$ transformation, ∂_μ can be replaced by the covariant derivation D^μ as defined in Eq. 2.18:

$$\mathcal{L} = (D_\mu \Phi)^\dagger (D^\mu \Phi) + \mu^2 \Phi^\dagger \Phi - \lambda (\Phi^\dagger \Phi)^2 - \frac{1}{4} W^a_{\mu\nu} W^{a,\mu\nu} - \frac{1}{4} B_{\mu\nu} B^{\mu\nu} \tag{2.27}$$

The most general potential, being invariant under $SU(2)_{L,I_w} \times U(1)_y$ and providing renormalizability, is given by:

$$V(\Phi) = -\mu^2 \Phi^\dagger \Phi + \lambda \left(\Phi^\dagger \Phi\right)^2, \ \lambda > 0 \tag{2.28}$$

This so called *Higgs potential* has a local minimum for non-vanishing values of Φ for $\mu^2 > 0$ and corresponds to a scenario in which the $SU(2)_{Y,I_w} \times U(1)_Y$ symmetry is broken. Fig. 2.1 shows a simplified example of such a potential, depending on two out of the four degrees of freedom in Φ.

Minimising Eq. 2.28 with respect to $\left(\Phi^\dagger \Phi\right)$ gives

$$\Phi_0^\dagger \Phi_0 = |\Phi_0|^2 = \frac{v^2}{2}, \ \ v = \sqrt{\frac{\mu^2}{\lambda}} \tag{2.29}$$

with the vacuum expectation value v. This ground state Φ_0 is continuously occupied by various configurations of the real fields Φ_1,...,Φ_4. Choosing a particular vacuum state as

$$\Phi_1 = \Phi_2 = \Phi_4 = 0, \ \ \Phi_3 = \sqrt{\frac{\mu^2}{\lambda}} = v \tag{2.30}$$

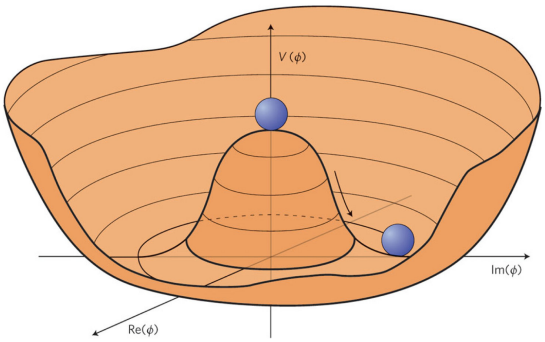

Figure 2.1.: Illustration of the Higgs-potential for two out of the four degrees of freedom for the case of spontaneous symmetry breaking [38].

leads to a ground state with $I_3 = -\frac{1}{2}$ and Y=1

$$\Phi_0 = \frac{1}{\sqrt{2}} \begin{pmatrix} 0 \\ v \end{pmatrix} \tag{2.31}$$

and breaks the symmetry of $SU(2)_L \times U(1)_Y$ spontaneously to $U(1)_Q$. Here, Φ_1 and Φ_2 are set to zero in order to obtain an electrically neutral ground state Φ_0, as the $U(1)_Q$ symmetry has to remain unbroken. Parametrizing Φ around the vacuum expectation value gives:

$$\Phi_0(x) = \frac{1}{\sqrt{2}} \exp\left(i \sum_{a=1}^{3} \frac{\tau_a G_a(x)}{v} \right) \begin{pmatrix} 0 \\ v + H(x) \end{pmatrix} \tag{2.32}$$

Here, four real fields $H(x), G_1(x), G_2(x), G_3(x)$ appear. While the $G_a(x)$ $(a = 1, 2, 3)$ fields lead to three massless scalar bosons, the so called Goldstone-bosons [39, 40], they can be eliminated by applying a so called unitary gauge invariant transformation to Φ such as:

$$\Phi_0(x) \mapsto \exp\left(-i \sum_{a=1}^{3} \frac{\tau_a G_a(x)}{v} \right) \Phi_0(x) \tag{2.33}$$

The vacuum expectation value v can be determined by measuring the Fermi constant $G_F = 1/\sqrt{2}v^2$, for instance in measurements of the muon life time, and is found to be 246.22 GeV [22]. The real field $H(x)$ can be considered as the excitation from the ground state. Then, the Lagrangian density, as defined in Eq. 2.34, reads [20]:

$$\begin{aligned} \mathcal{L}_{Higgs} =& \frac{1}{2} (\partial_\mu H) (\partial^\mu H) - \lambda v^2 H^2 - \lambda v H^3 - \frac{1}{4} \lambda H^4 \\ &+ \frac{1}{2} (\frac{1}{2} vg)^2 W^{\mu,+} W^-_\mu + \frac{1}{2} (\frac{vg}{2\cos(\theta_w)})^2 Z^\mu Z_\mu \\ &+ g(\frac{vg}{2}) H W^{\mu,+} W^-_\mu + g \frac{vg}{4\cos^2(\theta_w)} H Z^\mu Z_\mu \\ &+ \frac{g^2}{4} H^2 W^{\mu,+} W^-_\mu + \frac{g^2}{4\cos^2(\theta_w)} H^2 Z^\mu Z_\mu + \text{const.} \end{aligned} \tag{2.34}$$

Here, the parametrization of the physical gauge fields $W^\pm_\mu, Z_\mu$ as defined in Eq. 2.22 and Eq. 2.23 is used. This expression of the Lagrangian density allows to directly identify mass terms for the $W^\pm$-bosons and the Z^0-boson:

$$m_{W^\pm} = \frac{1}{2} vg \qquad m_{Z^0} = \frac{m_{W^\pm}}{\cos(\theta_w)} \tag{2.35}$$

Thus, the mass ratio of $W^{\pm}$- and Z^0-bosons is fully determined by the weak mixing angle $\cos(\theta_w)$. In addition, the excitation of the H-field results in the prediction of a new scalar particle with mass:

$$m_H = \sqrt{2\lambda}v \tag{2.36}$$

The expression in Eq. 2.34 describes cubic interactions of the Higgs-field H with the $W^{\pm}$-bosons and the Z^0-boson ($HV^{\dagger}V$) with a coupling strength proportional to the gauge bosons mass $m_{W^{\pm}/Z^0}$. In addition, also quartic couplings ($HHV^{\dagger}V$) appear. Their coupling strength is found to be proportional to the Higgs boson mass m_H. Furthermore, cubic (H^2) and quartic (H^3) Higgs self-couplings are described. Thus, the approach of spontaneous symmetry breaking provides a prediction for the relation between coupling strength and gauge boson masses, which can be experimentally tested.
In order to also describe fermion masses an additional coupling, invariant under $SU(2)_{L,I_w} \times U(1)_Y$ symmetries, is introduced. It is called *Yukawaw coupling* and describes the interaction between the Higgs-doublet, the left handed fermion $SU(2)_{L,I_w}$-doublets and the right handed fermion $U(1)_Y$-singlets. For leptons of the first generation, the Yukawa coupling is given by

$$\mathcal{L}^{lep}_{Yukawa} = -g_e \left(\bar{\nu_e}, \bar{e}\right)_L \Phi e_R + h.c. \tag{2.37}$$

with the doublet Φ as defined in Eq. 2.32 and $h.c.$ standing for the corresponding hermitian conjugate term. Thus, the electron acquires a mass, while the neutrino remains massless. For the Yukawa coupling of quarks, the charge conjugated Higgs doublet Φ_C has to be introduced to enable interactions with $I^3_w = \frac{1}{2}$ quarks:

$$\Phi_C(x) = \frac{1}{\sqrt{2}} \begin{pmatrix} v + H(x) \\ 0 \end{pmatrix} \tag{2.38}$$

Then, the Lagrangian density for first generation quarks reads

$$\mathcal{L}^{quarks}_{Yukawa} = -g_d \left(\bar{u}, \bar{d}\right)_L \Phi d_R + g_u \left(\bar{u}, \bar{d}\right)_L \Phi_C u_R + h.c. \tag{2.39}$$

In the same way, Yukawa interactions of second and third generation fermions are provided. The coupling constants g_f are found to be directly proportional to the corresponding fermion masses:

$$m_f = \frac{1}{\sqrt{2}} v g_f \tag{2.40}$$

Considering the excitation from the ground state h, the Lagrangian density describing the interaction with fermions f reads:

$$\mathcal{L}_{Yukawa} = -m_f \bar{f} f \left(1 + \frac{H}{v}\right) \tag{2.41}$$

Finally, the full Lagrangian density of the SM can be expressed as:

$$\mathcal{L} = \mathcal{L}_{Higgs} + \mathcal{L}_{EW} + \mathcal{L}_{QCD} + \mathcal{L}_{Yukawa} \tag{2.42}$$

Since the masses of gauge bosons and fermions are experimentally measured with high precision, λ remains as the only free coupling parameter. Thus, by measuring the Higgs-boson mass m_H, all coupling parameters included in the SM are determined.

2.2. The Higgs Boson

The SM with the incorporated Higgs mechanism provides a fully consistent description of the experimentally observed phenomena in particle physics. As shown in the previous section, it predicts the existence of a new particle, the Higgs boson, with certain properties. The SM Higgs boson is electrically neutral, carries no colour charge and has a spin-parity configuration of $J^{CP} = 0^+$. In particular, it has positive eigenvalues under charge conjugation and parity transformation, also called CP-transformation. Furthermore, its coupling to fermions and gauge bosons is proportional to their respective mass.
The observation of a Higgs boson in 2012 at the ATLAS [9] and CMS [10] experiments at CERN is followed by precise measurements of its properties. Any deviation from the SM predictions would directly indicate the need for physics beyond the SM.
The SM Higgs boson has a very short lifetime of about 10^{-22} s at a mass of 125 GeV. Therefore, only its decay particles are experimentally accessible. In addition, as Fig. 2.2 shows, several processes with higher cross sections are produced in hadron collision. This puts high demands on detector performance and analysis strategies. A description of the signal and background processes considered in this analysis and their production cross sections is given in Chapter 3.
In the first part of this section constrains on the Higgs-boson mass based on SM predictions and direct measurements and their compatibility with the results from the ATLAS and CMS experiments are discussed. Next, a description of Higgs-boson production and decay channels at the LHC is given, followed by an overview of its observation in 2012 and a description of the measurements of Higgs-boson properties.

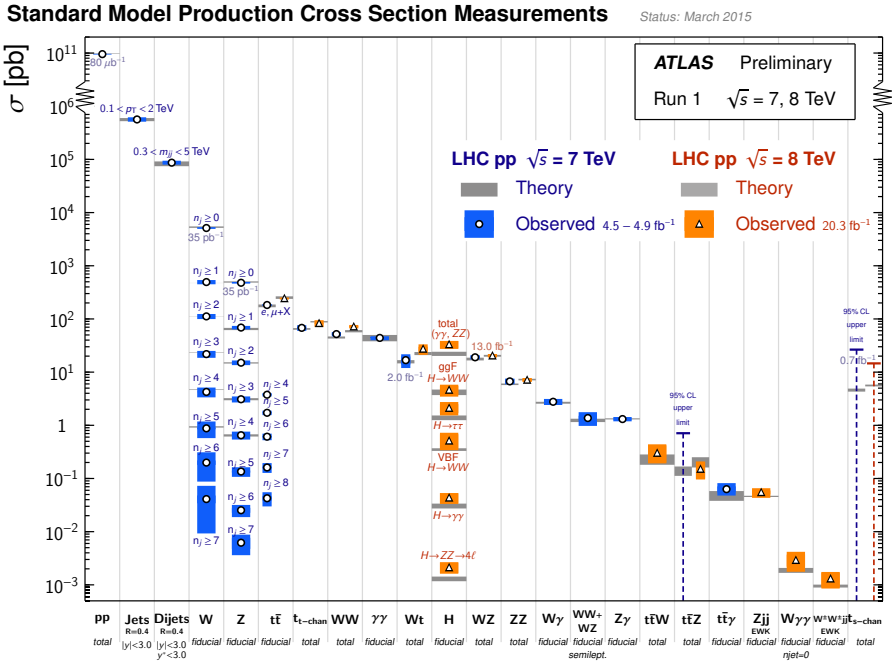

Figure 2.2.: Summary of SM cross section measurements for proton proton collisions compared to the theoretical predicitions [41].

2.2.1. Constrains on the Higgs Boson Mass

Although the mass of the Higgs boson is a free parameter in general, constrains on possible values of m_H can be constructed with experimental observations and theoretical arguments, which are briefly summarized here.
On the theory side, divergences in the cross section for the scattering of longitudinal polarized W-bosons at high energies are observed if $m_H \leq 1\,\text{TeV}$ [42] does not hold. Furthermore, depending on the energy scale Λ up to which the SM is assumed to be valid, upper and lower bounds on the Higgs boson mass can be derived. Fig. 2.3 shows these bounds depending on the scale Λ at which new physic effects become relevant. If the SM remains valid up to $\Lambda \sim 10^{19}\,\text{GeV}$ the mass has to lie in a band between $120 \leq m_H \leq 170\,\text{GeV}$. A wider range of $50 \leq m_H \leq 800\,\text{GeV}$ is allowed if no new physics appear below the TeV scale [43–46].
Moreover, experimental measurements at LEP, Tevatron and LHC are able to put direct constrains on m_H, which can be compared to indirect limits from electroweak precision tests. Fig. 2.4 shows the results of a global fit to electroweak measurements. Without including direct m_H measurements, the best-fit value of $m_H = 93^{+25}_{-22}\,\text{GeV}$ is obtained. This is consistent with the combined results of the ATLAS and CMS experiments of
$m_H = 125.09 \pm 0.21(\text{stat}) + 0.11(\text{syst})\,\text{GeV}$ [11] within two standard deviations.

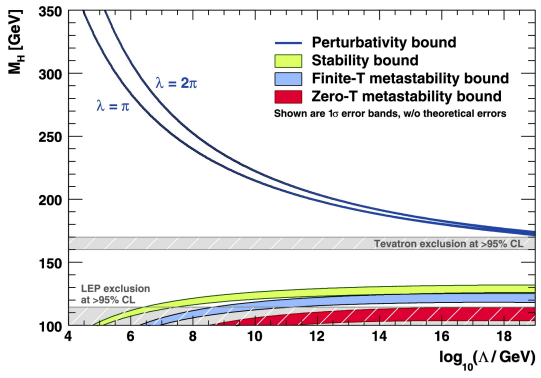

Figure 2.3.: Upper and lower bound on m_H depending on the scale Λ on which new physics has to appear. The shaded bands refer to the exclusion range from direct searches at Tevatron and LEP [47].

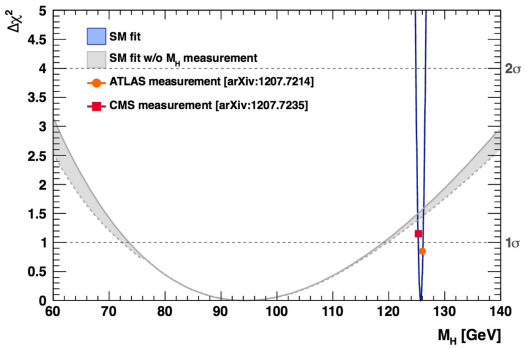

Figure 2.4.: $\Delta\chi^2$ as a function of m_H for a global fit of electroweak precision measurements and data points from ATLAS and CMS. The grey (blue) band shows the results when excluding (including) the direct m_H measurements. The solid (dotted) lines illustrate the fit results including (ignoring) theoretical uncertainties [48].

2.2.2. Higgs-Boson Production in Proton-Proton Collisions

As protons are composite particles, their interaction in collider experiments can be described in the context of hard scattering processes of quarks and gluons. The parton distribution functions (PDFs) $f(x_i, Q^2)$ give the probability to find a particular parton i with momentum fraction x_i of the total proton momentum in a collision with momentum transfer Q^2. The total cross section σ_X for a process $pp \to X$ is then calculated by integrating over the partonic cross section $\hat{\sigma}_{ij}$ for the interaction of parton i and j multiplied with the PDFs according to the factorization theorem [49]:

$$\sigma_X = \iint dx_i dx_j f(x_i, Q^2) f(x_j, Q^2) \hat{\sigma}_{ij} \tag{2.43}$$

The partonic cross section is given by

$$\hat{\sigma}_{ij} = \int \frac{|\mathcal{M}(ij \to X)|^2}{F} dQ \tag{2.44}$$

where $\mathcal{M}$ refers to the matrix element for the transition from initial to final state, F gives the particle flux and dQ is the phase space factor of the given kinematics. The transition probability is then given by the squared amplitude $|\mathcal{M}|^2$.

The production of a Higgs boson in proton-proton collisions can be classified into several processes, which differ in their cross section and phenomenology. Fig. 2.5 shows the leading order Feynman diagrams for the four main production mechanims discussed here.

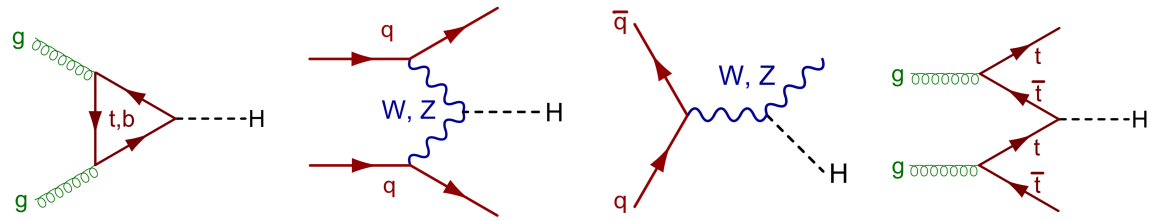

(a) gluon fusion (b) vector boson fusion (c) Higgs-Strahlung (d) associated production with top-quarks

Figure 2.5.: Feynman diagrams of the most important production modes of the Higgs boson at the LHC [50]. The highest cross section is provided by the (a) gluon fusion, followed by the (b) vector boson fusion, the (c) Higgs-Strahlung and the (d) associated production with top-quarks.

Due to the large contribution of gluons to the proton PDF for small momentum fraction x, the Higgs boson production in gluon fusion via heavy quark loops dominates. As its coupling to fermions is proportional to their mass, a top quark loop is strongly favoured. No additional particles are produced at leading order (LO), therefore the Higgs-boson receives a total transverse momentum of zero. However, at next-to-leading order (NLO) final states with additional jets are possible. Here, the Higgs boson recoils against the jet system and acquires a transverse momentum. The Higgs boson production in gluon fusion with two associated jets is further described in Section 3.1.
The vector-boson fusion (VBF) mode is one order of magnitude smaller in its cross section compared to the gluon fusion. Here, $W^{\pm}/Z^0$-bosons radiated from initial state quarks fuse to a Higgs boson. The jets from the final state quarks provide a distinct signature in the

detector as they are widely separated in pseudorapidity η, which is defined in Eq. 5.2. This can be used for the suppression of background processes.
The association production with a weak vector boson, also called Higgs-Strahlung, describes the annihilation of quark pairs into a weak vector boson, which then radiates the Higgs boson. Higgs boson production in association with a top quark pair is is suppressed by an order or magnitue as the high invariant mass required to produce the heavy quarks limits the available phasespace and reduces the corresponding cross section.
The cross sections for the different production modes are shown in Fig. 2.6 as function of the Higgs-boson mass m_H and Table 2.4 summarizes them for $m_H = 125\,\text{GeV}$.

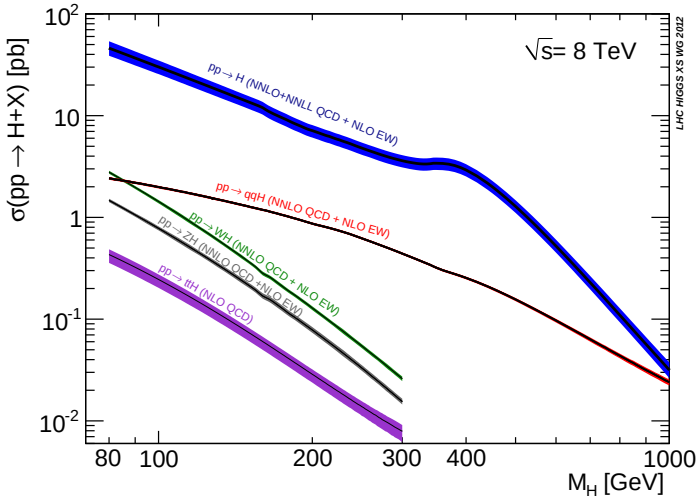

Figure 2.6.: Production cross sections for the Higgs boson at the LHC for a center of mass energy of $\sqrt{s} = 8\,\text{TeV}$ as a function of its mass m_H [51].

Process	σ_{incl} [pb]	$\delta_{\text{QCD scale}}$	$\delta_{\text{PDF}+\alpha_s}$
ggF	19.27	$^{+7.2\%}_{-7.8\%}$	$^{+7.5\%}_{-6.9\%}$
VBF	1.58	$^{+0.2\%}_{-0.2\%}$	$^{+2.6\%}_{-2.9\%}$
WH	0.705	$^{+1.0\%}_{-1.0\%}$	$^{+2.3\%}_{-2.3\%}$
ZH	0.415	$^{+3.1\%}_{-3.1\%}$	$^{+2.5\%}_{-2.5\%}$
ttH	0.129	$^{+3.9\%}_{-9.3\%}$	$^{+8.1\%}_{-8.1\%}$

Table 2.4.: Higgs boson production cross sections with theory QCD scale and PDF+α_s uncertainties, $\delta_{\text{QCD scale}}$ and $\delta_{\text{PDF}+\alpha_s}$, for proton-proton collisions at $\sqrt{s} = 8\,\text{TeV}$ and a Higgs-boson mass of $m_H = 125\,\text{GeV}$ [51].

2.2.3. Higgs Boson Decay Channels

As discussed in Section 2.1.3 the Higgs boson couples to vector bosons V and fermions f with a coupling strength proportional to m_V^2/v and m_f/v. Therefore, the branching ratio, defined as the ratio of a particular decay width to the total width

$$BR(H \to X) = \frac{\Gamma_{H\to X}}{\Gamma_{\text{tot}}} \tag{2.45}$$

rises with increasing mass of the decay particles. Possible decay channels with bosonic final states are $H \to WW^*$, $H \to ZZ^*$, $H \to gg$, $H \to Z\gamma^*$ and $H \to \gamma\gamma$. The coupling the Higgs boson to the massless gluons take place via a heavy quark loop, while for the Higgs-photon coupling additional loops containing W-boson loops contribute. For the decay into fermions the dominant channels are $H \to b\bar{b}$, $H \to \tau^+\tau^-$, $H \to c\bar{c}$ and $H \to \mu^+\mu^-$.
Fig. 2.7 shows the branching ratios for the different decay modes as a function of the Higgs-boson mass and Table 2.5 summarizes the corresponding values for m_H=125 GeV. For this mass the decay into a pair of b-quarks with a branching ratio of 57.7 % is dominant, followed by the decay into a pair of W-bosons with a branching ratio of 21.5 %. The production of virtual vector bosons V^* is allowed due to their intrinsic width. Furthermore, an important contribution to the Higgs boson decay modes is provided by the decay into τ-leptons with a branching ratio of 6.3 %, on which this analysis is focused.
The mass resolution in the different channels vary depending on the final state particles. In the channel $H \to ZZ^* \to 4l$ and $H \to \gamma\gamma$ the best mass resolution is reached as the energy of leptons and photons can be measured well. For decay channels with neutrinos in the final state, due to subsequent decays of $W^{\pm}/Z^0$-bosons or τ-leptons, the missing transverse energy E_T^{miss}, defined in Eq. 6.2, does not allow for a full mass reconstruction, but requires the application of various approximations, which are discussed in Section 7.1.

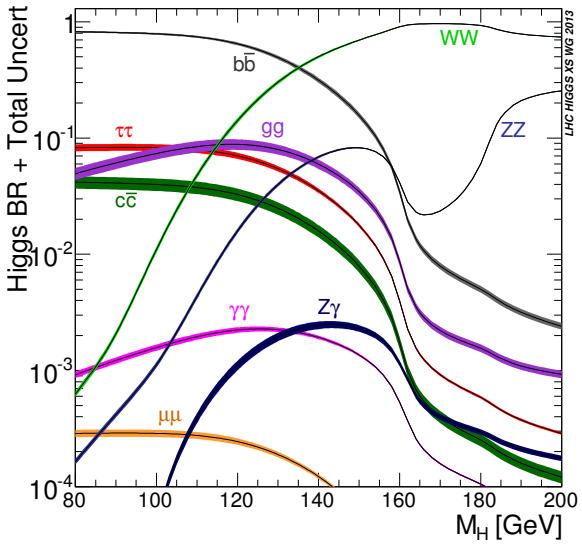

Figure 2.7.: Predicted branching ratio for the SM Higgs boson as a function of its mass m_H [51].

Decay channel	BR [%]
$b\bar{b}$	57.7
WW	21.5
gg	8.75
$\tau\tau$	6.32
$c\bar{c}$	2.91
ZZ	2.64
$\gamma\gamma$	0.23
Zγ	0.15
$\mu\mu$	0.02

Table 2.5.: Branching ratios for various decay channels for a Higgs-boson mass of $m_H = 125$ GeV [51].

2.2.4. Observation of a New Resonance and Measurement of its Properties at the LHC

In July 2012 the ATLAS and CMS experiments at CERN announced the observation of a new resonance with a mass of about 125 GeV and a significance of 5.9σ and 5.0σ, respectively [9, 10]. As shown in Fig. 2.8, this corresponds to a local p0-value of 1.7×10^{-9} for the ATLAS experiment and 4.2×10^{-6} for the CMS experiment. The local p0 value gives the probability for fluctuating backgrounds faking the observed resonance. In order to claim an observation a p0 value corresponding to 5σ is required.
With the full dataset of $25\,\mathrm{fb}^{-1}$ taken in 2011 and 2012 the ATLAS experiment measures the mass of the new resonance to be $m_H = 125.36 \pm 0.37(\mathrm{stat.}) \pm 0.18(\mathrm{sys.})\,\mathrm{GeV}$ [52], which is consistent with CMS measurements of $m_H = 125.02 \pm 0.27(\mathrm{stat.}) \pm 0.15(\mathrm{sys.})\,\mathrm{GeV}$ [53]. The combination of ATLAS and CMS results gives [11]:

$$m_H = 125.09 \pm 0.21(\mathrm{stat.}) \pm 0.11(\mathrm{syst.})\,\mathrm{GeV}.$$

In addition, the determination of the signal strength parameter $\mu = \sigma_{\mathrm{obs}}/\sigma_{\mathrm{SM}}$ for different production and decay channels provide a measure of potential deviations from the SM prediction. Thus, a consistency with the SM is obtained for a measured signal strength compatible with one. Fig. 2.9 shows the measurements of μ for various Higgs boson decay channels, where SM cross section ratios of different production modes are assumed. The results are so far all compatible with $\mu = 1$ within total uncertainties. The combination of these decay channels results in a measured coupling strength of [54]

$$\mu = 1.18 \pm 0.10\,(\mathrm{stat.}) + 0.07\,(\mathrm{syst.})^{+0.08}_{-0.07}\,(\mathrm{theo.})\,,$$

which is consistent with the SM expectation within 1.2 total standard deviations.
Furthermore, the signal strength can also be measured in different Higgs-boson production channels. Fig. 2.10 shows the results for the production in gluon fusion μ_{ggF}, in vector boson fusion μ_{VBF}, the Higgsstrahlung μ_{VH} and the associated production with top quarks μ_{ttH}. Here, SM values for the Higgs-boson decay branching ratios in the considered channels are assumed. The signal strength measurements are in reasonable agreement with the SM predictions.

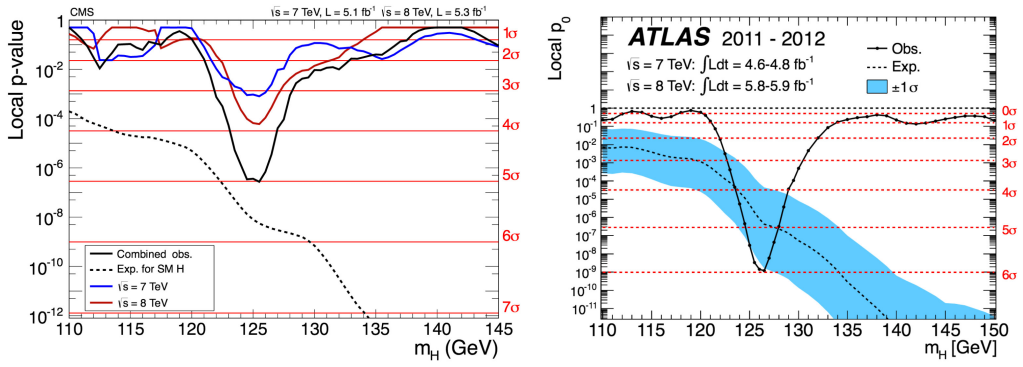

Figure 2.8.: The observed (solid) and expected (dashed) local p-value as function of m_H in the low mass range for the ATLAS [9] (left) and CMS [10] (right) experiments.

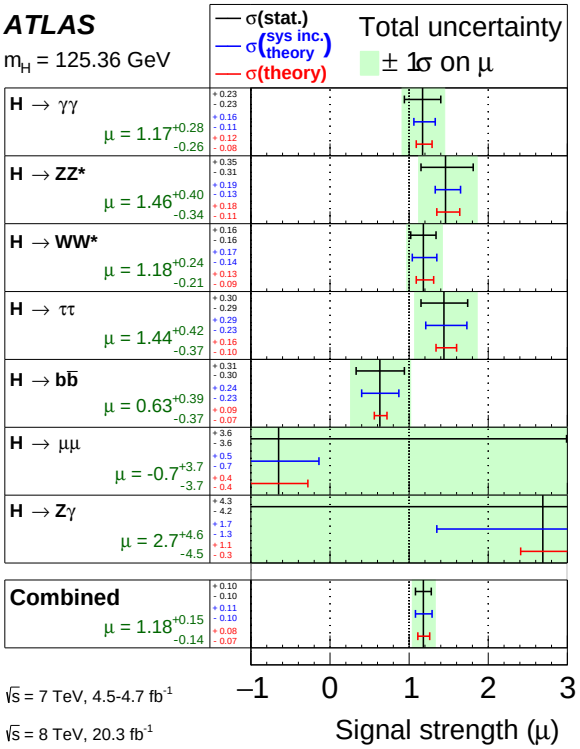

Figure 2.9.: The observed signal strengths and uncertainties for different Higgs-boson decay channels and their combination. The best-fit values are shown by the solid vertical lines. The total uncertainties are indicated by green shaded bands, with the individual contributions from the statistical uncertainty, the total experimental and theoretical systematic uncertainty, and the signal theoretical uncertainty [54].

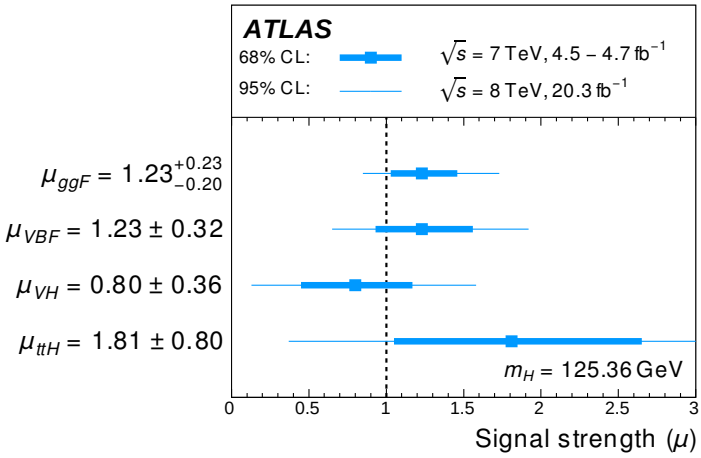

Figure 2.10.: Best-fit signal strength values for different production modes. The light (dark) blue band indicates the 68%(95%) CL intervals. The uncertainties include statistical, systematic and theoretical uncertainties. The fit assumes SM branching ratios for the Higgs boson [54].

2.2.5. Determination of Higgs-Boson CP Properties

In the SM, the Higgs boson is a CP even particle with a spin J of zero: $J^{\mathrm{CP}} = 0^+$. In general, the CP nature describes the particle's behaviour under **C**harge conjugation and **P**arity transformation. If all fundamental interactions of the particle remain invariant under such a transformation, this is called CP conservation. The particle is then an eigenstate of the CP operator with even (+1) or odd (-1) eigenvalue. On the other hand, if the particle is not found to be an CP eigenstates this results in a violation of CP invariance and would be direct evidence for beyond SM physics (BSM).
Results by the ATLAS and CMS experiments in the $H \to ZZ^* \to 4l$, $H \to WW^* \to 2l2\nu$ and $H \to \gamma\gamma$ final states indicate, that the Higgs boson indeed carries $J^{CP} = 0^+$ while other non-SM J^{CP}-configurations are excluded at more than 99.9% confidence level [15, 55]. However, an important study is to investigate if a mixing between CP even and CP odd eigenstate is present, which would result in the violation of CP invariance.
The CP properties of the Higgs boson can be associated with its coupling to other elementary particles. In its most general form, the tensor structure of this interaction vertex contains contributions from both CP even and CP odd couplings. An anomalous coupling of the Higgs boson is obtained, if a non-vanishing CP odd coupling contributes to the CP even prediction by the SM. Various measurements of CP properties have been performed in the past with most of them relying on the coupling of the Higgs boson to weak vector-bosons [15, 16]. Fig. 2.11 shows the test statistic distributions for the combination of $H \to WW^* \to 2l2\nu$ and $H \to ZZ^* \to 4l$ channels investigating the underlying coupling structure. In the coupling of the Higgs boson to weak vector-bosons, the CP-odd contribution is suppressed at loop level. Therefore, it is promising to study possible CP violation in the coupling of the Higgs boson to quarks and leptons, where both CP even and odd contributions enter at the same level. The next section gives a description of Higgs-gluon interactions in the context of effective field theories and introduces a parametrization for anomalous CP-odd contributions to the SM CP-even coupling.

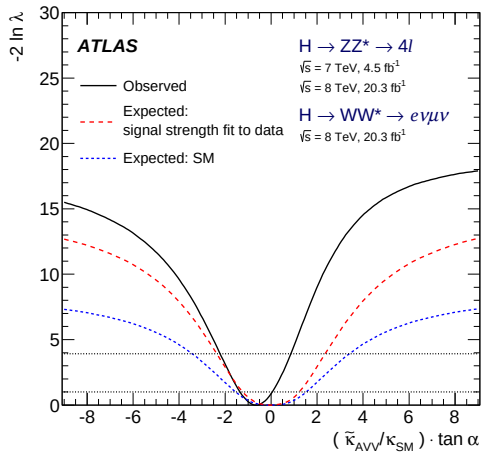

Figure 2.11.: Expected an observed distributions of the test statistics for the combination of $H \to ZZ^* \to 4l$ and $H \to WW^* \to 2l2\nu$ analyses as a function of the BSM coupling ratio $(\widetilde{\kappa}_{AVV}/\kappa_{SM}) \cdot \tan\alpha$. Here, κ_{SM} and κ_{AVV} denote the coupling constants corresponding to the interaction of a SM CP-even and BSM CP-odd particle with dibosons VV. The angle α allows for the production of CP mixed states between SM CP-even and BSM CP-odd [15].

2.3. Description of Higgs-gluon Couplings

The most general form of a Lagrangian density describing the interaction of a CP-even Higgs boson H, as predicted by the SM, with fermions f can be written as:

$$\mathcal{L}^f = \sum_{f=t,b,\tau} g_{Hff}\kappa_{Hff}\overline{\Psi}_f H \Psi_f \tag{2.46}$$

The fermion fields are given by Ψ_f, g_{Hff} refers to the corresponding Yukawa coupling strength and the constant κ_{Hff} can be taken as dimensionless. For simplicity, the assumption is made that only third generation fermions couple to the SM Higgs boson. In addition, a related Lagrangian can be constructed for the interaction of SM fermions with a CP-odd state A:

$$\widetilde{\mathcal{L}}^f = \sum_{f=t,b,\tau} g_{Aff}\kappa_{Aff}\overline{\Psi}_f \mathrm{A} i\gamma_5 \Psi_f \tag{2.47}$$

Here, g_{Aff} and κ_{Aff} are equivalent to the parameters in Eq. 2.46. Without loss of generality, the mixing between these scalar and pseudo-scalar states, both coupling to SM fermions, can be expressed in terms of a mixing angle α [56]:

$$\mathcal{L}_0^f = \sum_{f=t,b,\tau} \overline{\Psi}_f \left(\cos(\alpha) g_{Hff}\kappa_{Hff}\mathrm{H} + i\sin(\alpha) g_{Aff}\kappa_{Aff}\mathrm{A}\gamma_5\right)\Psi_f \tag{2.48}$$

The SM CP-even state is obtained with $\cos\alpha = 1$ and $\kappa_{Hff} \neq 0$, while a CP-odd state is represented by setting $\sin(\alpha) = 1$ and $\kappa_{Aff} \neq 0$. This parametrisation of the mixing between CP even and CP odd states is entirely independent of non-vanishing values for κ_{Hff} and κ_{Aff}. Therefore, CP violation is obtained for $\alpha \neq 0$ and $\alpha \neq \pi/2$ with non-vanishing $(g_{Hff}\kappa_{Hff})$ and $(g_{Aff}\kappa_{Aff})$.
As described in Section 2.2, the coupling of the Higgs-boson to gluons in the gluon-fusion production is dominated by a top-quark loop. Hence, the contribution from Higgs-boson couplings to b-quarks and τ-leptons in the gluon fusion production can be neglected. In the infinite top-quark mass limit $m_{top} \to \infty$ the Lagrangian in Eq. 2.48 can be approximated by an effective Higgs-gluon interaction

$$\mathcal{L}_{eff} = \left(\cos(\alpha) g_{Hgg}\kappa_{Hgg} G^a_{\mu\nu} G^{a,\mu\nu}\mathrm{H} + \sin(\alpha) g_{Agg}\kappa_{Agg} G^a_{\mu\nu}\tilde{G}^{a}_{\rho\sigma}\varepsilon^{\mu\nu\rho\sigma}\mathrm{A}\right) \tag{2.49}$$

with the gluon field strength tensors $G^a_{\mu\nu} = \partial_\mu G^a_\nu - \partial_\nu G^a_\mu + g_s f^{abc} G^b_\mu G^a_\nu$ and the total asymmetric tensor $\varepsilon^{\mu\nu\rho\sigma}$. The tensor structure for the effective Higgs-gluon interaction vertex is then given by

$$T^{\mu\nu} = g_{Hgg}\kappa_{Hgg}\left(q_1 q_2 g^{\mu\nu} - q_1^\nu q_2^\mu\right) + g_{Agg}\kappa Agg\varepsilon^{\mu\nu\rho\sigma} q_{1\rho} q_{2\sigma} \tag{2.50}$$

where q_1,q_2 give the four momentum vectors of the gluons. The couplings strengths g_{Hgg} and g_{Agg} can be expressed as [56]:

$$g_{Hgg} = -\frac{\alpha_s}{3\pi v} \qquad g_{Agg} = \frac{\alpha_s}{2\pi v} \tag{2.51}$$

with the vacuum expectation value v. In this analysis, the dimensionless constants κ_{Hgg} and κ_{Agg} are not varied, as the mixing between CP-even and CP-odd state is entirely parametrized in terms of the mixing angle α. Thus, $\kappa_{Hgg} = 1$ and $\kappa_{Agg} = -\frac{2}{3}$ are used in order to obtain $(g_{Hgg}\kappa_{Hgg}) = (g_{Agg}\kappa_{Agg})$.

In this thesis, the contribution of anomalous couplings in the Higgs-gluon interaction is investigated by measuring the underlying $\cos(\alpha)$-value. This is done by using observables, which show a distinct variation in their distributions for different contributions of CP-even and CP-odd couplings. The following section gives a short introduction into the general idea of testing CP invariance and describes the observables, which are used in this analysis to investigate the Higgs-gluon coupling structure.

2.4. Probing Higgs-gluon Couplings

2.4.1. Model-independet Test of CP Invariance

Assuming a CP conserving interaction, the expectation value of a CP odd observable $\mathcal{A}$ integrated over the whole CP-symmetric phase space Ω will be zero:

$$\langle \mathcal{A} \rangle = \int \frac{\mathcal{A}\, \mathrm{d}\Omega}{\mathrm{d}\Omega} = 0 \tag{2.52}$$

On the other hand, a non-vanishing expectation value implies CP violation in the process of interest. Thus, the deviation from zero provides a measurement of the amount of CP violation. This approach is called model-independet as no assumption of the underlying CP structure is made.
The following section introduces the CP odd observables, which are used in this analysis to investigate the CP structure of the effective Higgs-qluon coupling.

2.4.2. CP sensitive Observables

Signed Azimuthal-angle Difference $\Delta\Phi_{jj}^{sign}$

Investigations of the Higgs-gluon coupling structure in the process ggF H+2jets rely on the kinematic distributions of the outgoing jets, denoted as j_1, j_2. In particular, the azimuthal-angle difference between the jets $\Delta\Phi_{jj}$ provides a clear distinction between pure CP even and CP odd couplings [57]. However, $\Delta\Phi_{jj}$ is a CP even observable and therefore does not provide any sensitivity to anomalous CP odd contributions to the CP even coupling structure. Instead, a CP odd observable is obtained by defining an unambiguous sign for $\Delta\Phi_{jj}$ taking into account the correlation between jets and beam axis: Let $b_{+/-}$ be the normalized four momentum vector of the proton beams in positive/negative z-axis direction. Then $p_{+/-}$ can be defined as the four momentum vector of the tagging jet pointing into the same direction as $b_{+/-}$. The signed azimuthal angle difference between the tagging jets $\Delta\Phi_{jj}^{sign}$ is then defined as [57]:

$$\varepsilon_{\mu\nu\rho\sigma} b_+^\mu p_+^\nu b_-^\rho p_-^\sigma = 2 p_{T+} p_{T-} \sin(\Phi_+ - \Phi_-) = 2 p_{T+} p_{T-} \sin(\Delta\Phi_{jj}^{sign}) \tag{2.53}$$

In other words, $\Delta\Phi_{jj}^{sign}$ gives the azimuthal angle difference between the jet in the positive detector hemisphere (Φ_+) and the jet in the negative detector hemisphere (Φ_-). Therefore, the following requirement is applied in order to construct this observable:

$$\eta_{j1} \cdot \eta_{j2} < 0 \tag{2.54}$$

The distribution of $\Delta\Phi_{jj}^{sign}$ for pure SM, CP odd and a CP mixed coupling for ggF H+2jet events generated with MadGraph5 [58] at leading-order (LO) parton level for $\sqrt{s} = 8\,\mathrm{TeV}$ is shown in Fig. 2.12. The observable enables a clear distinction not only for pure SM and CP odd couplings, but also for CP mixed states.

As expected, no deviation from zero in terms of the expectation value $< \Delta\Phi_{jj}^{sign} >$ is observed for CP conserving interactions. However, the variation in $\Delta\Phi_{jj}^{sign}$ also depends on the rapidity separation Δy_{jj} between the tagging jets. As Fig. 2.13 shows, the variation in $\Delta\Phi_{jj}^{sign}$ for SM and CP odd coupling gets more pronounced for jets having a large rapidity separation. Therefore, requiring $\Delta y_{jj} > 3.0$ will reduce the number of events on the one hand, but also improve the sensitivity of the observable to anomalous contribution in the Higgs-gluon interaction, as shown in Fig. 2.14. A detailed study on the effect of these requirements on the event yield can be found in Section 7.3.3.

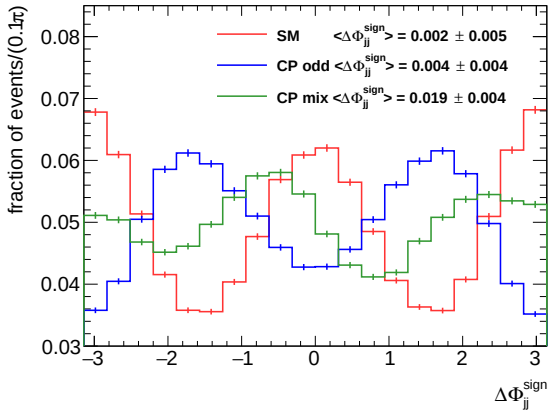

Figure 2.12.: The $\Delta\Phi_{jj}^{sign}$ distribution for SM,CP odd and CP mixed coupling with $\cos^2(\alpha) = 0.5$. The distributions are normalized to unit area.

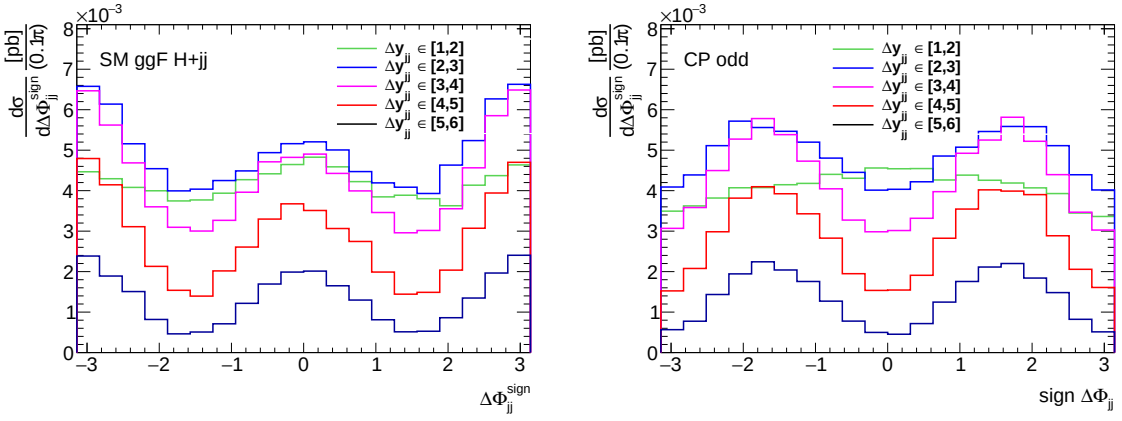

Figure 2.13.: The $\Delta\Phi_{jj}^{sign}$ distributions for SM (left) and CP odd (right) coupling for different rapidity separation intervals Δy_{jj} between the outgoing jets.

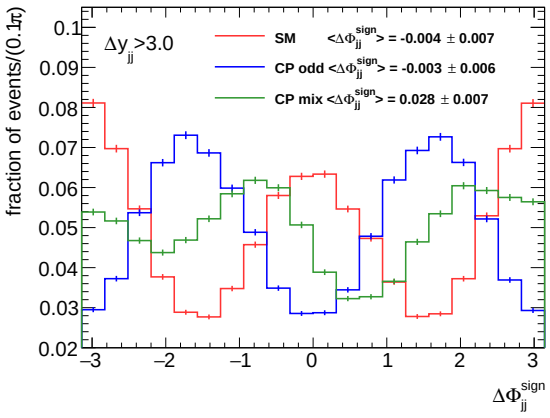

Figure 2.14.: The $\Delta\Phi_{jj}^{sign}$ distribution for SM, CP and CP mixed coupling with $\cos^2(\alpha) = 0.5$ by requiring a rapidity separation of the tagging jets of greater than 3.0. The distributions are normalized to unit area.

The Optimal Observable

The Optimal Observable *OO* [59–61] provides another possibility to test anomalous contribution in the effective Higgs-Gluon coupling. First applications of this observable can be found in the determination of τ-polarisation and dipol moment in $Z \to \tau\tau$ [63, 64] and in a sensitivity study for measuring CP violation in the Higgs-Strahlungs process at a future e^+e^- collider [65]. The following section presents the general parametrization, introduced in Section 2.3, for the construction of the matrix element, which includes CP even and CP odd contributions, and describes the Optimal Observable as used in this analysis.
The matrix element $\mathcal{M}$ of a process, where additional contribution to the SM coupling from CP odd interactions is considered, can be parametrized in the following way:

$$\mathcal{M} = \cos(\alpha)\mathcal{M}_{\mathrm{SM}} + \sin(\alpha)\mathcal{M}_{\mathrm{CPodd}} \tag{2.55}$$

Here the subscripts SM and CPodd refer to the case of pure SM and CP odd coupling respectively. As explained in Section 2.3, the parameter α defines the relative amount of SM and CP odd contribution. The squared matrix element is then given by:

$$|\mathcal{M}|^2 = \cos^2(\alpha)|\mathcal{M}_{\mathrm{SM}}|^2 + \cos(\alpha)\sin(\alpha)2\,\mathrm{Re}\,\{\mathcal{M}_{\mathrm{SM}}^*\mathcal{M}_{\mathrm{CPodd}}\} + \sin^2(\alpha)|\mathcal{M}_{\mathrm{CPodd}}|^2 \tag{2.56}$$

The CP odd interference term is sensitive to any possible CP violation, whereas terms quadratic in $\cos(\alpha)$ and $\sin(\alpha)$ do not change sign under CP transformation, but only change the total cross section with $\cos(\alpha)$.
A CP odd observable, taking into account matrix elements for CP even and CP odd interactions, is given by the Optimal Observable *OO* defined as

$$OO = \frac{2\,\mathrm{Re}\,\{\mathcal{M}_{\mathrm{SM}}^*\mathcal{M}_{\mathrm{CPodd}}\}}{|\mathcal{M}_{\mathrm{SM}}|^2} \tag{2.57}$$

The Optimal Observable combines the informations of the seven-dimensional phase space into one single observable, and therefore provides the highest sensitivity of a one-dimensional observable.
The matrix elements depend on the kinematics of initial and final state particles in terms of four momentum vectors:

$$\mathcal{M} = \mathcal{M}(p_{p1}^\mu, p_{p2}^\mu, p_{k1}^\mu, p_{k2}^\mu, p_H^\mu) \tag{2.58}$$

Here $p_{1/2}$ and $k_{1/2}$ refer to the four momentum vector of the incoming and outgoing partons respectively and p_H gives the four momentum vector of the Higgs-boson. Due to energy and momentum conservation, the four momentum vectors are not independent.
However, when calculating the matrix element for an experimentally measured event (reconstruction level), the outgoing partons will be measured as color-neutral jets in the detector and no information about the kinematics of the initial state partons $p_{1,2}$ are directly accessible. Therefore, the missing components have to be calculated from the final state:

$$\begin{aligned} p^{\mu}_{p1} &= x_1 \frac{\sqrt{s}}{2}(1,0,0,1) \quad \text{with} \quad x_1 = \frac{M_{final}}{\sqrt{s}} e^{+y_{final}} \\ p^{\mu}_{p2} &= x_2 \frac{\sqrt{s}}{2}(1,0,0,-1) \quad \text{with} \quad x_2 = \frac{M_{final}}{\sqrt{s}} e^{-y_{finale}} \end{aligned} \tag{2.59}$$

Here, M_{final} and y_{final} are the invariant mass and rapidity of the vectorial sum of the Higgs boson and the outgoing jets. In Section 7.1 the reconstruction of the Higgs-boson four momentum vector is discussed. The matrix element given in Eq. 2.58 also depends on the color-flavor combination of the initial and final state partons. Therefore, a weighted matrix element calculation is used:

$$\mathcal{M}(p^{\mu}_{p1}, p^{\mu}_{p2}, p^{\mu}_{k1}, p^{\mu}_{k2}, p^{\mu}_{H}) = \sum_{f_1 f_2 \to f_3 f_4} \mathcal{M}(p^{\mu}_{p1,f1}, p^{\mu}_{p2,f2}, p^{\mu}_{k1,f3}, p^{\mu}_{k2,f3}, p^{\mu}_{H}) \cdot F(x_1, f_1) \cdot F(x_2, f_2) \tag{2.60}$$

Here, the summation goes over all possible flavour combinations of incoming and outgoing partons $f_1 f_2 \to f_3 f_4$. The matrix element for each flavor combination is then weighted with the corresponding parton-distribution factors $\mathrm{F}(x_i, f_i)$ providing the probability for parton i with flavour f_i to have a momentum fraction x_i. These weights are calculated using the LHAPDF package [66] with the CT10 PDF set [67]. Fig. 2.15 shows the Optimal Observable for SM coupling, CP odd coupling and CP mixed coupling with $\cos^2(\alpha) = 0.50$. The matrix elements have been calculated with MadGraph5 [58]. As expect, the Optimal Observable distribution shows an asymmetry for the CP violating coupling with $\cos^2(\alpha) = 0.50$. For this coupling a non-zero mean value $< \mathrm{OO} >$ is obtained, while the SM and CP odd couplings result in a symmetric distribution with a mean value compatible with zero.

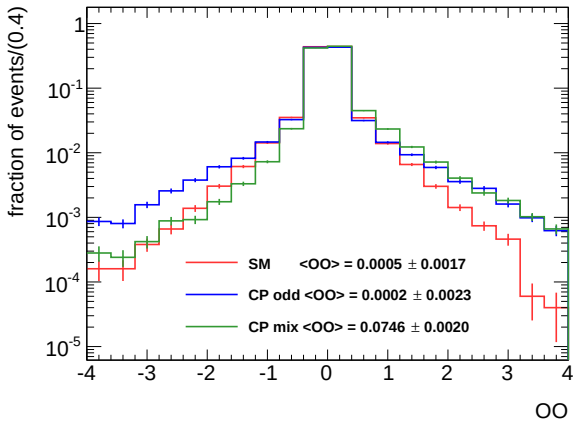

Figure 2.15.: The Optimal Observable distribution for SM, CP odd and CP mixed coupling with $\cos^2(\alpha) = 0.5$. The distributions are normalized to unit area.

3 Signal and Background Processes

This chapter describes the experimental signature of Higgs-boson production in gluon fusion in association with two jets and discusses the main background processes. As shown in Fig. 2.2 the Higgs-boson production cross sections are much lower compared to the total production cross section at the LHC. Therefore, the relevant background processes must be well-known and modelled. The prediction of signal and background processes with simulated events is discussed in Section 3.3.1. In addition, Section 3.3.2 describes the reweighting procedure in order to simulate Higgs-boson production with anomalous couplings. The parametrization of these anomalous couplings and the description of effective Higgs-gluon interactions can be found in Section 2.3.

3.1. Signal Process

This analysis focuses on the Higgs-boson production in the gluon-fusion channel with two jets in the final state, which will be referred to as ggF H+2jets. The gluon-fusion production yields the highest cross section for $m_H = 125\,\text{GeV}$. The coupling of the Higgs boson to the massless gluons take place via heavy quark loops and can be approximated by an effective Higgs-gluon interaction vertex for $m_{top} \to \infty$, as described in Section 2.3. At leading order (LO), the gluon fusion production has no additional partons in the final state. However, due to the color charged initial state partons and the heavy quark loops, additional partons can be produced via higher-order QCD corrections. Fig. 3.1 shows Feynman diagrams for H+2jet production in gluon fusion with an effective Higgs-gluon coupling for gluon-gluon, quark-gluon and quark-quark initial states. These initial state configurations can be grouped in different sub-processes. The kinematic of these sub-processes and their contribution to the total ggF H+2jet production is discussed in detail in Section 4.2.
Due to their colour charge, the final state partons hadronize and can be reconstructed as jets in the detector. In the presence of additional jets, the Higgs boson recoils against the jet system and receives a transverse momentum.
This analysis focuses on the Higgs boson decay into a pair of τ-leptons $H \to \tau\tau$ with a branching ratio of 6.3 %. The τ-lepton itself decays after a mean lifetime of $2.9 \times 10^{-13}\,\text{s}$ via weak interactions into leptons or hadrons. Therefore, three different sub-channels depending on the final state particles can be define: The full-leptonic states, where both τ-leptons decay into electrons or muons with corresponding neutrinos, the semi-leptonic state with one τ-lepton decaying hadronically and the other one leptonically, and the full-hadronic state. The combined branching ratios for full-leptonic, full-hadronic states and semi-leptonic are 12%, 42% and 46% respectively. Although the semi-leptonic and full-hadronic channels provide the highest combined branching ratio, these channels have to deal with significant contributions from multi-jet QCD events, which are described below. For the full-leptonic state, this background contribution is considerably less. Furthermore, lepton triggers provide a higher efficiency compare to hadronic trigger systems. Therefore, this analysis focuses on the full-leptonic channel $H \to \tau\tau \to 2l4\nu$. This results in a final state signature of the signal process

including two jets, two leptons with opposite electric charge and missing transverse energy due to the neutrinos.
As the τ-system originates from the resonant Higgs-boson state, combining the four momenta of the final state particles allows in principle to reconstruct its invariant mass and to suppress other background processes, where the final state particles do not originate from a Higgs-boson decay. However, due to neutrinos in the final state, which are reconstructed as missing transverse energy in the detector, the four momentum of the Higgs boson cannot be fully determined. Instead, several approximations have to be applied, which are described in Section 7.1.

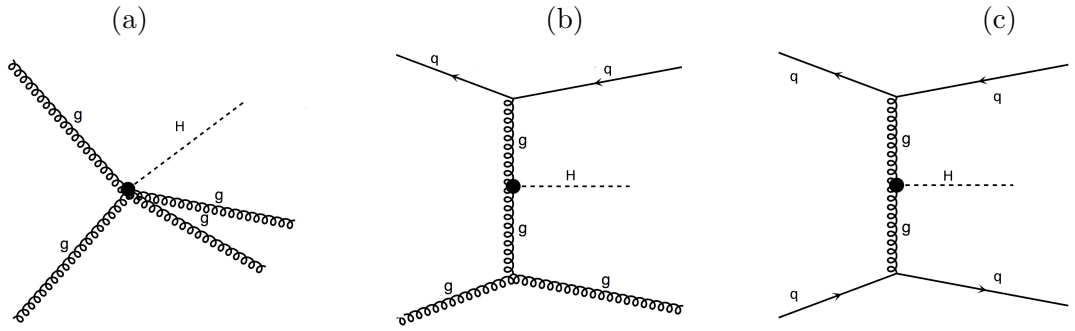

Figure 3.1.: Feynman diagrams for H+2jet production at leading order in an effective Higgs-gluon interaction for (a) gluon-gluon, (b) quark-gluon and (c) quark-quark initial states.

3.2. Background Processes

Background processes contributing to the ggF H+2jet signal as discussed above, can be divided into reducible and irreducible processes. Events with final state topologies different from the signal process, but where misidentification of physical objects and deficient reconstruction of missing transverse energy in the detector can lead to classification as signal events, are called reducible backgrounds. Irreducible backgrounds, on the other hand, provide same final state signatures as the signal process and are therefore more difficult to suppress. The following section describes the main background contributions, which are considered in this analysis.

Higgs-Boson Background Processes

In contrast to Higgs-boson searches, where different production modes are combined in order to increase the sensitivity, this analysis aims to investigate the Higgs-gluon coupling structure in the gluon fusion channel and therefore relies on sufficient rejection of other Higgs-boson production modes, where no anomalous couplings are expected. For the ggF H+2jet signal, Higgs-boson production in the VBF and VH channel provide similar final state topologies compared to signal events. However, the characteristic signature of VBF events yields final state jets, which are well separated in pseudorapidity and tend to have higher values in their invariant mass m_{jj} compared to jets from gluon-fusion production. In addition, the associated VH production with hadronically decaying $W^{\pm}/Z^{0}$-bosons features same final state signatures, but is less important than the VBF production due to its smaller production

cross-section (see Section 2.2.2).
For all Higgs-boson production modes the decay into $W^{\pm}$-bosons $H \to W^+W^-$ give a non-negligible background contribution. Leptonic decays of the $W^{\pm}$-bosons result in final states with opposite charged leptons, jets and missing transverse energy. Since the investigation of Higgs-gluon couplings does not depend on the Higgs-boson decay channel but focuses on the production mode, $H \to W^+W^-$ events produced in gluon fusion gives an additional signal contribution in principle. This analysis, however, does not include $H \to W^+W^-$ events in the investigation of the Higgs-gluon coupling structure.

W/Z-Boson Production in Association with Jets

The production of Z^0-bosons or virtual photons γ^* in association with jets with subsequent leptonic decays give an important background contribution to the ggF H+2jet signal. In particular, final states with leptonically decaying τ-leptons $Z/\gamma^* \to \tau\tau \to ll + 2\nu$ contribute as an irreducible background, since it features the same final state topology as the signal. Processes with Z/γ^*-decays into electrons or muons are the dominant background contribution to final states with same-flavor leptons $(ee), (\mu\mu)$. In such events missing transverse energy can arise due to deficient reconstruction of jets. Fig. 3.2 shows the Feynman diagrams for Z^0-boson production with up to two jets.
Another background contribution arises from $W^{\pm}$-boson production in association with jets, where the $W^{\pm}$-boson decays into leptons. In case of misidentification of a further jet as a lepton, this process provides final state signatures with two leptons and missing transverse energy. In Fig. 3.3 Feynman diagrams contributing to $W^{\pm}$-production with up to two jets are shown.

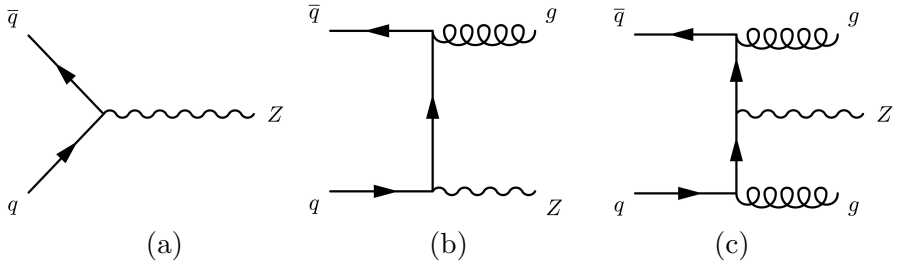

Figure 3.2.: Feynman diagrams for Z-boson production in association with (a) no jets, (b) one jet and (c) two jets.

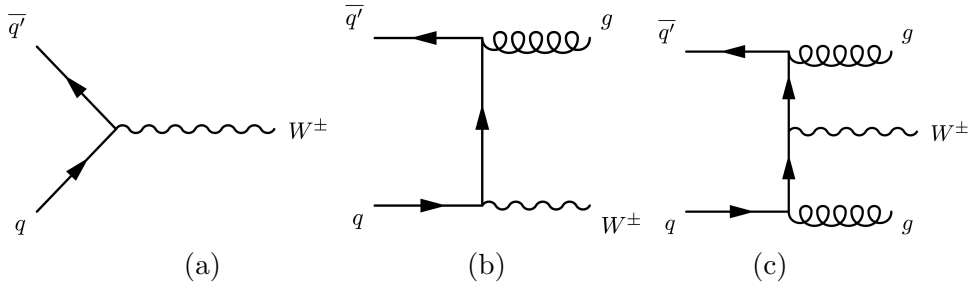

Figure 3.3.: Feynman diagrams for $W^{\pm}$-boson production in association with (a) no jets, (b) one jet and (c) two jets.

Di-boson Production

This background contribution combines all processes with WW-, ZZ- or WZ-di-boson production. The W- and Z-bosons can decay either leptonically or hadronically, therefore providing final states including leptons and jets. Since the signal process features missing transverse energy from two neutrinos in the final state, the most import di-boson background contribution comes from full leptonic WW-boson decays $WW \to l\nu l\nu$. In Fig. 3.4 Feynman diagrams for several di-boson production modes are shown.

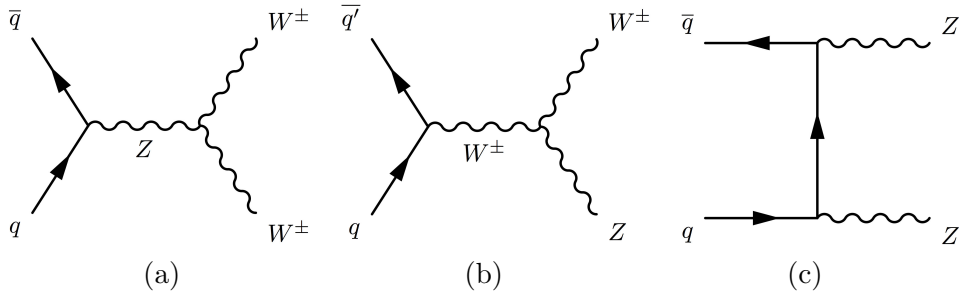

Figure 3.4.: Feynman diagrams for (a) WW-, (b) WZ- and (c) ZZ- di-boson production

Single Top-quark and Top-quark Pair Production

As Fig. 3.5 shows single top-quarks can be produced in the s-channel, t-channel and in association with a W-boson. The top quark then decays with a branching ratio of almost 100% into a W-boson and a b-quark. Therefore, further leptonic decays of the W-boson or misidentification of jets result in a final state signature similar to the signal process.
However, the major background contribution involving top quarks comes from top-quark pair production with decays into b-quarks and W-bosons. Subsequent leptonic decays of the W-bosons feature events topologies with two jets, two leptons and missing transverse energy in the final state. Fig. 3.5 and Fig. 3.6 show Feynman diagrams for single and top-quark pair production. Background contributions including top quarks can be significantly suppressed by using flavor-tagging information, described in Section 6.4, in order to reject events with b-jets.

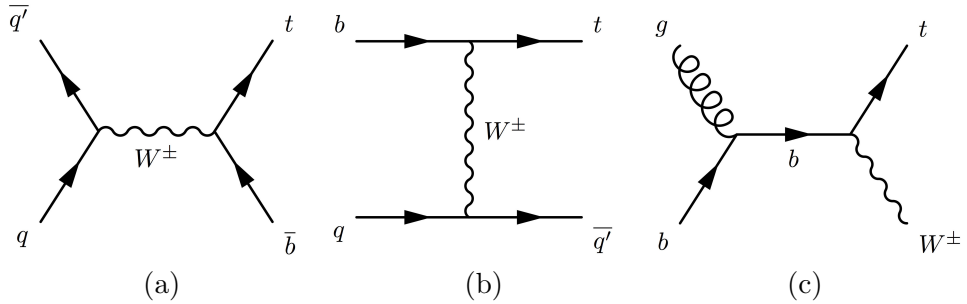

Figure 3.5.: Feynman diagrams for single top-quark production in the (a) s-channel, (b) t-channel and (c) in association with a W-boson.

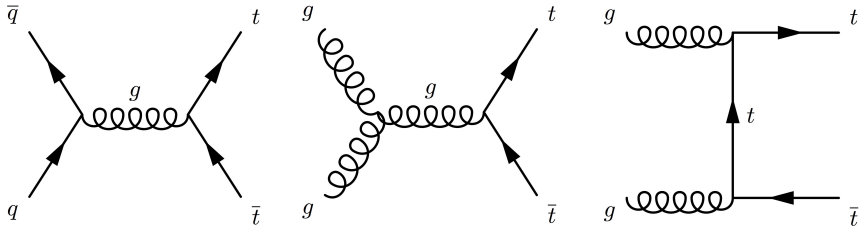

Figure 3.6.: Feynman diagrams for top-quark pair production $t\bar{t}$.

QCD Multi-jet Production

At hadron colliders various QCD processes involving outgoing quarks and gluons arise with large production cross sections. Fig. 3.7 shows examples of such QCD multi-jet processes. The color-charged partons hadronize and produce final states with multiple jets. In such events, deficient jet reconstruction and misidentification of jets as leptons can lead to final state signatures including leptons and missing transverse energy. Tight lepton selection requirements and isolation criteria can reduce this background contribution.

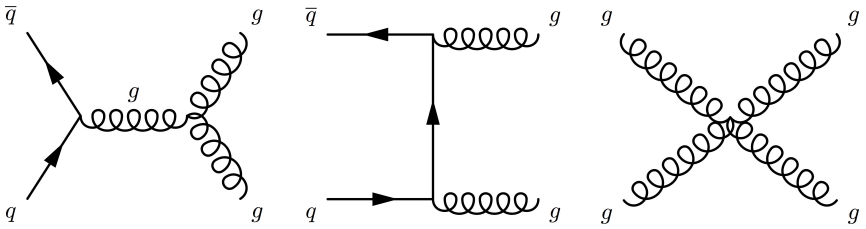

Figure 3.7.: Feynman diagrams for multijet production in QCD processes.

3.3. Monte-Carlo Simulations

3.3.1. Generators

Events for ggF H+2jets are simulated with the Multi scale-improved NLO MC Generator MINLO [68]. In this analysis, a MINLO one-jet sample at NLO is used, which describes the Higgs-boson production with two jets at LO accuracy. The Higgs-boson production in the VBF channel is simulated with POWHEG+PYTHIA [69], while for the associated Higgs-boson production PYTHIA8 [70] is used.
Events coming from Z^0/γ^*+jets and $W^{\pm}$+jets processes are simulated with ALPGEN [71]. For top-quark pair events $t\bar{t}$ and single top-quark production in association with $W^{\pm}$-bosons MC@NLO [72–74] is used, whereas single top-quark production in the s/t-channel is simulated with AcerMC [75]. Diboson events are generated with HERWIG [76].
In Table 3.1 an overview of the cross sections for signal and background processes is given.
For all background processes parton shower and hadronization are simulated with HERWIG and the underlying event with JIMMY [77]. The CT10 [67] parton distribution function (PDF) is used for processes generated with POWHEG and MC@NLO, while CTEQ6L1 [78] is used for PYTHIA and ALPGEN samples. The detector simulation is performed with GEANT4 [79]. A detailed description on the MC simulations and the generators can be found in Ref. [104].

Process	Sample	$\sigma \times$ BR [pb]	
SM $H \to \tau\tau$			
	ggF $H + 2\text{jets} \to 2l4\nu$	0.151	
	VBF $H \to 2l4\nu$	0.012	
	WH $H \to 2l4\nu$	0.006	
	ZH $H \to 2l4\nu$	0.003	
SM $H \to WW$			
	ggF $H \to 2l2\nu$	0.216	
	VBF $H \to 2l2\nu$	0.018	
	WH $H \to 2l2\nu$	0.015	
	ZH $H \to 2l2\nu$	0.009	
$Z/\gamma^* \to ee, \mu\mu$		ee	$\mu\mu$
	$60\,\text{GeV} \leq m_{ll} \leq 2\,\text{TeV}$ $NP = 0$	848.4	848.6
	$60\,\text{GeV} \leq m_{ll} \leq 2\,\text{TeV}$ $NP = 1$	207.3	207.4
	$60\,\text{GeV} \leq m_{ll} \leq 2\,\text{TeV}$ $NP = 2$	69.5	69.5
	$60\,\text{GeV} \leq m_{ll} \leq 2\,\text{TeV}$ $NP = 3$	18.5	18.5
	$60\,\text{GeV} \leq m_{ll} \leq 2\,\text{TeV}$ $NP = 4$	4.7	4.7
	$60\,\text{GeV} \leq m_{ll} \leq 2\,\text{TeV}$ $NP = 5$	1.5	1.5
	$10\,\text{GeV} \leq m_{ll} \leq 40\,\text{GeV}$ $NP = 0$	699.7	726.4
	$10\,\text{GeV} \leq m_{ll} \leq 40\,\text{GeV}$ $NP = 1$	51.1	52.0
	$10\,\text{GeV} \leq m_{ll} \leq 40\,\text{GeV}$ $NP = 2$	24.9	25.4
	$10\,\text{GeV} \leq m_{ll} \leq 40\,\text{GeV}$ $NP = 3$	5.8	5.8
	$10\,\text{GeV} \leq m_{ll} \leq 40\,\text{GeV}$ $NP = 4$	1.8	1.9
	$40\,\text{GeV} \leq m_{ll} \leq 60\,\text{GeV}$ $NP = 0$	36.4	36.7
	$40\,\text{GeV} \leq m_{ll} \leq 60\,\text{GeV}$ $NP = 1$	6.4	6.4
	$40\,\text{GeV} \leq m_{ll} \leq 60\,\text{GeV}$ $NP = 2$	2.2	2.3
	$40\,\text{GeV} \leq m_{ll} \leq 60\,\text{GeV}$ $NP = 3$	0.6	0.6
	$40\,\text{GeV} \leq m_{ll} \leq 60\,\text{GeV}$ $NP = 4$	0.2	0.2
	VBF-filtered $NP = 2$	3.8	1.4
	VBF-filtered $NP = 3$	2.2	1.2
	VBF-filtered $NP = 4$	0.9	0.6
	VBF-filtered $NP = 5$	0.4	0.4
	Electroweak	0.4	0.4
Top-quark			
	Single top, s-channel, leptonic decay	1.8	
	Single top, t-channel, leptonic decay	22.4	
	Single top, (W+t)-channel	22.4	
	$t\bar{t}$	129.3	
Di-boson			
	ZZ	1.6	
	WZ	6.8	
	$qq \to WW \to ll\nu\nu$ $NP = 0$	3.0	
	$qq \to WW \to ll\nu\nu$ $NP = 1$	1.5	
	$qq \to WW \to ll\nu\nu$ $NP = 2$	0.7	
	$qq \to WW \to ll\nu\nu$ $NP = 3$	0.4	
	$qq \to WW \to qql\nu$ $NP = 0$	12.6	
	$qq \to WW \to qql\nu$ $NP = 1$	6.3	
	$qq \to WW \to qql\nu$ $NP = 2$	3.0	
	$qq \to WW \to qql\nu$ $NP = 3$	1.7	
	$gg \to WW \to ll\nu\nu$ $NP = 3$	0.2	

Table 3.1.: Predicted cross sections for the signal and background processes at $\sqrt{s} = 8\,\text{TeV}$ and $m_H = 125\,\text{TeV}$. The MC generators are described in the text. NP refers to the number of associated partons.

3.3.2. Reweighting Procedure for Anomalous Couplings

In order to investigate the Higgs-gluon coupling structure a variety of signal samples for different coupling models are required. However, due to limited computational resources it is not feasible to simulate the signal events for each of the various coupling models of interest all over again. Instead, a matrix-element based reweighting method is applied on the existing SM ggF H+2jet signal sample. In this procedure, the weight w depends on the squared matrix elements of the considered Higgs-gluon coupling model and the SM coupling:

$$w(\cos(\alpha)) = \frac{|\mathcal{M}(\cos(\alpha))|^2}{|\mathcal{M}_{SM}|^2} \quad \text{with } \mathcal{M}_{SM} = \mathcal{M}(\cos(\alpha) = 1) \tag{3.1}$$

Here, the parameter $\cos(\alpha)$ drives the mixing between CP-even and CP-odd contributions in the Higgs-gluon coupling structure as described in Section 2.3. The reweighting method takes as input truth level information about the initial and final state particles as well as the flavor combination of the involved partons. The matrix element calculations are performed with MadGraph5 [80] at leading order.
In order to validate this reweighting procedure, a comparison between reweighted signal events and events, which are directly generated with MadGraph5 within the *Higgs-Characterisation* framework [56] for different coupling models, is shown in Fig. 3.8. The distributions for the Optimal Observable and $\Delta\Phi_{jj}^{sign}$ show a good agreement for reweighted and directly produced events.

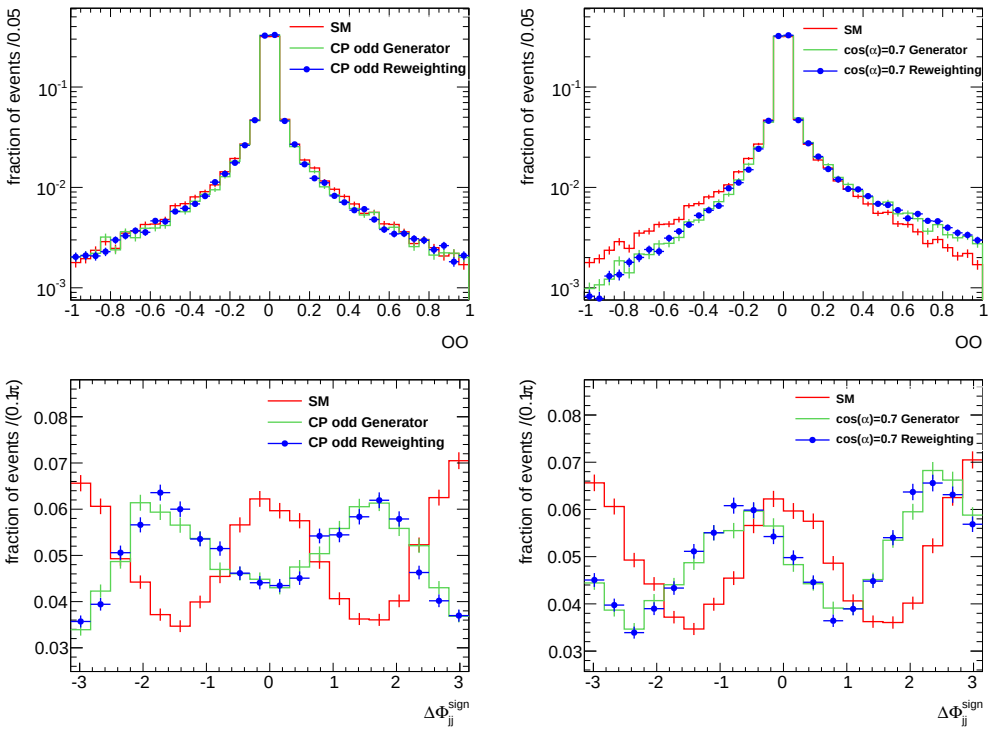

Figure 3.8.: Comparison between generated ggF H+2jet signal events with MadGraph5 [80] and reweighted events, as discussed in the text, for the Optimal Observable OO (top) and $\Delta\Phi_{jj}^{sign}$ (bottom). The distributions of generated and reweighted signal events for a CP odd (left) and a CP mixed coupling with $\cos^2(\alpha) = 0.50$ (right) are in good agreement for both the Optimal Observable and $\Delta\Phi_{jj}^{sign}$.

4 Investigation of Anomalous Higgs-gluon Couplings at Generator Level

This chapter describes the investigation of the sensitivity to anomalous contributions in the Higgs-gluon coupling structure for the Optimal Observable and $\Delta\Phi_{jj}^{sign}$, introduced in Section 2.4.2, for simulated H+2jet events in the gluon-fusion production generated with MadGraph5 [80]. The sensitivity is estimated by considering the mean value of the observables for different coupling models in terms of the mixing parameter $\cos(\alpha)$. As described in Section 2.4 CP-odd observables, as the Optimal Observable and $\Delta\Phi_{jj}^{sign}$, provide a mean value which is compatible with zero for CP conserving couplings, while a non-zero mean value is obtained for CP violating couplings. Thus, considering the mean value for different coupling models allows to derive a sensitivity estimate on how well these models can be separated. The H+2jet production in gluon-fusion can be grouped into different sub-channels depending on the flavour combination of the initial and final state partons. The sensitivity estimate to anomalous contributions depending on the initial state configurations will also be discussed in this chapter.
The events are generated at leading-order parton level for $\sqrt{s} = 8\,\text{TeV}$ within the *Higgs Characterisation* model [56]. The outgoing partons will be denoted as jets in the following. The `NNPDF23LO1` pdf set [81] is used and the events are simulated in a 4 quark-flavour scheme without parton shower. The Higgs boson is further decayed into a pair of τ-leptons, which are then assumed to be stable. However, the analysis presented here does not depend on the decay channel of the Higgs boson.
Several kinematic cuts are applied on generator level to jets and τ-leptons, which are summarized in Table 4.1. They ensure a phase space region, which is experimentally accessible. In addition, the observable $\Delta\Phi_{jj}^{sign}$ requires the jets to be in different detector hemisspheres: $\eta_{j1}\eta_{j2} > 0$. The events are simulated for an effective SM Higgs-gluon coupling and are then reweighted for various $\cos(\alpha)$-models with the reweighting precdure described in Section 3.3.2. In the following, only the sensitivity of the signal process is investigated, therefore no background processes are considered. A detailed analysis of the sensitivity estimate for signal and background expectations with a full simulation of the detector is given in Section 10.
The chapter is organized as follows: The first part describes the investigation of the sensitivity for ggF H+2jet events on parton level by using the Optimal Observable and $\Delta\Phi_{jj}^{sign}$. Then, the contributing sub-processes are described and their sensitivity to anomalous couplings in the Optimal Observable and $\Delta\Phi_{jj}^{sign}$ is discussed.

Variable	Jets	τ-leptons
p_T	$> 20\,\text{GeV}$	$> 10\,\text{GeV}$
$\lvert\eta\rvert$	< 5.0	< 2.5
$\Delta R(jj(\tau\tau))$	> 0.4	> 0.4

Table 4.1.: Kinematic cuts applied to jets and τ-leptons for ggF H+2jet events generated with Madgraph5. The τ-leptons are not further decayed. The outgoing partons are referred to as jets, where the events are generated in a 4 quark-flavour scheme.

4.1. Investigation of Sensitivity of ggF H+2jets

The observables used in this analysis are the Optimal Observable and $\Delta\Phi_{jj}^{sign}$, which are introduced in Section 2.4.2 and Section 2.4.2. In Fig. 2.15 and Fig. 2.12 the distributions for the Optimal Observable and $\Delta\Phi_{jj}^{sign}$ are shown for SM ($\cos(\alpha) = 1$), CP odd ($\cos(\alpha) = 0$) and a CP mixed coupling with $\cos^2(\alpha) = 0.50$. For $\Delta\Phi_{jj}^{sign}$ the outgoing jets are required to be in different detector hemis spheres, which reduces the available statistics by 60% and increases statistical uncertainties.
As explained in Section 2.4.1 the sensitivity of an CP-odd observable to CP-violating interactions can be measured in terms of the deviation of its mean value from zero. Fig. 4.1 shows the mean value of the Optimal Observable and $\Delta\Phi_{jj}^{sign}$ including statistical uncertainties for various $\cos(\alpha)$-values. As expected, the mean value for SM and CP odd couplings is compatible with zero within statistical uncertainties, while CP-violating couplings result in a non-zero mean value. In addition, a mean value of zero is obtained for a CP-conserving coupling with $\cos(\alpha) = -1$. Although this $\cos(\alpha)$-model does not directly correspond to a SM Higgs-gluon coupling with $\cos(\alpha) = 1$, the squared matrix element itself is not sensitive to the absolute sign of the SM coupling: $|\mathcal{M}(\cos(\alpha) = 1)|^2 = |\mathcal{M}(\cos(\alpha) = -1)|^2$. Therefore, the Optimal Observable and $\Delta\Phi_{jj}^{sign}$do to differ between $\cos(\alpha) = \pm 1$.
A maximum deviation of the mean value from zero is observed for $\cos(\alpha) = \pm 0.70$, which corresponds to a contribution of SM and CP odd coupling of approximately equal size[1]. Furthermore, a positive mean value refers to $\cos(\alpha) \in (0, 1)$, while a negative mean value is obtained for $\cos(\alpha) \in (-1, 0)$. The error bars correspond to the statistical uncertainty of the mean value.
Both, the Optimal Observable and $\Delta\Phi_{jj}^{sign}$, provide a good separation for the considered $\cos(\alpha)$-models. However, the increased statistical uncertainties for $\Delta\Phi_{jj}^{sign}$ dilutes its separation power in terms of mean value differences compared to the Optimal Observable.
In order to directly compare the sensitivity of the observables for different coupling models Fig. 4.2 shows the mean value normalized to the root mean square (RMS) for the Optimal Observable and $\Delta\Phi_{jj}^{sign}$. The Optimal Observable provides a larger variation in terms of the normalized mean value compared to $\Delta\Phi_{jj}^{sign}$ for a wide $\cos(\alpha)$-range.

[1]The exact same amount of CP even and CP odd contribution is obtained for $\cos(\alpha) = \sqrt{\frac{1}{2}}$=0.7071

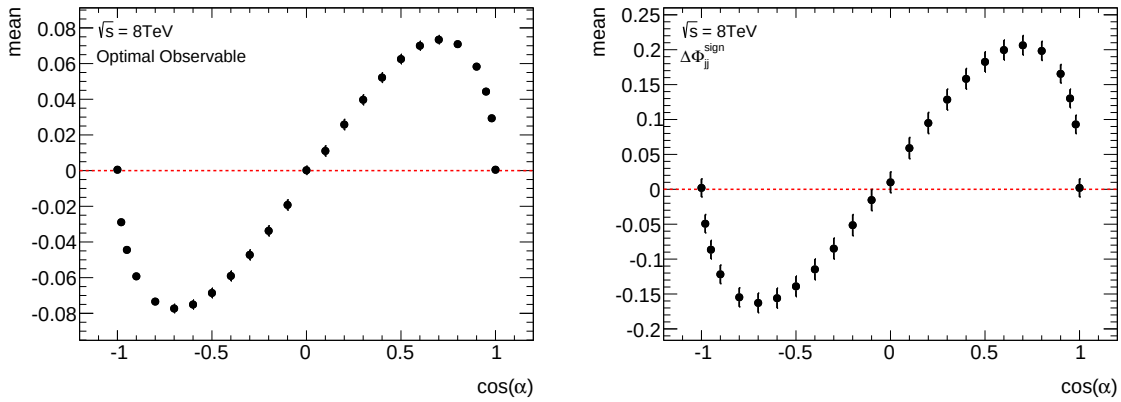

Figure 4.1.: Mean of the Optimal Observable (left) and $\Delta\Phi_{jj}^{sign}$(right) including statistical uncertainties for different cos(α)-values. The dotted line indicates the expectation of a mean value compatible with zero for CP-conserving couplings (cos(α) = $\pm 1, 0$). The events are generated with MadGraph5 [80] at leading order parton level for H+2jet production in gluon fusion.

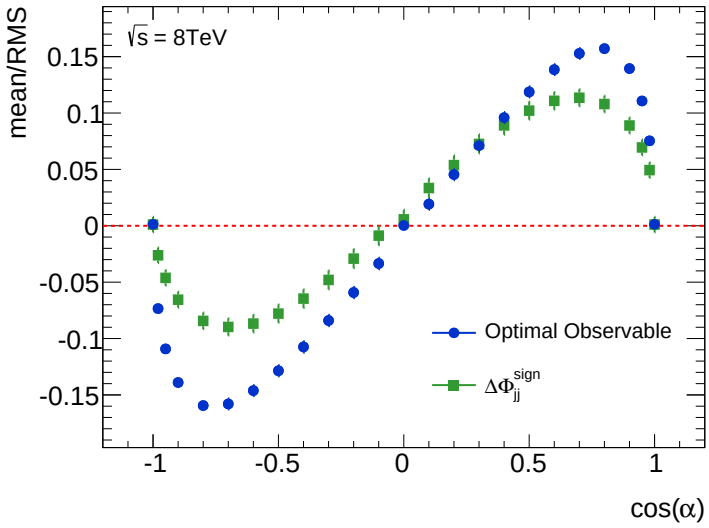

Figure 4.2.: Comparison of the mean value normalized to the root mean square (RMS) for the Optimal Observable (blue) and $\Delta\Phi_{jj}^{sign}$ (green) for different cos(α)-values including statistical uncertainties. The dotted line indicates the expectation of a mean value compatible with zero for CP-conserving couplings (cos(α) = $\pm 1, 0$). The events are generated with MadGraph5 [80] at leading order parton level for H+2jet production in gluon fusion.

4.2. Investigation of Sensitivity of Sub-Processes

The production of a Higgs boson in gluon fusion with two jets can be classified into different groups depending on the flavour combination of the initial state partons: The gluon-gluon, gluon-quark and quark-quark initial states. Fig. 4.3 shows leading-order Feynman diagrams for these groups. By also considering the final state partons, twelve different sub-processes can be defined in total. Table 4.2 lists these sub-processes and summarizes the relative contribution of the initial state combinations to the total H+2jet production. The dominant contribution is given by gluon-gluon (60%) and gluon-quark initial states (37%), while the contribution of quark-quark initiated sub-processes is rather small (3%).
In order to investigate the properties of the outgoing jets for the different initial state processes, Fig. 4.4 shows the rapidity and azimuthal angle difference between the jets as well as their invariant mass for gluon-gluon, gluon-quark and quark-quark initial states. While the sub-process including gluon-gluon and gluon-quark initial states provide a rather small rapidity separation between the outgoing jets, the distribution for quark-quark initial states is shifted to higher values. In addition, the jets azimuthal angle difference shows a distinct variation for quark-quark sub-processes compared to events with gluon-gluon and gluon-quark initial states. Furthermore, quark-quark initiated sub-processes provide a larger invariant mass of the jet system.
As the CP-sensitive observables also rely on the jet properties, Fig. 4.5 and Fig. 4.6 show the Optimal Observable and $\Delta\Phi_{jj}^{sign}$ distributions comparing SM, CP odd and a CP mixed ($\cos^2(\alpha) = 0.50$) coupling for gluon-gluon, gluon-quark and quark-quark initial states. For both the Optimal Observable and $\Delta\Phi_{jj}^{sign}$ the largest variation between CP-conserving and CP-violating models is observed for quark-quark initiated sub-processes, while the variation for gluon-gluon initial state processes is rather small.
In order to systematically compare the sub-processes sensitivity to anomalous couplings, the mean values of the observables are compared for various $\cos(\alpha)$-models for the different sub-processes. This is shown in Fig. 4.7 for the Optimal Observable. The largest variation in the mean value for anomalous couplings is observed for quark-quark sub-processes, while initial states involving gluons provide a less distinct variation. Fig. 4.8 shows the mean value of $\Delta\Phi_{jj}^{sign}$ for various $\cos(\alpha)$-models for the different sub-process. Also for this observable, the largest variation in terms of the mean value is obtained for quark-quark initial state events, while the sensitivity for gluon-gluon initiated sub-processes is diluted. However, as shown in Table 4.2, such processes contribute to the total H+2jet production only with about 3%. In addition, the sub-processes with the smallest sensitivity (gluon-gluon initial states) provide the dominant contribution.
This study shows, that the sensitivity of ggF H+2jet events to anomalous Higgs-gluon couplings may be improved by enhancing the contribution of quark-quark initiated sub-processes. As shown in Fig 4.4, the sub-processes vary in various kinematic variables of the outgoing jets, which can be used in order to impose kinematic cuts and suppress gluon-gluon and gluon-quark initiated processes. Such an investigation is beyond the scope of this thesis and left for further studies.

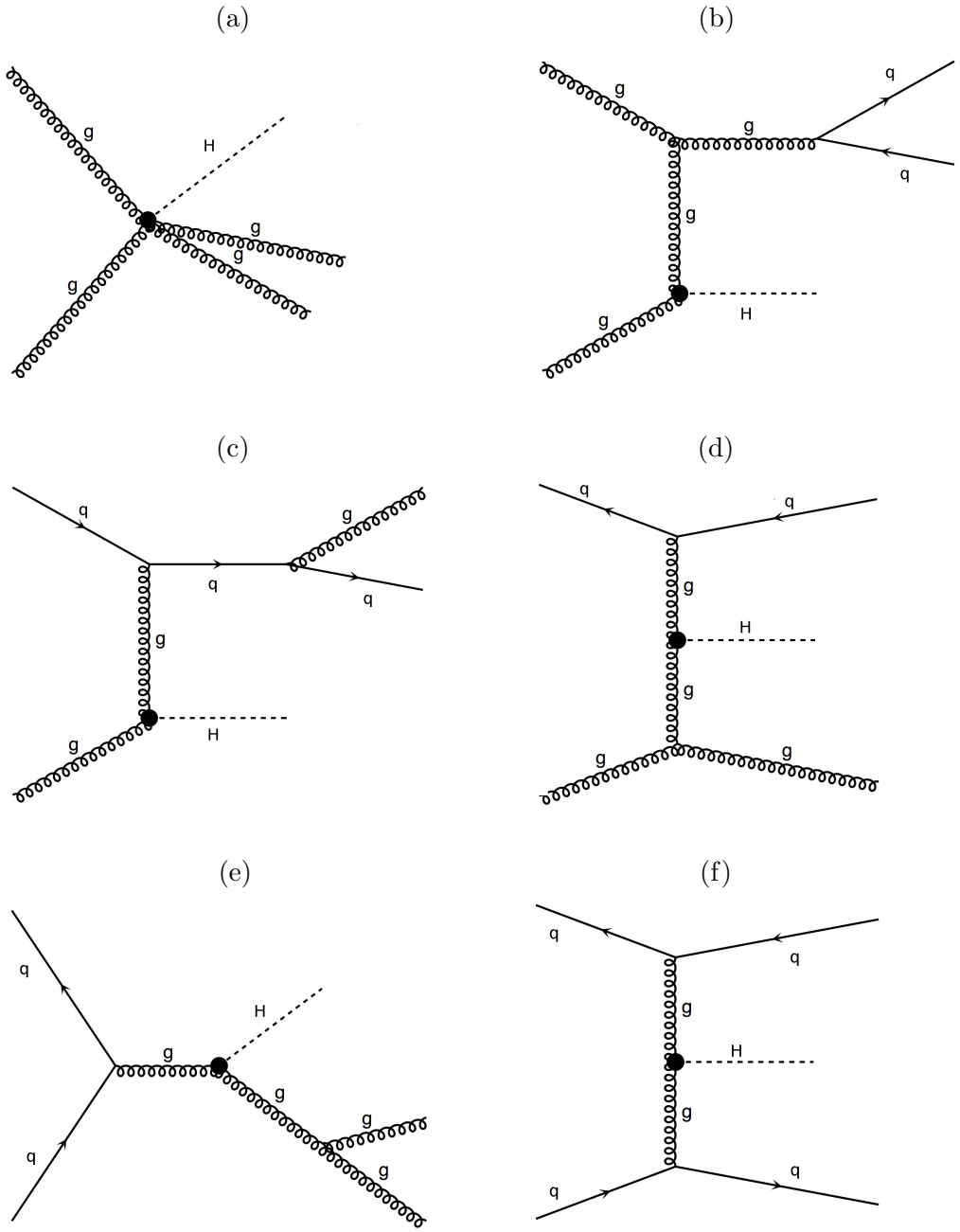

Figure 4.3.: Examples of leading-order Feynman diagrams for various sub-processes classified with respect to involved partons in the initial and final states of H+2jet production in gluon fusion for an effective Higgs-gluon coupling: (a) $gg \to Hgg$, (b) $gg \to Hq\bar{q}$, (c) $gq \to Hgq$ (d) $g\bar{q} \to Hg\bar{q}$, (e) $q\bar{q} \to Hgg$ (f) $q\bar{q}' \to Hq\bar{q}'$.

Initial state	Sub-process	Contribution
gluon-gluon	$gg \to gg$ $gg \to qq$	$\sim 60\%$
gluon-quark	$gq \to gq$ $g\bar{q} \to g\bar{q}$	$\sim 37\%$
quark-quark	$qq' \to qq'$ $q\bar{q}' \to q\bar{q}'$ $qq \to qq$ $q\bar{q} \to q'\bar{q}'$ $q\bar{q} \to gg$ $q\bar{q} \to q\bar{q}$ $\bar{q}\bar{q}' \to \bar{q}\bar{q}'$ $\bar{q}\bar{q} \to \bar{q}\bar{q}$	$\sim 3\%$

Table 4.2.: Relative contribution of the sub-processes for gluon-gluon, gluon-quark and quark-quark initial state configurations for ggF H+2jet events. As a Higgs boson is produced in all cases, the sub-processes only indicate the involved partons.

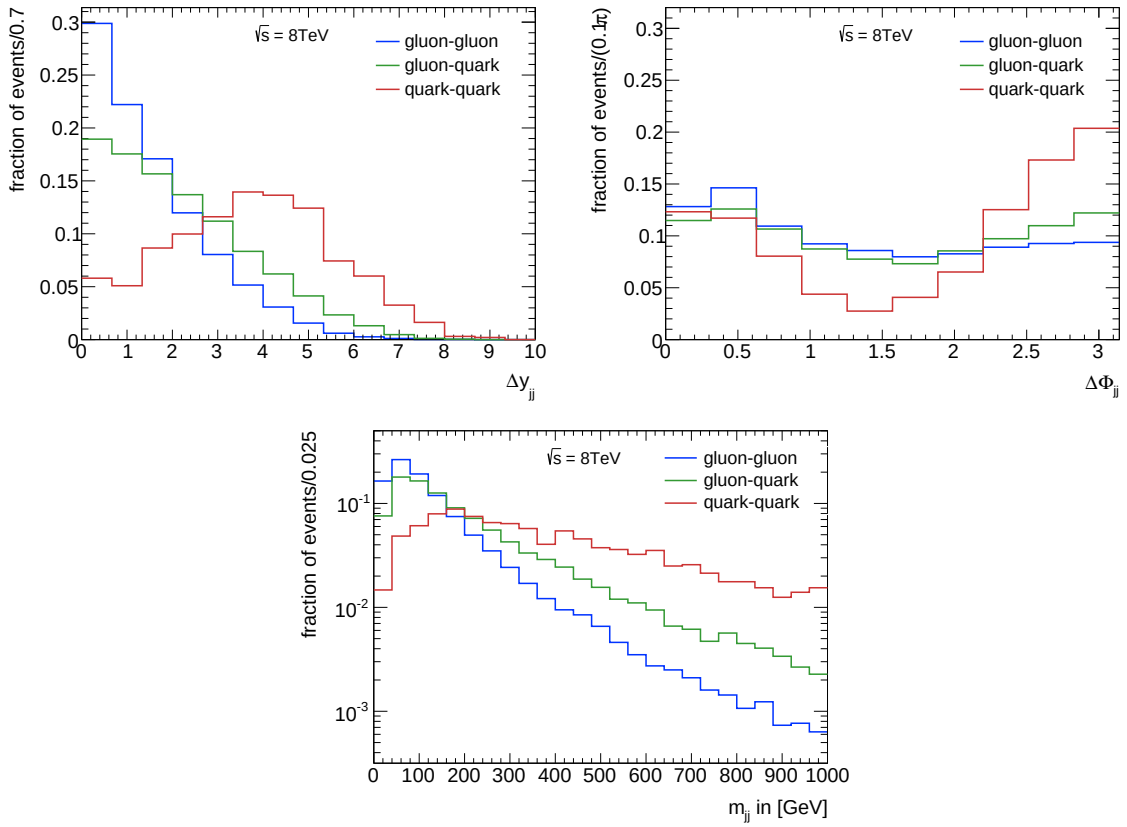

Figure 4.4.: Distributions of the rapidity difference Δy_{jj} (top left), the azimuthal-angle difference $\Delta\Phi_{jj}$ (top right) between the outgoing jets and the invariant dijet mass m_{jj} (bottom) for gluon-gluon, gluon-quark and quark-quark initial states. The distributions are normalized to unit area.

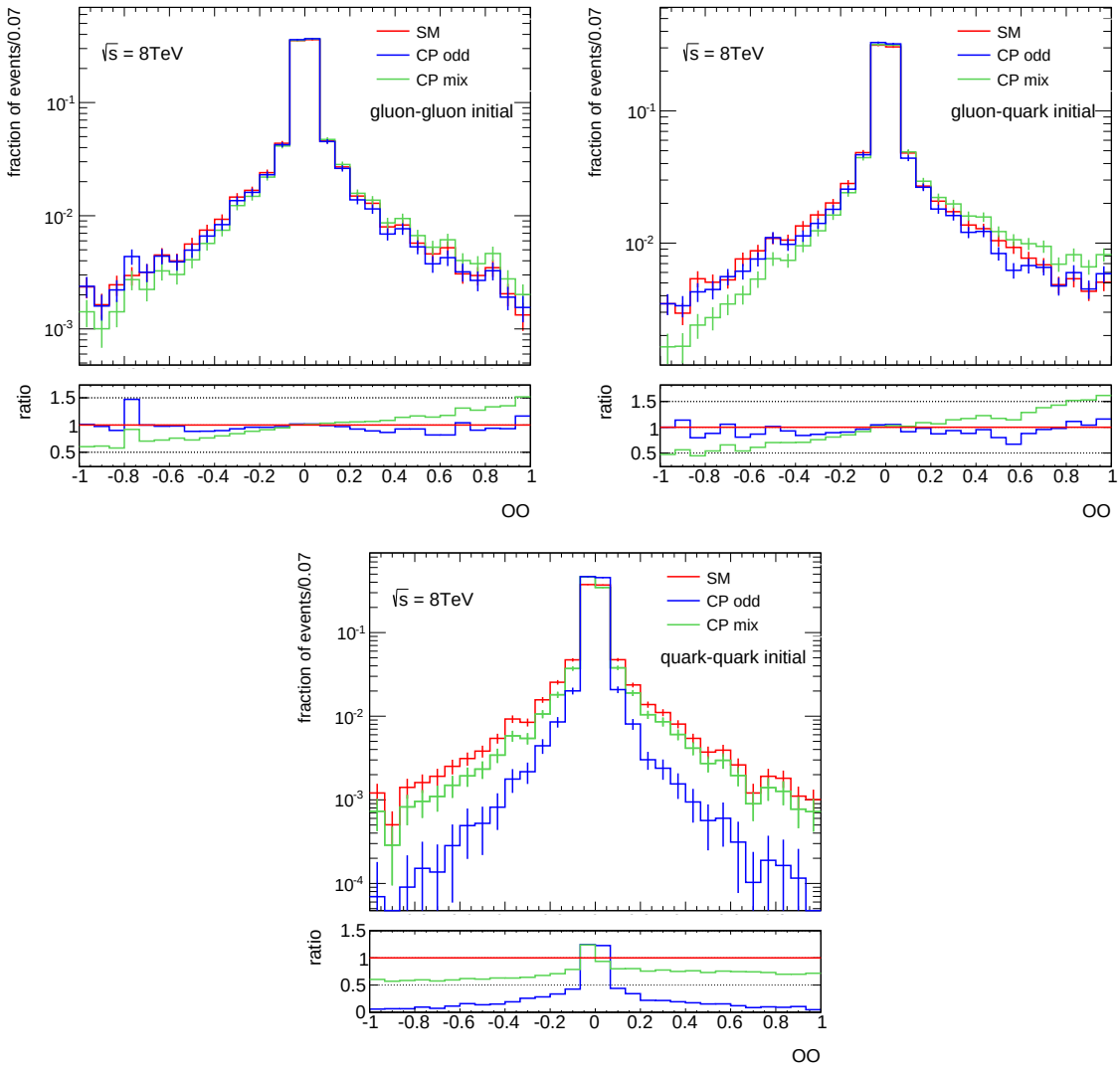

Figure 4.5.: Comparison of SM (red), CP odd (blue) and CP mixed coupling with $\cos^2(\alpha) = 0.50$ (green) of the Optimal Observable distribution for gluon-gluon (top left), gluon-quark (top right) and quark-quark (bottom) initiated events. The distributions are normalized to unit area. The ratio refers to CP odd(mix) over SM distribution.

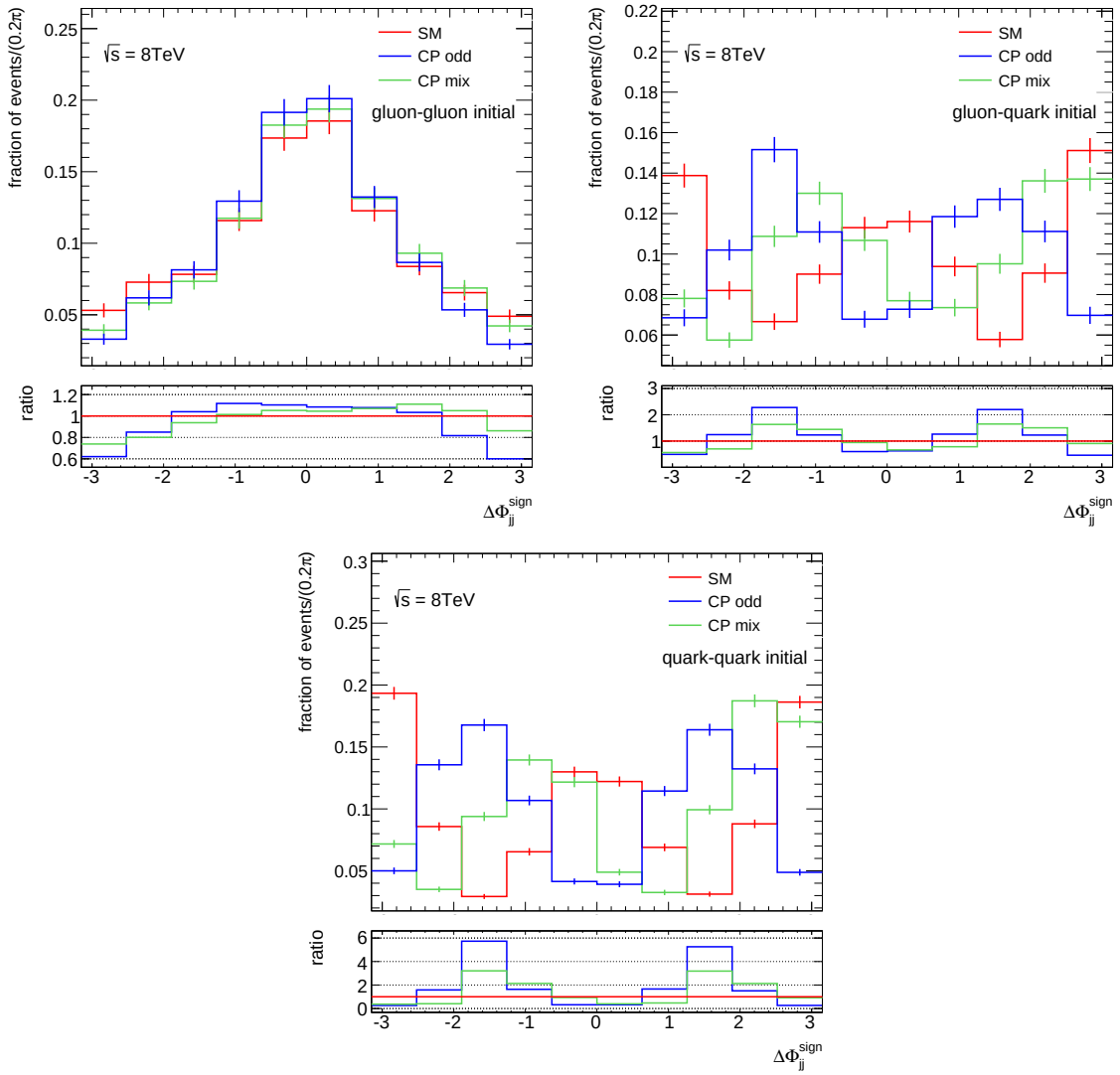

Figure 4.6.: Comparison of SM (red), CP odd (blue) and CP mixed coupling with $\cos^2(\alpha) = 0.50$ (green) of the $\Delta\Phi_{jj}^{sign}$ distribution for gluon-gluon (top left), gluon-quark (top right) and quark-quark (bottom) initiated events. The distributions are normalized to unit area. The ratio refers to CP odd(mix) over SM distribution.

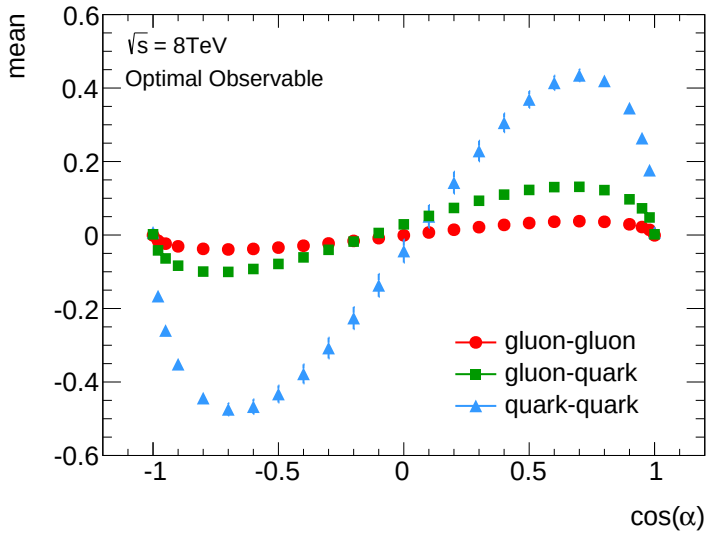

Figure 4.7.: Comparison of the mean value of the Optimal Observable distribution for sub-process with gluon-gluon (red), gluon-quark (green) and quark-quark (blue) initial states includingg statistical uncertainties.

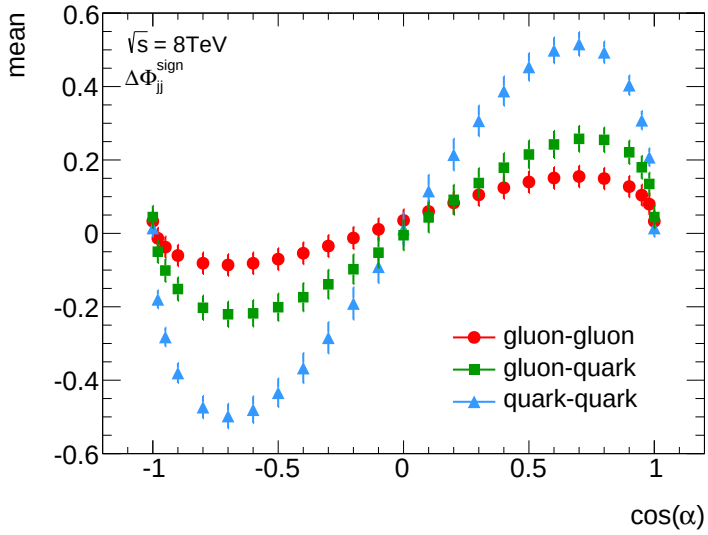

Figure 4.8.: Comparison of the mean value of the $\Delta\Phi_{jj}^{sign}$ distribution for sub-process with gluon-gluon (red), gluon-quark (green) and quark-quark (blue) initial states including statistical uncertainties.

5 The ATLAS Experiment at the LHC

5.1. The Large Hadron Collider

The Large Hadron Collider (LHC) [82], located at CERN near Geneva, is a two-ring hadron accelerator and collider. It was built inside a 27 km-circumference tunnel about 100 m below groundlevel, which was constructed for the former Electron-Positron-Collider (LEP) machine that ran from 1989 to 2000.
The LHC is able to accelerate protons and heavy ions (Pb) in two beams running in opposite directions. For proton-proton collisions the beams contain up to 2808 bunches with 10^{11} particles each, with a time distance of 25 ns. The beams are bent by 1232 superconducting dipole magnets, generating magentic fields up to 8.3 T. Additional quadrupole magnets are installed to focus the particle beams.
The performance of the LHC is mainly defined by its center of mass energy $\sqrt{s}$ and the provided instantaneous luminosity $\mathcal{L}$. For two colliding particle bunches with equally gaussian shape distribution the instantaneous luminosity can be written as [83]:

$$\mathcal{L} = n_b \frac{N^2 \gamma_r f_{rev}}{4\pi\beta^* \varepsilon_n} F \tag{5.1}$$

where N is the number of particles per bunch, n_b the number of bunches per beam, f_{rev} the revolution frequency, γ_r the relativistic gamma-factor, ε_n the normalized transverse beam emittance, β^* the beta-function at the collision point and F the geometric luminosity reduction factor due to the beam crossing angles at the interaction point. The LHC is designed for an instantaneous luminosity up to $10^{34}\,\mathrm{cm}^{-1}\mathrm{s}^{-1}$ with a beam energy of up to 7 TeV resulting in a collision center of mass energy of $\sqrt{s} = 14\,\mathrm{TeV}$ [82].
The collisions take place at four different points in the ring, where the main experiments of the LHC are located: ALICE, LHCb and the multi-purpose detectors ATLAS and CMS.
The experiments are constructed to investigate and adress different physical questions. Fig. 5.1 shows a schematic view of the LHC ring and its main experiments. The ATLAS experiment is described in detail in Section 5.2.
In 2011 the LHC was operating at a center of mass energy of $\sqrt{s} = 7\,\mathrm{TeV}$, which was increased to $\sqrt{s} = 8\,\mathrm{TeV}$ in 2012. At this energy an integrated luminosity of $20.3\,\mathrm{fb}^{-1}$ was recorded [1], which is analysed in this thesis.
In early 2013 the LHC was shut down for two years of planned maintenance and consolidation preparing the machine to operate at its design energy of $\sqrt{s} = 14\,\mathrm{TeV}$. In March 2015 first collisions at $\sqrt{s} = 13\,\mathrm{TeV}$ were successfully recorded.

[1] 1 b (barn)=$1 \times 10^{-22}\mathrm{cm}^2$

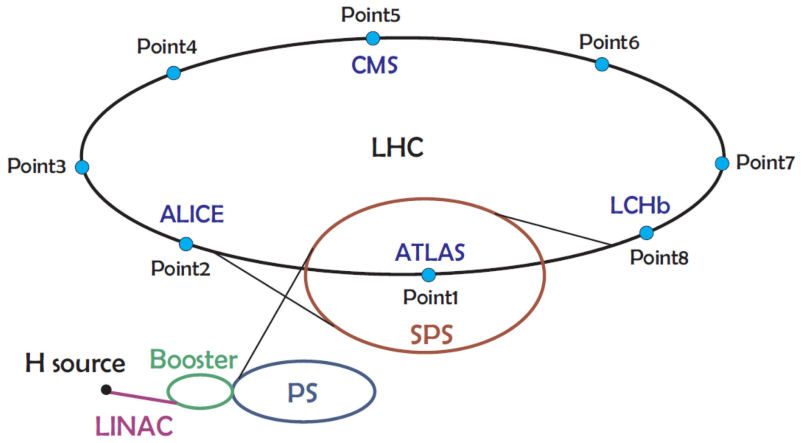

Figure 5.1.: Schematic view of the location of the four main experiments (ATLAS, CMS, ALICE and LHCb) at the LHC ring. The pre-accelerators and their connection to the LHC are shown as well [81].

5.2. The ATLAS Detector

The ATLAS detector is a multi-purpose detector aiming at precision measurements of SM particles and the discovery of new particles in hadron collisions at the high energies and luminosity provided by the LHC. Its cylindrical symmetry covering almost 4π, the high density detector material and the fast, but radiation-hard electronics allow for very good reconstruction of hard scattering processes in proton-proton collisions. A superconducting solenoid generating magnetic fields up to 2 T covers the inner-detector cavity. Additional three large superconducting toroid magnets around the muon system give the ATLAS detector its distinct look.
The detector consists of several sub-detectors as illustrated in Fig.5.2: the inner detector system, the electromagnetic and hadronic calorimeters and the muon system.
In 2008 the construction of the ATLAS detector was finished and successful operation in long-term runs from 2009 to 2013 followed. During the first long shutdown of the LHC in 2013 and 2014 the ATLAS detector was upgraded to account for new challenges of the upcoming collisions at $\sqrt{s} = 13\,\text{TeV}$ and $\sqrt{s} = 14\,\text{TeV}$. The description of the sub-detectors mainly follows [84] for the detector setup in 2011 and 2012.
The commonly used right-handed coordinate system of the ATLAS detector is originated at the interaction point with the z-axis pointing in beam direction, y-axis pointing upwards and x-axis pointing towards the center of the LHC ring. The azimuthal angle ϕ is defined in the (x-y)-plane and the polar angle θ is measured with respect to the z-axis.
The so called pseudo-rapidity η is defined as

$$\eta = -\ln\left(\tan(\theta/2)\right) \tag{5.2}$$

For massive objects the rapidity

$$y = \frac{1}{2}\ln\left(\frac{E + p_z}{E - p_z}\right) \tag{5.3}$$

is used instead, where E refers to the particle energy and p_z gives the momentum in z-direction. The rapidity difference Δy turns out to be *lorentz invariant* under boost along the z-axis.

This feature also holds for the quantity ΔR, which describes the separation of two objects in the $(\eta - \phi)$-plane:

$$\Delta R = \sqrt{(\Delta\eta)^2 + (\Delta\phi)^2} \tag{5.4}$$

Transverse observables, such as the transverse momentum p_T or the transverse energy E_T, are defined as the projection of the corresponding observable in the (x-y)-plane:

$$\begin{aligned} p_T &= \sqrt{p_x^2 + p_y^2} \\ E_T &= \sqrt{E_x^2 + E_y^2} \end{aligned} \tag{5.5}$$

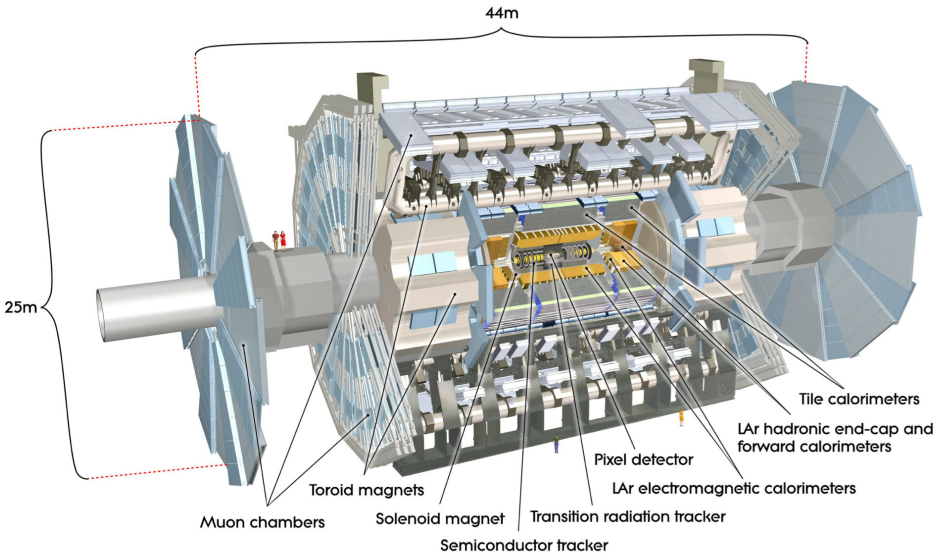

Figure 5.2.: Overview of the ATLAS detector showing the muon system, the toroidal and solenoid magnets, the calorimeters and the inner detector [84].

5.2.1. Inner Detector

The ATLAS inner detector system is designed to provide reliable momentum measurement as well as primary and secondary vertex reconstruction for charged particle tracks. It consists of pixel detector, semiconductor tracker (SCT), transition radiation tracker (TRT) and covers a pseudo-rapidity range of $|\eta| < 2.0$, see Fig. 5.3. A magnetic field of 2 T is generated by thin solenoid magnets covering the inner tracking cavity. The inner detector has a length of 6.2 m with a radius of 2.1 m. Since its components are very close to the interaction point the detector material has to cope with high radiation and high temperature conditions. To reduce damages, the pixel detector and SCT are cooled down to about -7°C.

The pixel detector is the subdetector closest to the interaction point and enables precise primary and secondary vertex reconstruction. The pixel sensors are arranged in three layers of concentric hollow cylinders in the barrel region and three layers of disks installed perpendicular to the beam axis in the end-cap regions. This positioning ensures that particles typically pass three of these layers. The pixel detector consist of 250 µm thick silicon semiconductors with 46080 readout channels for each of the 1744 sensors. The pixels have a size

of $(R-\phi)\times$z=50 $\times$ 400 µm^2 up to $(R-\phi)\times$z=50 $\times$ 600 µm^2 while reaching an intrinsic hit resolution of 10 µm in the (R-ϕ)-plane and 115 µm in z-direction.

The pixel detector is surrounded by the semiconductor tracker (SCT). It consists of four layers of silicon strip detector modules in the barrel region and nine layers in the end-cap regions, therefore providing at least four measured space points for every transversing charged particle. The semiconductor sensors are built of 758 active strips of 12 cm length and 285 µm thickness each. The modules in the barrel region contain two layers, which are rotated by 40 mrad against each other to allow for position measurement along the strips. The SCT has a nominal hit resolution of 17 µm in the $(R-\phi)$-plane, 580 µm along z-direction and contains about 6.3 million readout channels.

The transition radiation tracker (TRT) forms the outermost part of the inner detector and covers a rapidity range of $|\eta| < 2.0$. It consists of gas-filled straw tubes of 4 mm diameter, which are stabilised by carbon fibres. The tubes are installed along the z-axis with a length of 144 cm and radially in the end-caps with 37 mm length. In the barrel region the TRT provides only a position measurement in the $(R-\phi)$-plane with a resolution of about 130 µm. Additionally the gas-filled tubes enable the potential for particle identification, since the transition radiation is inversely proportional to the mass of the particle. Therefore, electrons, which are by far the lightest stable particles produced, emit the most transition radiation and can be identified by the TRT.

A summary of the resolution goals on momentum and energy measurement in the different subdetectors is given in Table 5.1.

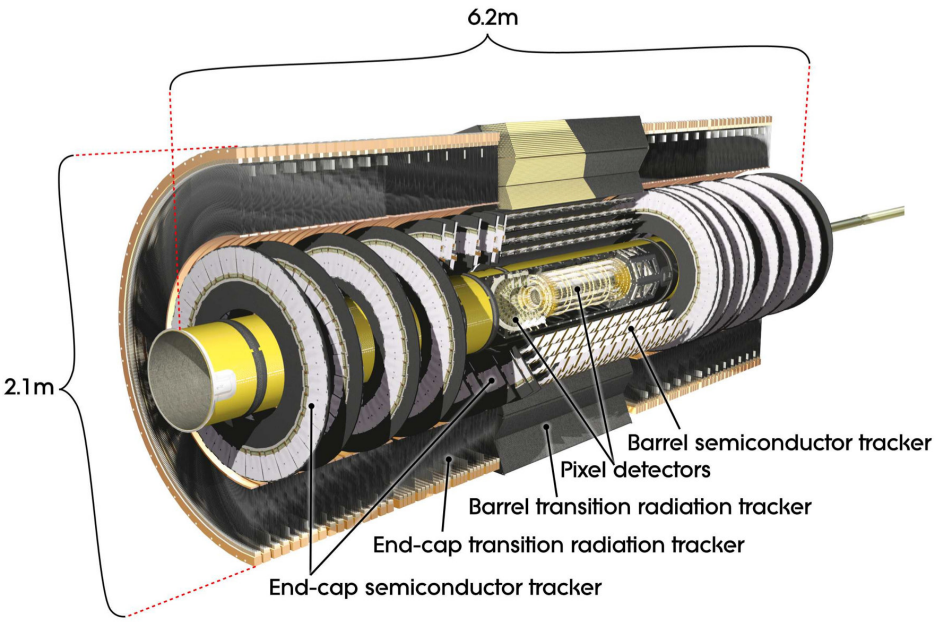

Figure 5.3.: Schematic view of the inner detecor with the pixel detectors, SCT and TRT [84].

5.2.2. Calorimeters

The ATLAS calorimeter system surrounds the inner detector and covers a pseudo-rapidity range of $|\eta| \leq 4.9$ in the full ϕ range. Fig. 5.4 shows the geometry of the calorimeter system build around the beam axis. It consists of the electromagnetic calorimeter (ECAL) for energy measurement of electrons and photons and of the hadronic calorimeter (HCAL), which is responsible for jet energy and E_T^{miss} measurements, defined in Eq. 6.2, together with the ECAL. Both calorimeter systems are sampling calorimeters, which means that they consist of layers of active detector and absorber material. Since the calorimeter response differs for electromagnetic and hadronic shower, the calorimeters are called *non-compensating*.

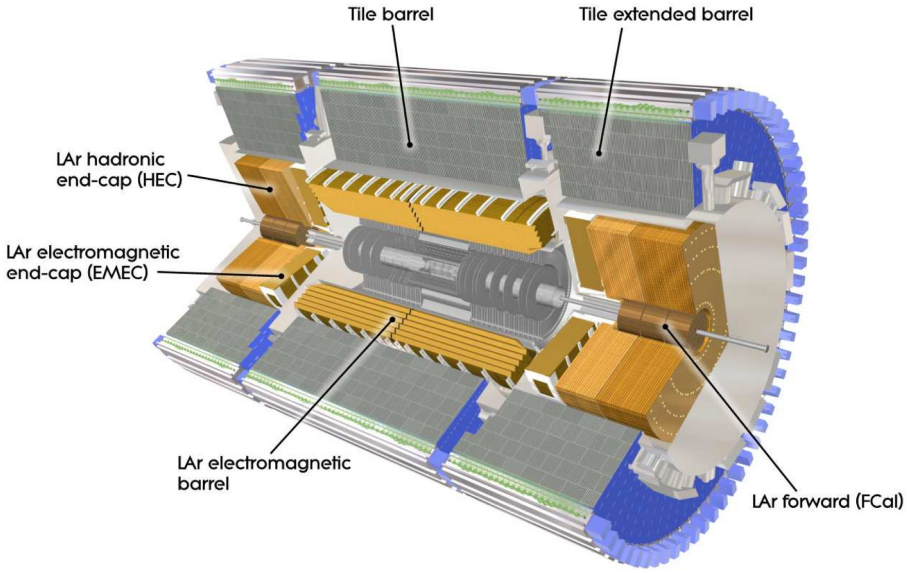

Figure 5.4.: Schematic view of the electromagnetic and hadronic calorimeters [84].

The electromagnetic calorimeter is a liquid argon (LAr) sampling calorimeter with lead absorbers. It can be divided into the barrel region with $|\eta| < 1.475$ and the end-cap regions covering $1.375 < |\eta| < 3.2$. The central component with $1.375 < |\eta| < 2.5$ provides a finer resolution than the forward region with $2.5 < |\eta| < 3.2$. The highest granuality of $(\Delta\eta \times \Delta\phi)$=0.025×0.025 is mainly accomplished in the barrel region layer and in the second layer of the end-cap central region. Fig. 5.5 shows the energy resolution of the ECAL for simulation and test beam measurements.
The electromagnetic calorimeter uses kapton electrodes installed in a accordian geometry to enables full coverage in ϕ-direction. The fine granuality of the electromagnetic calorimeter allows for precise energy and position measurement, especially for electron and photons. For $|\eta| < 2.5$ the energy deposition and position measurement of charged particles in the calorimeter can be matched to track information of the inner detector. For this region the precision measurement is obtained by first ECAL layer, which is finely segmented in η.

The hadronic calorimeter can be divided into the central region, the hadronic end-cap sys-

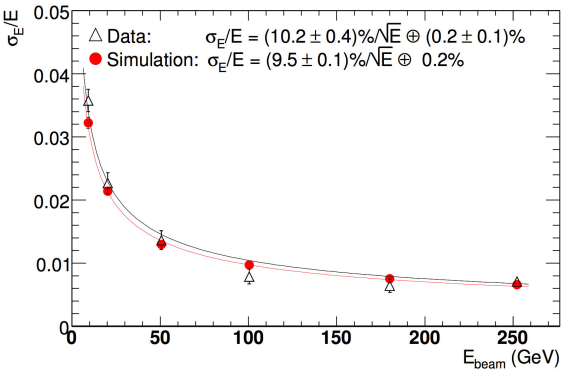

Figure 5.5.: Energy resolution of the EM calorimetry comparing simulation and test beam measurements [84].

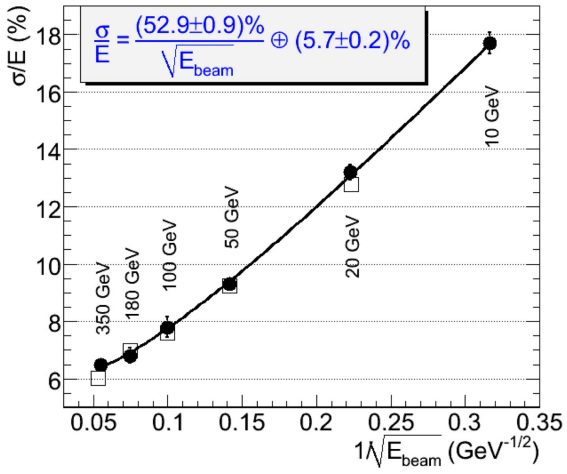

Figure 5.6.: Energy resolution of the Tile-Calorimetry comparing simulation (open squares) and test beam measurements with pions (filled cirec) [84].

tem and the forward detector, see Fig. 5.4. Since the forward detector covers a range of $3.1 < |\eta| < 4.9$ it enables the measurement of particles close to the beam pipe. The central region with $|\eta| < 1.7$ consists of scintillating tiles as active and steel as absorber material. Fig. 5.6 shows the energy resolution of the central tile region for simulation and test beam measurements.

The hadronic end-cap detector uses 8.5 mm gaps of LAr as active material and copper plates for absorbing. The forward detector is not only responsible for the reconstruction of jets and E_T^{miss}, but is also able to detect electrons and photons. Therefore, it consists of 3 different modules: The first one, using copper as absorber material is optimized for electromagnetic showers. The other two modules employ tungsten as absorber material. All modules of the forward calorimeter use LAr as active detector material.

5.2.3. Muon System

The Muon system forms the outermost part of the ATLAS detector and is responsible for detection and energy measurement of charged particles exiting the inner detector and calorimeter. It is divided into three regions: the barrel region covering a pseudorapidity range of $|\eta| < 1.4$, the end-caps region with $1.6 < |\eta| < 2.7$ coverage and the transition region with $1.5 < |\eta| < 1.6$. The momentum measurements is based on the magnetic field provided by large toroidal magnets. Since the magnetic field is mostly generated orthogonal to the particle trajectory, the particles are bent in the (R-z)-plane rather than in the (R-ϕ)-plane. Separate toroidal magnetic systems are used for the barrel and end-cap regions producing magnetic field strengths up to 2.5 T and 3.5 T respectively.
The muon trajectory is detected by different muon chamber types: Monitored Drift Tubes (MDT) are used for most of the pseudorapidity range. Only for particle detection in large η-ranges cathode strip chambers (CSC) were selected, as they provide better spatial resolution to cope with higher signal rates.
The muon system is also designed to trigger particles in the region $|\eta| < 2.4$. In order to achieve a response time of a few nanosecond resistive plate chambers (RPC) are installed in the barrel region while thin gap chambers (TGC) are used in the end-cap region of the muon system.

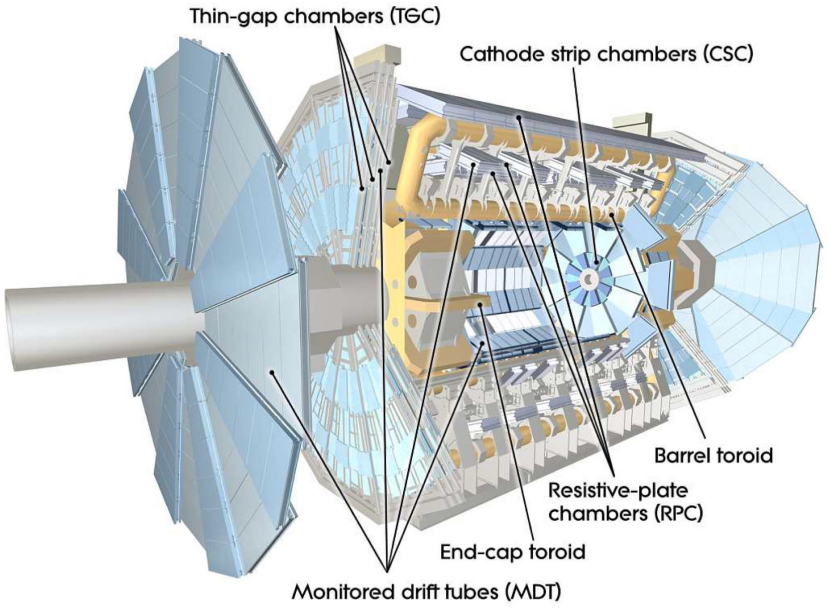

Figure 5.7.: Schematic view of the ATLAS Muon system including barrel and end-cap toroid [84].

5.2.4. Trigger System

The design event rate provided by the LHC is about 40 MHz, hence only a small fraction of the arising data can be recorded. Thus, the event rate has to be reduced to about 200 Hz. A multi-level triggering system has to decide which events are physically relevant to be recorded and further processed. The trigger-system of ATLAS can be divided into three stages: L1 trigger, L2 trigger and the event filter (EF).
The hardware-based L1 trigger uses the trigger chambers of the muon system and the full calorimeter system in a coarse granuality to search for objects with high transverse energy, such as electrons, photons and jets. Furthermore, the L1 trigger transfers the η- and ϕ- coordinate of so called *regions of interest* (RoI) to the next trigger level stage. The L1 trigger takes decision within 15 ns and reduces the rate to about 75 kHz in the first step.
The software-based L2 trigger uses the full precision of detector information inside the RoIs. It reduces the event rate to about 3.5 kHz by applying stricter criteria with a decision time of 40 ms per event.
The event filter (EF) provides the final triggering-stage. It takes decision within 4 s and uses the full detector information to reduce the event rate to about 200 Hz. All events passing the EF are recorded for further offline analysis.
Fig. 5.8 shows the event rate and the distributions to so called trigger-menus for data taking in 2012. By reaching about 400 Hz the target event rate of 200 Hz was exceeded by a factor of two.

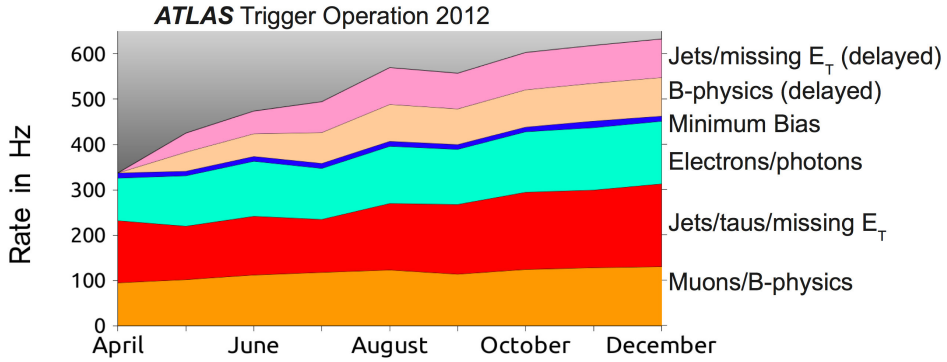

Figure 5.8.: Recorded event rate and distributions to different trigger menus for data taking in 2012 [85].

5.2.5. Data taking in 2012

In 2010 and 2011 the ATLAS experiment was able to record data from proton-proton collisions at $\sqrt{s} = 7$ TeV, which corresponded to an integrated luminosity of 5.61 fb^{-1}. In 2012 the center of mass energy was increased to $\sqrt{s} = 8$ TeV. An integrated luminosity of 20.3 fb^{-1} was recorded with an uncertainty of ± 3.6 %.
The analysis presented in this thesis is based on data collected in 2012 at $\sqrt{s} = 8$ TeV. In this period up to 40 interactions per bunch crossing with a time distance of 25 ns between the bunches where observed with the ATLAS detector. Fig. 5.9 shows the progress in time for the maximal number of interaction per proton-proton collision in 2011 and 2012. The mean number of interactions per bunch crossing (*pile-up*) is compared for 2011 and 2012 data in Fig. 5.10.

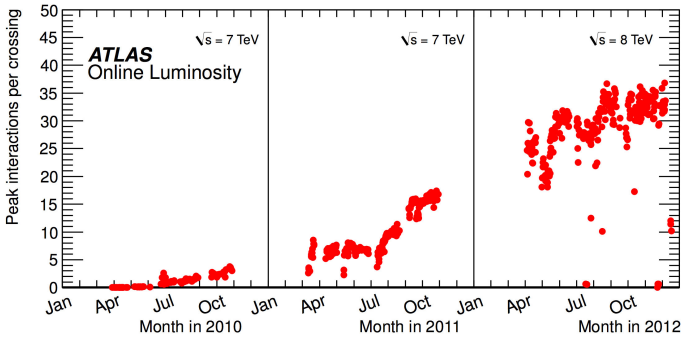

Figure 5.9.: Progress in time for the maximal number of interactions per collision [86].

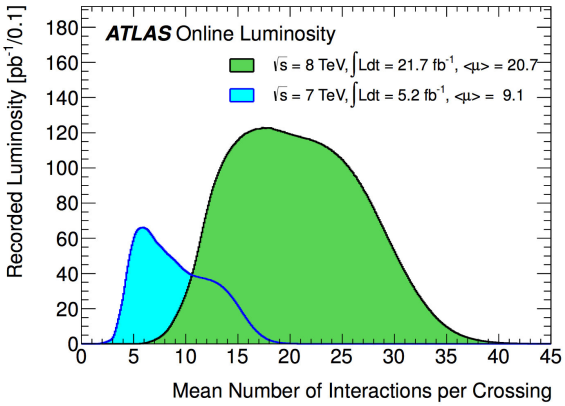

Figure 5.10.: Luminosity-weighted distribution of the mean number of interactions per bunch crossing for data taken in 2011 and 2012 [87].

Subdetector	Required resolution	η-coverage	
		Measurement	Trigger
Inner detector	$\sigma_{p_T}/p_T = 0.05\%\, p_T \oplus 1\%$	± 2.5	
Electromagnetic calorimetry	$\sigma_E/E = 10\%/\sqrt{E} \oplus 0.7\%$	± 3.2	± 2.5
Hadronic calorimetry			
- barrel and end-cap	$\sigma_E/E = 50\%/\sqrt{E} \oplus 3\%$	± 3.2	± 3.2
- forward	$\sigma_E/E = 100\%/\sqrt{E} \oplus 10\%$	$3.1 < \lvert\eta\rvert < 4.9$	$3.1 < \lvert\eta\rvert < 4.9$
Muon spectrometer	$\sigma_{p_T}/p_T = 10\%$ at p_T=1 TeV	± 2.7	± 2.4

Table 5.1.: General resolution goals of the subdetectors of the ATLAS detector. Energy and momentum values are given in units of GeV. The notation a$\oplus$b=$\sqrt{a^2 + b^2}$ is used [84].

6 Reconstruction and Identification of Physics Objects

In order to analyse the signal and background processes described in Chapter 3, the particles created in proton-proton collision and traversing the ATLAS detector have to be identified and reconstructed. In this analysis, the identification and reconstruction of jets, leptons and missing transverse energy are of particular interest. In addition, jet flavour-tagging methods, such as *b-tagging* and the identification of hadronically decaying τ-leptons, are important tools for background rejection. The event reconstructions are performed on both data and simulation. In addition, correction factors, accounting for differences in reconstruction, identification and trigger efficiencies between data and simulated events, are applied to simulations in order to better described the collision data.
This chapter is organized as follows: In the first section, the reconstruction of tracks and vertices in the inner detector system is described. They provide the basic ingredients for the reconstruction of leptons and jets, which are discussed in the following sections. In addition, a brief overview of the *b-tagging* procedure is given. Then, a description of the missing transverse energy reconstruction, which is in particular important for final states including neutrinos, is given. The next sections provides a brief overview of the identification of hadronically decaying τ-leptons and describe the overlap removal between jets and leptons. Then, the triggers, which are used in this analysis to selected same flavour and different flavour final states, are discussed. The chapter closes with a description of *pile-up* simulation, accounting for multiple proton-proton interactions per bunch crossing.

6.1. Tracks and Vertices

The reconstruction of tracks and vertices in the inner detector (ID) system allows to measure the momentum of charged particles and identify primary and secondary vertices in an event. To achieve this, various track reconstruction algorithms are used, which take into account hit information in the pixel, the SCT and the TRT detectors of the ID system. In particular, three dimensional space points corresponding to energy deposition in the pixel and SCT detector are combined with so called drift-circles around the wires of the TRT detector. Several track quality criteria, such as a minimum number of nine hits in the SCT, are applied in order to reject badly reconstructed or misidentified tracks.
Interaction vertices can be reconstructed by looking for intersections of the extrapolation of reconstructed tracks. Due to multiple proton interactions in a bunch crossing, called *pile-up*, more than one vertex per collision is reconstructed in general. The vertex with the largest sum of squared transverse momenta of tracks associated to it

$$\sum_{i=1}^{\text{Ntracks}} p_{T,i}^2 \tag{6.1}$$

is chosen as the primary vertex corresponding to the point of hardest interaction. A detailed description of the track and vertex reconstruction methods in proton-proton collisions can be found in Reference [88].

6.2. Electrons

Electrons constitute important experimental signatures as their energy and momentum can be measured with high precision. Furthermore, electrons are identified with high efficiency and large background rejection. This is achieved by combining energy measurements in the calorimeter with informations provided by the tracking detectors. Electron candidates are reconstructed from a cluster in the electromagnetic calorimeter. This cluster has to be matched with the extrapolation of a a reconstructed track within a certain ΔR-range. Furthermore, additional energy deposition in the hadronic calorimeter and the number of tracks in the tracking detector are considered in order to suppress contributions from jets, hadronically decaying τ-leptons and pile-up events. Different electron identification criteria, denoted as *loose, medium, tight*, exist [89]. They differ in background rejection and electron identification efficiency.
In this analysis, electrons have to pass the *medium* identification criteria with $p_T > 15\,\text{GeV}$ and $\eta < 2.47$. In this η-range information from the pixel detector and the SCT are available and can be used for the reconstruction. In addition, electrons with $1.37 < \eta < 1.52$ are discarded due to the poor identification and reconstruction performance in this range.
In order to further increase the background rejection, especially with respect to hadronic jets, two isolation criteria are applied to electron candidates: The sum of all transverse momenta of additional tracks with $p_T > 1\,\text{GeV}$ within a cone of $\Delta R < 0.4$ around the reconstructed electron has to be less than 17% of the electron's transverse momentum. In addition, the sum of transverse energy depositions within $\Delta R < 0.2$ around the track of the reconstructed electron has to be less than 9% of the electrons transverse energy. Transverse energy and transverse momentum are defined in Eq. 5.5.
The electron reconstruction and identification efficiency is measured using a *tag-and-probe technique* in $Z \to ee$ and $J/\Psi \to ee$ events [90]. For this, tight requirements are applied to one *tag* electron. As this event then contains a second *probe* electron with high probability, the electron efficiency can be measured. Fig. 6.1 shows the electron identification efficiency as a function of the transverse energy and the number of primary vertices comparing data and simulation. The ratio between measured and simulated efficiency is used to derive a scalefactor, which is applied to simulated samples in order to correct for differences in identification and reconstruction efficiencies between data and simulation.
In addition, $Z \to ee$ and $J/\Psi \to ee$ events are used to determine the electron energy resolution and to correct for differences between data and simulation. The electron energy resolution in data is found to be about 1% larger than in simulation, which is accounted for by applying an additional energy smearing to simulated events.

6.3. Muons

As muons traverse the detector material with minimum energy loss, they provide a clear experimental signature and can be well distinguished from electrons and jets. Muon tracks are measured in the inner detector (ID), while their momentum can be determined very precisely by the deflection in the magnetic field of the muon spectrometer (MS).

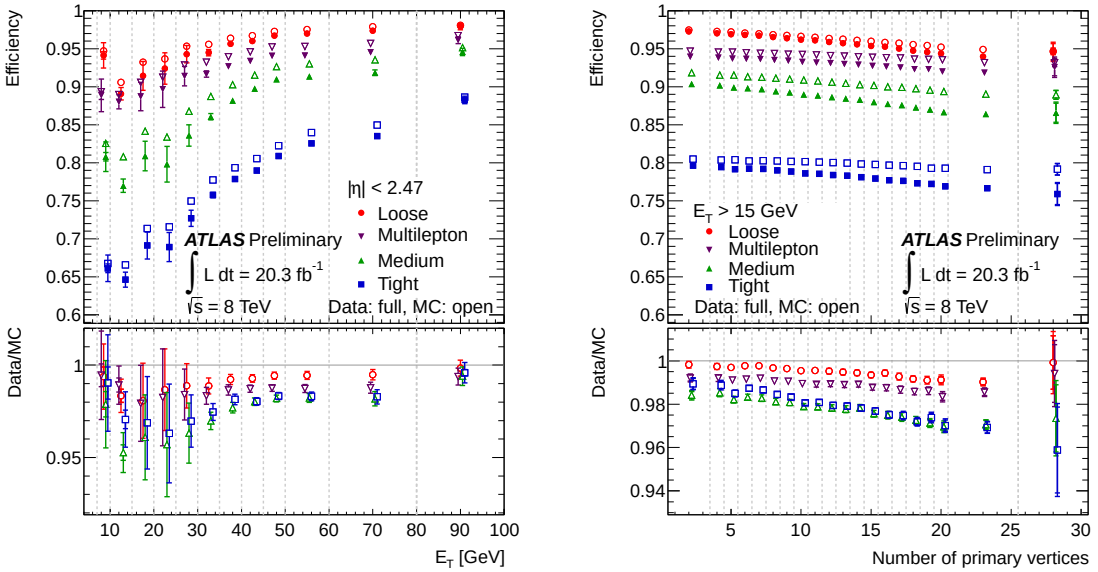

Figure 6.1.: Electron identification efficiency for loose, medium and tight working points as function of the transverse energy of the electron (left) and the number of reconstructed vertices (right) for data and simulation. The ratio between measured and simulated efficiency is used to correct the simulated events [90].

Three different muon reconstruction algorithms are used depending on the combination of information from different sub-detectors: For the reconstruction of stand-alone (SA) muons only information from the MS spectrometer is used. Segment-tagged (ST) muons are reconstructed from the track information in the ID, where the track has to be associated with at least one MS track segment. The highest purity and momentum resolution is obtained for combined (CB) muons, where track informations from the ID and MS are combined.
In order to reduce background contribution from cosmic muons, the impact parameter, defined as minimum distance between muon track and primary vertex, has to be smaller than 1 cm. In addition, muon candidates have to be isolated: The sum of all transverse momenta of additional tracks with $p_T > 1\,\text{GeV}$ within a cone of $\Delta R < 0.4$ around the reconstructed muon has to be less than 18% of the muon transverse momentum. Moreover, the sum of transverse energy depositions within $\Delta R < 0.2$ around the track of the reconstructed muon has to be less than 9% of the muons transverse energy. In this analysis, muons have to be identified as *tight* with $p_T > 10\,\text{GeV}$ and $|\eta| < 2.5$ [91].
The muon reconstruction and identification efficiency is measured with a *tag-and-probe* technique in $Z \to \mu\mu$ events [92]. Fig. 6.2 shows the reconstruction efficiency for CB muons as a function of the transverse momentum and rapidity for data and simulations. The ratio between measured and simulated efficiency is used to derive scalefactors in order to correct simulated events. In addition, a correction of the muon momentum resolution of up to 2% is determined by the invariant mass spectrum of $Z \to \mu\mu$ events.

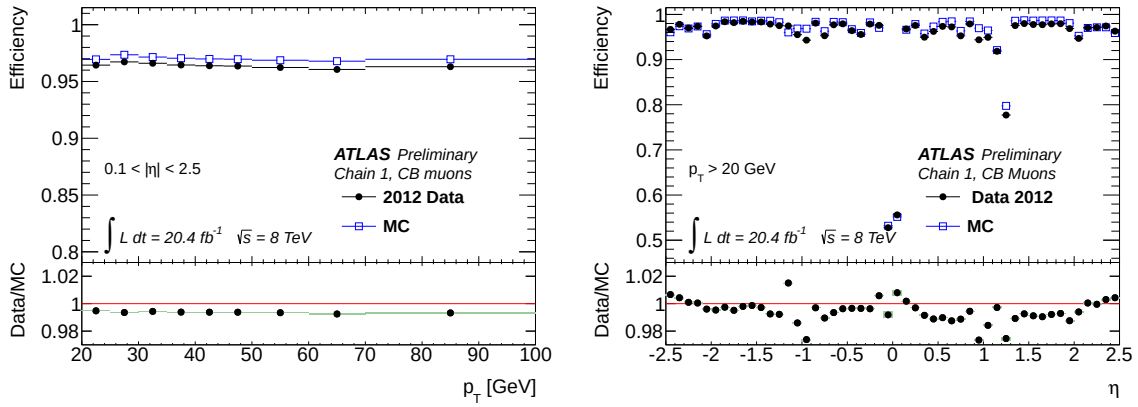

Figure 6.2.: Muon reconstruction efficiency as a function of the muon transverse momentum (left) and the pseudorapidity (right) for combined (CB) muons for data and simulation. The ratio between measured and simulated efficiency is used to correct the simulated events [92].

6.4. Jets

Quarks and gluons carrying color charge cannot exist in free unbound states, as discussed in Section 2.1.2. They hadronize and produce collimated sprays of particles, called *jets*. These jets deposit their energy in the electromagnetic and hadronic calorimeters. The differnt approaches for jet reconstruction can be classified into cone and cluster algorithms. Cone algorithms reconstruct jets based on defining a geometrical cone of a certain radius around a jet axis. Cluster algorithms, on the other hand, combine objects based on their energy and angular variables. In this analysis, jets with $p_T > 20\,\text{GeV}$ and $|\eta| < 4.5$ are cluster by using the anti-kt algorithm [93] with radius parameter $R = 0.4$.
In order to suppress jets from pile-up events a jet vertex fraction JVF, defined as the ratio of the scalar sum of transverse momenta of tracks within the jet associated to the primary vertex to the scalar sum of the transverse momenta of all tracks associated with that jet, is used. Thus, reconstructed jets with $p_T < 50\,\text{GeV}$ and $|\eta| < 2.4$ have to pass $|\text{JVF}| > 0.5$.
Several correction factors have to be applied to the jet energy in order to account for missing energy deposition due to particles which are not reconstructed in the calorimeter or not cluster in the jet. The calibration of the jet energy is derived by comparing the jet energy to a reference object, for which the energy scale is well know. For instance, in $Z + jet$ events, the jet energy is compared to the recoiled Z-boson [94]. By requiring conservation of transverse momentum, the imbalance between the reconstructed systems allows to derive a correction factor. Various systematic uncertainties arise from this jet energy scale calibration, which are discussed in Section 9.1.

Flavour tagging algorithms allow to identify the flavour of hard scatterd quarks causing jets. In particular, algorithms, which identify jets originate from b-quarks, so called *b-jets*, are widely used. This is called *b-tagging*. Such algorithms make use of the relatively long lifetime of the b-flavoured hadrons (1.5 ps) resulting in a secondary vertex several mm away from the primary interaction point of the hard process. These secondary vertices can be reconstructed by extrapolating the tracks of particles contained in the jet, which are measured in the ID system (see Section 6.1). The identification of b-jets is in particular important in this analysis to reject events from top-quark processes.

In this analysis, the b-tagging is performed with the MVA1 algorithm [95] at a working point of 70%. Fig. 6.3 shows the b-tagging efficiency measured in $t\bar{t}$ events and compared to simulations at a 70% b-jet efficiency working point. The ratio between data and simulation is used to derive a scalefactor in order to correct the b-tagging efficiency in simulated events.

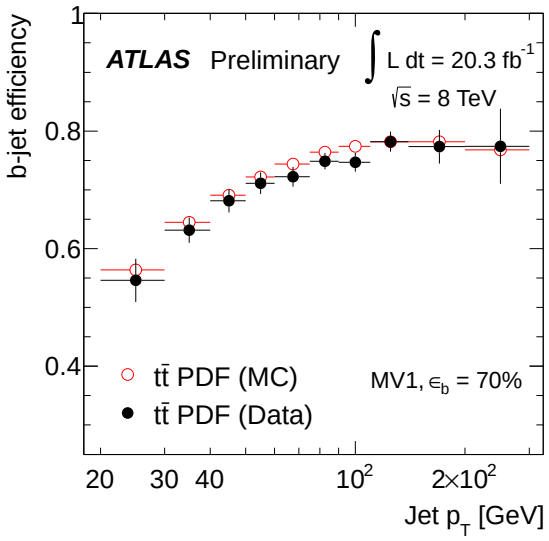

Figure 6.3.: The b-tagging efficiency as a function of jet transverse momentum measured in $t\bar{t}$ events compared to simulation for the MVA1 b-tagging algorithm at the 70% b-jet efficiency working point [96].

6.5. Missing Transverse Energy

In proton-proton collisions the energy and momentum of the initial state partons participating in the hard scattering process along the beam axis is unknown. Thus, four-momentum conservation can only be used in the transverse plane, as the initial state partons are assumed to have negligible transverse momenta. This results in a final state transverse momentum of zero. The missing transverse energy E_T^{miss} quantifies the momentum vector in the transverse plane which is missing to achieve a total final state transverse momentum of zero:

$$E_T^{miss} = \sqrt{(E_x^{miss})^2 + (E_y^{miss})^2} \tag{6.2}$$

The E_T^{miss} mainly arises from particles, which are not measured in the detector, such as weakly-interacting neutrinos. As the full-leptonic final state of the ditau decay in $H \to \tau\tau \to 2l4\nu$ provides four neutrinos in the final state, a significant amount of the tau-momenta is carried by the neutrinos. Thus, reconstructing the resulting E_T^{miss} value is important to reduce other background components, where no missing transverse energy is expected. In addition, the determination of E_T^{miss} is necessary in order to reconstruct the invariant ditau mass as discussed in Section 7.1.

The missing transverse energy is calculated as the negative sum of measured energy depositions in the calorimeter corrected for the energy of reconstructed muons:

$$E_{x,y}^{miss} = -E_{x,y}^{calo} - E_{x,y}^{muons} \tag{6.3}$$

The energy deposition in the calorimeter

$$E_{x,y}^{calo} = \sum_{obj} E_{x,y}^{obj} + E_{x,y}^{soft} \tag{6.4}$$

includes fully reconstructed and calibrated physical objects ($obj = e, \mu, \tau, \gamma, jets$). Here, the muon energy deposition in the calorimeter is only taken into account for non-isolated muons. Furthermore, E_T^{jets} only contains the energy deposition of jets with $p_T > 20\,\text{GeV}$. Contributions from energy depositions which are not assigned to any of these objects are accounted for by $E_{x,y}^{soft}$.
The reconstruction and performance of E_T^{miss} is mostly affected by the production of low momentum particles in pile-up events. Requirements on the JVF applied to the soft term, referred to as soft term vertex fraction (STVF), are used in order to suppress these contributions and increase the E_T^{miss} performance. Fig. 6.4 shows the resolution of E_x^{miss} and E_y^{miss} as a function of the total transverse energy for simulated $H \to \tau\tau$ events. Comparing the resolution before and after pile-up suppression shows a significant improvement.

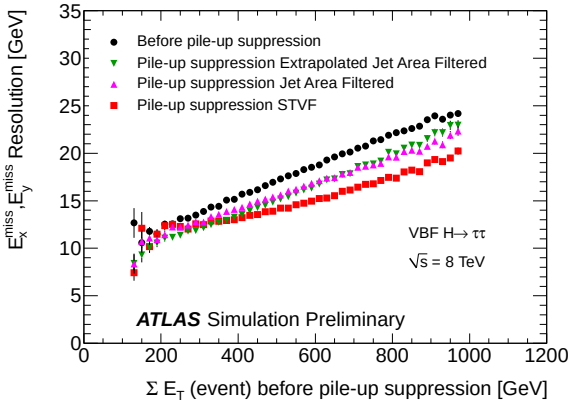

Figure 6.4.: Resolution of E_x^{miss} and E_y^{miss} as a function of the total transverse energy for simulated VBF $H \to \tau\tau$ events before and after pile-up suppression [97].

6.6. Hadronic τ-lepton Decays

As described in Section 3.1 τ-leptons decay with a mean lifetime of about $2.9 \times 10^{-13}\,\text{s}$ into leptons or hadrons. This analysis focuses on the full leptonic final state in $H \to \tau\tau$, while events with an hadronically decaying τ-lepton are discarded (see Section 7.2).
Hadronic decays of the τ-lepton are classified by the number of associated charged tracks. Here, events with one (three) charged tracks associated are referred to as *1(3)-prong* events. Events with five associated charged tracks are very rare.
The τ-lepton decay products are highly collimated and provide a more narrow shower profile compared to jets caused by quarks or gluons. In this analysis, hadronically decaying τ-leptons are seeded by reconstructed jets, while the BDT algorithm `JetBDTSigMedium` [98] is used for the identification of hadronic τ-leptons with $p_T > 20\,\text{GeV}$ and $|\eta| < 2.47$. As this η-region is covered by the pixel and SCT detectors, additional track informations can be used.

6.7. Overlap Removal between Leptons and Jets

The detector signature caused by one single particle can satisfy reconstruction requirements of different object types. Therefore, it is possible that a particle is reconstructed and selected as different objects, e.g. electron and jet. To avoid this, an overlap removal based on the ΔR distance in the $(\eta - \phi)$ plane of the reconstructed objects, is applied.
First, jets within a cone of $\Delta R < 0.2$ around a hadronically decaying τ-lepton, a muon or an electron are removed. Then, hadronic τ-leptons found within $\Delta R < 0.2$ around a muon or an electron are removed. Finally, electrons are remove if they are reconstructed within $\Delta R < 0.2$ around a muon.

6.8. Trigger Selection

As discussed in Section 5.2.4 the trigger system of the ATLAS detector consists of three stages: the hardware-based L1 level, the software-based L2 trigger and the final event filter (EF) level. At the EF level, single- and di-lepton triggers are used to select $(\mu\mu), (e\mu)$ and (ee) final states.
In the following a brief overview of the triggers used in this analysis is given. A detailed description of the identification criteria applied to electrons and muon can be found in Reference [99, 100].

$(\mu\mu)$ final state:
The di-muon trigger `EF_mu18_tight_mu8_EFFS` is used to select events in this final state. It requires muon objects with $p_T > 18\,\text{GeV}$ and $p_T > 8\,\text{GeV}$. In addition, the highest p_T (*leading*) muon object has to pass the *tight* identification criteria applied to cluster and track properties. For the sub-leading muon object an event filter full scan (EFFS) is performed. Here, not only information from the regions of interest (RoIs) are included, but a scan of the full inner detector system is performed.

$(e\mu)$ final state:
The single-electron trigger `EF_e24vhi_medium1` requires an electron object with $p_T > 24\,\text{GeV}$ passing the *vhi_medium1* identification criteria. Furthermore, the di-lepton trigger `EF_e12Tvh_medium1_mu8` looks for an muon object with $p_T > 8\,\text{GeV}$ and an electron object with $p_T > 12\,\text{GeV}$. In addition, the electron object has to pass the *Tvh_medium1* identification criteria. The event is accepted if it passes any of the two trigger selection criteria.

(ee) final state:
The single-electron trigger `EF_e24vhi_medium1` requires one electron object with $p_T > 24\,\text{GeV}$ passing the *vhi_medium1* identification criteria. Additionally, the di-electron trigger `EF_2e_12Tvh_loose1` is used to select events in this final state. It looks for two electron objects with $p_T > 12\,\text{GeV}$, which pass the *Tvh_loose1* identification criteria. The event is accepted if it passes any of the two trigger selection criteria.

6.9. Simulation of Pile-Up

The presence of additional energy deposition in the detector due to multiple proton-proton interactions is called *pile-up*. In particular, the deposition of additional energy in the detector due to these multiple interactions per bunch crossing is denoted as *in-time pile-up*. Another form of pile-up is caused by the time difference between the bunches of only 50 ns. Here, some of the detector response can be assigned to the wrong bunch crossing, which is referred to as *out-of-time pile-up*.
For data taken in 2012 an average number of interactions per bunch crossing of about 20 was measured. Thus, the modelling of this background in simulation is an important task for the analysis. This is done be generating inclusive samples of proton-proton collisions, which are overlayed with the hard scattered event. This is done for different numbers of interactions per bunch crossing to model the varying luminosity conditions during data taking in 2012. However, the simulated pile-up from MC does not match perfectly with data. Thus, scalefactors are applied to simulated event samples depending on the observed mean number of interactions per bunch crossing in data. By applying theses correction factors, the simulated events are reweighted to match the shape of the measured distributions for the mean number of interactions per bunch crossing. A detailed description of the simulation of pile-up effects in the ATLAS detector is given in Ref. [101].

7 Event Selection

This chapter describes the selection criteria applied to data and simulated samples in order to select signal candidate events. In a first step, preselection requirements select events with final state objects as expected for the signal process. In addition, a multivariate analysis is used to further separate signal and background processes.
In the following, all distributions show the estimation of background contributions as described in Section 8. Since no normalization factors are applied up to cut 12 of the preselection, slight discrepancies between simulation and data can appear. Furthermore, at this stage of the analysis only statistical uncertainties are considered.
The chapter is organized as follows: The first section gives a brief overview of the applied invariant mass reconstruction methods and describes the basic preselection requirements. Then, an introduction into multivariate analysis techniques is given followed by the signal region definition.

7.1. Invariant Mass Reconstruction

The invariant mass of the di-tau system is an important variable to discriminate between signal and background processes, especially for the $Z/\gamma^* \rightarrow ll$ contributions, and allows to access the reconstructed Higgs-boson mass. However, the full leptonic decay channel of the di-tau system provides four neutrinos in the final state, which are reconstructed as missing transverse energy in the detector. Therefore, the di-tau invariant mass is not directly accessible. The following sections gives a brief overview of the mass reconstruction methods used in this analysis.

7.1.1. Collinear Approximation

The collinear mass approximation [102] is a method to reconstruct the neutrino four momentum by assuming that the missing transverse energy E_T^{miss} is only caused by the decay neutrinos and that they are emitted in the same direction as the decay leptons. In the following, the neutrino system will be referred to as *invisible* decay products, while the lepton system is called *visible* decay products. Then, the invariant mass of the di-tau system can be calculated in the collinear approximation as

$$m_{coll} = \frac{m_{vis}}{\sqrt{x_1 x_2}} \tag{7.1}$$

where m_{vis} is the invariant mass of the visible τ-decay products and x_1,x_2 are the momentum fractions carried by the visible particles, the two leptons l_1 and l_2, from each τ-decay:

$$\begin{aligned} \vec{p}_{vis,1(2)} &= x_{1(2)} \left(\vec{p}_{vis,1(2)} + \vec{p}_{miss,1(2)} \right) \\ &= x_{1(2)} \vec{p}_{\tau 1(2)} \end{aligned} \tag{7.2}$$

In the collinear approximation the momentum fractions can be reconstructed by using the measured missing transverse momentum $\vec{E}_T^{miss} = \left(E_T^{miss,x}, E_T^{miss,y}\right)$:

$$x_{1(2)} = \frac{p^x_{vis,2}p^y_{vis,1} - p^y_{vis,2}p^x_{vis,1}}{p^x_{2vis,}p^y_{vis,1} + (-)E_T^{miss,x}p^x_{vis,1(2)} - p^y_{vis,2}p^x_{vis,1} - (+)E_T^{miss,y}p^x_{vis,1(2)}} \tag{7.3}$$

This method gives a reasonable mass resolution for events where the di-tau system is boosted and the collinear assumption is valid. However, for events with a back-to-back topology, $\phi_{l_1 l_2} = \pi$, the transverse momentum of the neutrinos partially cancel out and Eq. 7.3 can not be solved anymore. Thus, events with unphysical solutions ($x < 0$, $x > 1$) are typically discarded and can not be used for further analysis. Since the collinear approximation provides an invariant mass distributions with long tails, this complicates the signal separation from backgrounds and reduces the significance.

7.1.2. Missing Mass Calculator

In contrast to the collinear mass approximation described above, the missing mass calculator (MMC) [103] does not rely on the collinearity assumption, but can be used for any di-tau event topology. The algorithm takes into account probability density functions for τ-decay properties in order to estimate the most probable configuration of neutrino kinematics. For full leptonic decays of the di-tau system the MMC has to determine eight unknown variables: the components of the three-vectors of the invisible momentum carried by the decay neutrinos for each τ-lepton and the invariant mass of the two neutrinos from each leptonic τ-decay. However, only four independent equations can be used to determine the unknown variables:

$$\begin{aligned}
E_T^{miss,x} &= p_{miss,1}\sin(\theta_{miss,1})\cos(\phi_{miss,1}) + p_{miss,2}\sin(\theta_{miss,2})\cos(\phi_{miss,2}) \\
E_T^{miss,y} &= p_{miss,1}\sin(\theta_{miss,1})\sin(\phi_{miss,1}) + p_{miss,2}\sin(\theta_{miss,2})\sin(\phi_{miss,2}) \\
m^2_{\tau_1} &= m^2_{miss_1} + m^2_{vis,1} + 2\sqrt{p^2_{mis,1} + m^2_{miss,1}}\sqrt{p^2_{vis,1} + m^2_{vis,1}} \\
&\quad - 2p_{vis,1}p_{miss,1}\cos(\theta_{vis,1} - \theta_{miss,1}) \\
m^2_{\tau_2} &= m^2_{miss_2} + m^2_{vis,2} + 2\sqrt{p^2_{mis,2} + m^2_{mis,2}}\sqrt{p^2_{vis,2} + m^2_{vis,2}} \\
&\quad - 2p_{vis,2}p_{miss,2}\cos(\theta_{vis,2} - \theta_{miss,2})
\end{aligned} \tag{7.4}$$

Here, the same notation as described above is used: the subscript $miss, i$ (i=1,2) refers to the neutrinos system from the decay of τ_i and the subscript vis, i corresponds to lepton l_i from the decay of τ_i. As a system with eight unknown variables and four conditions is under-constrained, the available information is not sufficient to find the solutions of all unknown variables. However, different solutions are not equally likely when taking into account information about the properties of τ-decay kinematics taken from MC simulations. The MMC algorithm scans the four dimensional parameter space, such as $(\phi_{miss,1}, \phi_{miss,2}, m_{miss,1}, m_{miss,2})$, of all solutions and applies weights to each phase-space point according to a probability density of the decay kinematic properties of this chosen point. As the MMC algorithm depends on the E_T^{miss} resolution the dimensionality of the parameter space is increased by adding two variables for the resolution of the E_x^{miss} and E_y^{miss} components. Out of this sample of weighted solutions the most probable value is used to calculate the final estimator m_{MMC} for the reconstructed di-tau mass in the event.
The MMC algorithm provides a higher efficiency in terms of physical solutions for the reconstructed mass compared to the collinear mass approximation, as it does not rely on specific

τ-decay topologies. Furthermore, it improves the invariant mass resolution by taking into account E_T^{miss} resolution effects for each event.
The di-tau four momentum vector can be reconstructed fully analogously to the calculation of the mass as described above and is used in this analysis for the construction of the Optimal Observable, see Section 2.4.2.

7.2. Preselection

In a first step various cuts are applied on data and simulated events to provide sufficient data quality. These requirements mainly follow the analysis in Ref. [104].

(1) Good runs list:
Data events have to be included in the good runs list (GRL) ensuring that all sub-detectors have been working correctly during data taking.

(2) Primary vertex:
A primary vertex with at least four associated tracks is required.

(3) Jet cleaning:
A set of cuts is applied to jet properties in data and MC to ensure that additional energy deposition in the calorimeter, due to hardware failure or cosmic ray contributions, can be suppressed [105].

(4) Hot-cell veto:
For runs in period B1 and B2 one cell of the Tile calorimeter was not working properly. Therefore, events are removed, if an energy deposition of reconstructed jets with tracks associated to the affected $(\eta-\phi)$-range, is found to be $E_{\text{frac}}/E_{\text{jet}} > 0.6$ in this cell [106].

(5) Event cleaning:
Data events are removed, if parts of the detector, in particular the LAr calorimeter and the tile calorimeter, were not working properly.

Furthermore, basic preselection cuts including trigger requirements are applied to select events with final state objects expected in the signal process and to suppress background contributions.

(6) Hadronic tau veto:
In order to provide an orthogonality to the semi-leptonic and full-hadronic final states, events are rejected, if a hadronically decaying τ-lepton with $p_T > 20\,\text{GeV}$ and $|\eta| < 2.47$ passing the *medium* criteria is reconstructed.

(7) Two leptons:
Two leptons $(ee, \mu\mu, e\mu, \mu e)$[1] with opposite electric charge passing the reconstruction criteria described in Section 6 are required.

(8) Trigger:
The event has to have been triggered by one of the lepton triggers described in Section 6.8.

(9) Trigger matching:
The reconstructed leptons have to be associated with the triggered leptons. The corresponding trigger thresholds are described in Section 6.8.

[1] the lepton with highest p_T is listed first

(10) Two jets:
At least two reconstructed jets are required with transverse momentum $p_T^{\text{lead}} > 40\,\text{GeV}$ for the highest p_T-jet and $p_T^{\text{sublead}} > 30\,\text{GeV}$ for the jet with the second highest p_T.

(11) Dilepton mass:
Different cuts are applied on the invariant mass m_{ll} of the leptons depending on the lepton flavour combination of the final state. In the different flavour channel $(e\mu, \mu e)$ $30 < m_{ll} < 100\,\text{GeV}$ is required, while a tighter cut of $30 < m_{ll} < 75\,\text{GeV}$ is applied to same flavour final states $(ee, \mu\mu)$ in order to suppress $Z/\gamma^* \to ee, \mu\mu$ events. The

(12) Momentum fraction:
This cut requires $0.1 < x_{1,2} < 1.0$, where x_1,x_2 are the momentum fractions carried by the visible part of the τ-decay. Within the collinear mass approximation, the momentum fractions are calculated as given in Eq. 7.3.

(13) b-jet veto:
Events containing a b-jet are rejected. The *b-tagging* method, described in Section 6.4, is used at a working point of 70% for jets with $p_T > 25\,\text{GeV}$ and $|\eta| < 2.5$. The b-jet veto reduces the background contribution from single top and $t\bar{t}$ events significantly.

(14) Collinear mass:
For the collinear mass as defined in Eq. 7.1 the requirement $m_{coll} > m_Z - 25\,\text{GeV}$ has to hold in order to ensure orthogonality with the $H \to WW$ channel. Fig. 7.1 shows the m_{coll} distribution after cut 13.

(15) Missing transverse energy:
In the different flavour channel $(e\mu, \mu e)$ missing transverse energy of $E_T^{miss} > 20\,\text{GeV}$ is required. A tighter cut of $E_T^{miss} > 70\,\text{GeV}$ is applied on events with same flavor final states $(ee, \mu\mu)$ in order to reject $Z/\gamma^* \to ee, \mu\mu$ background contribution. Fig. 7.2 shows the E_T^{miss} distributions for $(ee, \mu\mu)$ and $(e\mu, \mu e)$ final states after cut 14.

(16) $\boldsymbol{E_T^{miss}}$(HPTO)
The missing transverse energy for high-p_T objects (HPTO) is calculated with the decay leptons l_1, l_2 and jets having $p_T > 25\,\text{GeV}$ according to:

$$\begin{aligned} E_{x,y}^{miss}(\text{HPTO}) &= -p_{x,y}(l_1) - p_{x,y}(l_2) - \sum_{jets} p_{x,y}(jet) \\ E_T^{miss}(\text{HPTO}) &= \sqrt{(E_x^{miss}(\text{HPTO}))^2 + (E_y^{miss}(\text{HPTO}))^2} \end{aligned} \tag{7.5}$$

By requiring $E_T^{miss}(\text{HPTO}) > 50\,\text{GeV}$ in the $(ee, \mu\mu)$-final state, the contribution from Drell-Yan $Z/\gamma^* \to ee, \mu\mu$ event is further reduced. Fig. 7.3 shows the $E_T^{miss}(\text{HPTO})$ distribution in the different flavour final state after cut 15.

(17) $\sum \boldsymbol{p_T}$(l):
The scalar sum of the transverse momenta of the decay leptons $p_T(l_1) + p_T(l_2)$ has to be greater than 45 GeV to suppress contributions from events with misidentified leptons. Fig. 7.4 shows the $\sum p_T(\text{l})$ distribution after cut 16.

(18) MMC mass:
Events are discarded, if the MMC algorithm described above does not converge. Thus, $m_{MMC} > 0$ has to hold for the event to not be rejected.

This preselection reduces the contribution from background processes as a first step. Table 7.1 shows the expected event yield for SM signal and each background component after cut 18. The signal to background ratio is about $\frac{s}{b} = \frac{19.78}{2692.46} = 7.4 \times 10^{-3}$ with largest contribution arising from $Z \to \tau\tau$ (66%), top-quark (25%) and Diboson (6%) processes. In order to be sensitive to anomalous Higgs-gluon couplings, further background suppression is crucial.
The distributions of the Optimal Observable and $\Delta\Phi_{jj}^{sign}$ are shown in Fig. 7.5 at an early stage of the preselection. In addition, Fig. 7.6 shows the observables after the full preselection. While the shape of the Optimal Observable is not affected by the preselection, $\Delta\Phi_{jj}^{sign}$ is slightly distorded. However, a good agreement between simulation and data is obtained. As the construction of $\Delta\Phi_{jj}^{sign}$ requires the outgoing jets to be in different detector hemisspheres, $\eta_{j1}\eta_{j2} < 0$, only a fraction of the signal and background events passing the preselection are available. In addition, the sensitivity of $\Delta\Phi_{jj}^{sign}$ to anomalous coupling models can be enhanced by requiring $\Delta y_{j1j2} > 3.0$, as discussed in Section 2.4.2. Table 7.2 summarizes the expected event yield for signal and background processes, which pass these requirements. For the construction of $\Delta\Phi_{jj}^{sign}$ with $\eta_{j1}\eta_{j1} < 0$ only 42% of the signal events after the preselection are available. Also the total background contributes with only 43% of the availabe events after the preselection. The largest suppression is found for events in the VH production channel, VH $H \to \tau\tau$ and VH $H \to WW$, where only about 25% of the events after preselection are obtained. In the VBF production channel, VBF $H \to \tau\tau$ and VBF $H \to WW$, however, about 83% of the events after the preselection provide jets in different detector hemisspheres. This results in a signal over background ratio of $\frac{s}{b} = \frac{8.34}{1158.41}$.
Requiring the jets to also have a separation of $\Delta y_{j1j2} > 3.0$ reduces the available statistics further. Here, only 9% of signal events and 6% of background events after preselection satisfy this requirement. Events arising from the VH production, VH $H \to \tau\tau$ and VH $H \to WW$, are reduced most, as only about 1% of the events after the preselection can be used. The VBF production, on the other hand, contributes with about 35% of the events after the preselection. This results in a signal over background ratio of $\frac{s}{b} = \frac{1.68}{158.64}$. Therefore, $\Delta\Phi_{jj}^{sign}$ with $\Delta y_{j1j2} > 3.0$ will not be considered for further analysis.

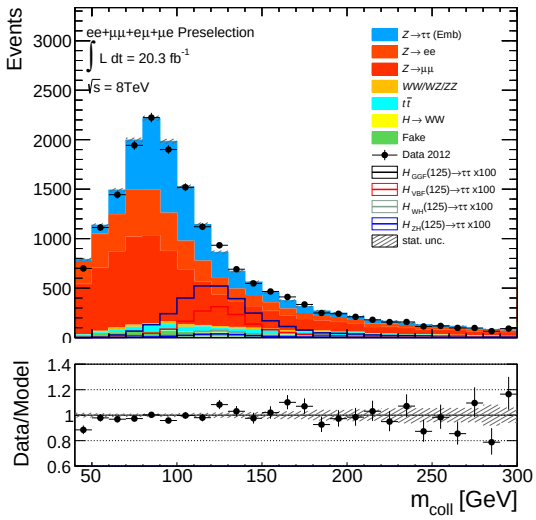

Figure 7.1.: Distribution of the collinear mass m_{coll} after cut 13 of the preselection with statistical uncertainties.

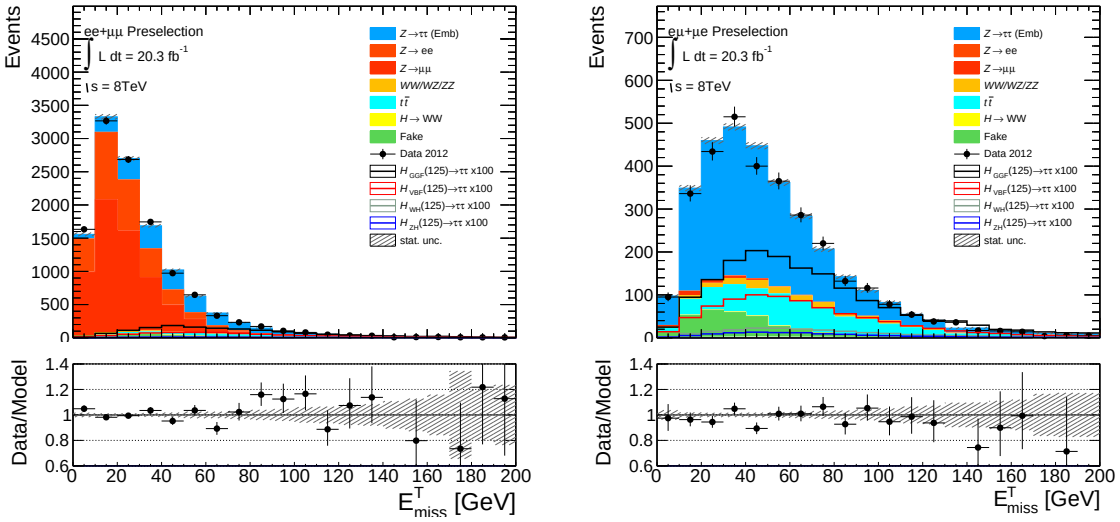

Figure 7.2.: Distribution of the missing transverse energy E^T_{miss} for the same-flavour region (left) and different-flavour region (right) after cut 14 of the preselection with statistical uncertainties.

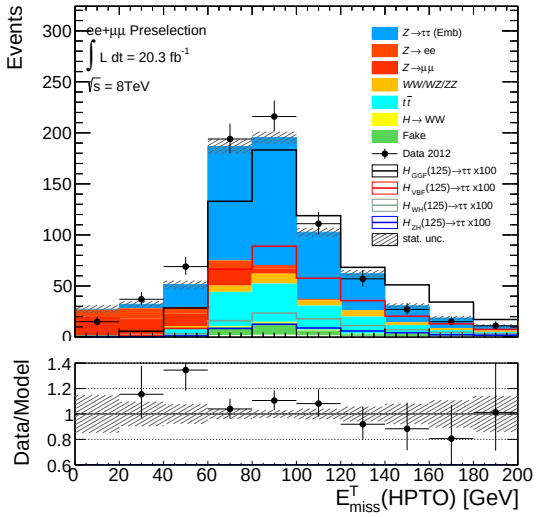

Figure 7.3.: Distribution of the missing transverse energy for high p_T objects E^T_{miss}(HPTO) after cut 15 of the preselection with statistical uncertainties.

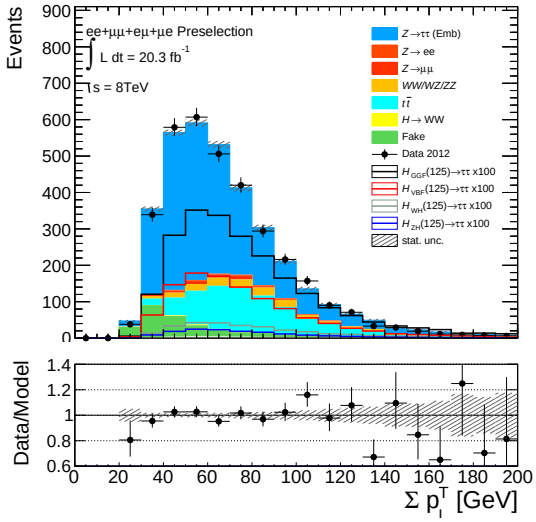

Figure 7.4.: Distribution of the transverse momentum of the leptons $\sum p_l^T$ after cut 16 of the preselection with statistical uncertainties.

Process	Event yield
ggF H + 2jets $\rightarrow \tau\tau$	19.79 ± 0.25
VBF H $\rightarrow \tau\tau$	9.51 ± 0.04
VH H $\rightarrow \tau\tau$	3.93 ± 0.02
$Z \rightarrow \tau\tau$	1765.28 ± 14.16
$Z \rightarrow ee, \mu\mu$	63.02 ± 5.89
Diboson	151.06 ± 6.83
Top	668.64 ± 14.38
ggF H→WW	7.74 ± 0.30
VBF H→WW	3.73 ± 0.08
VH H→WW	1.47 ± 0.17
Fake leptons	118.08 ± 4.69
$\sum$ bkgs	2792.46 ± 22.60
Data	2792.00 ± 52.83

Table 7.1.: Expected event yield after the preselection with statistical uncertainties for SM signal and each background component compared to the observed data for $\sqrt{s} =$ 8 TeV.

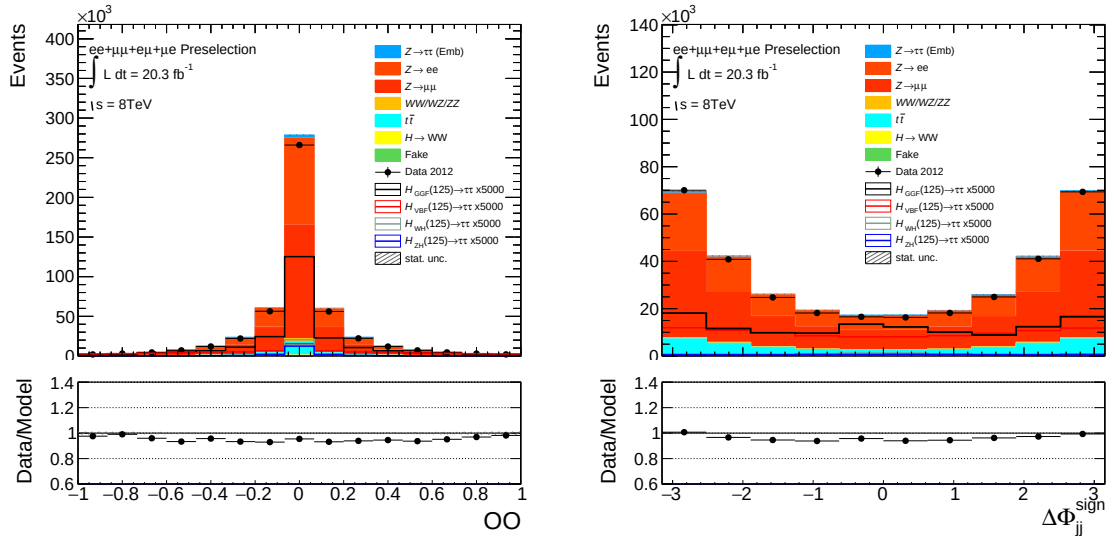

Figure 7.5.: Distribution for the Optimal Observable (left) and $\Delta\Phi_{jj}^{sign}$(right) after cut 10 of the preselection with statistical uncertainties.

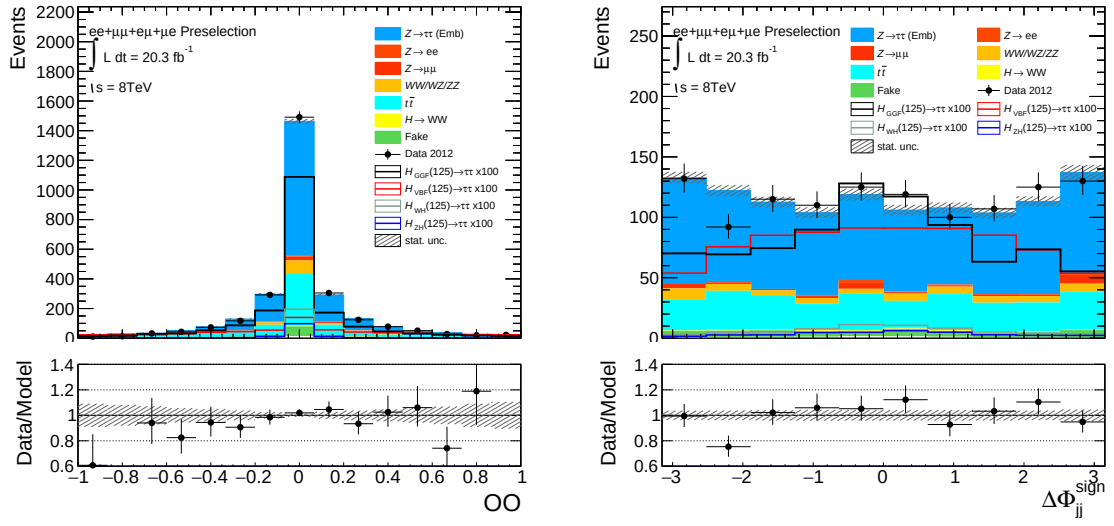

Figure 7.6.: Distributions for the Optimal Observable (left) and $\Delta\Phi_{jj}^{sign}$(right) after cut 18 of the preselection with statistical uncertainties.

Process	Event yield	
	$\eta_{j1}\eta_{j2} < 0$	$\eta_{j1}\eta_{j2} < 0,\ \Delta y_{j1j2} > 3.0$
ggF H + 2jets $\to \tau\tau$	8.34 ±0.16 (42%)	1.68 ± 0.07 (9%)
VBF H $\to \tau\tau$	7.87 ± 0.04 (83%)	3.25 ± 0.02 (34%)
VH H $\to \tau\tau$	0.99 ± 0.01 (25%)	0.03 ± 0.01(1%)
$Z \to \tau\tau$	736.24 ± 9.10 (42%)	99.64 ± 3.19 (6%)
$Z \to ee, \mu\mu$	31.68 ± 4.98 (51%)	7.27 ± 1.95 (12%)
Diboson	58.12 ± 4.23 (34%)	7.60 ± 1.54(5%)
Top	268.67 ± 9.05 (40%)	29.99 ± 2.86 (5%)
ggF H→WW	3.59 ± 0.20 (46%)	0.75 ± 0.09 (10%)
VBF H→WW	3.08 ± 0.07 (83%)	1.27 ± 0.04 (34%)
VH H→WW	0.40 ± 0.09 (27%)	< 0.01 (<1%)
Fake leptons	47.77 ± 2.95 (41%)	8.84 ± 1.19 (8%)
$\sum$ bkgs	1158.41 ± 14.70 (43%)	158.64 ± 5.10 (6%)
Data	1155.0 ± 33.98 (43%)	162.0 ± 12.72 (6%)

Table 7.2.: Expected event yield after the preselection with statistical uncertainties for SM signal and each background component compared to the observed data for $\sqrt{s} =$ 8 TeV with additional requirements on the jet topology in order to reconstruct the observable $\Delta\Phi_{jj}^{sign}$. The numbers in brackets give the fraction of events passing the corresponding requirement with respect to the event yield after the preselection given in Table 7.1.

7.3. Multivariate Analysis

After the basic event selection, presented in Section 7.2, further discrimination between the signal and background processes is needed to increase the sensitivity. One method is to apply additional one- or two sided cuts on single variables discriminating between signal and background events. However, such a cut-based approach does not provide an optimal separation, as it is not able to make use of the correlations between variables. Multivariate analysis methods enable the inclusion of multiple variables, while using their correlations to supply maximum signal to background separation. Opposed to the cut-based approach, events are not removed from the sample, but are rather classified as signal- or background-like by assigning an event weight.
While several multivariate techniques exist, a boosted decision tree (BDT), as implemented in the *Toolkit for MultiVariate Data Analysis* (TMVA) package [107], is used in this analysis. The following section gives a brief introduction into the general idea of BDTs and describes the training procedure, the input variables and the signal region definition for this analysis.

7.3.1. BDT Construction and Configuration

In general, a decision tree consists of several nodes each representing a binary decision. Based on a certain input variable, each decision divides the event sample further into signal- and background-like sub-samples. A typical choice to define these splittings is the so called *Gini Index* G, given by

$$G = p\,(1-p) \tag{7.6}$$

with signal purity p for a given node after the split. Each splitting is optimized by using the cut on the input variable which maximizes the *Gini Index*. This procedure is repeated recursively for each sub-sample until a stopping criterion is reached. The splitting optimization is usually referred to as *training* of a decision tree on a given training sample. In principle, the decision tree could continue splitting until each sub-sample is left with exactly one event, which would offer perfect signal separation. However, in this case the splitting performance on an independent test sample would be significantly worse as the decision tree exploits statistical fluctuations during training. This is referred to as *overtraining*. Several approaches can reduce overtraining: restrictions of the *tree depth*, giving the maximum number of decision nodes an event can pass, as well as limiting the minimal number of events in each node or using a *pruning* method, which reduces the number of nodes after the training. A schematic view of a decision tree with depth four is given in Fig. 7.7.
While single decision trees have a rather low separation performance, combining various decision trees can improve the separation power significantly and enhance the robustness against overtraining. Such a series of decision trees are called *Boosted Decision Trees* (BDTs). The *boosting* concept is based on using different training samples for each tree by applying weights to the training events, which depend on the classification of the preceding tree. One important boosting method is the so called *Gradient Boosting* [108], which is used in this analysis. *Gradient boosting* estimates a function $F(\vec{x})$ depending on the full set of variables $\vec{x}$ for each event, which minimizes a so called *loss function*. The loss function quantifies the quality of a decision tree's separation power and provides a weight w for each decision tree. The final classifier $F(\vec{x})$ is given as a combination of all iteration steps

$$F(\vec{x}) = \sum_{i=1}^{N} w_i h_i(\vec{x}) \tag{7.7}$$

where the sum runs over all N decision tree and $h_i(\vec{x}) = +1(-1)$ refers to the event classification being signal(background)-like based on $\vec{x}$ for tree i. This maps the final classification function of all decision trees to a score value in the range $(-1, +1)$. This score value is called BDT output in the following.
To stabilize the classification with respect to statistical fluctuations, a learning rate β with $0 < \beta < 1$ is introduced, scaling down the weights w_i in Eq. 7.7. While this procedure, also known as *shrinkage*, can improve the BDT performance significantly, a low learning rate β requiring a large number of iterations comes at the price of increased computation time. Furthermore, *Stochastic Gradient Boosting* [109] is used. Here, each decision tree is trained with only a fraction of the available event sample, selected on a random basis. This reduces the overtraining due to statistical fluctuations in the training sample and improves the BDT classification power.

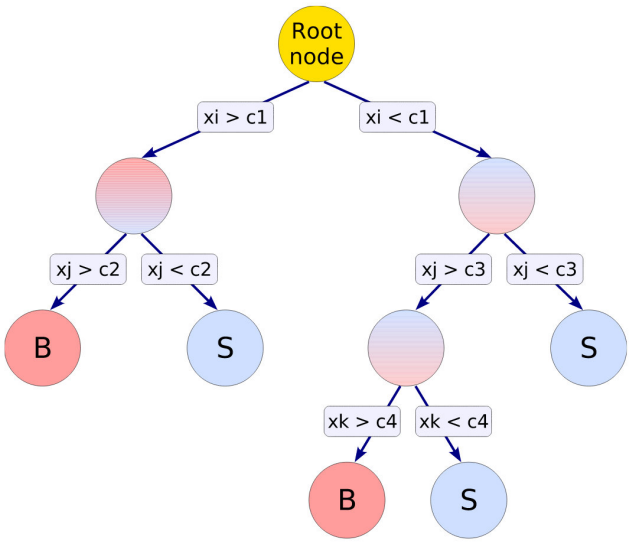

Figure 7.7.: Schematic view of a single decision tree. Starting from the first decision based on variable x_i the events are grouped into a signal-like and a background-like sub-samples (S and B) for a specific cut value c_1 [110]. Each node then splits the classified events further into so called leaf-nodes based on cut-values c_i until a stopping criterion is reached.

7.3.2. BDT Training and Performance

To avoid a bias during training, the BDT performance is checked for overtraining by using an independent event sample. This is accomplished by dividing the full event set into a *training* and a *testing* sample. However, this reduces the available training statistics by half and favours overtraining. Therefore, this analysis uses a *cross-evaluation* method to check the BDT performance. In this method, signal and background events are divided into two samples A and B depending on their event number. Events with even event number are assigned to sample A, while events corresponding to an odd event number are assigned to sample B. Both samples are used for training and testing of two independent but identically constructed BDTs, referred to as BDT A and BDT B in the following. Events of sample A are used for training of BDT A, while events of sample B are used for training of BDT B. As sample A and B are statistically independent, events from sample B can be used for testing

the performance of BDT A and vice versa. If the BDTs separation power is significantly better for training than for testing events, statistical fluctuations in the training sample have an impact on the performance, thus the BDT is overtrained. With this method, the full set of available statistics can be exploited for further analysis.
As described in Section 3.3.1 the analysis uses simulated signal samples for H+1jet at NLO. In order to increase the training statistics and therefore reduce the BDT liability for overtraining, the signal sample for training consists of simulated events for H+1jet at NLO and H+2jets at NLO. To ensure, that this does not result in a bias for the BDT separation, the test sample only contains H+1jet at NLO events.
The background sample consists of all processes discussed in Section 3.2. In case of additional normalization factors for specific background processes derived in Section 3.2, these factors are applied before the training.
In this analysis, two distinct BDTs are constructed in order to increase the signal over background ratio and also reduce the contribution from VBF H$\rightarrow \tau\tau$ events. The first BDT exploits the full set of considered background processes and will be referred to as $\mathrm{BDT_{bkg}}$ in the following. While in general BDTs can be trained by using an arbitrary large set of input variables, the decision tree always chooses the variable which gives the greatest separation power between signal and background events. Table 7.3 summarizes the variables, which are used for the training of $\mathrm{BDT_{bkg}}$ with their corresponding distributions shown in Fig. 7.8 and Fig. 7.9. The variables enter the training after the basic preselection described in Section 7.2. In total, a set of 10 variables is used for the training. The choice of these variables is based on their contribution to the separation power of the BDT, which can be quantified by the number of splittings based on a specific variable. The resulting variable ranking, shown in Table 7.4, gives an indication for the variable importance in the training. As expected, mass variables, such as m_{MMC} and m_{ll} are ranked high, but also angular correlations between the jets and leptons, as $\Delta R_{j,l}^{min}$, and kinematic variables of the reconstructed Higgs boson are used in the BDT. The BDT performance is improved by employing differences in the correlation of input variables signal and background events. Fig. 7.10 shows the correlation between the input variables for $\mathrm{BDT_{bkg}}$ for signal and background events in the training sample.
The BDT performance also depends on parameter settings, defining the construction of a single tree, as well as the boosting procedure. Table 7.5 shows the parameter settings for $\mathrm{BDT_{bkg}}$. The main parameters are the number of combined decision trees N_{tree}, the maximum number of node splitting MaxDepth and the minimum sample yield for each node nEventsMin. As described above, Gradient boosting is used and the splitting decision is based on the Gini Index. All parameter settings are optimized with regard to maximum separation power on the test events.
To quantify the separation power, the *Receiver Operating Characteristic* (ROC) curves are used. They provide the dependence between signal efficiency and background rejection, as shown in Fig. 7.11. No significant deviations between $\mathrm{BDT_{bkg}}$ A and $\mathrm{BDT_{bkg}}$ B are observed, which indicates that no overtraining took place. An additional test of overtraining in shown in Fig. 7.12. Here the separation performances of $\mathrm{BDT_{bkg}}$ A and $\mathrm{BDT_{bkg}}$ B are compared for training and testing samples. If the BDT is overtrained, this would results in a clear difference of the BDT performance for training and testing events. For $\mathrm{BDT_{bkg}}$ A the *Kolmogorov-Smirnov compatibility test* [111, 112] provides a good agreement of the BDT output for training and testing samples for both signal and background distributions, while a slight overtraining is present for $\mathrm{BDT_{bkg}}$ B. However, this does not result in a bias of the $\mathrm{BDT_{bkg}}$ performance, as training and testing samples are statistically independent.
The final classification of $\mathrm{BDT_{bkg}}$ is shown in Fig. 7.13 (a) for signal and background processes. The data agrees well with the SM expectations. A good separation is achieved for

signal and non-Higgs backgrounds. However, events of VBF and VH production H$\rightarrow \tau\tau$ are still classified as signal-like and have to be further suppressed.
Therefore, a second BDT is used in this analysis. This BDT has been optimized to separate ggF H+2jets events from VBF production and will be referred to as $\mathrm{BDT_{VBF}}$ in the following. Here, the same signal sample, but only VBF H$\rightarrow \tau\tau$ background events are considered for the BDT training. The same optimization procedure in selecting variables and parameter settings was performed as described above for $\mathrm{BDT_{bkg}}$. Table 7.3 shows the input variables with their corresponding ranking index given in Table 7.4(b). As expected, the BDT mainly takes advantage from typical VBF topolgies as $\Delta\eta_{jj}$ and m_{jj}, but also the jet separation ΔR_{jj} and $\Delta R_{j,l}^{min}$ contribute to the separation. Table 7.5 shows the parameter settings for BDT_vbf, which mainly agree with the settings derived for $\mathrm{BDT_{bkg}}$. The performance can be evaluated by considering the ROC curve shown in Fig. 7.5(b). The overtraining test for $\mathrm{BDT_{VBF}}$ is shown in Fig. 7.12 and shows a good agreement between training and testing events. In comparison to $\mathrm{BDT_{bkg}}$ this BDT seems provides a higher background rejection for the same signal selection efficiency. However, for $\mathrm{BDT_{VBF}}$ only ggF H+2jets against VBF events H$\rightarrow \tau\tau$ are tested. Fig. 7.13(b) shows the distribution of the $\mathrm{BDT_{VBF}}$ output for all signal and background processes. A good separation power is achieved for ggF H+2jet and VBF events, while processes not considered in the BDT training, such as $Z \rightarrow \tau\tau$ and $t\bar{t}$, are classified as signal-like. This is expected, as the variables used for the training exploit typical VBF topologies.

Variable	Definition	$\mathrm{BDT_{bkg}}$	$\mathrm{BDT_{VBF}}$
ΔR_{jj}	separation of the leading jets	•	•
ΔR_{ll}	separation of the leptons	•	
p_T^H	$(p_T^{l1} + p_T^{l1} + p_T^{miss})$	•	
$\Delta R_{jl}^{\mathrm{min}}$	min separation of (sub)leading jet and (sub)leading lepton	•	•
m_{Hj}	invariant mass of Higgs-boson+leading-jet system	•	
m_{MMC}	invariant Higgs-boson mass with MMC	•	
$\Delta\phi_{ll}$	ϕ-angle between leptons	•	
m_{ll}	invariant mass of leptons	•	
m_{coll}	invariant Higgs-boson mass with collinear approximation	•	
E_T^{miss}	missing transverse energy	•	
m_{jj}	invariant mass of leading jets		•
$\Delta\eta_{jj}$	η-separation of leading jets		•

Table 7.3.: Discriminating variables used for the BDT training of $\mathrm{BDT_{bkg}}$ and $\mathrm{BDT_{VBF}}$ as described in the text.

Variable	Ranking index
m_{MMC}	0.18
m_{coll}	0.14
m_{ll}	0.11
$\Delta R_{j,l}^{min}$	0.10
$\Delta\phi_{ll}$	0.09
ΔR_{jj}	0.09
E_T^{miss}	0.09
ΔR_{ll}	0.08
m_{Hj}	0.07
p_T^H	0.07

Variable	Ranking index
$\Delta\eta_{jj}$	0.38
ΔR_{jj}	0.24
m_{jj}	0.20
$\Delta R_{j,l}^{min}$	0.18

Table 7.4.: Importance ranking of the discriminating variables used for the training of $\mathrm{BDT_{bkg}}$ (left) and $\mathrm{BDT_{VBF}}$ (right).

Parameter	Value $\mathrm{BDT_{bkg}}$ ($\mathrm{BDT_{VBF}}$)
NTrees	450 (200)
nEventsMin	1.3 % of training events
MaxDepth	4
BoostType	Grad
SeparationType	GiniIndex
nCuts	30 (40)
PruneMethod	no pruning
NegWeightTreatment	IgnoreNegWeightsInTraining

Table 7.5.: Configuration parameters of the BDT training in TMVA notation [110] for $\mathrm{BDT_{bkg}}$ and $\mathrm{BDT_{VBF}}$. If no value is given in brackets, the settings for $\mathrm{BDT_{bkg}}$ and $\mathrm{BDT_{VBF}}$ are the same.

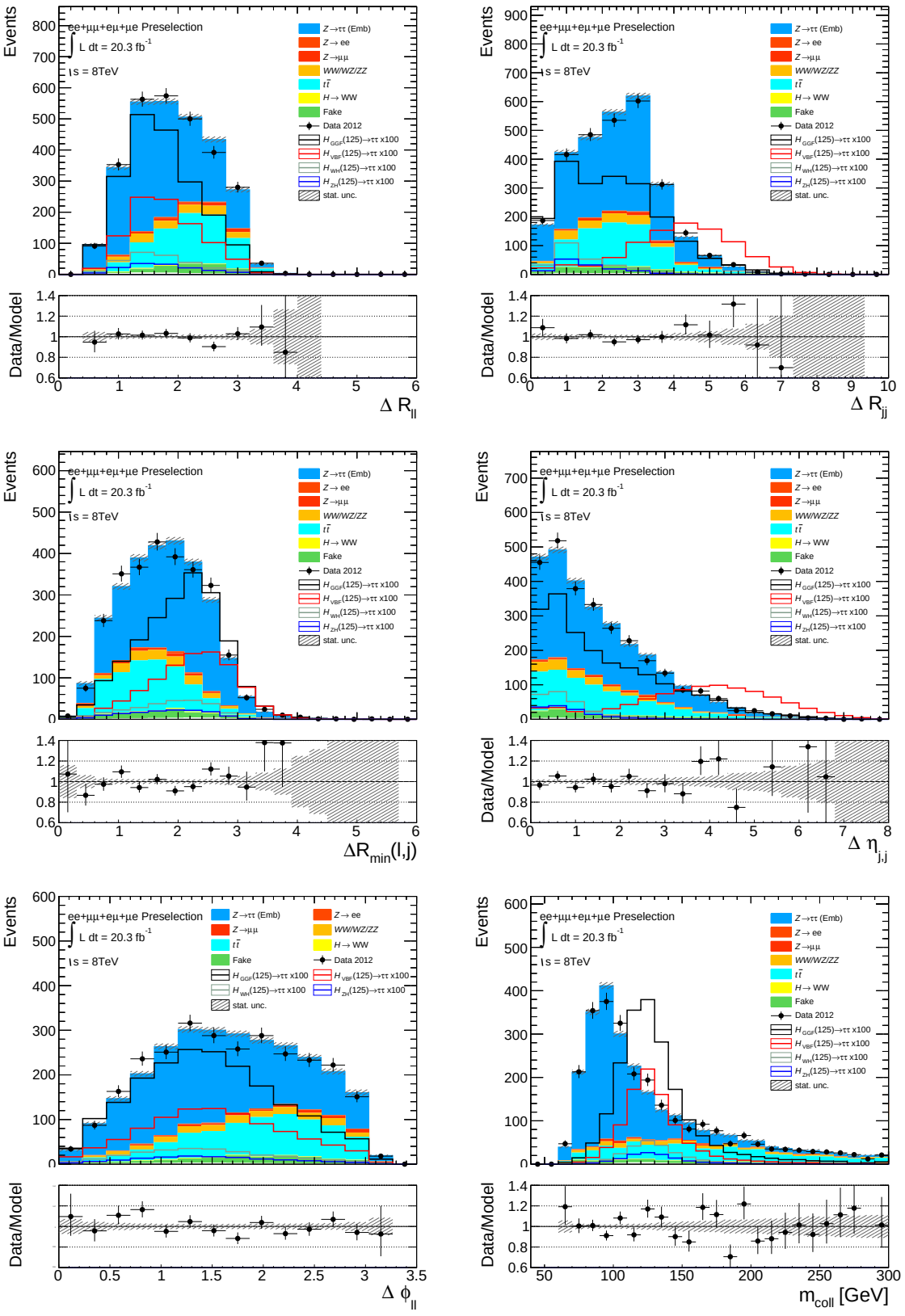

Figure 7.8.: Input variables for the training of $\mathrm{BDT_{bkg}}$ and $\mathrm{BDT_{VBF}}$ after the preselection with statistical uncertainties. A description of the input variables can be found in Table 7.3.

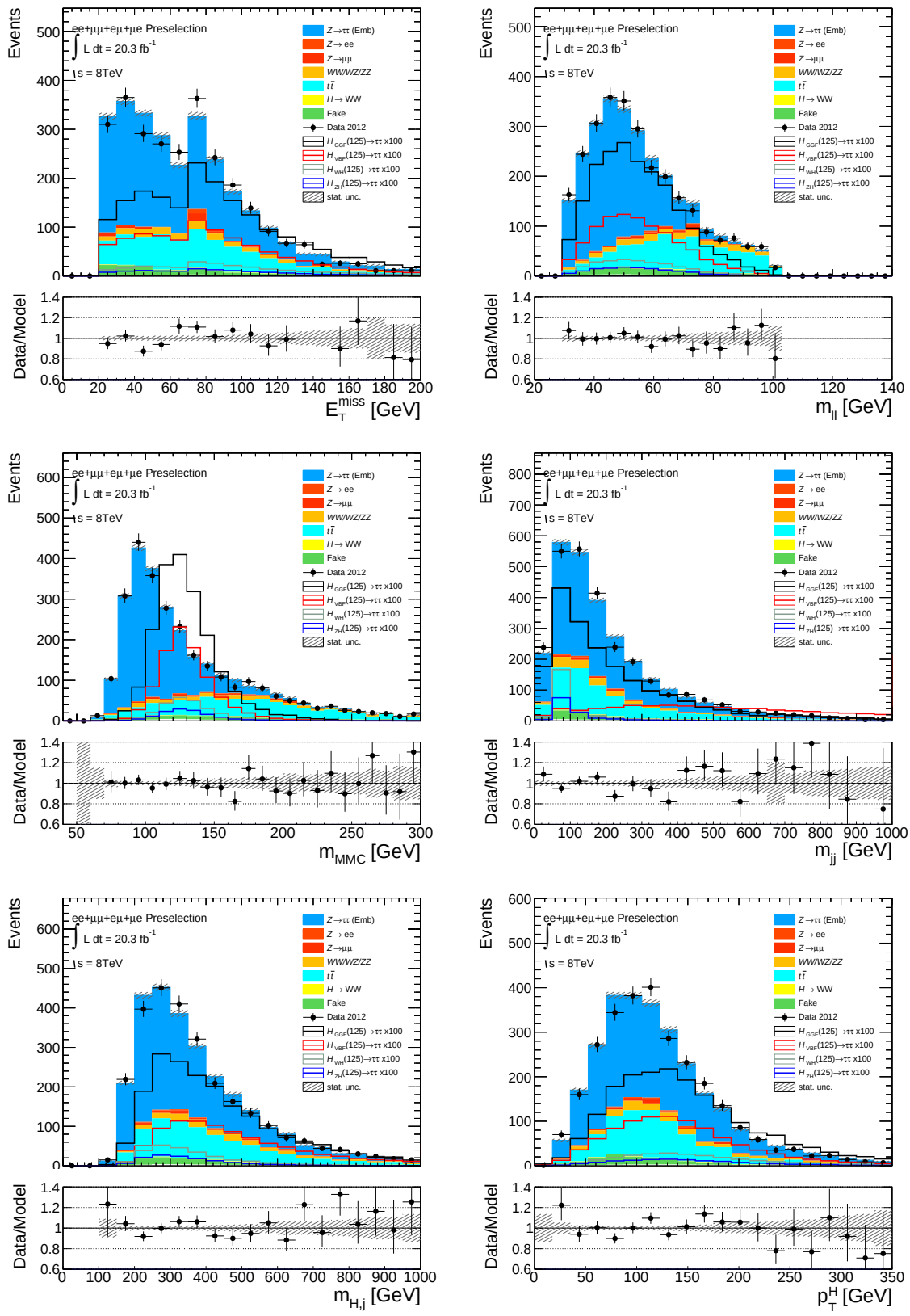

Figure 7.9.: Input variables for the training of $\mathrm{BDT_{bkg}}$ and $\mathrm{BDT_{VBF}}$ after the preselection with statistical uncertainties. A description of the input variables can be found in Table 7.3.

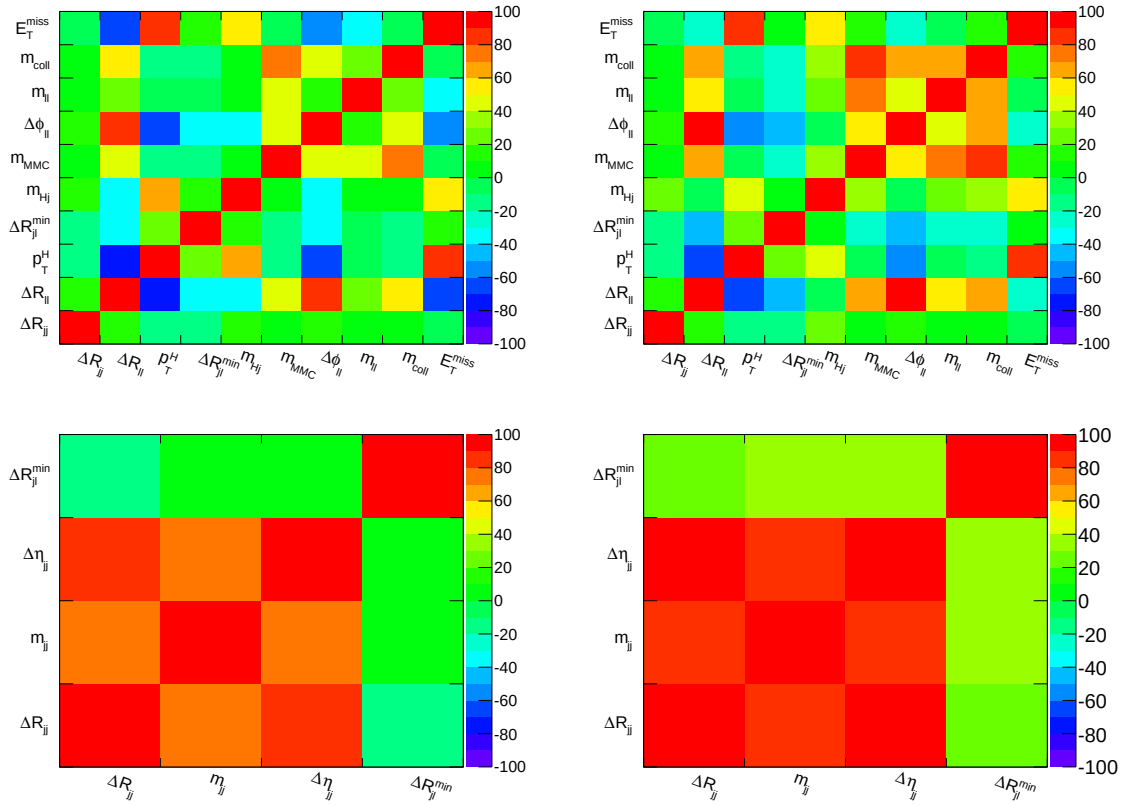

Figure 7.10.: Linear correlation coefficients of input variables for signal (left) and background (right) for $\mathrm{BDT_{bkg}}$ (top) and $\mathrm{BDT_{VBF}}$ (bottom).

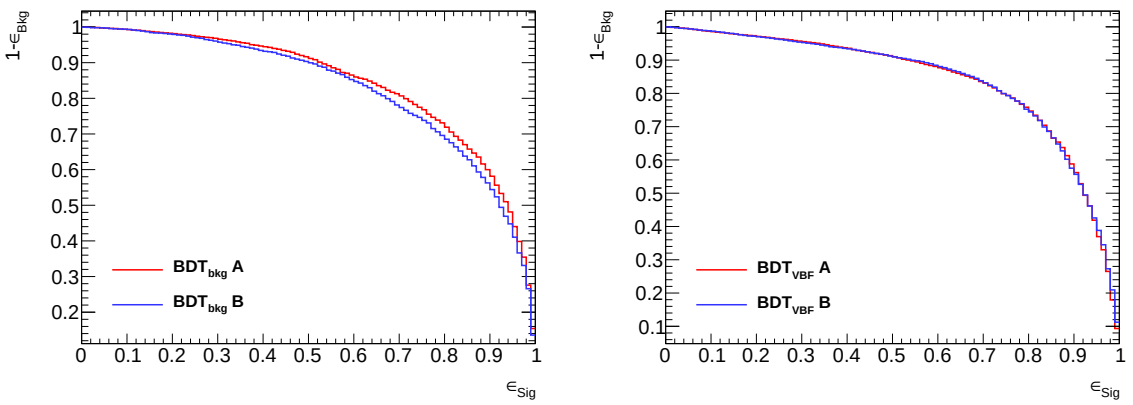

Figure 7.11.: Background rejection vs. signal efficiency for $\mathrm{BDT_{bkg}}$ (left) and $\mathrm{BDT_{VBF}}$ (right) each comparing the performance of BDT A and BDT B as defined in the text.

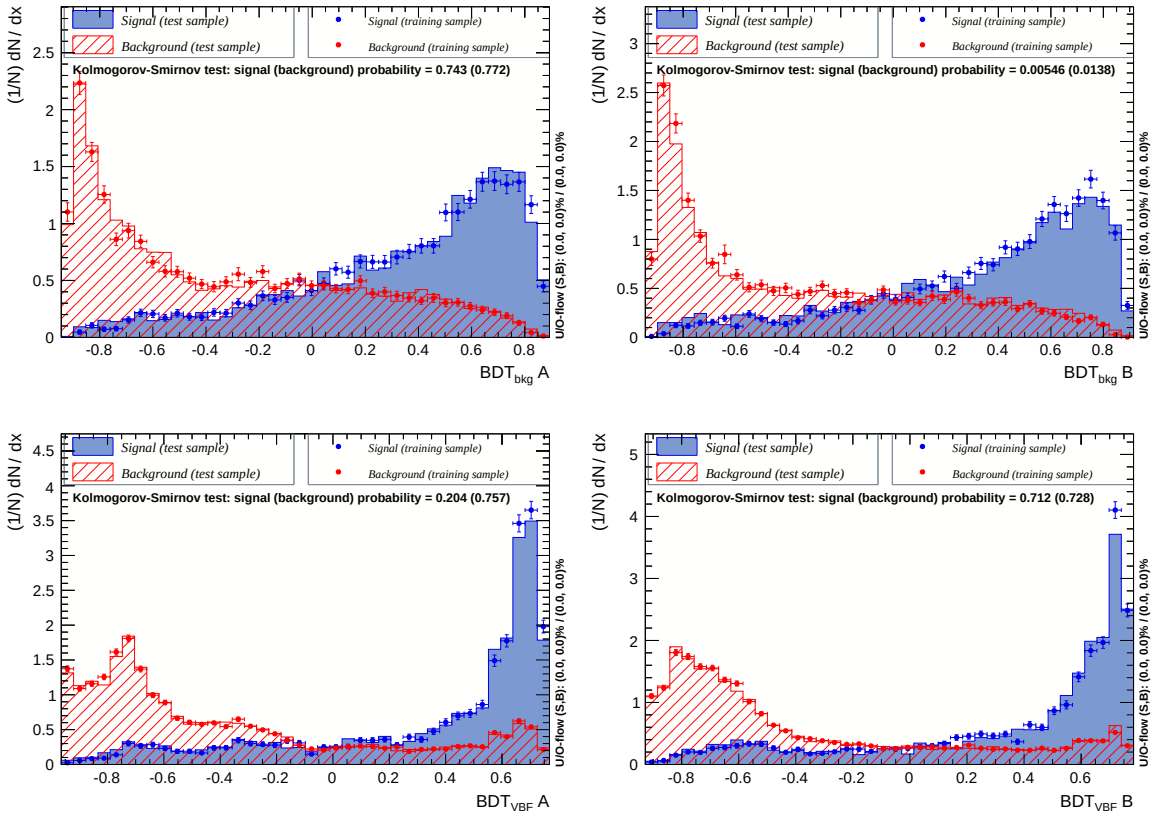

Figure 7.12.: Overtraining test for $\mathrm{BDT_{bkg}}$ A (top left), $\mathrm{BDT_{bkg}}$ B (top right), $\mathrm{BDT_{VBF}}$ A (top left) and $\mathrm{BDT_{VBF}}$ B (top right). The normalized distributions of signal and background events are compared for the corresponding training and testing samples.

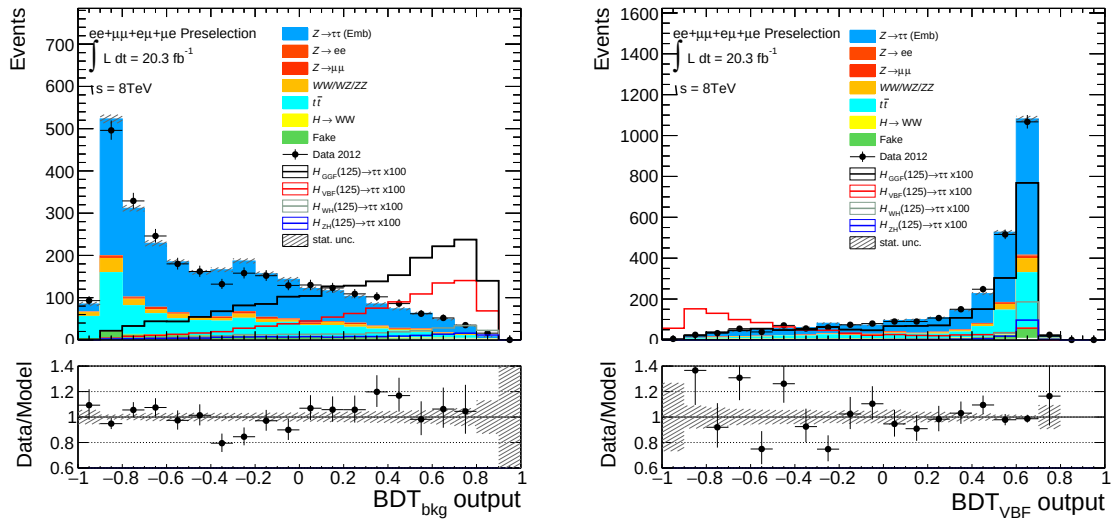

Figure 7.13.: Distributions of the BDT output for $\mathrm{BDT_{bkg}}$ (left) and $\mathrm{BDT_{VBF}}$ (right) after the preselection with statistical uncertainties.

7.3.3. Signal Region Definition

The sensitivity to anomalous Higgs-gluon coupling contributions strongly depends on the suppression of SM background processes. By cutting on the BDT outputs shown in Fig. 7.13, the signal over background ratio is increased significantly. Fig. 7.14 shows the correlation between $\mathrm{BDT_{bkg}}$ output and $\mathrm{BDT_{VBF}}$ output for the ggF H+2jets signal, VBF events and the sum of all other background processes. As expected, ggF H+2jets events are identified as signal-like for both classifiers, while VBF events and other background processes show opposed correlations for $\mathrm{BDT_{bkg}}$ and $\mathrm{BDT_{VBF}}$.

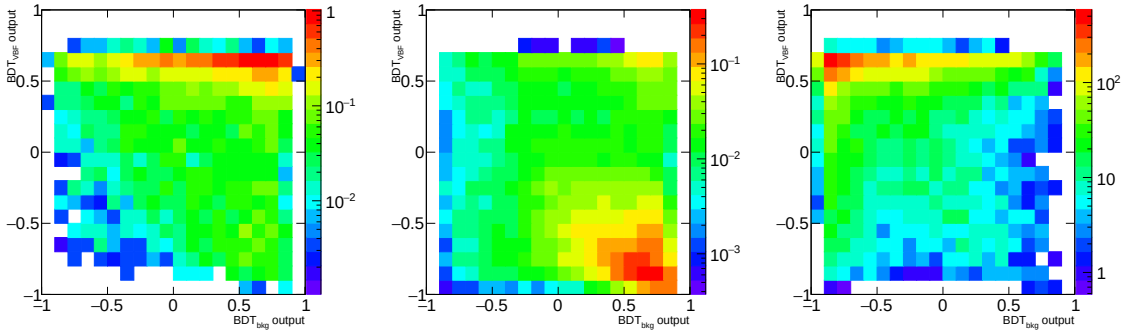

Figure 7.14.: Correlation between the output of $\mathrm{BDT_{bkg}}$ and $\mathrm{BDT_{VBF}}$ for the SM ggF H+2jets signal (left), VBF $H \to \tau\tau$(middle), and the sum of other background processes (right). The distributions are shown after preselection.

In order to combine the two classifications, an optimization in the two-dimensional space spanned by the output of $\mathrm{BDT_{bkg}}$ and $\mathrm{BDT_{VBF}}$ is performed. An event cut is applied by scanning the output of $\mathrm{BDT_{VBF}}$ in steps of 0.2, $\mathrm{BDT_{VBF}} > z_i$ with $z_i = (-1, -0.8, ...)$, and calculating the ratio of VBF to ggF H+2jet events, denoted as $\frac{vbf}{ggf}$. For each cut i on $\mathrm{BDT_{VBF}}$ the maximum significance S is calculated by cutting on the output of $\mathrm{BDT_{bkg}}$ in steps of 0.2. As only statistical uncertainties are considered here, the significance is defined as $S = \frac{s}{\sqrt{s+b}}$ with s corresponding to the number of signal events and b to the sum of all background contributions including VBF events. This approach provides the correlation between $\frac{vbf}{ggf}$ and the maximum significance as shown in Fig. 7.15: A maximum significance of $S = 0.62$ with $\frac{vbf}{ggf}$=0.50 is achieved for $\mathrm{BDT_{bkg}} > 0.6$ and no cut on $\mathrm{BDT_{VBF}}$. A lower VBF contribution $\frac{vbf}{ggf} < 0.50$, however, comes at the cost of degraded significance $S < 0.62$. In this analysis, $\frac{vbf}{ggf}$ is required to be less than 20%. With this requirement the maximum significance obtained is $S = 0.58$, which is achieved by applying the cuts $\mathrm{BDT_{bkg}} > 0.6$ and $\mathrm{BDT_{VBF}} > -0.3$. In the following, the phase space region including this requirement is referred to as *high BDT signal region*.

The expected event yields for signal and background components in the high BDT signal region are given in Table 7.6. The dominant contribution still arises from $Z \to \tau\tau$ (65%), top-quark (17%) and Diboson (9%) events. However, compared to the event yields after the preselection given in Table 7.1, signal events are reduced by a factor 14, while the contribution from all background processes is suppressed by about two orders of magnitude.The observed data events are in agreement with the signal-plus-background expectation within statistical uncertainties. In Table 7.7 the expected event yield for signal and background processes is given in the signal region for $\Delta\Phi_{jj}^{sign}$. Due to additional requirements on the jet topology, only 30% of the expected signal events and 32% of the expected background events can be used

for the construction of $\Delta\Phi_{jj}^{sign}$. Also here, the dominant contribution arises from $Z \to \tau\tau$ (65%),top-quark (17%) and Diboson (9%) events. The observed data are in agreement with the signal-plus-background expectation within statistical uncertainties.
The distributions of the Optimal Observable and $\Delta\Phi_{jj}^{sign}$ in the high BDT signal region are shown in Fig. 7.16. For $\Delta\Phi_{jj}^{sign}$ a coarser binning is chosen compared to Fig. 7.6 to account for the reduced statistics. As the observables in the high BDT signal region are used to investigate anomalous contributions to the Higgs-gluon coupling structure, one has to ensure that no significant distortion in case of SM couplings is caused by cutting on the BDT output. This is done by comparing the mean value of the Optimal Observable and $\Delta\Phi_{jj}^{sign}$ in bins of $\mathrm{BDT_{bkg}}$ and $\mathrm{BDT_{VBF}}$ output, as shown in Fig. 7.17. For the mean value in bins of $\mathrm{BDT_{VBF}}$ output, the cut $\mathrm{BDT_{bkg}} > 0.6$ is already applied, as only this region of phase space is of interest. As expected for pure SM couplings the mean values for signal and backgrounds are fluctuating around zero. No significant dependence of the mean value of the Optimal Observable and $\Delta\Phi_{jj}^{sign}$ on the BDT output is observed.

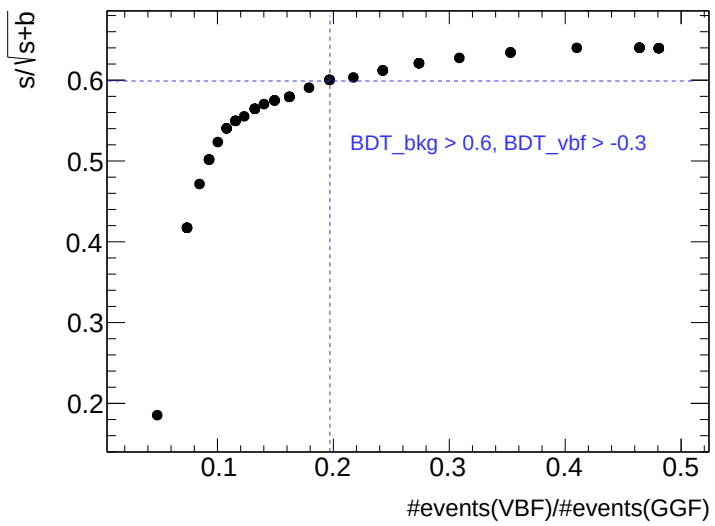

Figure 7.15.: Maximal $\frac{s}{\sqrt{s+b}}$ as function of the ratio of VBF H$\to \tau\tau$ events to ggF H+2jets events for cuts on $\mathrm{BDT_{bkg}}$ and $\mathrm{BDT_{VBF}}$. The line indicates the signal region definition.

Process	Event yield
ggF H+2jets$\rightarrow \tau\tau$	5.13 ± 0.12
VBF H$\rightarrow \tau\tau$	0.79 ± 0.01
VH H$\rightarrow \tau\tau$	1.23 ± 0.01
$Z \rightarrow \tau\tau$	47.81 ± 2.47
$Z \rightarrow ee, \mu\mu$	1.45 ± 0.41
Diboson	6.70 ± 1.42
Top	12.75 ± 1.85
ggF H$\rightarrow$WW	0.71 ± 0.09
VBF H$\rightarrow$WW	0.12 ± 0.01
VH H$\rightarrow$WW	0.23 ± 0.08
Fake leptons	1.73 ± 0.79
$\sum$ bkgs	73.52 ± 3.51
Data	86.0 ± 9.27

Table 7.6.: Expected event yield in the signal region as defined in the text with statistical uncertainties for SM signal and each background component compared to the observed data for $\sqrt{s} = 8\,\text{TeV}$.

Process	Event yield
ggF H+2jets$\rightarrow \tau\tau$	1.59 ± 0.07
VBF H$\rightarrow \tau\tau$	0.33 ± 0.00
VH H$\rightarrow \tau\tau$	0.24 ± 0.00
$Z \rightarrow \tau\tau$	15.18 ± 1.36
$Z \rightarrow ee, \mu\mu$	0.10 ± 0.05
Diboson	2.13 ± 0.82
Top	4.08 ± 0.11
ggF H$\rightarrow$WW	0.16 ± 0.04
VBF H$\rightarrow$WW	0.04 ± 0.00
VH H$\rightarrow$WW	0.03 ± 0.02
Fake leptons	1.15 ± 0.56
$\sum$ bkgs	23.44 ± 1.69
Data	21.00 ± 4.58

Table 7.7.: Expected event yield for $\Delta\Phi_{jj}^{sign}$ in the signal region as defined in the text with statistical uncertainties for SM signal and each background component compared to the observed data for $\sqrt{s} = 8\,\text{TeV}$.

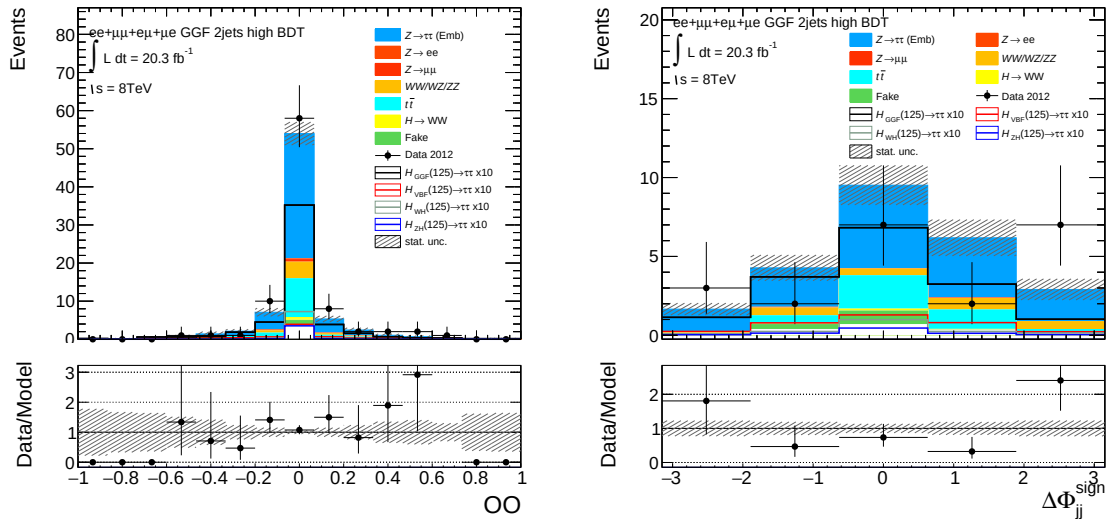

Figure 7.16.: Distributions of the Optimal Observable (left) and $\Delta\Phi_{jj}^{sign}$(right) in the signal region with statistical uncertainties.

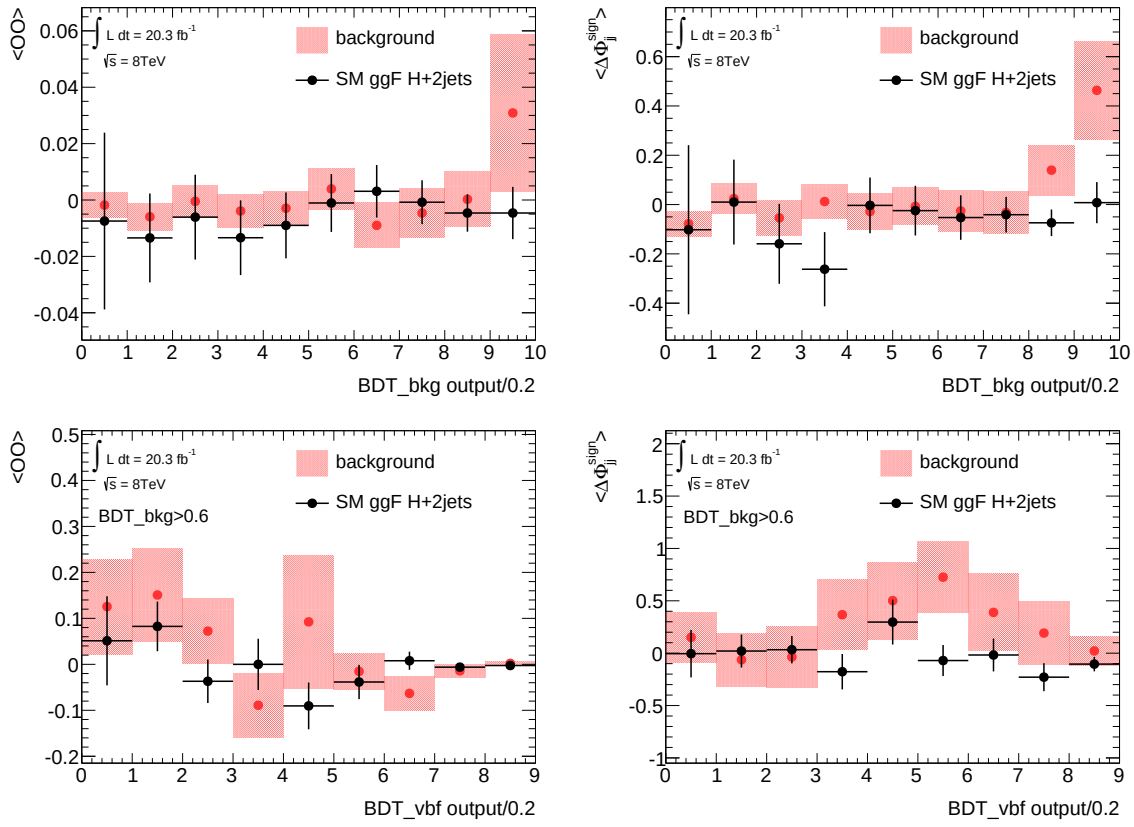

Figure 7.17.: Mean of the Optimal Observable $< OO >$ (left) and $< \Delta\Phi_{jj}^{sign} >$ (right) as function of $\mathrm{BDT_{bkg}}$ ouput (top) and $\mathrm{BDT_{VBF}}$ output (bottom) with statistical uncertainties.

8 Background Estimation

In order to analyse the Higgs-gluon coupling structure, a good knowledge of the contributing background processes, described in Section 3.2, is important. While their contribution to the signal region is mostly modeled with MC simulations, data-driven background estimation techniques allow to obtain a better control over the impact of simulations on the analysis and to reduce the influence of systematic uncertainties. In this analysis, the background contribution of $Z \to \tau\tau$ processes and of events with misidentified leptons are estimated in a data-driven way.
The chapter is organized as follows: The first section describes the *embedding* method, which is used for the $Z \to \tau\tau$ background estimation. This is followed by an overview of the background estimation for events with misidentified leptons. The last section describes the determination of normalization factors for simulated $Z/\gamma^* \to ee, \mu\mu$ and top-quark events in order to allow a comparison between data and background estimation before the likelihood fit, which is described in Chapter 10.

8.1. Background Estimation of $Z \to \tau\tau$

In this analysis events arising from $Z \to \tau\tau$ processes constitute the largest background contribution to the ggF H+2jet signal. However, it is difficult to select a sufficiently pure $Z \to \tau\tau$ sample from data since the mass distributions of signal and $Z \to \tau\tau$ background events are overlapping in a wide range. The *embedding* method [113] provides a possibility to estimate the $Z \to \tau\tau$ background contribution in a data-driven way by using $Z \to \mu\mu$ data events. The embedded $Z \to \tau\tau$ samples contains identical conditions, such as underlying event and pile-up activity, as the analysed data sample, while also the kinematic of additionally produced jets does not rely on simulation.
Due to lepton universality the decay channels $Z \to \tau\tau$ and $Z \to \mu\mu$ are kinematically identical expect for the difference in their lepton mass. Therefore, the kinematic of the Z-boson and additionally produced jets are independent of the Z-decay mode and can be used for estimating the $Z \to \tau\tau$ background contribution. Events with $Z \to \mu\mu$ decays can be selected from data with high efficiency and purity, while the contribution from $H \to \mu\mu$ decays is negligible due to the small Higgs-muon coupling strength. The $Z \to \mu\mu$ events are selected by requiring two oppositely charged muons with $p_T^{\mu 1} > 20\,\text{GeV}$, $p_T^{\mu 2} > 15\,\text{GeV}$. In addition, the muons have to be isolated: the scalar sum of other track transverse momenta found within an isolation cone of $\Delta R < 0.4$ around the muon track has to be smaller than 20 % of the muon transverse momentum. Furthermore the invariant di-muon mass $m_{\mu\mu}$ has to be greater than 40 GeV and a common vertex for the muons has to exist.
In a next step the $Z \to \tau\tau$ decay with full leptonic final states is simulated using the reconstructed Z-boson kinematics from the $\mu\mu$ data event. To account for differences in the lepton-mass, the tau momentum is given by

$$p_\tau = \sqrt{E_\mu^2 - m_\tau^2} \tag{8.1}$$

The tau decay products are simulated using TAUOLA [114] and PHOTOS [115] for photon radiation from charged leptons. These MC simulations are then passed to a full detector simulation and reconstruction. In the next step the detector response to the Z-decay muons are removed and replaced by the corresponding information from the simulated τ-leptons. This information does not only contain the lepton track, but also energy deposition in calorimeter and muon spectrometer cells. As a final step a re-reconstruction of the resulting *hybrid* events is performed. In Fig. 8.1 an illustration of the embedding procedure with input $Z \to \mu\mu$ data event, simulated $Z \to \tau\tau$ decay and the resulting *hybrid* event is shown.
The substitution results in a $Z \to \tau\tau$ model where only the decay and the detector response to the τ decay products are taken from simulation, but all other event informations are obtained directly from data.

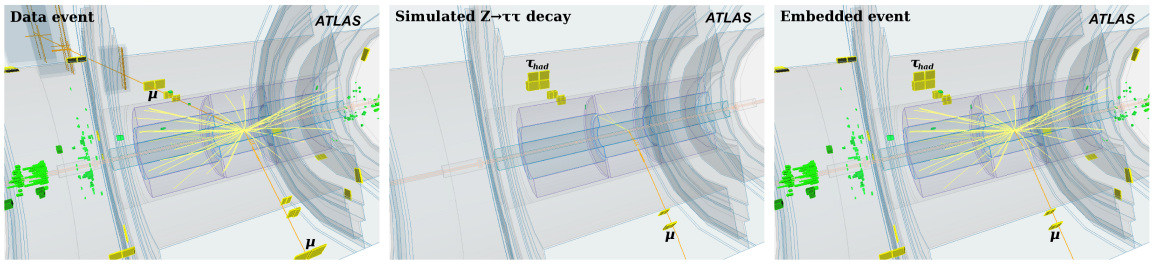

(a) (b) (c)

Figure 8.1.: Display of a $Z \to \mu\mu$ event selected from data (a), the corresponding $Z \to \tau\tau$ simulation with one tau decaying into a muon and the other one decaying hadronically (b) and the embedded hybrid event (c) [113].

The embedded sample is scaled to the expected number of events using $Z \to \tau\tau$ simulations with ALPGEN [71]. The normalization factor for each final state ($ee, e\mu, \mu e, \mu\mu$) is obtained by the ratio $\alpha = N_{\mathrm{MC}}/N_{\mathrm{Emb}}$, where N_{Emb} and N_{MC} give the number of events in the embedded sample and in the ALPGEN simulation respectively. The simulated events have been normalized to $\sigma\times$BR for the corresponding luminosity. Table 8.1 gives the normalization factors for each final state. The final normalization of $Z \to \tau\tau$ background events is determined in a fit to the observed data, which is described in Chapter 10.

Channel	Normalization factor
ee	0.21
$\mu\mu$	0.15
$e\mu$	0.17
μe	0.17

Table 8.1.: Normalization factors for embedded $Z \to \tau\tau$ events derived from ALPGEN simulations.

8.2. Background Estimation of Events with Misidentified Leptons

This background contribution consists of events with one or more leptons, which do not originate from the leptonic decay of a τ-lepton or a W/Z-boson. Such background processes mainly contain events from multi-jet QCD production, W-boson production with associated jets and semileptonic decays of top-pairs $t\bar{t}$. In the following, this background contribution is referred to as *fake background.*
The estimation of the fake background contribution is based on a control region definition by reverting the isolation condition for one of the leptons while applying all other signal region requirements. In particular, the energy isolation condition is removed and the transverse momentum isolation is reverted. Furthermore, the anti-isolated lepton is removed if an overlap with a jet within a cone of $\Delta R < 0.4$ is found.
Due to the anti-isolation requirement, slighly different trigger combinations as described in Section 6.8 are used: In the *ee* final state the trigger `EF_e24vhi_medium1` is required, if the transverse momentum of the isolated electron is greater than 26 GeV. Otherwise the trigger `EF_2e12Tvh_loose1` is required. For the $\mu\mu$ final state the same trigger configuration is used as in the nominal case (see Section 7). For $e\mu$ final states with an isolated electron of transverse momentum greater than 26 GeV the trigger `EF_e24vhi_medium` is required. Otherwise if the electron is found to be anti-isolated the trigger `EF_e12_Tvh_medium1_mu8` is required and the events are weighted with the muon efficiency to account for a decrease in the event yield compared to the nominal case.
In this control region all other background processes without fake leptons, Diboson, $Z \to ll$, $Z \to \tau\tau$, $H \to WW$, leptonic top decays, are subtracted from data. The remaining distribution is called *fake distribution.* The normalization is then obtained by a template fit of the p_T-distribution of the sub-leading lepton in the control region to the same distribution in the signal region, where two isolated leptons are required. Therefore, a χ^2 minimization is performed:

$$\chi^2 = \sum_{i=1}^{N} \frac{(N_{MC,i} + fN_{fake,i} - N_{data,i})^2}{\sigma_{MC,i}^2 + f^2\sigma_{fake,i}^2 + \sigma_{data,i}^2} \tag{8.2}$$

Here $i = 1, ..., N$ refers to the corresponding bin, N_{MC} give the number of background events without misidentified leptons, N_{fake} give the number of fake background events and N_{data} give the number of data. The statistical errors are indicated by σ_i and the factor f refers to the fake normalization factor, which has to be adjusted during minimization. This template fit is performed at an early stage in the preselection, namely after cut 10, where the contribution from signal events can be neglected. The resulting normalization factors for the fake background contribution are given in Table 8.2. To determine the fake background contribution in a certain variable, the distribution in the fake control region is scaled with the corresponding normalization factors, assuming that they do not change between control region for fake background events and signal region. The final normalization of this background component is determined in a fit to the observed data, which is described in Chapter 10.

Channel	Normalization factor
ee	0.27 ± 0.06
$\mu\mu$	0.11 ± 0.04
$e\mu$	0.13 ± 0.01
μe	0.06 ± 0.03

Table 8.2.: Normalization factors with statistical uncertainties in each final state for background contribution arising from events with misidentified leptons.

8.3. Normalization of $t\bar{t}$- and $Z \to ll$- Background Contribution

An important background contribution is also given by $Z/\gamma^* \to ll$ decays with $l = e, \mu$ and leptonically decaying single top-quark and top-quark pair events. In particular, the $Z/\gamma^* \to ll$ background contribution is important for same flavor final states ee and $\mu\mu$. While the shape of the distributions for these background processes is taken from MC simulations, their normalizations can be obtained in specific control regions. In the following the control region definition for $Z/\gamma^* \to ll$ and top-quark events and the obtained normalization factors are described.
Since the signal region requires a low mass cut window of $30 < m_{ll} < 75$ GeV for same flavor final states and $30 < m_{ll} > 100\,\text{GeV}$ for different flavor final states, the high mass region with $80\,\text{GeV} < m_{ll} < 100\,\text{GeV}$ can be used as a control region for $Z/\gamma^* \to ll$ events. The control region for top-quark events is obtained by requiring at least one b-tagged jet (see Section 6.4) applying all other preselection cuts described in Section 7). The normalization factor in each control regions is given by

$$f_{Top/Zll} = \frac{N_{data} - N_{other}}{N_{Top/Zll}} \tag{8.3}$$

where N_{data} referrs to the number of data, $N_{Top/Zll}$ the number of top-quark or $Z/\gamma^* \to ll$ events respectively and N_{other} the number of events for all other background processes in in each control region. The correction factor applied to $Z/\gamma^* \to ee/\mu\mu$ and top-quark events are given in 8.3. Table 8.4 summarizes the contribution from signal and background events in these specific control regions. In the top control region the realtive contribution of top-qaurk events is about 91%, while Z/γ^*-decays with ee and $\mu\mu$ final states contribute in the $Z/\gamma^* \to ll$ control region with about 82%. Fig. 8.2 shows the invariant di-lepton mass distributions m_{ll} in the $Z/\gamma^* \to ll$ and top control region respectively. A good agreement between signal-plus-background expectation and data is observed. The final normalization of the $Z/\gamma^* \to ll$ and top-quark background contribution are determined in a fit to the observed data, which is described in Chapter 10.
As the signal region definition, described in Section 7.3.3, relies on the BDTs' separation power, Fig. 8.3 shows the output of BDT_{bkg} and BDT_{VBF} in the $Z/\gamma^* \to ll$ and top-quark control regions after the full preselection. A good agreement between simulation and data is observed. In addition, Fig. 8.4 shows the distributions of the Optimal Observable and $\Delta\Phi_{jj}^{sign}$in the $Z/\gamma^* \to ll$ and top-quark control regions after the full preselection. For both observables a good agreement between background expectation and observed data in the control regions is found.

Background	Normalization factor
$Z \to ee$	0.94 ± 0.08
$Z \to \mu\mu$	0.95 ± 0.08
Top	1.03 ± 0.02

Table 8.3.: Normalization factors for $Z/\gamma^* \to ll$ and top-quark background contributions with statistical uncertainties after the full preselection as described in Section 7.2.

Process	Event yield in Top CR	Event yield in Zll CR
ggF H+2jets$\to \tau\tau$	1.73 ± 0.07	0.12 ± 0.01
VBF H$\to \tau\tau$	0.54 ± 0.01	0.05 ± 0.00
VH H$\to \tau\tau$	0.70 ± 0.02	0.02 ± 0.00
$Z \to \tau\tau$	240.11 ± 5.38	5.41 ± 0.91
$Z \to ee, \mu\mu$	5.44 ± 1.68	558.35 ± 20.12
Diboson	17.32 ± 2.32	33.86 ± 2.90
Top	3551.15 ± 31.15	79.39 ± 4.97
ggF H$\to$WW	0.58 ± 0.08	0.00 ± 0.00
VBF H$\to$WW	0.23 ± 0.02	0.01 ± 0.00
VH H$\to$WW	0.27 ± 0.05	0.13 ± 0.01
Fake leptons	82.46 ± 4.41	1.66 ± 0.54
$\sum$ bkgs	3898.80 ± 32.05	678.88 ± 20.95
Data	3906.00 ± 62.49	684.00 ± 26.14

Table 8.4.: Expected event yield in the top-quark control region (Top CR) and the $Z/\gamma^* \to ll$ control region (Zll CR) for SM signal and each background component with statistical uncertainties compared to the observed data for $\sqrt{s} = 8\,\text{TeV}$.

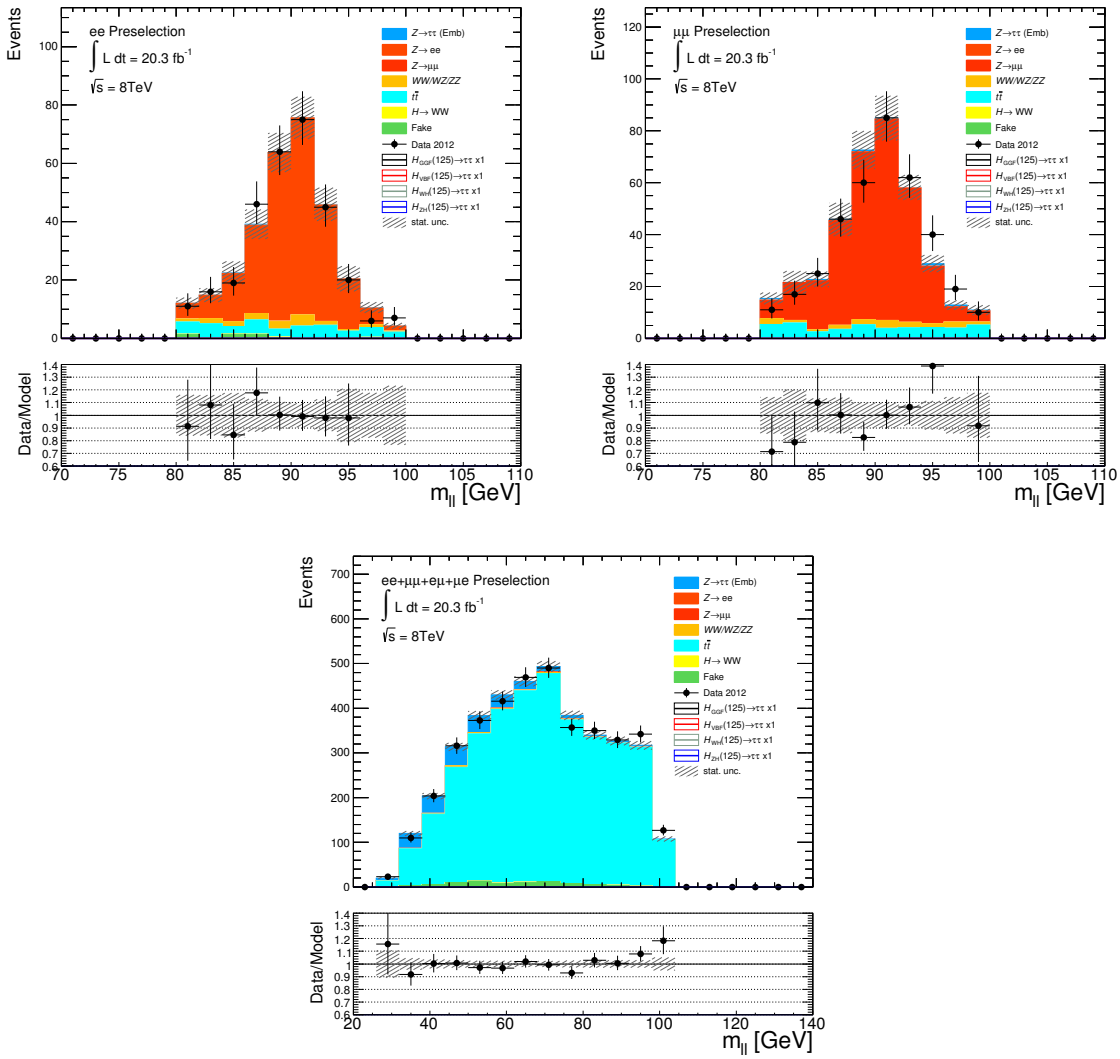

Figure 8.2.: Invariant di-lepton mass distribution m_{ll} in the $Z/\gamma^* \to ll$ control region for ee-final state (top left) and $\mu\mu$-final states (top right) and in the top-quark control region (bottom) after the full preselection.

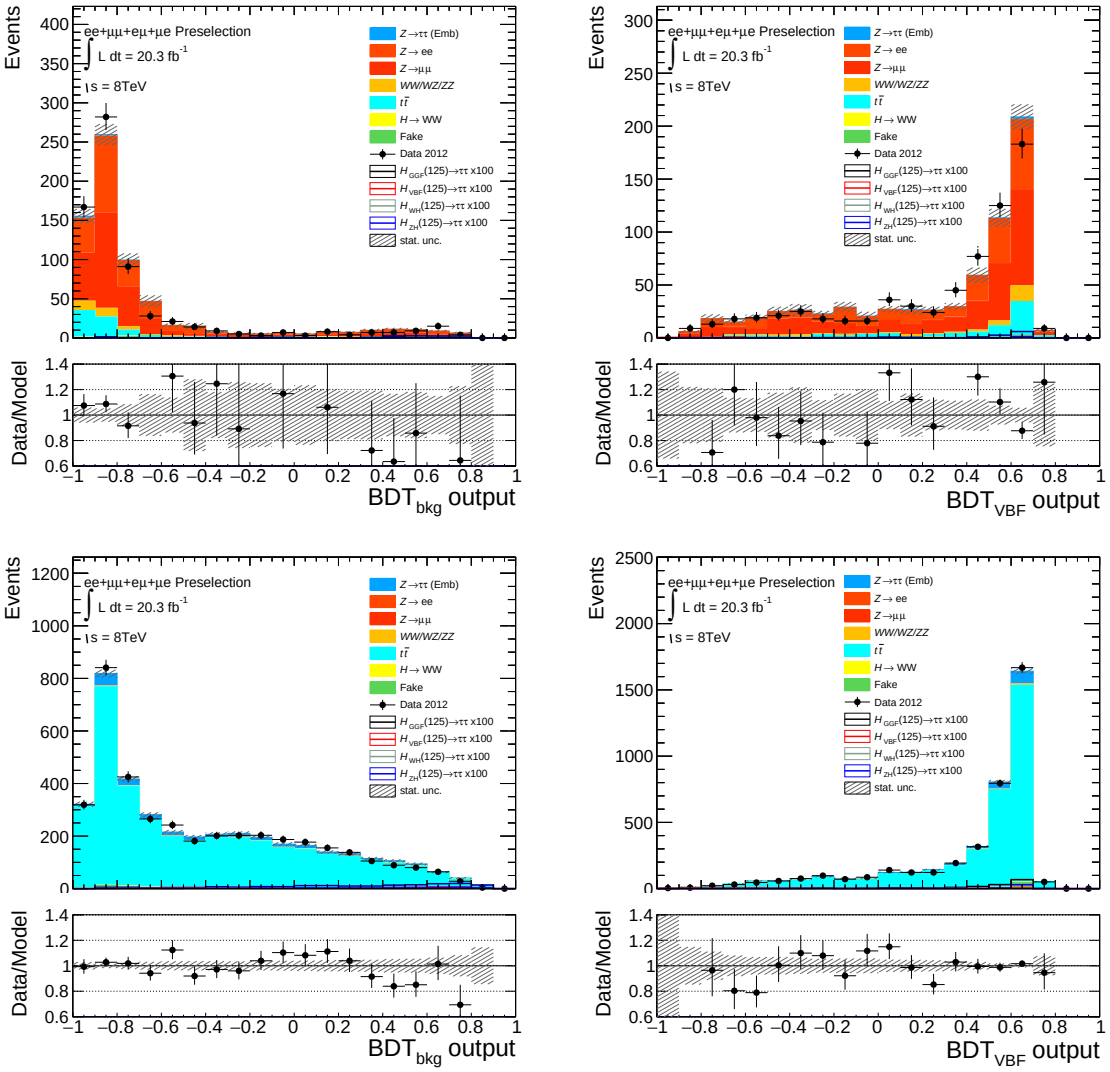

Figure 8.3.: Distributions of the BDT output for $\mathrm{BDT_{bkg}}$ (left) and $\mathrm{BDT_{VBF}}$ (right) in the $Z/\gamma^* \to ll$ control region (top) and the top-quark control region (bottom) with statistical uncertainties after the full preselection.

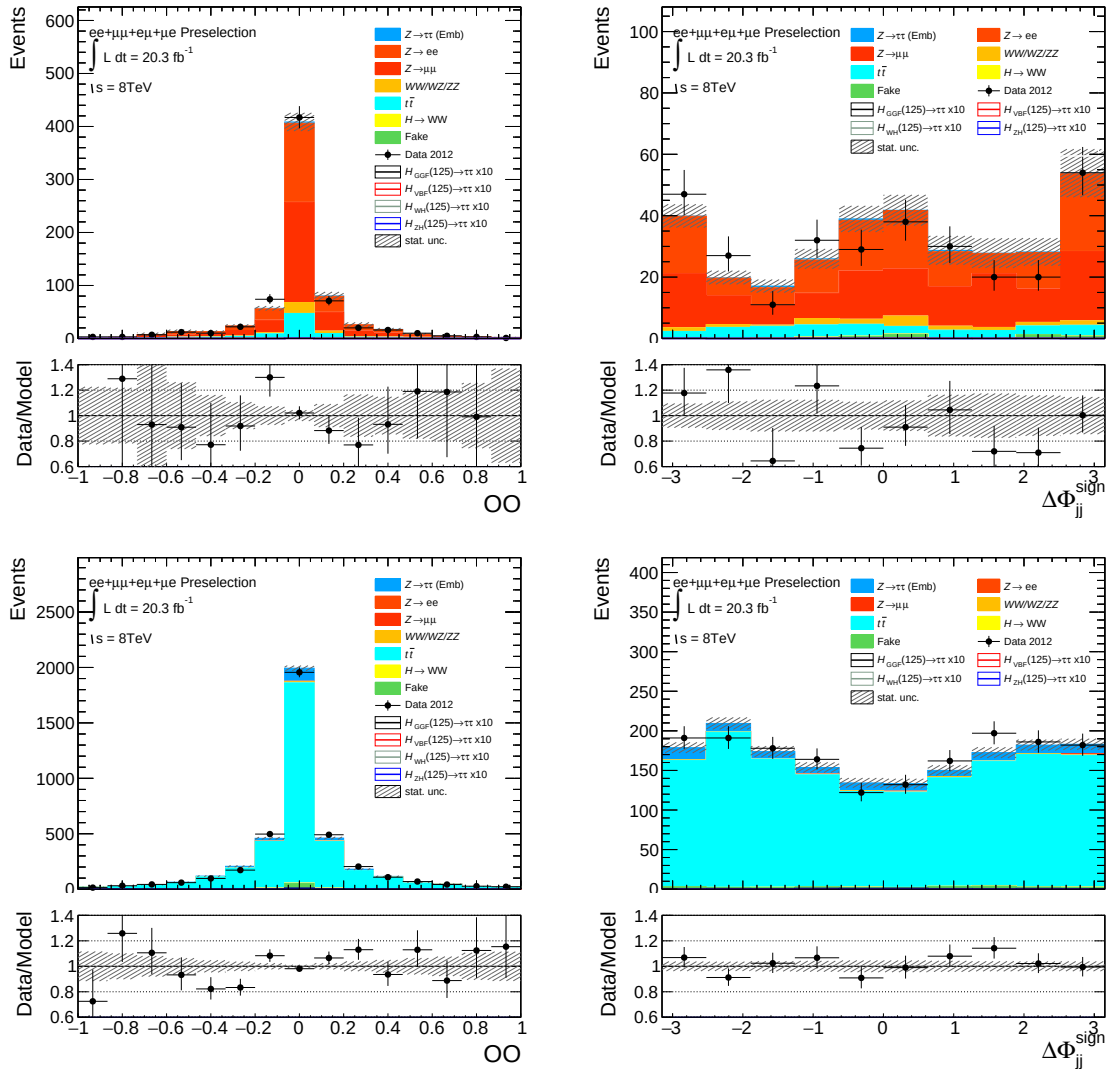

Figure 8.4.: Distributions of the Optimal Observable OO (left) and $\Delta\Phi_{jj}^{sign}$(right) in the $Z/\gamma^* \to ll$ control region (top) and the top-quark control region (bottom) with statistical uncertainties after the full preselection.

9 Systematic Uncertainties

The impact of systematic uncertainties on the expected event yield and the shape of the Optimal Observable and $\Delta\Phi_{jj}^{sign}$ distributions is an important aspect in order to statistically interpret the obtained results. The uncertainties can be divided into *shape uncertainties* affecting the shape of the variables and *normalization* uncertainties, which have an impact on the overall signal and background expectation. In order to propagate the systematic uncertainties to the final variables, the source of each uncertainty is varied within one standard deviation upwards and downwards and the full analysis is repeated. The impact of this uncertainty on the shape of the distribution and on the expected signal and background yield is then compared to the nominal case. Here, a *pruning* procedure is performed in order to investigate the impact of the systematic uncertainties on the shape of the nominal distribution, see Section 10.2. In addition to the Optimal Observable and $\Delta\Phi_{jj}^{sign}$ distributions in the signal region, further control regions are included in the fit, which are described in Section 10.3. The effect of the systematic uncertainties in the signal region and the control regions are computed separately, while their correlation is taken into account in the fit. Thus, including control regions in the fit allows to constrain systematic uncertainties and will be further discussed in Section 10.4.2. A summary of systematic uncertainties considered in the control regions can be found in Appendix B.
While this chapter focuses on the impact of the systematic uncertainties on the signal and background expectation and intends to give an overview of the shape uncertainties on the Optimal Observable and $\Delta\Phi_{jj}^{sign}$distributions, the inclusion of these uncertainties in the likelihood fit and their impact on the final results is discussed in detail in Chapter 10.

This chapter is organized as follows: The first section describes the experimental uncertainties, while the next section gives an overview of the theoretical uncertainties, which have been adopted from the analysis described in Ref. [104]. As both the Optimal Observable and $\Delta\Phi_{jj}^{sign}$ are used in order to investigate the Higgs-gluon coupling structure, the impact of the systematic uncertainties is discussed for both observables. Table 9.1 and Table 9.2 summarize the impact of the experimental and theoretical uncertainties on the expectation of the signal and the main background processes for the Optimal Observable and $\Delta\Phi_{jj}^{sign}$ respectively. In addition, the systematic uncertainties which are found to have a non-negligible impact on the distribution shape are summarized.

9.1. Experimental Uncertainties

Luminosity: The uncertainty on the integrated luminosity is $\pm 2.8\,\%$ for data taken in 2012. A detailed description on the determination of this uncertainty is given in Reference [116].

Jet energy resolution: The uncertainty on the jet energy resolution (JER) is obtained by smearing each jet energy with a factor accounting for the uncertainty in the energy resolution measurement [117]. This 1σ-variation is assumed to be symmetric such that a two

sided uncertainty is obtained by applying the variation from the nominal value also in the opposite direction. To evaluate the impact on the distribution shape, the symmetrization is applied in each bin of the Optimal Observable and $\Delta\Phi_{jj}^{sign}$.
The impact of this uncertainty on the ggF H+2jet signal normalization is on the order of (1-2)% for the Optimal Observable and $\Delta\Phi_{jj}^{sign}$. The largest effect arises for the $t\bar{t}$ normalization with up to 30% normalization variation for $\Delta\Phi_{jj}^{sign}$.
For the $Z \to \tau\tau$ process no JER uncertainties are considered, as this background contribution is estimated from data (see Section 8.1). Fig. 9.1 shows the impact of the JER uncertainty on the Optimal Observable and $\Delta\Phi_{jj}^{sign}$ for ggF H+2jet events. The JER uncertainty is also considered as a shape uncertainty on the Optimal Observable and $\Delta\Phi_{jj}^{sign}$ distribution.

Jet energy scale: The jet energy scale (JES) uncertainty is grouped into several components accounting for pile-up effects, η-intercalibration, jet-flavour composition, high p_T jets and other effects. A full list of considered uncertainties can be found in Reference [104]. Each systematic is evaluated by varying the scale correction, which is applied to simulated data, within their 1σ uncertainty. Fig. 9.2 shows the impact of one component of the total JES uncertainty on the Optimal Observable and $\Delta\Phi_{jj}^{sign}$for ggF H+2jets.
This uncertainty has an impact on the signal normalization on the order of (7-14)%, while the impact on the $t\bar{t}$-background rises up to 36%. Thus, it provides the dominant experimental uncertainty source for signal and background. The JES uncertainty is also considered as a shape uncertainty on the Optimal Observable and $\Delta\Phi_{jj}^{sign}$ distribution.

Jet vertex fraction: The Jet vertex fraction (JVF) is used in order to suppress jets from pile-up events, see Section 6.9. Thus, jets with $p_T < 50\,\text{GeV}$ and $|\eta| < 2.4$ are rejected if JVF ≤ 0.25. The variation of this threshold can be considered as a systematic uncertainty. The impact on signal and background normalization is rather small. A variation of the yield of the order of (0.7-1.8)% is observed.

b-tagging efficiency: This systematic refers to the uncertainty on the tagging efficiency of b-jets, see Section 6.4, which affect the analysis due to the b-jet veto in the signal region and the b-tag requirement in the top control region. As b-jets dominantly arise in top-quark events the impact of this uncertainty on the $t\bar{t}$-normalization is on the order of $(10 - 11)\%$, while it has a small impact of 0.1% on the ggF H+2jets normalization.

Missing transverse energy: This systematic uncertainty accounts for the scale and resolution uncertainty on the soft term contribution to the missing transverse energy E_T^{miss}. The ggF H+2jets normalization is affected by this uncertainty on the order of (1-2)%, while the largest impact is observed for $Z \to \tau\tau$ and $t\bar{t}$ events in $\Delta\Phi_{jj}^{sign}$ with about 20% variation in the expected event yield. The E_T^{miss} uncertainty is found to have an impact on the shape of the Optimal Observable distribution.

Lepton energy and momentum resolution: The uncertainty on the energy and momentum resolution of electrons and muons is determined by smearing the energy and momentum components with the recommended tools [118, 119]. This uncertainty has a small impact on the order of 1% for the ggF H+2jets normalization, while the normalization of the $Z/\gamma^* \to ll$ varies by 6% for the Optimal Observable. It is found to have an non negligible impact on the shape of the Optimal Observable and $\Delta\Phi_{jj}^{sign}$ distribution.

Lepton energy and momentum scale: The uncertainties on the electron and muon energy and momentum scales have a small impact on the analysis. For the ggF H+2jets normalization a variation on the order of 1% is observed. The largest impact of this uncertainty is found for $Z \to \tau\tau$ events in $\Delta\Phi_{jj}^{sign}$ with about 12% variation. Fig. 9.3 shows the impact of the 1σ variation of the electron energy and momentum scale on the Optimal Observable and $\Delta\Phi_{jj}^{sign}$ for ggF H+2jet events. This electron and muon scale uncertainty is also considered as a shape uncertainty for the Optimal Observable distribution.

Lepton reconstruction and identification efficiency: In order to account for efficiency differences between MC and data, efficiency corrections factors are applied to muons and electrons. The uncertainty on these reconstruction and identification efficiencies changes the ggF H+2jets normalization by less than 1%, while a normalization uncertainty of about 8% is obtained for $Z \to \tau\tau$ events in $\Delta\Phi_{jj}^{sign}$.

Trigger efficiency: The simulated events are corrected for differences in the trigger efficiency between simulation and data. This uncertainty has the largest impact on the $Z \to \tau\tau$ event yield with up to 8% for $\Delta\Phi_{jj}^{sign}$, while the variation of the ggF H+2jets normalization is less than 1%.

Embedding: In order to estimate the $Z \to \tau\tau$ background contribution, this analysis uses the embedding method, as described in Section 8.1. For the selected $Z \to \mu\mu$ events in data, the muons have to be isolated. The variation of this isolation requirement results in a systematic uncertainty on the $Z \to \tau\tau$ background. Furthermore, an additional systematic uncertainty is considered by varying the subtracted energy to account for the calorimeter deposition of the muons in $Z \to \mu\mu$ events. The uncertainty due to the muon isolation has an impact on the $Z \to \tau\tau$ normalization of about 19%. This systematic uncertainty has been symmetrized in order to avoid problems in the likelihood fit. For the cell subtraction uncertainty a variation in the event yield of about 15% is observed. In addition, a normalization uncertainty of 15% accounting for the normalization difference between same flavour and different flavour final states of the di-tau decay in $Z \to \tau\tau$ events is used.

Background estimation: A systematic uncertainty accounting for the background estimation as described in Chapter 8 is considered. For the $t\bar{t}$-background a normalization uncertainty of 6% is applied. The uncertainty on the $Z/\gamma^* \to ll$ normalization takes into account 6.4% variation.
The uncertainty on the background estimation arising from events with misidentified leptons (*fake*) is obtained by comparing normalization and shape of the distributions in the same-sign fake control region (one isolated lepton,one anti-isolated lepton) and the nominal signal region (two isolated leptons). A normalization uncertainty of 30% is determined, while the shape uncertainty is considered for both the Optimal Observable and $\Delta\Phi_{jj}^{sign}$.

9.2. Theory Uncertainties

QCD scale uncertainty: This systematic uncertainty takes into account cross-section uncertainties due to missing higher order corrections in the calculation. It is determined by varying the choice of renormalization and factorization scale by a factor of two upwards and downwards. The largest QCD scale uncertainty is provided for gluon-fusion production with up to 26%, while for the background processes an uncertainty of the order of (1-3)% is obtained.

Modelling of underlying event and parton shower: The uncertainty due to the modelling of underlying event (UE) and parton shower (PS) is derived by comparing the acceptance for different generators for VBF and ggF Higgs-boson production. A detailed description of the method and the generators, which are used for comparison, can be found in Reference [104]. The impact of the UE+PS uncertainty for gluon-gluon initial states on the ggF H+2jets normalization is 4%, while the impact on quark-quark initial states affects the expected event yield for VBF Higgs-boson production only by 1%.

PDF uncertainties: The uncertainties on the parton distribution functions (PDFs) are evaluated by comparing different parametrizations for various PDF sets [104]. The PDF uncertainty has an impact on the ggF H+2jet signal normalization of up to 10% and on the $t\bar{t}$ normalization of 8%.

Tau branching ratio: The uncertainty on the τ branching ratio is 5.7% for $m_H = 125\,\text{GeV}$.

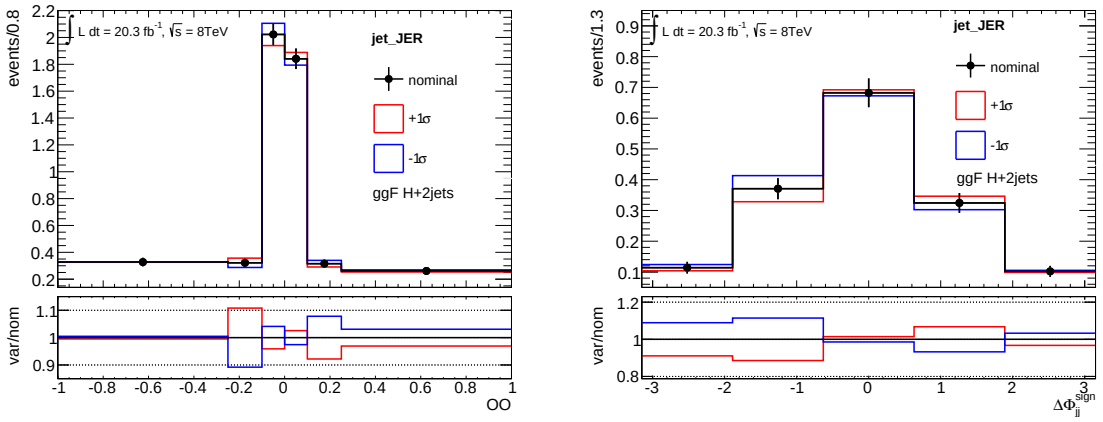

Figure 9.1.: Impact of the jet energy resolution uncertainty on the Optimal Observable (left) and $\Delta\Phi_{jj}^{sign}$(right) for ggF H+2jet events in the signal region. For the Optimal Observable a non-equidistant binning as described Section 10.3 is used.

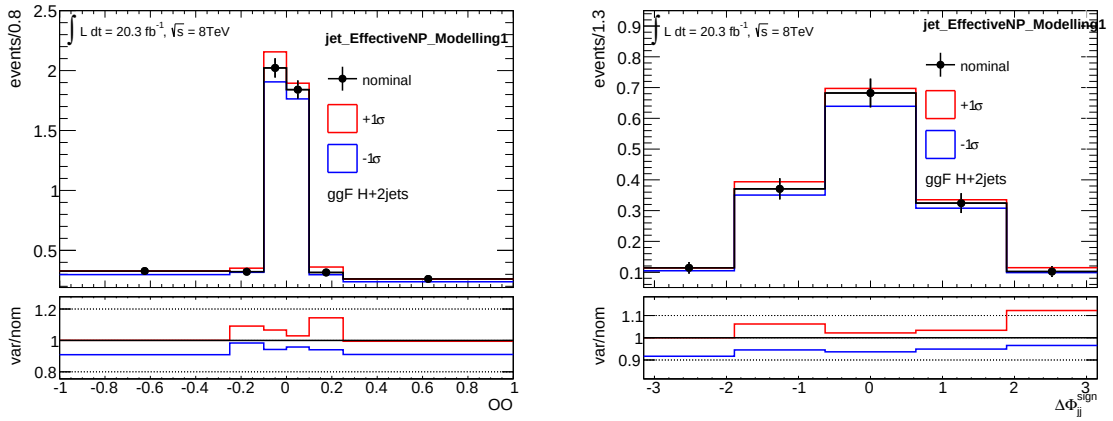

Figure 9.2.: Impact of one component of the jet energy scale uncertainty on the Optimal Observable (left) and $\Delta\Phi_{jj}^{sign}$(right) for ggF H+2jet events in the signal region. For the Optimal Observable a non-equidistant binning as described Section 10.3 is used.

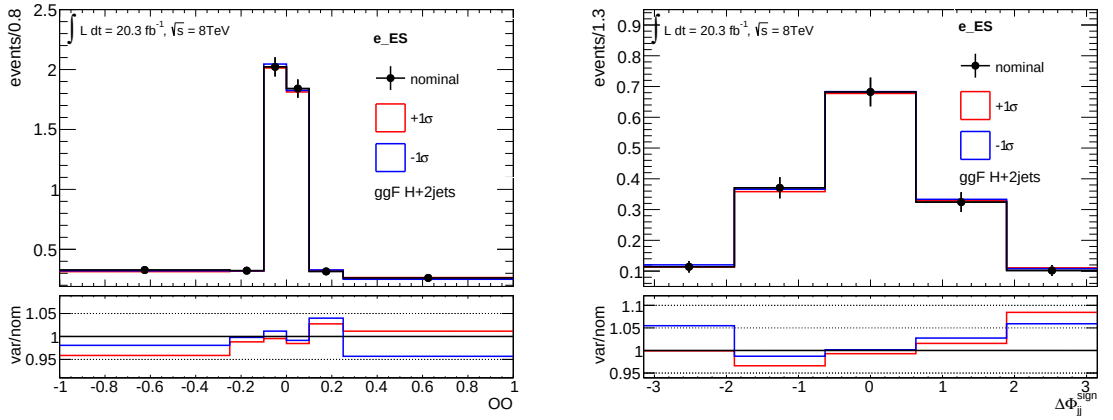

Figure 9.3.: Impact of the electron energy scale uncertainty on the Optimal Observable (left) and $\Delta\Phi_{jj}^{sign}$(right) for ggF H+2jet events in the signal region. For the Optimal Observable a non-equidistant binning as described Section 10.3 is used.

Systematic Uncert.	ggF H+2jets	VBFH	$Z \to \tau\tau$	$t\bar{t}$	Fake	Other	Shape
Normalization $Z \to \tau\tau$	-	-	$\pm 15.0\%$	-	-	-	
Normalization $t\bar{t}$	-	-	-	$\pm 6.0\%$	-	-	
Normalization fake leptons	-	-	-	-	$\pm 30.0\%$	-	
Normalization $Z/\gamma^* \to ll$	-	-	-	-	-	$\pm 6.4\%$	
Electron Efficiency	$\pm 0.7\%$	$\pm 0.6\%$	± 1.3	$\pm 5.0\%$	-	$\pm 0.6\%$	
Electron Energyscale	$+0.8\%$	$^{+0.8\%}_{-0.1\%}$	$^{+3.1\%}_{-4.7\%}$	$^{+4.0\%}_{-6.4\%}$	-	-4.0%	•
Electron Energyresolution	-	-	$^{+3.0\%}_{-4.2\%}$	$^{+2.0\%}_{-1.9\%}$	-	$^{+6.2\%}_{-0.1\%}$	•
Muon Efficiency	$\pm 0.8\%$	$\pm 0.8\%$	-	$\pm 0.8\%$	-	$\pm 0.8\%$	
Muon Energyscale	-	-	$^{+2.8\%}_{-2.4\%}$	$+1.5\%$	-	$+3.1\%$	•
Muon Energyresolution	$^{+1.1\%}_{-1.0\%}$	-	$^{+2.6\%}_{-4.2\%}$	$^{+1.9\%}_{-2.1\%}$	-	$^{+2.6\%}_{-3.1\%}$	•
E_T^{miss} Soft Term	$^{+1.2\%}_{-1.4\%}$	-	$^{+6.9\%}_{-22.0\%}$	$^{+6.8\%}_{-0.3\%}$	-	$^{+11.0\%}_{-8.4\%}$	•
Trigger Scalefactor	$\pm 1.0\%$	$\pm 1.0\%$	-	$\pm 1.0\%$	-	$\pm 1.2\%$	
JER	$\pm 0.7\%$	-	-	$\pm 4.2\%$	-	$^{+8.3\%}_{-3.1\%}$	•
JVF	$^{+0.4\%}_{-0.1\%}$	$^{+0.2\%}_{-0.6\%}$	-	$^{+1.7\%}_{-0.1\%}$	-	-1.8%	
JES	$^{+10.8\%}_{-13.2\%}$	$^{+10.5\%}_{-10.6\%}$	-	$^{+22.4\%}_{-13.8\%}$	-	$^{+20.9\%}_{-20.4\%}$	•
BCH Jet Cleaning	$\pm 0.3\%$	$\pm 2.5\%$	-	$\pm 3.0\%$	-	$\pm 0.3\%$	
b-Tagging	-	-	-	$^{+11.6\%}_{-9.9\%}$	-	-	
Emb. Muon Isolation	-	-	$\pm 18.9\%$	-	-	-	
Emb. Cell Subtraction	-	-	$^{+14\%}_{-17\%}$	-	-	-	
Emb. Muon Efficiency	-	-	$^{+1.2\%}_{-1.9\%}$	-	-	-	
QCD Scale	$^{+26.0\%}_{-21.0\%}$	$\pm 2.5\%$	-	$\pm 6.0\%$	-	$\pm 1.2\%$	
Underlying Event (gg)	$\pm 4\%$	-	-	-	-	-	
Underlying Event (qq)	-	$\pm 1\%$	-	-	-	-	
PDF (Hgg)	$^{+10.0\%}_{-9.2\%}$	-	-	-	-	-	
PDF (Hqq)	-	$\pm 3.2\%$	-	-	-	-	
PDF (gg)	-	-	-	$\pm 8.0\%$	-	-	
PDF (qq)	-	-	-	-	-	$\pm 4.0\%$	
NLO EW Higgs	-	$\pm 2.0\%$	-	-	-	-	
NLO Match accept	-	$\pm 4.2\%$	-	-	-	-	
BR $H \to \tau\tau$	$\pm 5.7\%$	$\pm 5.7\%$	-	-	-	-	

Table 9.1.: Source of systematic uncertainties and their relative impact on the normalization of the Optimal Observable for signal and important background processes in the signal region. In addition, systematic uncertainties with an impact on the shape of the Optimal Observable are labeled (•). Only systematic uncertainties with a normalization impact of $\geq 0.1\%$ are given. Here, *VBFH* stands for VBF produced $H \to \tau\tau$ events, *Other* refers to di-boson and $Z/\gamma^* \to ll$ events.

Systematic Uncertainty	ggF H+2jets	VBFH	$Z \to \tau\tau$	$t\bar{t}$	Fake	Other	Shape
Normalization $Z \to \tau\tau$	-	-	$\pm 15.0\%$	-	-	-	
Normalization $t\bar{t}$	-	-	-	$\pm 6.0\%$	-	-	
Normalization fake leptons	-	-	-	-	$\pm 30.0\%$	-	
Normalization $Z/\gamma^* \to ll$	-	-	-	-	-	$\pm 6.4\%$	
Electron Efficiency	$\pm 0.7\%$	$\pm 0.7\%$	$\pm 8\%$	$\pm 0.5\%$	-	-	
Electron Energyscale	$^{+0.2\%}_{-1.1\%}$	-	$^{+8.7\%}_{-12.3\%}$	$^{+4.7\%}_{-0.4\%}$	-	$^{+3.0\%}_{-0.8\%}$	
Electron Energyresolution	-	-	$^{+11.6\%}_{-10.7\%}$	-	-	-	•
Muon Efficiency	$\pm 0.7\%$	$\pm 0.8\%$	-	$\pm 0.9\%$	-	$\pm 0.9\%$	
Muon Energyscale	-	$^{+0.2\%}_{-0.6\%}$	$^{+3.6\%}_{-4.6\%}$	$+4.7\%$	-	$+0.8\%$	
Muon Energyresolution	$^{+1.1\%}_{-0.8\%}$	-	$^{+12.8\%}_{-10.1\%}$	$^{+1.7\%}_{-0.5\%}$	-	$^{+3.3\%}_{-0.8\%}$	•
E_T^{miss} Soft Term	$^{+1.2\%}_{-2.0\%}$	-	$^{+15.7\%}_{-17.7\%}$	$^{+20.1\%}_{-3.8\%}$	-	$^{+11.0\%}_{-13.9\%}$	
Trigger Scalefactor	$\pm 0.9\%$	$\pm 1.0\%$	-	$\pm 1.0\%$	-	$\pm 1.3\%$	
JER	$\pm 1.5\%$	$\pm 2.2\%$	-	$\pm 30.1\%$	-	$\pm 3.1\%$	•
JVF	$^{+0.7\%}_{-1.6\%}$	-	-	-	-	-1.1%	
JES	$^{+7.4\%}_{-12.9\%}$	$^{+7.8\%}_{-9.7\%}$	-	$^{+36.8\%}_{-31.0\%}$	-	$^{+28.5\%}_{-27.0\%}$	•
BCH Jet Cleaning	$\pm 0.3\%$	$\pm 0.3\%$	-	$\pm 0.3\%$	-	$\pm 0.3\%$	
b-Tagging	$\pm 0.1\%$	-	-	$^{+11.7\%}_{-10.5\%}$	-	-	
Emb. Muon Isolation	-	-	$^{+24.3\%}_{-24.4\%}$	-	-	-	
Emb. Cell Subtraction	-	-	$^{+12.3\%}_{-25.4\%}$	-	-	-	
Emb. Muon Efficiency	-	-	$\pm 2.0\%$	-	-	-	
QCD Scale	$^{+26.0\%}_{-21.0\%}$	$\pm 2.5\%$	-	$\pm 6.0\%$	-	$\pm 1.2\%$	
Underlying Event (gg)	$\pm 4.0\%$	-	-	-	-	-	
Underlying Event (qq)	-	$\pm 1.0\%$	-	-	-	-	
PDF (Hgg)	$^{+10.0}_{-9.2\%}$	-	-	-	-	-	
PDF (Hqq)	-	$\pm 3.2\%$	-	-	-	-	
PDF (gg)	-	-	-	$\pm 8.0\%$	-	-	
PDF (qq)	-	-	-	-	-	$\pm 4.0\%$	
NLO EW Higgs	-	$\pm 2.0\%$	-	-	-	-	
NLO Match accept	-	$\pm 4.2\%$	-	-	-	-	
BR $H \to \tau\tau$	$\pm 5.7\%$	$\pm 5.7\%$	-	-	-	-	

Table 9.2.: Source of systematic uncertainties and their relative impact on the normalization of $\Delta\Phi_{jj}^{sign}$ for signal and important background processes in the signal region. In addition, systematic uncertainties with an impact on the shape of the Optimal Observable are labeled (•). Only systematic uncertainties with a normalization impact of $\geq 0.1\%$ are given. Here, *VBFH* stands for VBF produced $H \to \tau\tau$ events, *Other* refers to di-boson and $Z/\gamma^* \to ll$ events.

10 Statistical Analysis and Results

This chapter describes the likelihood fit to determine the sensitivity to anomalous Higgs-gluon couplings. The first part introduces the likelihood function and gives an overview of the general concept of likelihood fits. Then, the fitting procedure of this analysis and the inclusion of systematic and statistical uncertainties as nuisance parameters is described. Finally, the results are presented along with validation checks of the fitting procedure.

10.1. Definition of the Likelihood Function

An extended maximum-likelihood fit [120] in the Optimal Observable and $\Delta\Phi_{jj}^{sign}$ is used to determine the sensitivity to anomalous contribution in the Higgs-gluon coupling structure. The fit is performed with the `HISTFACTORY` tool [121] including the `ROOSTATS` [122] and `ROOFIT` [123] packages. The following description of the likelihood function mainly follows Ref. [124].
In general, the distribution of a random variable x with contributions from signal and background processes in a finite data sample $(x_1, ..., x_N)$ is given by the combination of probability density functions (PDFs) $f_S(x;\boldsymbol{\theta})$ and $f_B(x;\boldsymbol{\theta})$ for signal and background, respectively. These PDFs are normalized to unity and depend on a set of unknown parameters $\boldsymbol{\theta} = (\theta_1, ..., \theta_m)$. The maximum likelihood approach is a technique for estimating the values of these parameters. If S and B refer to the expected number of signal and background events, a *signal strength* parameter μ can be introduced, such that $\mu = 1$ corresponds to the number of observed events equal to the signal+background expectation. Thus, the probability to observe N data events is given by

$$\mathcal{P}(\mathbf{x};\mu,\boldsymbol{\theta}) = \frac{e^{-(\mu S+B)}\,(\mu S+B)^N}{N!}\left\{\prod_{i=1}^{N}\frac{\mu S f_S(x_i;\boldsymbol{\theta}) + B f_B(x_i;\boldsymbol{\theta})}{\mu S+B}\right\} \tag{10.1}$$

Here, the first term gives the poisson probability to observe N events assuming that $(\mu S+B)$ events are expected, while the following term describes the probability to observes these N events at values x_i of the variable x. If one assumes the data to be fixed, the probability in Eq. 10.1 is usually referred to as likelihood function $\mathcal{L}(\mu,\boldsymbol{\theta})$. For binned distributions, such as histograms, Eq. 10.1 can be written as

$$\mathcal{L}(\boldsymbol{n_i};\mu,\boldsymbol{\theta}) = \mathcal{P}(\boldsymbol{n_i};\mu,\boldsymbol{\theta}) = \mathcal{N}_{\text{comb}}\prod_{i=1}^{N_{bins}}\frac{e^{-(\mu s_i(\boldsymbol{\theta})+b_i(\boldsymbol{\theta}))}\,(\mu s_i(\boldsymbol{\theta})+b_i(\boldsymbol{\theta}))^{n_i}}{n_i!} \tag{10.2}$$

where n_i corresponds to the number of data events in bin i, with expected number of signal events s_i and background events b_i in this bin. The prefactor $\mathcal{N}_{\text{comb}}$ is a combinatorial constant and can be neglected. The product in Eq. 10.2 can be considered to run over all bins of several variables x, taking into account binned distributions as well as single bin categories.

In this analysis, the negative logarithmic likelihood function (NLL) given by

$$-\ln(\mathcal{L}(\mu,\boldsymbol{\theta})) = \sum_{i=1}^{N_{bins}} \{\ln(\mu s_i(\boldsymbol{\theta}) + b_i(\boldsymbol{\theta}) + \ln(n_i!) - n_i \ln(\mu s_i(\boldsymbol{\theta}) + b_i(\boldsymbol{\theta}))\} \tag{10.3}$$

is considered. Here, $\sum_{i=1}^{N_{\text{bins}}} \ln(n_i!)$ can be neglected. The parameter estimators, for which the NLL becomes minimal are denoted as $\hat{\boldsymbol{\theta}} = (\hat{\theta}_1, ..., \hat{\theta}_m)$ and $\hat{\mu}$:

$$\text{NLL}_{\text{min}} = \min\{-\ln(\mathcal{L}(\mu,\boldsymbol{\theta}))\} = \ln \mathcal{L}(\hat{\mu},\hat{\boldsymbol{\theta}}) \tag{10.4}$$

The approximate variance $\hat{\sigma}$ of a single estimator $\hat{\theta}_i$ can then be estimated by profiling all other estimators and determining the parameter value for which the difference between NLL and minimum becomes 1/2 [124]:

$$\Delta\text{NLL} = \ln(\mathcal{L}(\hat{\theta}_i)) - \ln(\mathcal{L}(\hat{\theta}_i \pm \hat{\sigma}_{\hat{\theta}_i})) = \frac{1}{2} \tag{10.5}$$

In this analysis, the ΔNLL function is used is to derive confidence intervals for anomalous coupling contributions in terms of $\cos(\alpha)$, which is further described in Section 10.3.

10.2. Inclusion of Nuisance Parameters

As described in the previous section, the expectation of signal and background contributions, $s_i(\boldsymbol{\theta})$ and $b_i(\boldsymbol{\theta})$, depends on a set of unknown parameters $\boldsymbol{\theta}$, called *nuisance parameters* in the following. The impact of systematic uncertainties on the expected signal and background contribution, described in Section 9, can be propagated to the likelihood function in terms of nuisance parameters. Usually, systematic uncertainties enter the likelihood fit as binned distributions of a discriminating variable. For their determination, the analysis is performed fully analogously to the nominal case, but shifting the source of this systematic uncertainty by one standard deviation upwards and downwards. For each systematic uncertainty a nuisance parameter θ_i^{sys} is then introduced. The effect of this uncertainty on the expected signal and background contribution is then be parametrized in the likelihood function by considering a Gaussian distribution centered around zero and with a width of one. Therefore, a nuisance parameter value of one corresponds to a shift of the corresponding uncertainty by one standard deviation, while a nuisance parameter of zero stands for the nominal value. As only histograms for the upward and downward 1σ-variations are provided, the functional form of θ_i^{sys} is obtained by using a piecewise exponential and linear interpolation and extrapolation procedure [107].

Systematic uncertainties can have an impact on both the total expected event yield for signal and background contribution as well as on the shape of the binned distribution. In this analysis, only systematic uncertainties which have an impact on the expected event yield $> 0.1\%$ are considered. To investigate the impact of a systematic uncertainty on the shape, the binned distributions are normalized to the expected event yield for the nominal case. As the distributions of systematic variations can be affected by statistical fluctuations, additional methods, which are briefly described in the following, are applied to the distributions before they enter the likelihood fit.

As statistical fluctuations in the systematically varied histograms can complicate the estimation of shape uncertainties, a smoothing algorithm as implemented in the `ROOT` framework [125] is used in this analysis. The smoothing is applied to the ratio of varied to nominal histogram. The smoothed shape of the actual variation is then obtained by multiplying the

nominal histogram with the smoothed ratio.
For some systematics it can happen that a bin in the histogram of the upward or downward variation shows a deviation from the nominal expectation in the same direction. As this is caused mainly by statistical fluctuations, such bins are symmetrized: If the largest deviation is observed in the upward variation, the downward variation in the bin is set to the same value but in opposite direction with respect to the nominal expectation and vice versa.
In order to decide if a systematic is treated as a shape uncertainty the compatibility between the varied shape and the nominal expectation is evaluated by performing a χ^2-test. The systematic uncertainty is retained as a shape uncertainty if the test result of either the upward or downward variation is less than a threshold value. Otherwise, the systematic is treated only as a normalization uncertainty. In this analysis, the threshold value is set to 0.95. This pruning procedure is applied to all systematic uncertainties and samples before any smoothing or symmetrization is applied.
In addition to systematic uncertainties the statistical uncertainties of the MC simulations are included in the likelihood function as well. For each histogram bin i a nuisance parameter γ_i is introduced, if the statistical uncertainty of the total background expectation in it is greater than 5%. These nuisance parameters are constrained according to a Poisson distribution [107].
Furthermore, a set of floating parameters is introduced for the normalization of certain background expectations. In contrast to nuisance parameteres no prior knowledge about the value of these normalization uncertainties exist. In this analysis, normalization factors for $Z \to \tau\tau$, $Z/\gamma^* \to ll$ and top-quark processes are considered as they provide the dominant contribution to the total background. The inclusion of control regions for constraining these normalization factors is described in the next section.

10.3. Fitting Procedure

The sensitivity to anomalous contribution in the Higgs-gluon coupling structure is estimated by using a likelihood fit to the Optimal Observable and $\Delta\Phi_{jj}^{sign}$ distribution in the high BDT signal region, which are shown in Fig. 10.1. For the Optimal Observable a non-equidistant binning is chosen in order to avoid large statistical fluctuations in the outer bins. The SM signal samples for ggF H+2jets are reweighted for various $\cos(\alpha)$-values as described in Section 3.3.2. Fig. 10.2 shows a comparison of different signal models for the Optimal Observable and $\Delta\Phi_{jj}^{sign}$ distributions.
The likelihood function is maximized for each $\cos(\alpha)$-value assuming a signal expectation with this coupling. As explained in Sec 10.1 considering the NLL-value for each $\cos(\alpha)$-model results in a curve with its minimum at the most probable signal hypothesis for a given dataset. Then, the difference between this minimum and other NLL-values, ΔNLL, allows to directly read off the 1σ-confidence interval:

$$\Delta\text{NLL} = \ln\left(\mathcal{L}_{\max}\right) - \ln\left(\mathcal{L}(\hat{\cos(\alpha)} \pm \hat{\sigma}_{\hat{\cos(\alpha)}})\right) = \frac{1}{2} \tag{10.6}$$

The $\pm 1\sigma$ confidence interval is expected to contain the true value of $\cos(\alpha)$ in 68% of all cases. Fig. 10.3 shows a schematic sketch of an expected ΔNLL-curve for an arbitrary set of $\cos(\alpha)$-values with the 1σ confidence interval. In this example, a value of $\cos(\alpha) \leq 0.4$ can be excluded at the 1σ confidence level.
Only information about the shape of the observables is used in the fit, such that the signal strength μ is left free floating. The normalizations of the VBF and VH H$\to \tau\tau$ production and the H$\to$WW processes are fixed to their SM predictions.

Including additional kinematic regions in the fit allows to further constrain background normalization factors and nuisance parameters. Fig. 10.4 gives an overview of the kinematic regions included in the fit. The *low BDT region* is defined as $\mathrm{BDT_{bkg}} < -0.4$ and contains large contributions from several background processes. In this region, the $\mathrm{BDT_{bkg}}$ output distribution is used in the fit. In addition, the low BDT region allows to constrain the normalization of the $Z \to \tau\tau$ background, which gives the dominant contribution in the signal region. Further important contributions arise from $Z/\gamma^* \to ll$ and top-quark processes. Therefore, the top-quark and $Z/\gamma^* \to ll$ control regions as defined in Section 8.3 are included in the fit. Fig. 10.5 shows the distribution of $\mathrm{BDT_{bkg}}$ output in the low BDT and the event yield in the top-quark and the $Z/\gamma^* \to ll$ control regions. The distributions shown here are scaled with *prefit* normalization factors determined in Section 8.3.

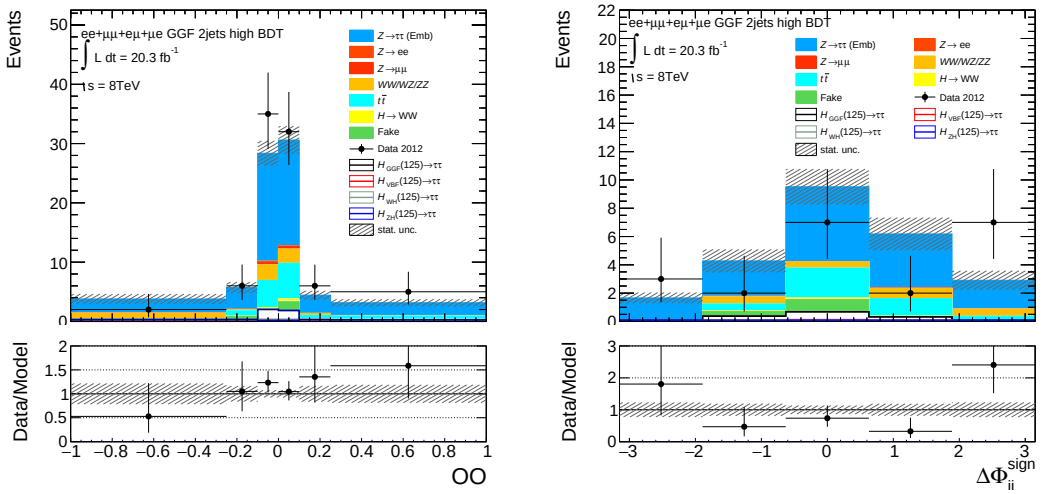

Figure 10.1.: Distributions of the Optimal Observable OO (left) and $\Delta\Phi_{jj}^{sign}$(right) in the high BDT signal region with statistical uncertainties.

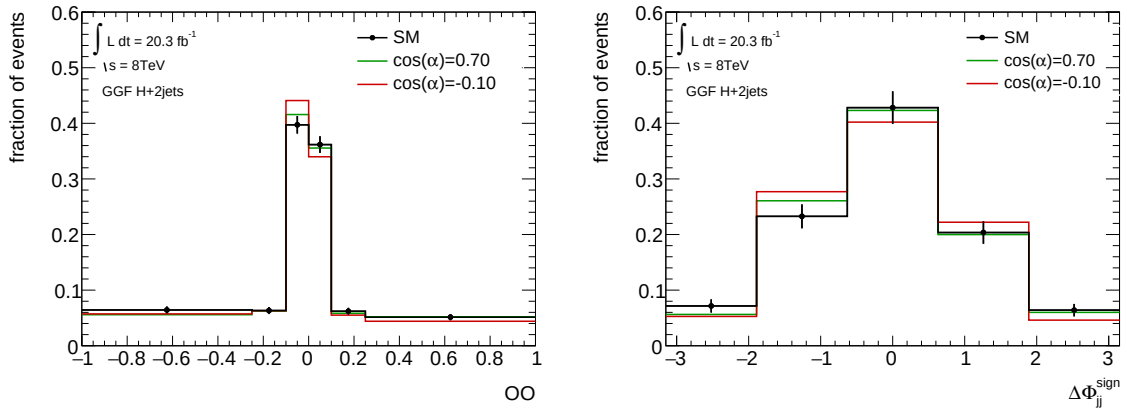

Figure 10.2.: Comparison of the ggF H+2jets signal for $\cos(\alpha) = 1$(SM), $\cos(\alpha) = 0.70$, $\cos(\alpha) = -0.10$ for the Optimal Observable OO (left) and $\Delta\Phi_{jj}^{sign}$(right) in the signal region. The distributions are normalized to unit area.

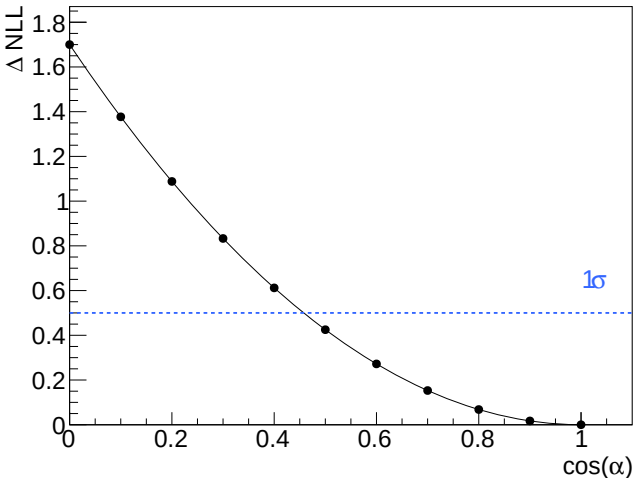

Figure 10.3.: Sketch of a ΔNLL-curve for different cos(α)-points. The dotted line indicates the 1σ exclusion limit. The points are set to arbitrary values with no physical meaning.

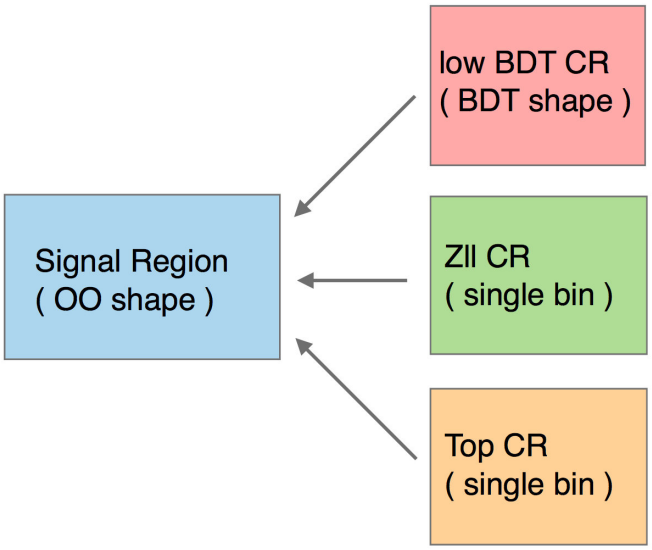

Figure 10.4.: A schematic view of the kinematic regions that are used in the likelihood fit: The signal region and the control regions (CR) as described in the text.

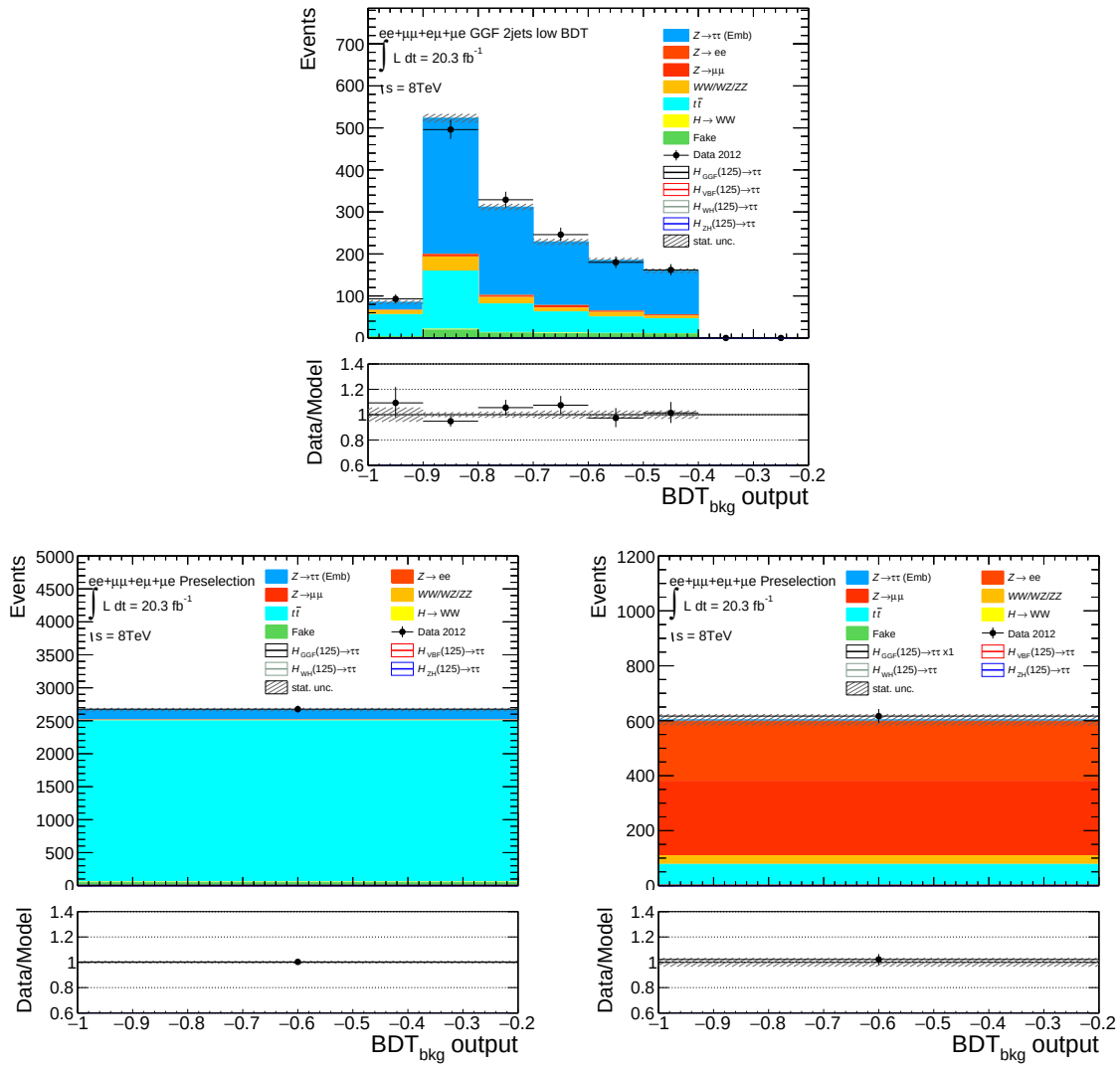

Figure 10.5.: Included control regions in the likelihood fit: The low BDT control region with the distribution of $\mathrm{BDT_{bkg}}$ output (top), the event yield in the top-quark control region (bottom left) and $Z/\gamma^* \to ll$ control region (bottom right). The error band includes statistical uncertainties only.

10.4. Results

As explained in the previous section a likelihood fit is used to investigate if confidence intervals for the exclusion of anomalous contribution in the Higgs-gluon coupling structure can be derived. The signal strength parameter μ is determined along with normalization factors for the background contributions arising from $Z \to \tau\tau$, $Z/\gamma^* \to ll$ and top-quark events. Furthermore, systematic and statistical uncertainties reflected by the nuisance parameters are estimated.
The first part of this section describes the expected results using *Asimov pseudo-data* [126] along with additional checks to ensure the validity of the fitting procedure. Then, the observed results for fit in the Optimal Observable and $\Delta\Phi_{jj}^{sign}$ are presented.

10.4.1. Expected Results and Validation of Fitting Procedure

In a first step the likelihood fit is performed blinded in order to avoid a bias in the analysis. This is done by using Asimov data, defined as the sum of signal-plus-background expectation, in the signal region, while the control regions contain real data. If not explicitly stated, the signal expectation in the Asimov dataset refers to a SM Higgs-gluon coupling scaled to the SM signal strength prediction. This allows to determine the expected ΔNLL-curve for the SM hypothesis, which is shown in Fig. 10.6 for the fit in the Optimal Observable and $\Delta\Phi_{jj}^{sign}$. The filled dots indicate the $\cos(\alpha)$-values for which the NLL-value is calculated, while the line is only drawn to guide the eye. As expected, the minimal NLL-value is obtained for a SM Higgs-gluon coupling with $\cos(\alpha) = 1$ for both the Optimal Observable and $\Delta\Phi_{jj}^{sign}$. As explained in Section 4.1, the squared matrix element is not sensitive to the absolute sign of the SM coupling. Therefore, the Optimal Observable and $\Delta\Phi_{jj}^{sign}$ distributions do not differ between $\cos(\alpha) = \pm 1$, which results in an additional minimum at $\cos(\alpha) = -1$. Larger NLL-values are obtained for anomalous couplings and a pure CP-odd model with $\cos(\alpha) = 0$. Thus, the fits are able to identify the most probable coupling hypothesis.

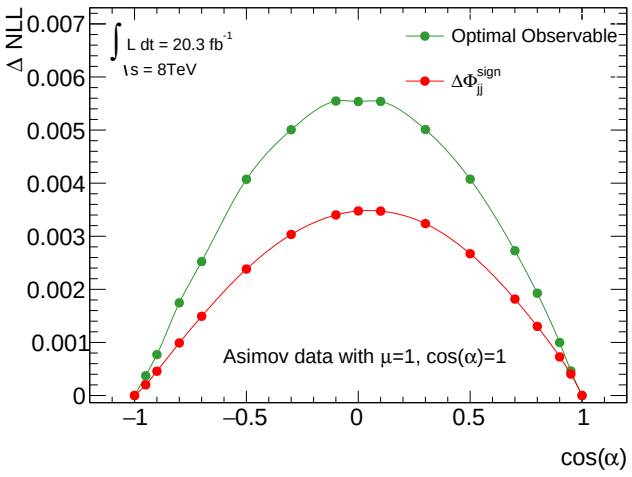

Figure 10.6.: Expected ΔNLL-curve as function of $\cos(\alpha)$-values representing the underlying signal hypothesis for the Optimal Observable (green) and $\Delta\Phi_{jj}^{sign}$(red). In the signal region Asimov data with μ=1 and SM coupling ($\cos(\alpha) = 1$) are used, the control regions contain real data. The filled dots indicate the $\cos(\alpha)$-values for which the NLL-value has been calculated.

The expected ΔNLL-curve for the Optimal Observable provides a higher sensitivity to anomalous couplings compared to the fit in $\Delta\Phi_{jj}^{sign}$. For the fit in the Optimal Observable ΔNLL = 0.0055 between SM and pure CP odd model is obtained, while the fit in $\Delta\Phi_{jj}^{sign}$ provides ΔNLL = 0.0035 between SM and pure CP odd model. However, a limited sensitivity in both fits is expected, as no exclusion of anomalous couplings at the 1σ confidence-level can be derived.
In Fig. 10.7 the best-fit signal strength μ_{bestfit} for each cos(α)-value for the fit in the Optimal Observable and $\Delta\Phi_{jj}^{sign}$ is shown. Both fits provide a signal strength larger than one, but still close to the SM expectation. For the SM hypothesis $\mu = 1.08^{+2.27}_{-2.03}$ and $\mu = 1.19^{+4.11}_{-3.81}$ is obtained for the fit in the Optimal Observable and $\Delta\Phi_{jj}^{sign}$, respectively. The small deviation from $\mu = 1$ is mainly caused by the inclusion of real data in the control regions. However the fit results are consistent with the SM prediction within uncertainties. For different cos(α)-models the uncertainty on the fitted signal strength is found to be of equal size.

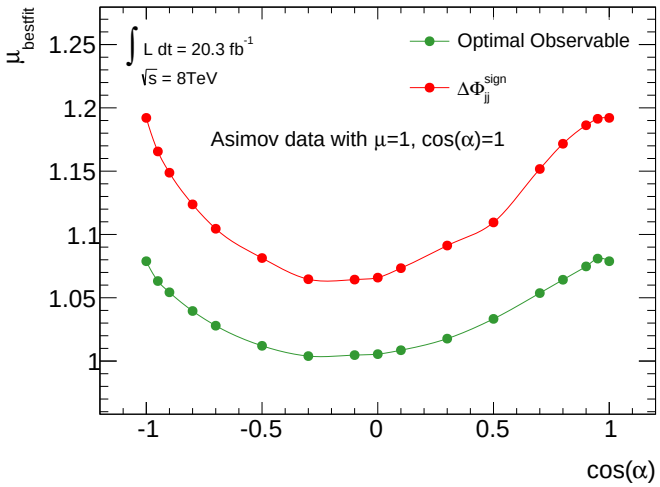

Figure 10.7.: Fitted signal strength μ_{bestfit} for each signal hypothesis in terms of cos(α). In the signal region Asimov data with μ=1 and SM coupling (cos(α) = 1) are used, the control regions contain real data. The filled dots indicate the cos(α)-values for which the NLL-value has been calculated. For the SM coupling signal strengths of $\mu = 1.08^{+2.27}_{-2.03}$ and $\mu = 1.19^{+4.11}_{-3.81}$ are obtained for the fit in the Optimal Observable and $\Delta\Phi_{jj}^{sign}$, respectively.

Fig. 10.8 shows the distributions of the Optimal Observable in the signal region and BDT_{bkg} output in the low BDT region with post-fit signal and background expectations including systematic and statistical uncertainties. In Fig. 10.19 post-fit distributions for $\Delta\Phi_{jj}^{sign}$ in the signal region and BDT_{bkg} output in the low BDT control region are shown. For all distributions a good agreement between data and signal-plus-background expectation is observed. Table 10.1 and Table 10.2 summarize the fit results for signal strength and normalization factors of the $Z \to \tau\tau$, $Z/\gamma^* \to ll$ and top-quark background expectations with their uncertainties for the Optimal Observable fit and the $\Delta\Phi_{jj}^{sign}$ fit, respectively. The normalization factors are close to one and also the signal strength is compatible with the SM expectation within uncertainties.

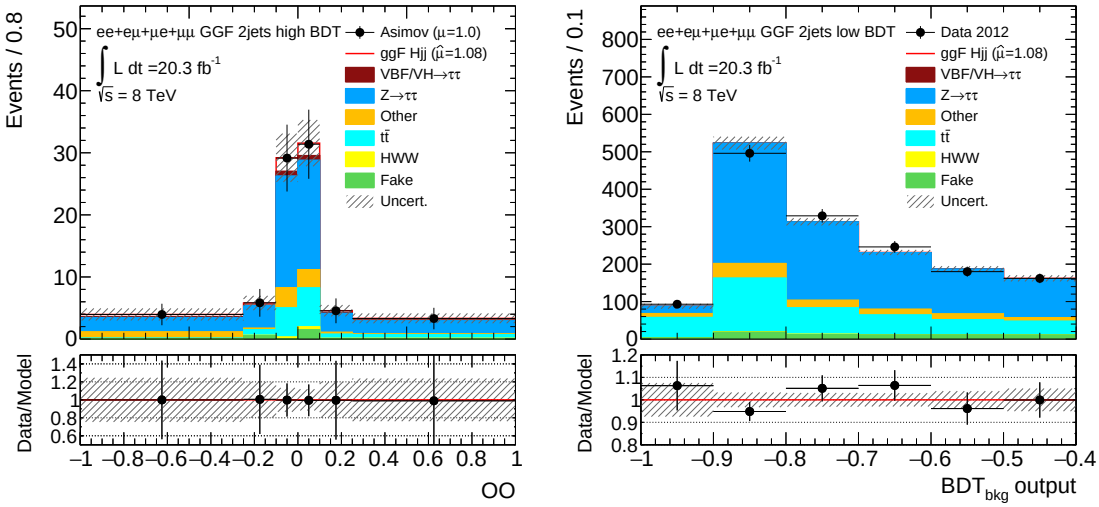

Figure 10.8.: Distributions of the Optimal Observable in the signal region (left) and $\mathrm{BDT_{bkg}}$ output in the low BDT control region (right) after the likelihood fit using Asimov data with μ=1 and SM coupling ($\cos(\alpha) = 1$) in the signal region and real data in the control regions. In the ratio plot *Model* contains the expectation of a SM signal. The error band includes systematic and statistical uncertainties.

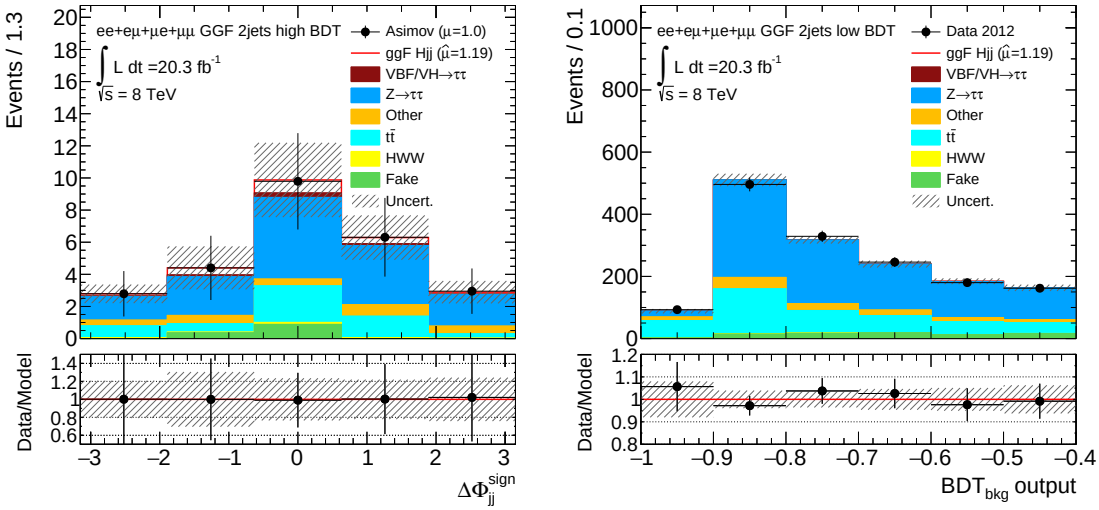

Figure 10.9.: Distributions of $\Delta\Phi_{jj}^{sign}$ in the signal region (left) and $\mathrm{BDT_{bkg}}$ output in the low BDT control region (right) after the maximum likelihood fit using Asimov data with μ=1 and SM coupling ($\cos(\alpha) = 1$) in the signal region and real data in the control regions. In the ratio plot *Model* contains the expectation of a SM signal. The error band includes systematic and statistical uncertainties.

Parameter	Postfit value
μ	$1.08^{+2.27}_{-2.03}$
norm(Top)	$1.01^{+0.12}_{-0.12}$
norm(Zll)	$0.99^{+0.46}_{-0.46}$
norm($Z\tau\tau$)	$0.99^{+0.11}_{-0.11}$

Table 10.1.: Fit results of the normalization factors for top-quark background contribution norm(Top), $Z\gamma^* \to ll$background contribution norm(Zll), $Z \to \tau\tau$ background contribution norm($Z\tau\tau$) and of the signal strength μ_{bestfit} for the fit in the Optimal Observable. In the signal region Asimov data with $\mu = 1$ and SM coupling ($\cos(\alpha) = 1$) is used, while the control regions contain real data.

Parameter	Postfit value
μ	$1.19^{+4.11}_{-3.81}$
norm(Top)	$1.01^{+0.14}_{-0.14}$
norm(Zll)	$1.00^{+0.49}_{-0.49}$
norm($Z\tau\tau$)	$0.98^{+0.12}_{-0.12}$

Table 10.2.: Fit results of the normalization factors for top-quark background contribution norm(Top), $Z\gamma^* \to ll$background contribution norm(Zll), $Z \to \tau\tau$ background contribution norm($Z\tau\tau$) and of the signal strength μ_{bestfit} for the fit in $\Delta\Phi_{jj}^{sign}$. In the signal region Asimov data with $\mu = 1$ and SM coupling ($\cos(\alpha) = 1$) is used, while the control regions contain real data.

To investigate the impact of individual uncertainties on the fitted signal strength, the absolute change $\Delta\mu$ with respect to the nominal estimate is calculated by fixing individual nuisance parameters to their post-fit $\pm 1\sigma$ estimates and re-minimizing the likelihood function with respect to all other parameters. The uncertainties can then be ranked with respect to their impact on the fitted signal strength. Fig. 10.10 and Fig. 10.11 display the deviations of the best-fit values for the 40 highest ranked uncertainties including systematic, statistic and theory uncertainties as well as normalization uncertainties for the fit in the Optimal Observable and $\Delta\Phi_{jj}^{sign}$, respectively. A description of the most important systematic uncertainties can be found in Appendix C. The highest ranked parameters for the Optimal Observable fit are nuisance parameters referring to the statistical uncertainty of the background expectation in bins of the Optimal Observable histogram in the signal region. The highest ranked systematic uncertainties are mainly related to the $Z \to \tau\tau$ component and the embedding procedure. Furthermore, systematic uncertainties related to the jet energy scale and the missing transverse energy also have a large impact on the fitted signal strength. The uncertainty on the gluon-fusion process due to QCD scale uncertainties is the highest ranked uncertainty on the theory side. For the $\Delta\Phi_{jj}^{sign}$ fit, also statistical uncertainties on the background expectation in the signal region are ranked high. The most important systematic uncertainties refer to jet and electron energy uncertainties along with uncertainties on the $Z \to \tau\tau$ component. The impact on the fitted signal strength is reasonable for all parameters and no significant pull of post-fit uncertainties is observed for the fit in the Optimal Observable and $\Delta\Phi_{jj}^{sign}$.

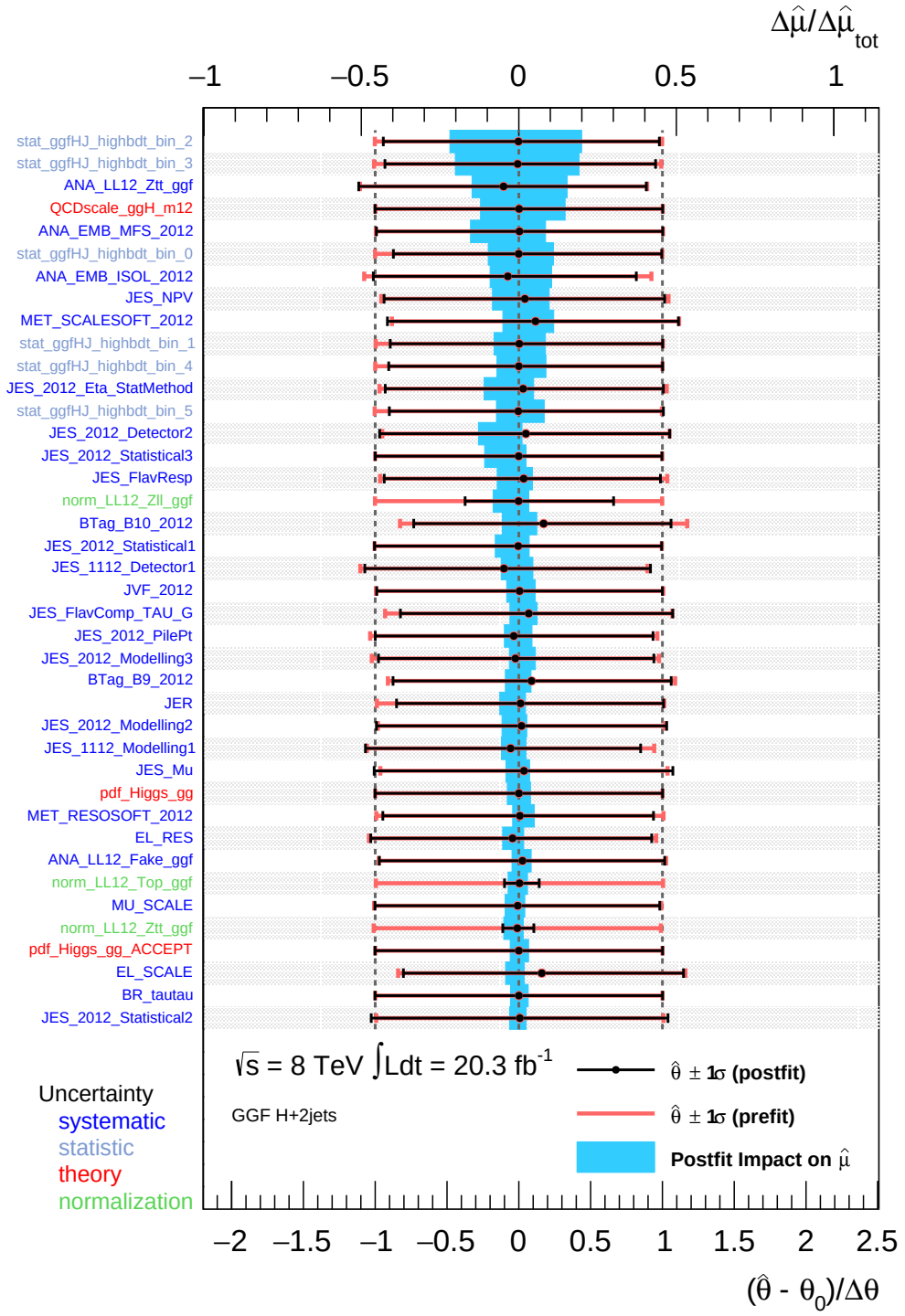

Figure 10.10.: Impact of systematic uncertainties on the fitted signal strength $\hat{\mu}$ for the fit in the Optimal Observable using Asimov data with $\mu = 1$ and SM coupling $(\cos(\alpha) = 1)$ in the signal region, the control regions contain real data. The systematic uncertainties are listed in decreasing order of their impact on $\hat{\mu}$ on the y-axis. The blue boxes show the variation $\Delta\hat{\mu}$ with respect to the total error $\Delta\hat{\mu}_{tot}$ when the corresponding nuisance parameter is fixed to its post-fit value $\hat{\theta}$ shifted by one standard deviation $\hat{\sigma}_{\hat{\theta}}$ upwards or downwards. The red line, referring to the bottom x-axis, shows the pre-fit uncertainty of the nuisance parameters. The filled black circles, referring to the bottom x-axis, show the deviation of the fitted parameters $\hat{\theta}$ from their nominal value θ_0 normalized to the nominal uncertainty $\Delta\theta$.

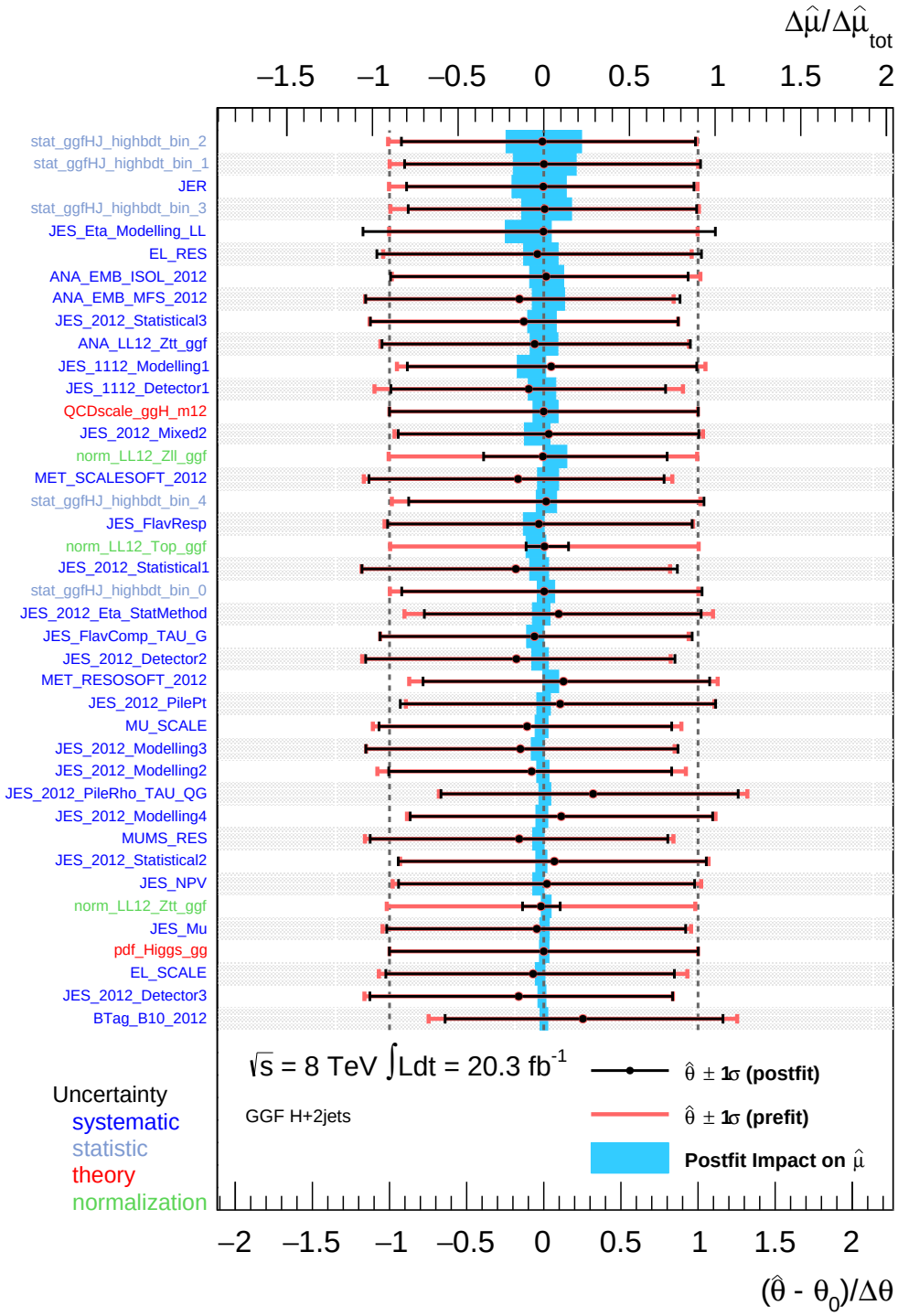

Figure 10.11.: Impact of systematic uncertainties on the fitted signal strength $\hat{\mu}$ for the fit in $\Delta\Phi_{jj}^{sign}$ using Asimov data with $\mu = 1$ and SM coupling ($\cos(\alpha) = 1$) in the signal region, the control regions contain real data. The systematic uncertainties are listed in decreasing order of their impact on $\hat{\mu}$ on the y-axis. The blue boxes show the variation $\Delta\hat{\mu}$ with respect to the total error $\Delta\hat{\mu}_{tot}$ when the corresponding nuisance parameter is fixed to its post-fit value $\hat{\theta}$ shifted by one standard deviation $\hat{\sigma}_{\hat{\theta}}$ upwards or downwards. The red line, referring to the bottom x-axis, shows the pre-fit uncertainty of the nuisance parameters. The filled black circles, referring to the bottom x-axis, show the deviation of the fitted parameters $\hat{\theta}$ from their nominal value θ_0 normalized to the nominal uncertainty $\Delta\theta$.

As an additional test of the fitting procedure, different signal strengths in the Asimov dataset can be injected to the likelihood fit. This ensures, that the fit is able to reproduce any underlying signal strength in a given dataset. Table 10.3 shows the fit results for the Optimal Observable with various injected signal strength values of the Asimov dataset. The fit results are in good agreement with the Asimov signal strength within uncertainties.
In addition, the ΔNLL-curve is expected to be sensitive to the injected coupling hypothesis of the signal expectation. In other words, a non-SM hypothesis in the Asimov dataset should result in a ΔNLL-curve with minimum at the corresponding $\cos(\alpha)$-value. Fig. 10.12 shows the ΔNLL curve for an Asimov dataset with $\cos(\alpha) = 0.80$ and $\cos(\alpha) = 0.50$. As expected, the minimum is restored at 0.80 and 0.50 for $\cos(\alpha)_{\text{Asimov}} = 0.80$ and $\cos(\alpha)_{\text{Asimov}} = 0.50$, respectively.

μ_{Asimov}	μ_{bestfit}
1.00	$1.08^{+2.27}_{-2.03}$
3.00	$3.21^{+2.74}_{-2.20}$
5.00	$5.27^{+3.23}_{-2.43}$

Table 10.3.: Comparison of injected signal strength in the Asimov dataset μ_{Asimov} to the result of the likelihood fit μ_{bestfit} for the fit in the Optimal Observable. The Asimov dataset is used in the signal region, while the control regions contain real data.

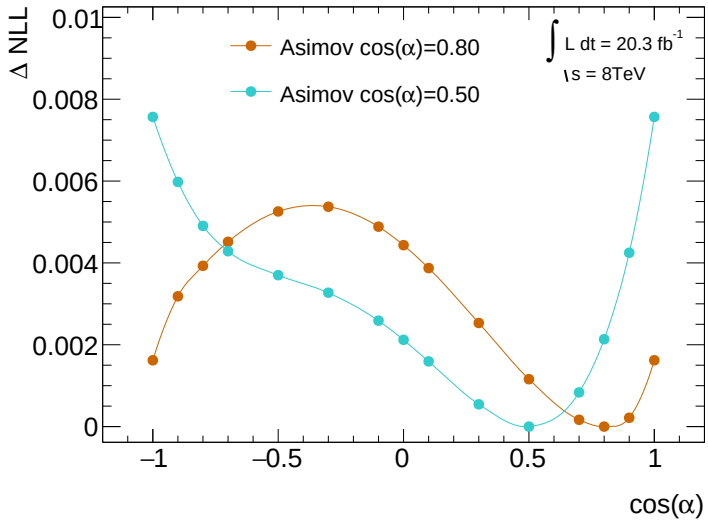

Figure 10.12.: Expected ΔNLL-curve for Asimov data with $\cos(\alpha) = 0.80$ (orange) and $\cos(\alpha) = 0.50$ (cyan) in the signal region and real data in the control regions for the fit in the Optimal Observable. The signal expectation in the signal region is scaled to the SM prediction ($\mu = 1$).

10.4.2. Observed Results

This section presents the results of the likelihood fit in the Optimal Observable and $\Delta\Phi_{jj}^{sign}$ using the observed data at $\sqrt{s} = 8\,\text{TeV}$ in the signal region and the control regions. The first part focuses on the results obtained with the fit in the Optimal Observable, while the second part discusses the results for $\Delta\Phi_{jj}^{sign}$.

The observed ΔNLL-curve for the fit in the Optimal Observable is shown in Fig. 10.13. The minimal NLL-value is obtained for a $\cos(\alpha)$-value of 0.50. A maximum difference of $\Delta\text{NLL} = 0.10$ is observed for a coupling model of $\cos(\alpha) = -0.95$. Therefore, no exclusion limit at the 1σ confidence-level is reached. Table 10.4 summarizes the fit results for signal strength and background normalizations for the SM signal expectation. The fitted signal strength of $\mu = 2.60^{+2.57}_{-2.08}$ is compatible with the SM expectation of one. The fit results for the background normalization factors are close to one, where the normalization of $Z/\gamma^* \to ll$ and $Z \to \tau\tau$ are shifted to smaller values.
As the likelihood fit provides a minimum NLL-value for a Higgs-gluon coupling with $\cos(\alpha) = 0.50$, Table 10.5 shows in addition the fit results for a signal expectation with $\cos(\alpha) = 0.50$. The fitted signal strength $\mu = 2.67^{+2.66}_{-2.03}$ is compatible with one as well. Also the fit results for the background normalization factors show no significant deviation.
The post-fit distributions of the Optimal Observable in the signal region and BDT_{bkg} output in the low BDT region including systematic and statistical uncertainties is shown in Fig. 10.14 for the SM expectation and in Fig. 10.15 for the $\cos(\alpha) = 0.50$ hypothesis. The post-fit event yields in the signal region for the signal and the background processes are summarized in Table 10.6 and Table 10.7 for the SM and $\cos(\alpha) = 0.50$ expectation, respectively. The event yields for both coupling models is in agreement with the pre-fit signal and background expectations, as shown in Table 7.6, within uncertainties.

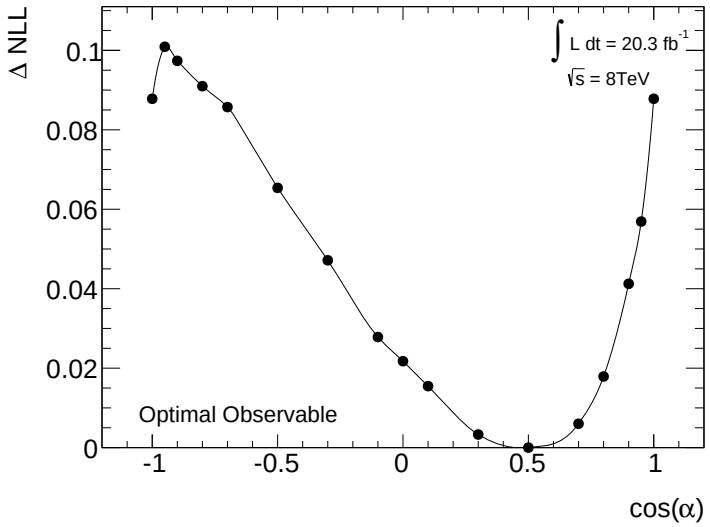

Figure 10.13.: Observed ΔNLL-curve as function of $\cos(\alpha)$-values representing the underlying signal hypothesis for the fit in the Optimal Observable. The filled dots indicate the $\cos(\alpha)$-values for which the NLL-value has been calculated.

The impact of the 40 highest ranked uncertainties on the fitted signal strength and their post-fit pulls can be found in Fig. 10.16 and Fig. 10.17 for the SM and $\cos(\alpha) = 0.50$ expectations, respectively. A summary of post-fit values for each nuisance parameter is given in Appendix D. The highest ranked parameter for both coupling models are the theory uncertainty corresponding to the gluon-fusion process and statistical uncertainties of the background expectation in the signal region. In addition, uncertainties referring to the $Z \to \tau\tau$ background component and the jet energy scale are found to have an non-negligible impact on the fitted signal strength. Theory uncertainties on the partons distribution functions of Higgs-boson production in gluon initiated state are ranked high, as well. Overall, no significant pull of post-fit uncertainties is observed for the SM and the $\cos(\alpha) = 0.50$ signal expectation.

Parameter	Postfit value (in σ units)
μ	$2.60^{+2.57}_{-2.08}$
norm(Top)	$1.00^{+0.12}_{-0.12}$
norm(Zll)	$0.93^{+0.42}_{-0.42}$
norm($Z\tau\tau$)	$0.99^{+0.11}_{-0.11}$

Table 10.4.: Fit results of the normalization factors for top-quark background contribution norm(Top), $Z\gamma^* \to ll$ background contribution norm(Zll), $Z \to \tau\tau$ background contribution norm($Z\tau\tau$) and of the signal strength μ for the fit in the Optimal Observable for the SM hypothesis ($\cos(\alpha) = 1$).

Parameter	Postfit value (in σ units)
μ	$2.67^{+2.66}_{-2.03}$
norm(Top)	$1.00^{+0.12}_{-0.12}$
norm(Zll)	$0.92^{+0.41}_{-0.41}$
norm($Z\tau\tau$)	$0.99^{+0.11}_{-0.11}$

Table 10.5.: Fit results of the normalization factors for top-quark background contribution norm(Top), $Z\gamma^* \to ll$ background contribution norm(Zll), $Z \to \tau\tau$ background contribution norm($Z\tau\tau$) and of the signal strength μ for the $\cos(\alpha) = 0.50$ hypothesis.

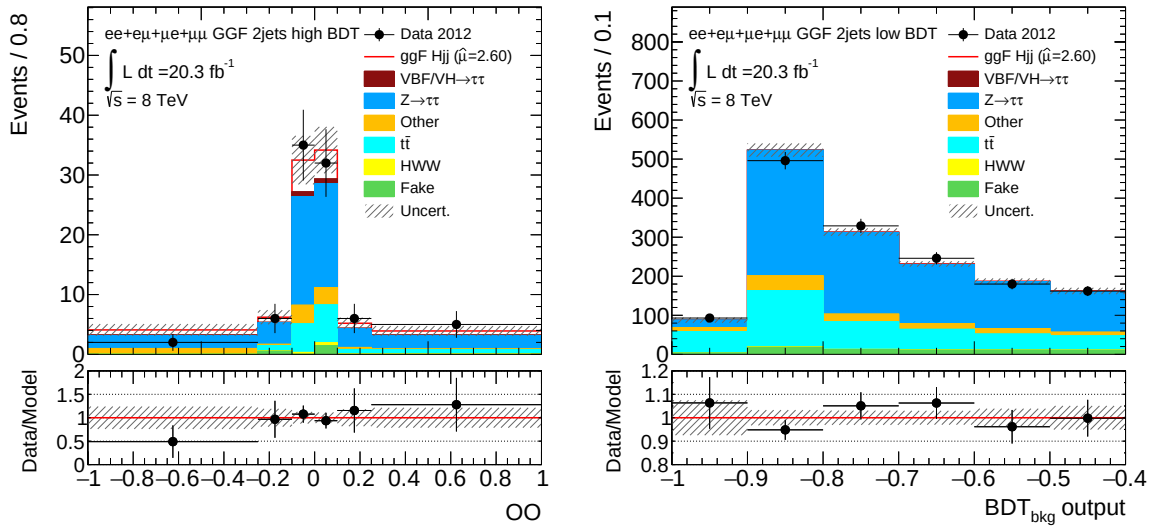

Figure 10.14.: Post-fit distributions of the Optimal Observable in the signal region (left) and $\mathrm{BDT_{bkg}}$ output in the low BDT control region (right) for the SM hypothesis ($\cos(\alpha) = 1$). The error band includes systematic and statistical uncertainties.

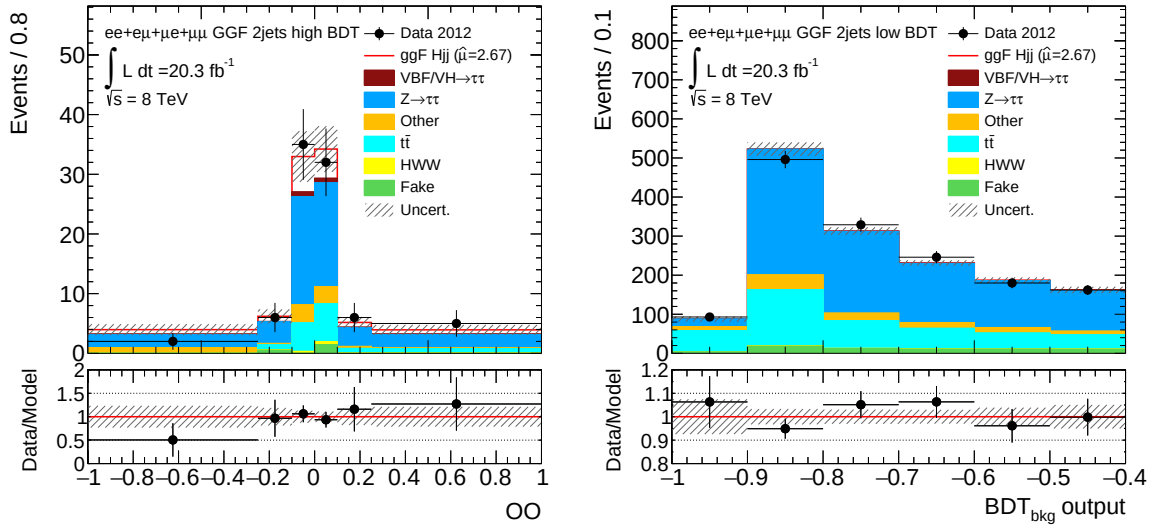

Figure 10.15.: Post-fit sistributions of the Optimal Observable in the signal region (left) and $\mathrm{BDT_{bkg}}$ output in the low BDT control region (right) for the $\cos(\alpha) = 0.50$ hypothesis. The error band includes systematic and statistical uncertainties.

Process	Event yield
ggF H+2jets$\to \tau\tau$	13.35 ± 10.80
VBF H$\to \tau\tau$	0.76 ± 0.11
VH H$\to \tau\tau$	1.24 ± 0.11
$Z \to \tau\tau$	46.67±5.02
Top	13.37 ± 2.78
Other	7.55 ± 3.12
ggF H$\to$WW	0.70 ± 0.22
VBF H$\to$WW	0.11 ± 0.02
VH H$\to$WW	0.36 ± 0.09
Fake leptons	1.96 ± 0.60
$\sum$ bkgs	72.72 ± 6.57
Data	86.0 ± 9.27

Table 10.6.: Post-fit event yield for the fit in the Optimal Observable in the signal region for the signal and each background component for the SM hypothesis ($\cos(\alpha) = 1$) including statistical and systematic uncertainties compared to the observed data for $\sqrt{s} = 8\,\text{TeV}$.

Process	Event yield
ggF H+2jets$\to \tau\tau$	13.39 ± 10.71
VBF H$\to \tau\tau$	0.76 ± 0.11
VH H$\to \tau\tau$	1.23 ± 0.10
$Z \to \tau\tau$	46.59 ± 4.96
Top	13.40 ± 2.78
Other	7.42 ± 3.18
ggF H$\to$WW	0.71 ± 0.22
VBF H$\to$WW	0.11 ± 0.02
VH H$\to$WW	0.36 ± 0.09
Fake leptons	1.96 ± 0.60
$\sum$ bkgs	72.54 ± 6.55
Data	86.0 ± 9.27

Table 10.7.: Post-fit event yield for the fit in the Optimal Observable in the signal region for the signal and each background component for the $\cos(\alpha) = 0.50$ hypothesis including statistical and systematic uncertainties compared to the observed data for $\sqrt{s} = 8\,\text{TeV}$.

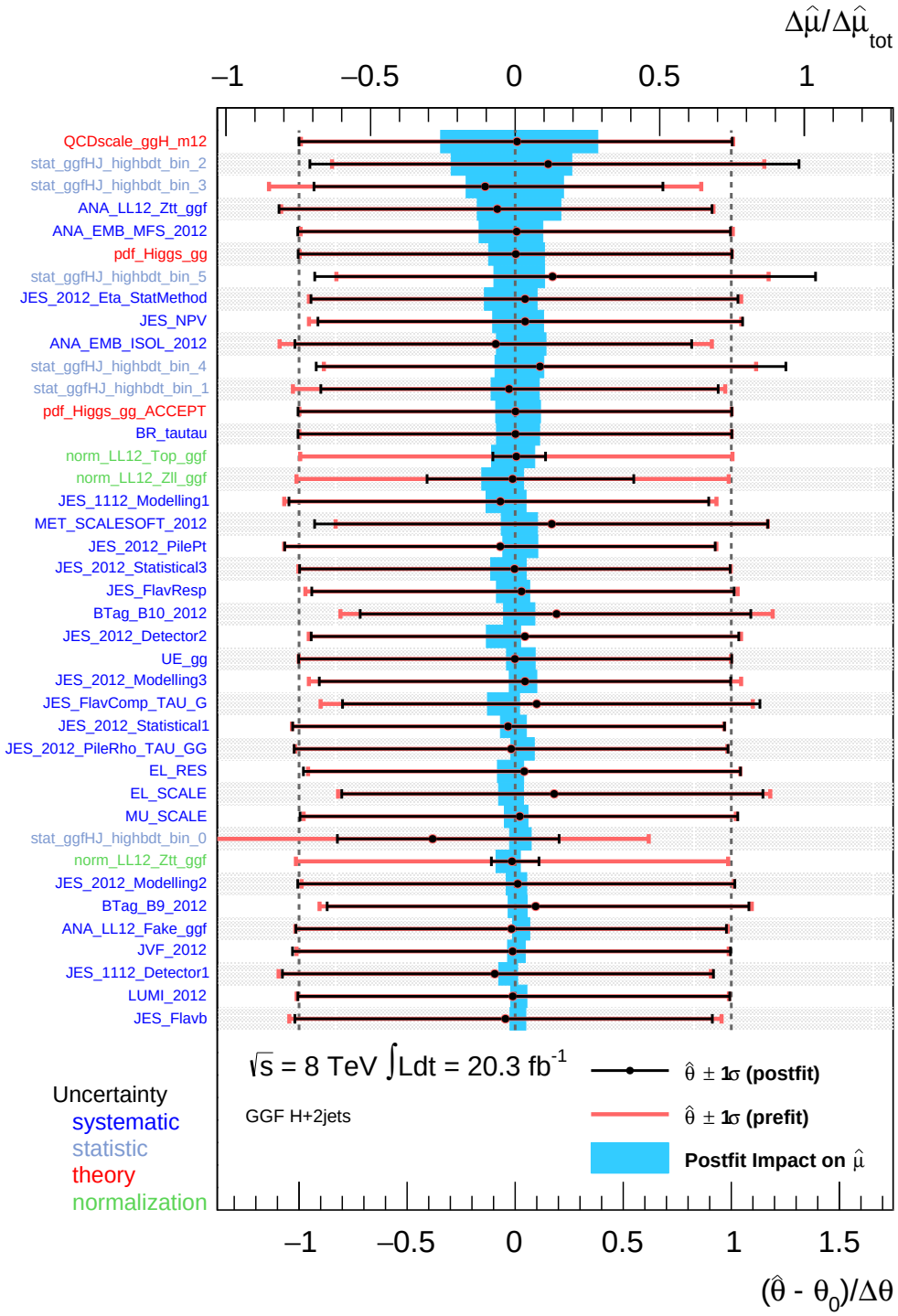

Figure 10.16.: Impact of systematic uncertainties on the fitted signal strength $\hat{\mu}$ for the fit in the Optimal Observable for the SM hypothesis ($\cos(\alpha) = 1$). The systematic uncertainties are listed in decreasing order of their impact on $\hat{\mu}$ on the y-axis. The blue boxes show the variation $\Delta\hat{\mu}$ with respect to the total error $\Delta\hat{\mu}_{tot}$ when the corresponding nuisance parameter is fixed to its post-fit value $\hat{\theta}$ shifted by one standard deviation $\hat{\sigma}_{\hat{\theta}}$ upwards or downwards. The red line, referring to the bottom x-axis, shows the pre-fit uncertainty of the nuisance parameters. The filled black circles, referring to the bottom x-axis, show the deviation of the fitted parameters $\hat{\theta}$ from their nominal value θ_0 normalized to the nominal uncertainty $\Delta\theta$.

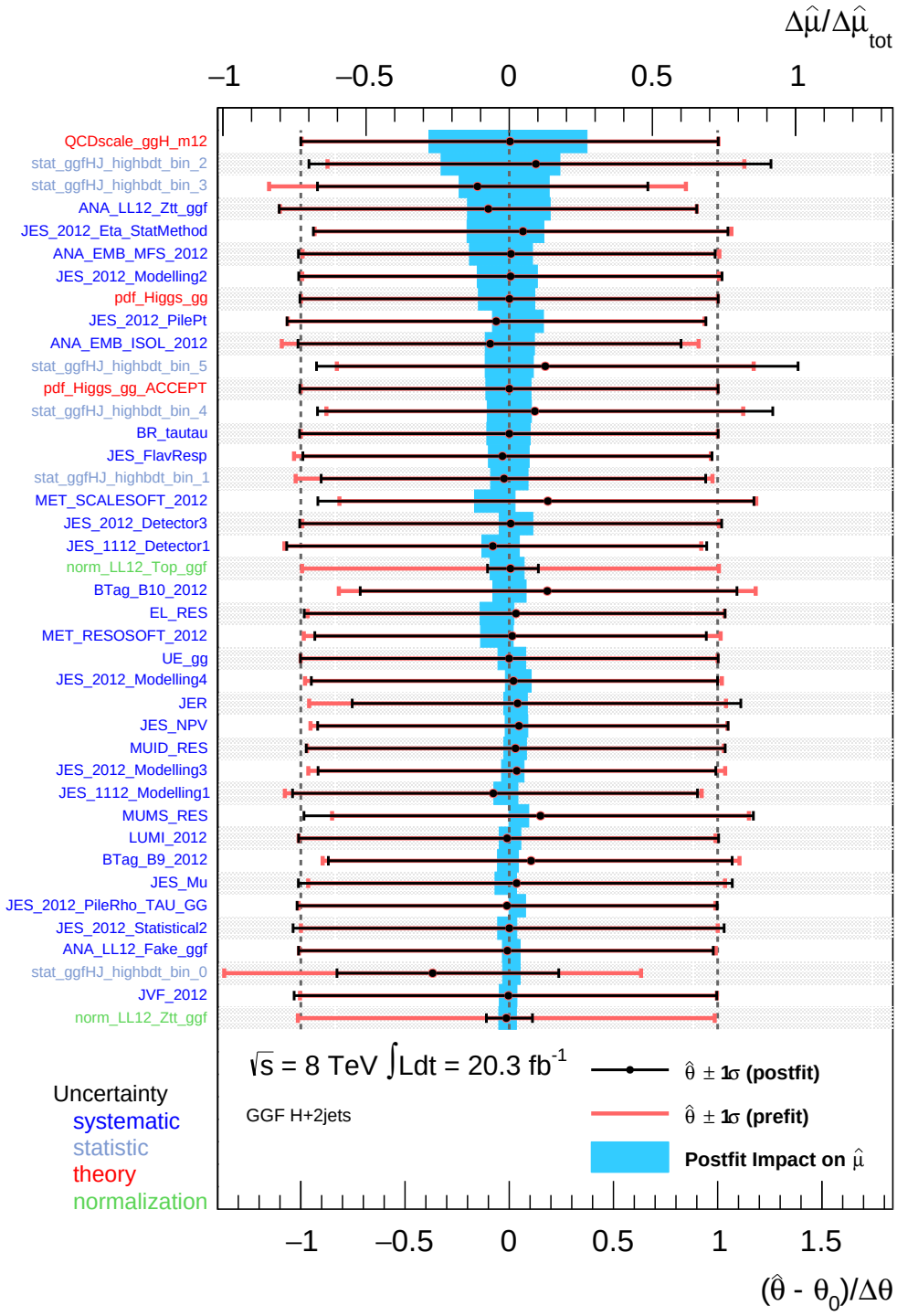

Figure 10.17.: Impact of systematic uncertainties on the fitted signal strength $\hat{\mu}$ for the fit in the Optimal Observable for the $\cos(\alpha) = 0.50$ hypothesis. The systematic uncertainties are listed in decreasing order of their impact on $\hat{\mu}$ on the y-axis. The blue boxes show the variation $\Delta\hat{\mu}$ with respect to the total error $\Delta\hat{\mu}_{tot}$ when the corresponding nuisance parameter is fixed to its post-fit value $\hat{\theta}$ shifted by one standard deviation $\hat{\sigma}_{\hat{\theta}}$ upwards or downwards. The red line, referring to the bottom x-axis, shows the pre-fit uncertainty of the nuisance parameters. The filled black circles, referring to the bottom x-axis, show the deviation of the fitted parameters $\hat{\theta}$ from their nominal value θ_0 normalized to the nominal uncertainty $\Delta\theta$.

The observed ΔNLL-curve for the fit in $\Delta\Phi_{jj}^{sign}$ is shown in Fig. 10.18. The minimal NLL-value is obtained for $\cos(\alpha) = -0.3$, while a maximum difference of $\Delta\text{NLL} = 0.32$ is obtained for a coupling model of $\cos(\alpha) = 0.95$. Therefore, no confidence interval at the 1σ level is obtained. The fit results for the signal strength and the normalization factors are shown in Table 10.8 and Table 10.9 for SM and $\cos(\alpha) = -0.30$ expectation, respectively. In both cases the fitted signal strength is negative, but compatible with the SM expectation within one standard deviation.
The post-fit event yield in the signal region for $\Delta\Phi_{jj}^{sign}$ is summarized in Table 10.10 and Table 10.11 for the signal and each background component for the SM and $\cos(\alpha) = -0.30$ expectation, respectively. The event yields for both coupling models are in good agreement with the pre-fit signal and background expectation, as shown in Table 7.7, within uncertainties. The post-fit distributions of $\Delta\Phi_{jj}^{sign}$ in the signal region and BDT_{bkg} output in the low BDT control region are shown in Fig. 10.19 and Fig. 10.20 for SM and $\cos(\alpha) = -0.30$ respectively. The observed data is in reasonable agreement with the post-fit distributions within statistical and systematic uncertainties.
The impact of these uncertainties on the fitted signal strength is shown in Fig. 10.21 for the 40 highest ranked parameters for the SM signal expectation. A description of the most important systematic uncertainties can be found in Appendix C. The uncertainties with the highest impact are given by statistical uncertainties in the signal region and the theoretical uncertainty on the gluon-fusion production process. The most important systematic uncertainties are related to jet energy scale and resolution uncertainties as well as to uncertainties on the $Z \to \tau\tau$ background component.
The impact of the uncertainties on the fitted signal strength for a signal expectation with $\cos(\alpha) = -0.30$ is given in Fig. 10.21 and shows a similar behavior. Although the impact of statistical uncertainties on the background model are found to be more important compared to the fit in the Optimal Observable, both coupling models show no significant post-fit pulls of nuisance parameters.

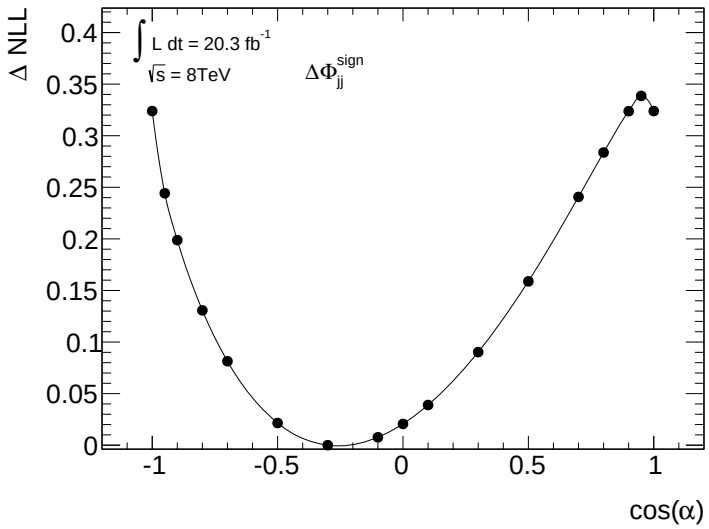

Figure 10.18.: Observed ΔNLL-curve as function of $\cos(\alpha)$-values representing the underlying signal hypothesis for the fit in $\Delta\Phi_{jj}^{sign}$. The filled dots indicate the $\cos(\alpha)$-values for which the NLL-value has been calculated.

Parameter	Postfit value
μ	$-3.36^{+4.51}_{-4.43}$
norm(Top)	$1.03^{+0.14}_{-0.14}$
norm(Zll)	$1.11^{+0.62}_{-0.62}$
norm($Z\tau\tau$)	$0.98^{+0.12}_{-0.12}$

Table 10.8.: Fit results of the normalization factors for top-quark background contribution norm(Top), $Z\gamma^* \to ll$ background contribution norm(Zll), $Z \to \tau\tau$ background contribution norm($Z\tau\tau$) and of the signal strength μ for the SM hypothesis ($\cos(\alpha) = 1$).

Parameter	Postfit value
μ	$-3.13^{+4.73}_{-3.92}$
norm(Top)	$1.02^{+0.14}_{-0.124}$
norm(Zll)	$1.12^{+0.62}_{-0.62}$
norm($Z\tau\tau$)	$0.98^{+0.17}_{-0.17}$

Table 10.9.: Fit results of the normalization factors for top-quark background contribution norm(Top), $Z\gamma^* \to ll$ background contribution norm(Zll), $Z \to \tau\tau$ background contribution norm($Z\tau\tau$) and of the signal strength μ for the $\cos(\alpha) = -0.30$ hypothesis.

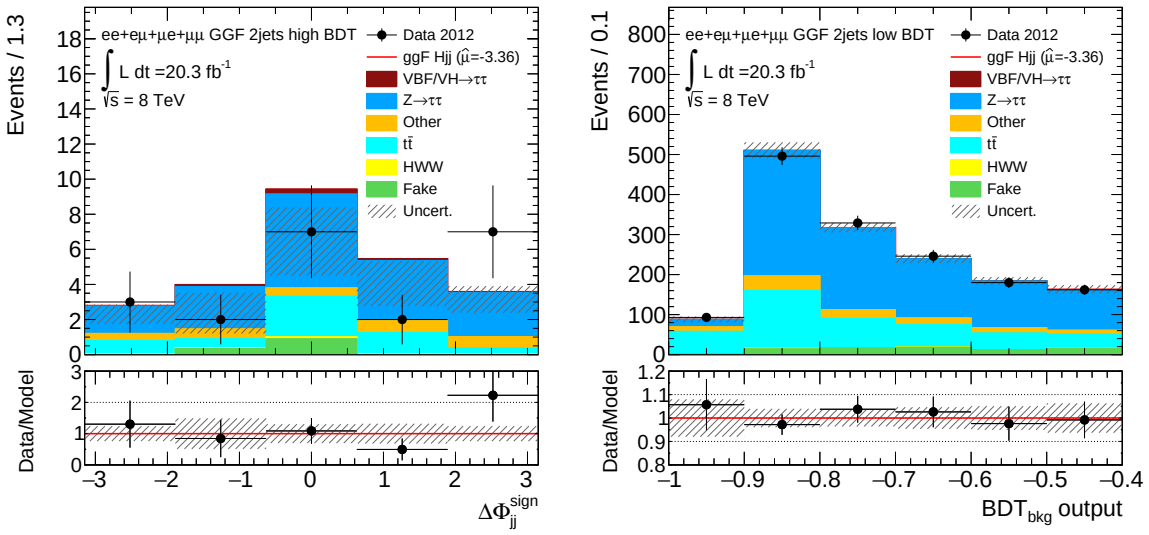

Figure 10.19.: Post-fit distributions of $\Delta\Phi_{jj}^{sign}$ in the signal region (left) and $\mathrm{BDT_{bkg}}$ output in the low BDT control region (right) for the SM hypothesis ($\cos(\alpha) = 1$). The error band includes systematic and statistical uncertainties.

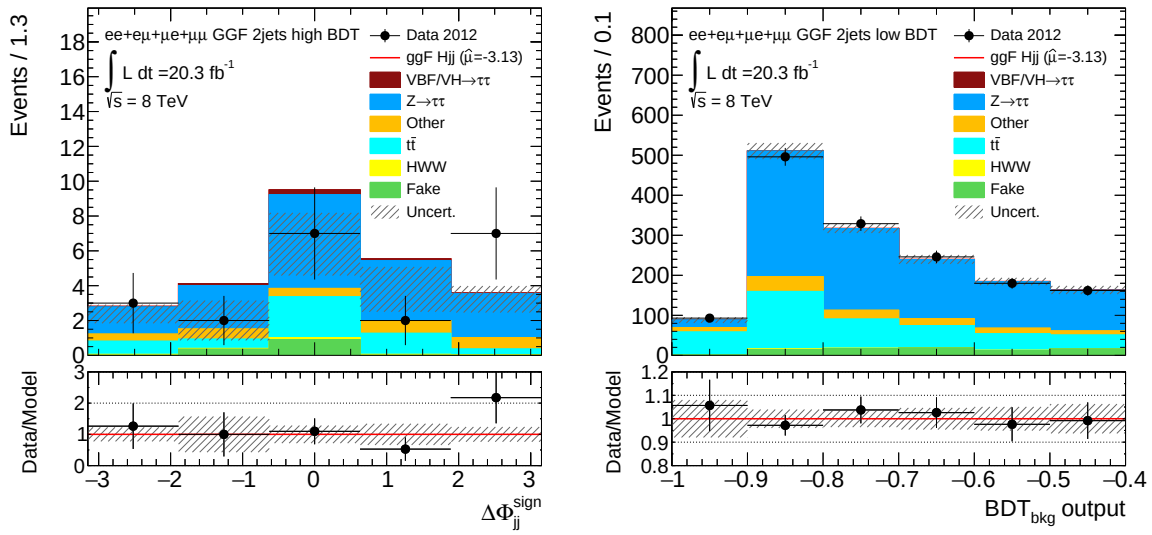

Figure 10.20.: Post-fit distributions of $\Delta\Phi_{jj}^{sign}$ in the signal region (left) and $\mathrm{BDT_{bkg}}$ output in the low BDT control region (right) for the $\cos(\alpha) = -0.30$ hypothesis. The error band includes systematic and statistical uncertainties.

Process	Event yield
ggF H+2jets→ $\tau\tau$	-5.33± 6.96
VBF H→ $\tau\tau$	0.33 ± 0.05
VH H→ $\tau\tau$	0.25 ± 0.02
$Z \to \tau\tau$	15.23 ± 2.42
Top	5.08 ± 2.39
Other	2.83 ± 1.65
ggF H→WW	0.20 ± 0.08
VBF H→WW	0.06 ± 0.02
VH H→WW	0.06 ± 0.07
Fake leptons	1.23 ± 0.38
$\sum$ bkgs	25.27 ± 3.81
Data	21.00 ± 4.58

Table 10.10.: Post-fit event yield for the fit in $\Delta\Phi_{jj}^{sign}$ in the signal region for the signal and each background component for the SM hypothesis ($\cos(\alpha) = 1$) including statistical and systematic uncertainties compared to the observed data for $\sqrt{s} =$ 8 TeV.

Process	Event yield
ggF H+2jets$\to \tau\tau$	-4.91 ± 7.75
VBF H$\to \tau\tau$	0.33 ± 0.05
VH H$\to \tau\tau$	0.25 ± 0.02
$Z \to \tau\tau$	15.36 ± 2.44
Top	5.15 ± 2.48
Other	2.87 ± 1.82
ggF H$\to$WW	0.21 ± 0.08
VBF H$\to$WW	0.06 ± 0.02
VH H$\to$WW	0.06 ± 0.08
Fake leptons	1.24 ± 0.83
$\sum$ bkgs	25.53 ± 4.02
Data	21.00 ± 4.58

Table 10.11.: Post-fit event yield for the fit in $\Delta\Phi_{jj}^{sign}$ in the signal region for the signal and each background component for the $\cos(\alpha) = -0.30$ signal hypothesis including statistical and systematic uncertainties compared to the observed data for $\sqrt{s} = 8\,\text{TeV}$.

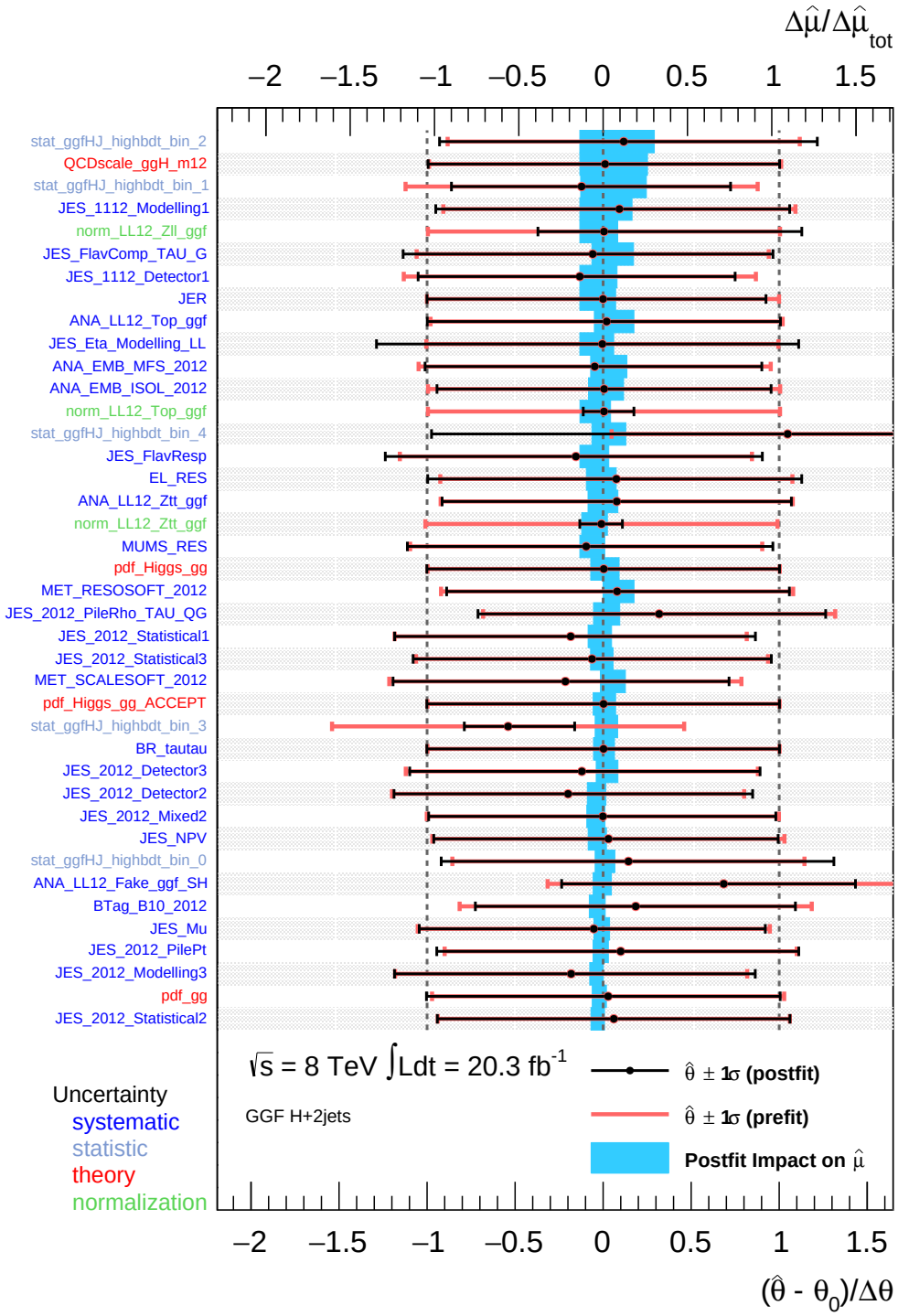

Figure 10.21.: Impact of systematic uncertainties on the fitted signal strength $\hat{\mu}$ for the fit in $\Delta\Phi_{jj}^{sign}$ for the SM hypothesis ($\cos(\alpha = 1)$). The systematic uncertainties are listed in decreasing order of their impact on $\hat{\mu}$ on the y-axis. The blue boxes show the variation $\Delta\hat{\mu}$ with respect to the total error $\Delta\hat{\mu}_{tot}$ when the corresponding nuisance parameter is fixed to its post-fit value $\hat{\theta}$ shifted by one standard deviation $\hat{\sigma}_{\hat{\theta}}$ upwards or downwards. The red line, referring to the bottom x-axis, shows the pre-fit uncertainty of the nuisance parameters. The filled black circles, referring to the bottom x-axis, show the deviation of the fitted parameters $\hat{\theta}$ from their nominal value θ_0 normalized to the nominal uncertainty $\Delta\theta$

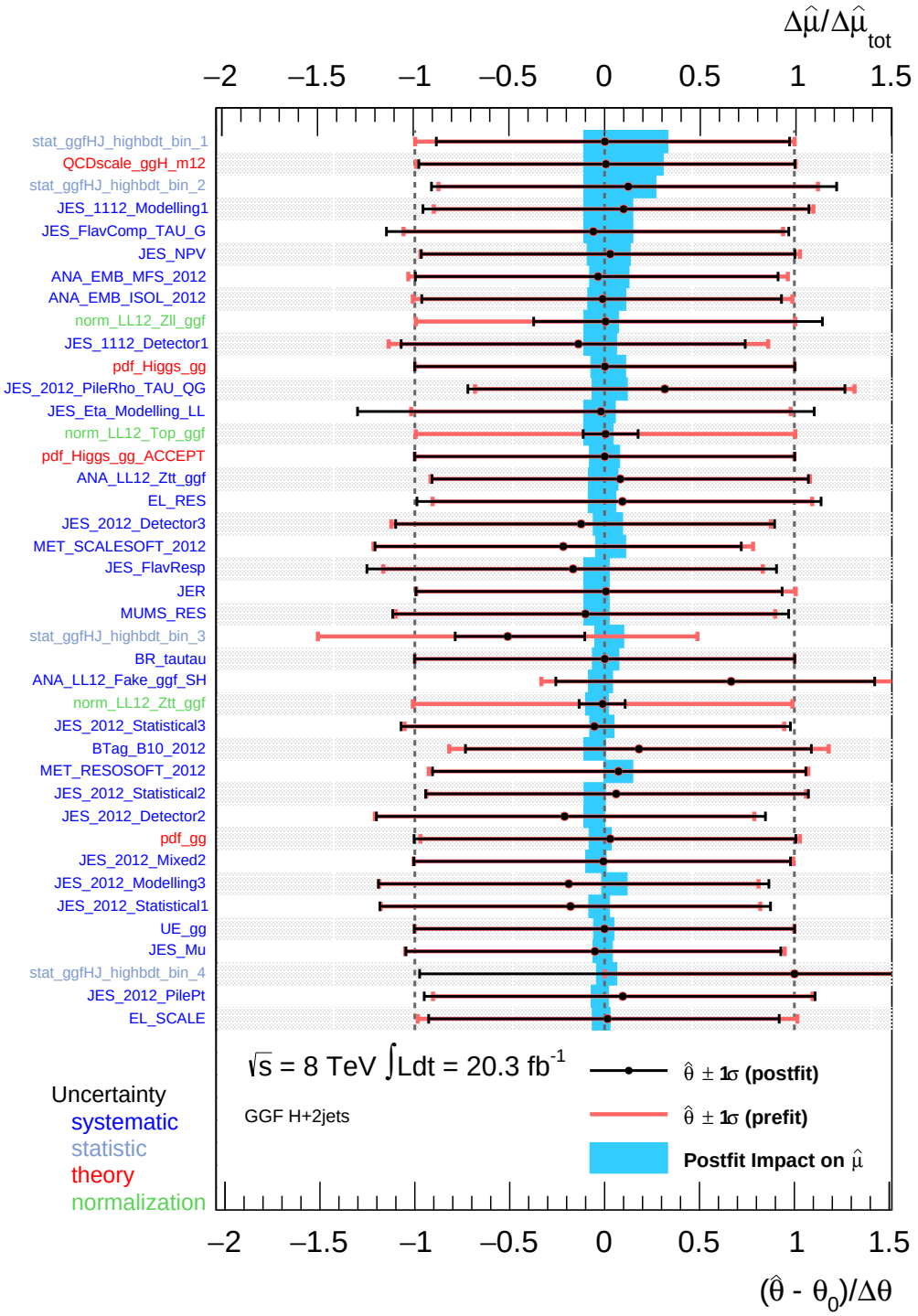

Figure 10.22.: Impact of systematic uncertainties on the fitted signal strength $\hat{\mu}$ for the fit in $\Delta\Phi_{jj}^{sign}$ for the $\cos(\alpha) = -0.30$ hypothesis. The systematic uncertainties are listed in decreasing order of their impact on $\hat{\mu}$ on the y-axis. The blue boxes show the variation $\Delta\hat{\mu}$ with respect to the total error $\Delta\hat{\mu}_{tot}$ when the corresponding nuisance parameter is fixed to its post-fit value $\hat{\theta}$ shifted by one standard deviation $\hat{\sigma}_{\hat{\theta}}$ upwards or downwards. The red line, referring to the bottom x-axis, shows the pre-fit uncertainty of the nuisance parameters. The filled black circles, referring to the bottom x-axis, show the deviation of the fitted parameters $\hat{\theta}$ from their nominal value θ_0 normalized to the nominal uncertainty $\Delta\theta$

10.4.3. Results for Modified Binning of the Optimal Observable

The lack of sensitivity in the results presented in the previous section prompted further investigations into possible ways to improve it. One possibility is to investigate the fit behavior for a different binning choice of the Optimal Observable. Therefore, an additional binning was chosen in order to obtain equal signal contribution in each of the six bins and extending the range to $[-1.5, 1.5]$. The Optimal Observable distribution with this binning choice is shown in Fig. 10.23. In the following, the binning as used in the previous section will be referred to as *binning A*, while the binning choice discussed here will be referred to as *binning B*.
Fig. 10.24 shows a comparison of the expected ΔNLL-curve for the Optimal Observable with binning A and binning B. Here, Asimov data with $\cos(\alpha) = 1$ and $\mu = 1$ are used in the signal region, while the control regions include real data. As expected, the minimal NLL-value is obtained for $\cos(\alpha) = \pm 1$ for binning B as well. In addition, binning B provides a higher sensitivity to anomalous couplings: By comparing the ΔNLL-value for a CP odd coupling ($\cos(\alpha) = 0$) an improvement of 18% is obtained for the Optimal Observable with binning B.
The observed ΔNLL-curve is shown in Fig. 10.24 for a comparison between binning A and binning B. While the minimal NLL-value for binning A is shifted to $\cos(\alpha) = 0.50$, the fit in the Optimal Observable with binning B results in ΔNLL-curve with minimum at $\cos(\alpha) = \pm 1$. However, also with this binning no 1σ-exclusion limit can be derived.
Table 10.12 summarizes the fit results for signal strength and normalization factors for the fit results of binning B, which are consistent with the obtained results for binning A within uncertainties. No significant deviation from the SM expectation is observed. In Fig. 10.26 the post-fit distributions for the Optimal Observable in the signal region and $\mathrm{BDT}_{\mathrm{bkg}}$ output in the low BDT region is shown. In addition, Table 10.13 summarized the post-fit event yield for SM signal and each background component. The signal-plus-background expectation is in good agreement with the observed data.
Further detailed investigations are beyond the scope of this thesis, but a binning choice such as proposed here looks promising for future studies.

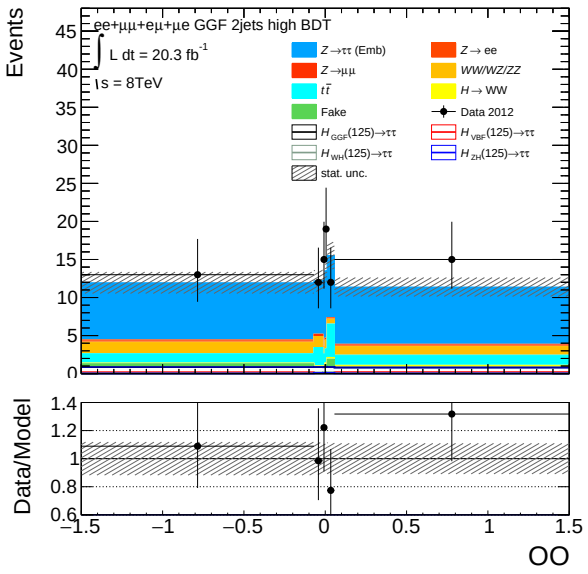

Figure 10.23.: Pre-fit distribution of the Optimal Observable in the high BDT signal region. Here, the binning was chosen in order to yield equal contribution of the SM signal in each bin. The error band includes statistical uncertainties only.

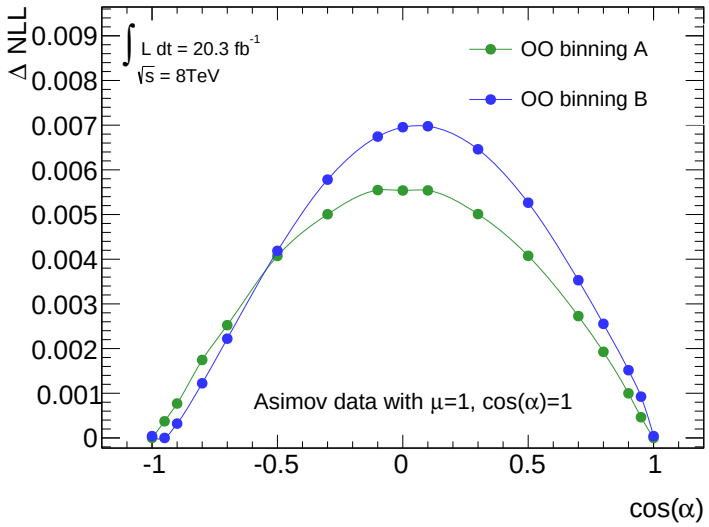

Figure 10.24.: Expected ΔNLL-curve as function of $\cos(\alpha)$ values representing the underlying signal hypothesis for the Optimal Observable with binning B as defined in the text. For comparison the expected ΔNLL-curve for the Optimal Observable with binning A is shown as well. In the signal region Asimov data with μ=1 and SM coupling ($\cos(\alpha) = 1$) are used, while the control regions include real data. The filled dots indicate the $\cos(\alpha)$-values for which the NLL-value has been calculated.

Nuisance parameter	Postfit value
μ	$2.54^{+2.64}_{-2.16}$
norm(Top)	$1.00^{+0.14}_{-0.14}$
norm(Zll)	$0.96^{+0.53}_{-0.53}$
norm($Z\tau\tau$)	$0.98^{+0.12}_{-0.12}$

Table 10.12.: Fit results in the Optimal Observable with binning B as defined in the text for the normalization factors for top-quark background contribution norm(Top), $Z/\gamma^* \rightarrow ll$ background contribution norm(Zll), $Z \rightarrow \tau\tau$ background contribution norm($Z\tau\tau$) and for the signal strength μ for the SM hypothesis ($\cos(\alpha) = 1$).

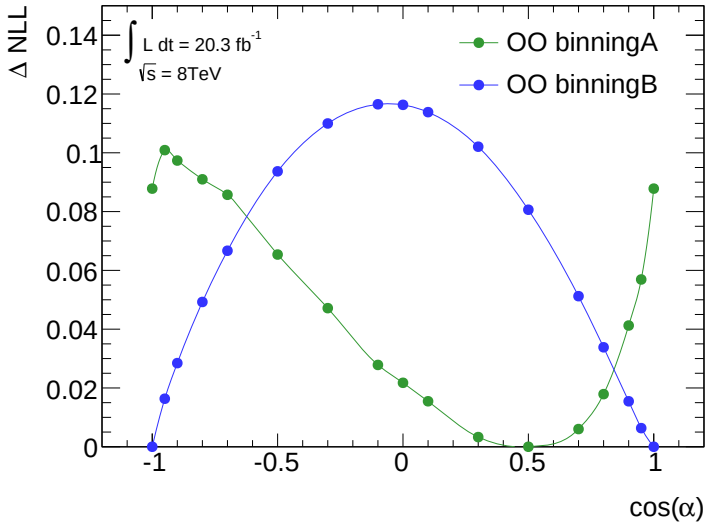

Figure 10.25.: Observed ΔNLL-curve as function of $\cos(\alpha)$ values representing the underlying signal hypothesis for the fit in the Optimal Observable with binning B as defined in the text. For comparison the observed ΔNLL-curve for the Optimal Observable with binning A is shown as well. The filled dots indicate the $\cos(\alpha)$-values for which the NLL-value has been calculated.

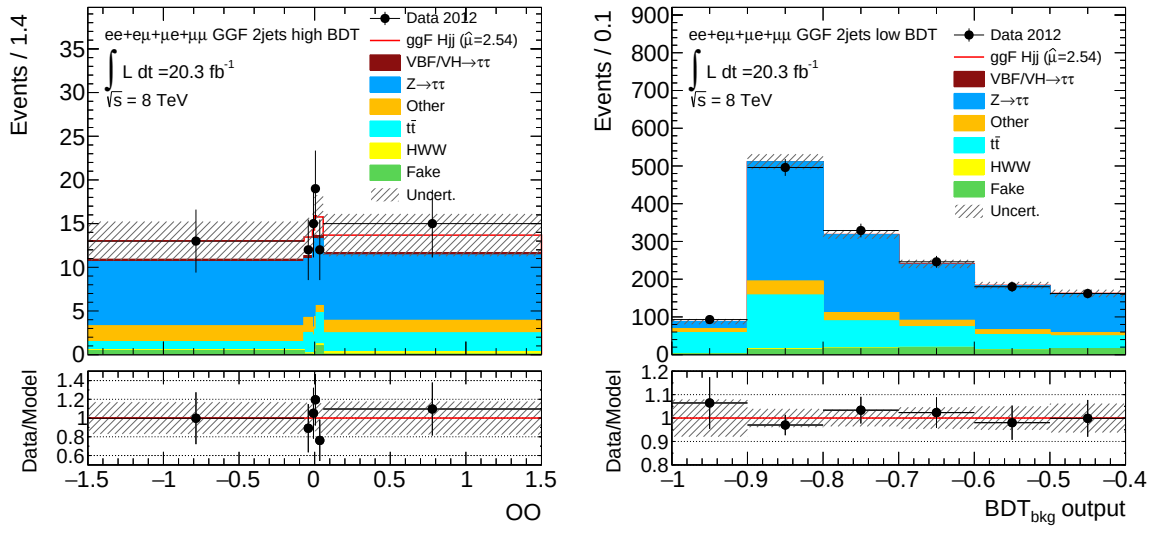

Figure 10.26.: Post-fit distributions of the Optimal Observable with binning B as defined in the text in the signal region (left) and $\mathrm{BDT_{bkg}}$ output in the low BDT control region (right) for the SM hypothesis ($\cos(\alpha) = 1$). The error band includes systematic and statistical uncertainties.

Process	Event yield
ggF H+2jets$\to \tau\tau$	12.83 ± 11.12
VBF H$\to \tau\tau$	0.80 ± 0.12
VH H$\to \tau\tau$	1.24 ± 0.12
$Z \to \tau\tau$	46.77 ± 5.56
Top	13.40 ± 2.96
Other	8.13 ± 4.18
ggF H$\to$WW	0.70 ± 0.22
VBF H$\to$WW	0.12 ± 0.02
VH H$\to$WW	0.34 ± 0.09
Fake leptons	1.87 ± 0.60
$\sum$ bkgs	73.37 ± 7.59
Data	86.0 ± 9.72

Table 10.13.: Post-fit event yield for the fit in the Optimal Observable with binning B in the signal region for the signal and each background component for the SM signal hypothesis including statistical and systematic uncertainties compared to the observed data for $\sqrt{s} = 8\,\text{TeV}$.

11 Conclusion and Outlook

In this thesis, an analysis of the CP properties of the Higgs boson is presented. The analysis focuses on the Higgs-boson production in gluon fusion in association with two jets, H+2jets, followed by the Higgs-boson decay into a pair of τ-leptons in the full leptonic final state.
The Higgs-gluon interaction in an effective model allows to directly probe CP odd contributions in addition to the pure CP even coupling, as predicted by the SM. This anomalous contribution is parametrized in terms of a mixing parameter $\cos(\alpha)$, with $\cos(\alpha) = 1$ giving a purely CP even coupling and $\cos(\alpha) = 0$ referring to a CP odd model. Any mixing between CP even and CP odd couplings, $\cos(\alpha) \neq 0, 1$, implies CP violation.
This analysis exploits two CP-odd observables in order to test the Higgs-gluon coupling for anomalous contributions: The Optimal Observable, which relies on the matrix elements for CP even and CP odd interactions, and the signed azimuthal angle difference between the outgoing jets $\Delta\Phi_{jj}^{sign}$. The analysis is based on data taken in proton-proton collisions with the ATLAS detector in 2012 at $\sqrt{s} = 8\,\text{TeV}$. The dataset corresponds to an integrated luminosity of $20.3\,\text{fb}^{-1}$.

In the first part of the thesis, the sensitivity of the H+2jet signal to anomalous couplings is investigated at parton level by neglecting all background contributions. Here, only the mean value of the Optimal Observable and $\Delta\Phi_{jj}^{sign}$ is considered. A mean value compatible with zero is expected for CP conserving interactions, while a non-zero mean value is expected for $\cos(\alpha)$-models corresponding to CP violation in the Higgs-gluon interaction. Signal models for different $\cos(\alpha)$-values are obtained by reweighting the SM signal. It is found that both observables provide a good separation between different anomalous coupling models in terms of the mean value variation. In comparison, the Optimal Observable is found to be more sensitive in a large $\cos(\alpha)$-range compared to $\Delta\Phi_{jj}^{sign}$. Furthermore, $\Delta\Phi_{jj}^{sign}$ suffers from enhanced statistical uncertainties due to additional requirements on the jet topology.
In addition, the sensitivity of the sub-processes contributing to the H+2jet production in gluon fusion is investigated. These sub-processes are grouped into gluon-gluon, gluon-quark and quark-quark initiated processes. It is found, that sub-processes with quark-quark initial states provide a larger variation in terms of the mean value for various $\cos(\alpha)$-models for both observables. These sub-processes, however, contribute only with about 3% to the total H+2jet production. On the other hand, gluon-gluon initiated processes, giving the largest contribution to the total H+2jet production, show a reduced sensitivity to anomalous couplings. It is shown, that the sub-processes can be distinguished by several kinematic variables, such as the rapidity difference between the outgoing jets or the jets invariant mass. This provides the possibility to enhance the contribution of quark-quark sub-processes and improve the overall sensitivity of H+2jet events to anomalous couplings.

In the second and main part of the thesis, the sensitivity at detector level is investigated and the $\cos(\alpha)$-value is measured in data by using simulated samples for the signal and various background processes. In this analysis, background contributions arising from $Z \to \tau\tau$, $Z/\gamma^* \to ll$, top-quark, di-boson processes and events with misidentified lepton are considered.

In addition, Higgs-bosons production in the VBF channel and the associated production VH constitute an important background contribution as well as $H \to WW$ decays for all production modes. Signal events for different coupling models are obtained by reweighting the SM signal sample.
First a basic preselection is applied. The selection follows the procedure in Reference [104] to a large extend, except for re-optimized specific cuts. Then, a multivariate analysis using BDTs is performed. Here, a first BDT is trained in order so separate the signal from all background processes, while a second BDT is used to additionally suppress contributions from VBF produced Higgs-boson events. The signal region is defined by applying a two-dimensional cut on the output of the two BDTs. This cut is chosen in order achieve maximum significance on the on hand and reduce the contribution of VBF events to be less than 20% of the signal events on the other hand. With this requirement a signal to background ratio of $\frac{s}{b} = \frac{5.13}{73.52}$ is obtained. The dominant background contribution arises from $Z \to \tau\tau$ (65%), top-quark (17%) and di-boson (9%) processes.
To measure the $\cos(\alpha)$-value in data a maximum likelihood fit is performed in the Optimal Observable and $\Delta\Phi_{jj}^{sign}$ distributions. Here, the negative logarithmic likelihood (NLL) value is determined for various signal hypothesis in terms of $\cos(\alpha)$. Systematic uncertainties as well as normalization factors on the top-quark, $Z/\gamma^* \to ll$ and $Z \to \tau\tau$ background contributions are included in the fit. The normalization of Higgs-boson backgrounds are fixed to the SM prediction, while the signal normalization for ggF H+2jet events is left free floating. The observed signal strength for the fit in the Optimal Observable and $\Delta\Phi_{jj}^{sign}$distributions are in good agreement with the SM predictions within uncertainties. The dominant systematic uncertainty arises from the $Z \to \tau\tau$ background contribution due to the embedding procedure, as well as from the theoretical uncertainty on the choice of QCD scale for gluon fusion cross-section calculations.
The expected sensitivity is found to be higher for the fit in the Optimal Observable with about 50% improvement in the maximum ΔNLL-value compared to the fit in $\Delta\Phi_{jj}^{sign}$. However, the sensitivity to anomalous Higgs-gluon couplings is found to be limited with the Run 1 dataset. For the fit in the Optimal Observable a maximum ΔNLL-value of 0.10 is observed, while the fit in $\Delta\Phi_{jj}^{sign}$ results in a maximum ΔNLL-value of 0.32. As the exclusion of anomalous couplings at the 1σ confindence-level corresponds to $\Delta\text{NLL} = 0.50$, no exclusion limits can be derived with the Run 1 dataset. However, it is shown in an additional study, that the sensitivity can be improved by optimizing the binning of the Optimal Observable.

As an outlook for future studies, promising proposals can be made. The selection of signal events can be optimized in order to enhance the contribution of quark-quark initiated sub-processes, which are found to be the most sensitive to anomalous couplings. While this would reduce the relative contribution from the dominant gluon-gluon initial state processes, the overall sensitivity may be improved. In addition, the sensitivity, can be increased by also including the semi-leptonic and full-hadronic final states arising from $H \to \tau\tau$ events and other Higgs-boson decay modes.
In this thesis, only the shape of the CP-sensitive observables is used in the analysis. Including additional information about the cross-section dependence on different coupling models can improve the sensitivity. Furthermore, the combination of the Optimal Observable as used in this thesis with a so called Optimal Observable of 2nd order provides the possibility to further increase the sensitivity and could allow to derive exclusion limits for anomalous Higgs-gluon couplings.

A Comparison of different PDF weightings for the Optimal Observable

The calculation of the Optimal Observable as used in this analysis is described in Section 2.4.2. In order to investigate the dependence of the Optimal Observable sensitivity to anomalous Higgs-gluon couplings an additional study on different PDF weighting methods was performed. In the following, two different methods are compared:

$$\textbf{(1)}\ O = \frac{\sum_{f_1 f_2 \to f_3 f_4} 2\,\mathrm{Re}\left\{\mathcal{M}^*_{\mathrm{SM}}\mathcal{M}_{\mathrm{CPodd}}\right\}\cdot F(x_1,f_1)F(x_2,f_2)}{\sum_{f_1 f_2 \to f_3 f_4} |\mathcal{M}_{SM}|^2 \cdot F(x_1,f_1)F(x_2,f_2)}$$

$$\textbf{(2)}\ O = \sum_{f_1 f_2 \to f_3 f_4} \frac{2\,\mathrm{Re}\left\{\mathcal{M}^*_{\mathrm{SM}}\mathcal{M}_{\mathrm{CPodd}}\right\}}{|\mathcal{M}_{SM}|^2} \cdot F(x_1,f_1)F(x_2,f_2)$$

Here, the PDFs for initial parton 1(2) with flavour $f_1(f_2)$ and momentum fraction $x_1(x_2)$ are given by $F(x_1, f_1)(F(x_2, f_2))$. The sum goes over all possible parton flavour combinations $f_1 f_2 \to f_3 f_4$. Fig. A.1 shows the mean value of the Optimal Observable normalized to the RMS for different $\cos(\alpha)$-models comparing method (1) and method (2). The events are generated with MadGraph5 at LO as described in Chapter 4. The Optimal Observable constructed with method (1) provides a higher sensitivity in terms of mean value variations compared to method (2). In this analysis, the Optimal Observable with a PDF weighting according to method (1) is used.

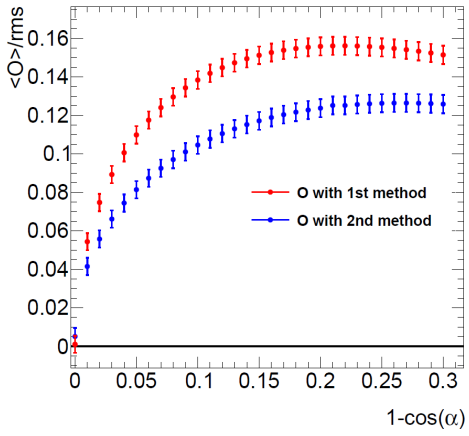

Figure A.1.: Mean value of the Optimal Observable O normalized to the RMS for different $(1-\cos(\alpha))$-values comparing two methods for the PDF weighting of the Optimal Observable.

B Impact of Systematic Uncertainties in the Control Regions

In the following, the impact of the considered systematic uncertainties on the expected event yield for signal and background processes and on the shape of the $\mathrm{BDT_{bkg}}$ output in the low BDT control region is given. A description of the uncertainties can be found in Chapter 9.

Systematic Uncertainty	ggF H+2jets	VBFH	$Z \to \tau\tau$	$t\bar{t}$	Fake	Other	Shape
Normalization $Z \to \tau\tau$	-	-	±15.0%	-	-	-	
Normalization $t\bar{t}$	-	-	-	±6.0%	-	-	
Normalization fake leptons	-	-	-	-	±30.0%	-	
Normalization $Z/\gamma^* \to ll$	-	-	-	-	-	±6.4%	
Electron Efficiency	±0.7%	±0.7%	±1.6%	±0.7%	-	±0.6%	
Electron Energyscale	$^{+3.2\%}_{-1.6\%}$	$^{+0.6\%}_{-1.1\%}$	$^{+1.4\$}_{-0.9\%}$	$^{+2.9\%}_{-0.6\%}$	-	$^{+0.2\%}_{1.9\%}$	•
Electron Energyresolution	-	-	$^{+0.3\%}_{-1.8\%}$	$^{+0.8\%}_{-0.4\%}$	-	-	•
Muon Efficiency	±0.8%	-	-	±0.8%	-	±0.9%	
Muon Energyscale	$^{+0.5\%}_{-1.3\%}$	$^{+0.6\%}_{-1.1\%}$	$^{+0.8\%}_{-0.6\%}$	±0.1%	-	−0.9%	
Muon Energyresolution	$^{+1.1\%}_{-1.7\%}$	$^{+0.9\%}_{-0.8\%}$	$^{+1.3\%}_{-0.8\%}$	-	-	$^{+0.6\%}_{-0.2\%}$	•
E_T^{miss} Soft Term	$^{+0.6\%}_{-4.2\%}$	$^{+1.6\%}_{-1.8\%}$	$^{+1.2\%}_{-1.4\%}$	$^{+0.6\%}_{-1.0\%}$	-	±2.1%	•
Trigger Scalefactor	$^{+0.6\%}_{-0.7\%}$	$^{+0.6\%}_{-0.7\%}$	-	±0.6%	-	±1%	
JER	±5.6%	±4.6%	-	-	-	±10%	•
JVF	$^{+0.6\%}_{-1.5\%}$	$^{+0.3\%}_{-1.4\%}$	-	-	-	$^{+0.2\%}_{-2.4\%}$	
JES	$^{+9.3\%}_{-6.8\%}$	$^{+3.4\%}_{-5.6\%}$	-	$^{+4.5\%}_{-6.3\%}$	-	$^{+18.9\%}_{-15.2\%}$	•
BCH Jet Cleaning	±0.3%	±0.3%	-	-	-	-	
b-Tagging	-	-	-	$^{+12.2\%}_{-11.7\%}$	-	-	
Emb. Muon Isolation	-	-	±12.0%	-	-	-	•
Emb. Cell Subtraction	-	-	$^{+5.5\%}_{-9.6\%}$	-	-	-	•
Emb. Muon Efficiency	-	-	±1.9%	-	-	-	
QCD Scale	$^{+26\%}_{-21\%}$	±2.5%	-	±6.0%	-	±1.2%	
Underlying Event (gg)	±4.0%	-	-	-	-	-	
Underlying Event (qq)	-	±1.0%	-	-	-	-	
PDF (Hgg)	$^{+10.0}_{-9.2\%}$	-	-	-	-	-	
PDF (Hqq)	-	±3.2%	-	-	-	-	
PDF (gg)	-	-	-	±8.0%	-	-	
PDF (qq)	-	-	-	-	-	±4.0%	
NLO EW Higgs	-	±2.0%	-	-	-	-	
NLO Match accept	-	±4.2%	-	-	-	-	
BR $H \to \tau\tau$	±5.7%	±5.7%	-	-	-	-	

Table B.1.: Source of systematic uncertainties and their relative impact on the normalization of signal and important background processes in the low BDT control. In addition, systematic uncertainties with an impact on the shape of $\mathrm{BDT_{output}}$ are labeled (•). Only systematic uncertainties with a normalization impact of $\geq 0.1\%$ are given. Here, *VBFH* stands for VBF produced $H \to \tau\tau$ events, *Other* refers to di-boson and $Z/\gamma^* \to ll$ events.

C Post-fit Nuisance Parameters

Nuisance parameter	postfit value (in σ unit)
ANA_EMB_ISOL_2012	$-0.075^{+0.873}_{-0.873}$
ANA_EMB_MFS_2012	$0.00398^{+0.973}_{-0.973}$
ANA_LL12_Fake_ggf	$0.0206^{+0.981}_{-0.981}$
ANA_LL12_Fake_ggf_SH	$0.123^{+0.757}_{-0.757}$
ANA_LL12_Top_ggf	$-8.98e-05^{+0.993}_{-0.993}$
ANA_LL12_Zll_ggf	$0.000471^{+0.994}_{-0.994}$
ANA_LL12_Zll_vbf_DETAJJ	$-0.000383^{+0.993}_{-0.993}$
ANA_LL12_Ztt_ggf	-0.116^{+1}_{-1}
BCH_LL12_ggf	$-1.29e-05^{+0.993}_{-0.993}$
BR_WW	$-0.000239^{+0.993}_{-0.993}$
BR_tautau	$-7.89e-05^{+0.994}_{-0.994}$
BTag_B10_2012	$0.167^{+0.889}_{-0.889}$
BTag_B1_2012	$0.0102^{+0.993}_{-0.993}$
BTag_B2_2012	$-3.6e-07^{+0.993}_{-0.993}$
BTag_B3_2012	$0.000389^{+0.993}_{-0.993}$
BTag_B6_2012	$0.00855^{+0.993}_{-0.993}$
BTag_B7_2012	$-0.024^{+0.991}_{-0.991}$
BTag_B8_2012	$-0.0193^{+0.992}_{-0.992}$
BTag_B9_2012	$0.0957^{+0.961}_{-0.961}$
BTag_C1_2012	$8.49e-06^{+0.993}_{-0.993}$
BTag_C2_2012	$-0.000121^{+0.993}_{-0.993}$
BTag_C3_2012	$-9.36e-05^{+0.993}_{-0.993}$
BTag_C4_2012	$0.000157^{+0.993}_{-0.993}$
BTag_L10_2012	$0.000102^{+0.993}_{-0.993}$
BTag_L11_2012	$5.75e-05^{+0.993}_{-0.993}$
BTag_L12_2012	$-0.000408^{+0.993}_{-0.993}$
BTag_L8_2012	$4.54e-07^{+0.993}_{-0.993}$
EL_EFF	$0.00429^{+0.993}_{-0.993}$
EL_RES	$-0.0459^{+0.967}_{-0.967}$
EL_SCALE	$0.178^{+0.987}_{-0.987}$
JER	$0.0537^{+0.937}_{-0.937}$
JES_1112_Detector1	-0.079^{+1}_{-1}
JES_1112_Modelling1	$-0.0918^{+0.948}_{-0.948}$
JES_2012_Detector2	$0.0449^{+1.01}_{-1.01}$
JES_2012_Detector3	$-0.0351^{+0.962}_{-0.962}$
JES_2012_Eta_StatMethod	$0.0332^{+0.938}_{-0.938}$
JES_2012_Mixed1	$-0.0507^{+0.958}_{-0.958}$
JES_2012_Mixed2	$-0.00499^{+0.991}_{-0.991}$
JES_2012_Modelling2	$0.0264^{+1.02}_{-1.02}$

Nuisance parameter	postfit value (in σ unit)
JES_2012_Modelling3	$-0.0144^{+0.928}_{-0.928}$
JES_2012_Modelling4	$0.0386^{+0.991}_{-0.991}$
JES_2012_PilePt	$-0.0278^{+0.942}_{-0.942}$
JES_2012_PileRho_TAU_GG	$0.00121^{+0.996}_{-0.996}$
JES_2012_PileRho_TAU_QG	$0.0445^{+0.957}_{-0.957}$
JES_2012_PileRho_TAU_QQ	$0.000712^{+0.993}_{-0.993}$
JES_2012_Statistical1	$-0.00651^{+0.996}_{-0.996}$
JES_2012_Statistical2	$0.0118^{+1.07}_{-1.07}$
JES_2012_Statistical3	$-0.00397^{+0.991}_{-0.991}$
JES_Eta_Modelling_LL	$-0.0299^{+0.953}_{-0.953}$
JES_FlavComp_TAU_G	$0.0949^{+0.97}_{-0.97}$
JES_FlavComp_TAU_Q	$0.000496^{+0.992}_{-0.992}$
JES_FlavResp	$0.0336^{+0.932}_{-0.932}$
JES_Flavb	$-0.0297^{+0.954}_{-0.954}$
JES_Mu	$0.036^{+1.08}_{-1.08}$
JES_NPV	$0.0368^{+0.971}_{-0.971}$
JVF_2012	$0.00101^{+0.97}_{-0.97}$
LUMI_2012	$-9.31e-05^{+0.993}_{-0.993}$
MET_RESOSOFT_2012	$0.000728^{+0.909}_{-0.909}$
MET_SCALESOFT_2012	$0.121^{+1.03}_{-1.03}$
MUID_RES	$0.0354^{+0.997}_{-0.997}$
MUMS_RES	$-0.0018^{+1.01}_{-1.01}$
MU_EFF_2012	$1.95e-05^{+0.993}_{-0.993}$
MU_EFF_2012_Emb	$0.000328^{+0.993}_{-0.993}$
MU_SCALE	$-0.0107^{+0.979}_{-0.979}$
Matching_ACCEPT	$3.79e-05^{+0.993}_{-0.993}$
TRIG_LL12_SF	$-0.000571^{+0.993}_{-0.993}$
UE_gg	$-2.58e-05^{+0.993}_{-0.993}$
UE_qq	$4.03e-06^{+0.993}_{-0.993}$
NLO_EW_Higgs	$8.06e-06^{+0.993}_{-0.993}$
QCDscale_VH	$-9e-05^{+0.993}_{-0.993}$
QCDscale_VV	$8.32e-05^{+0.993}_{-0.993}$
QCDscale_ggH_m12	$9.12e-05^{+0.996}_{-0.996}$
QCDscale_qqH	$1.01e-05^{+0.993}_{-0.993}$
pdf_Higgs_gg	$3.89e-05^{+0.994}_{-0.994}$
pdf_Higgs_gg_ACCEPT	$-8.31e-05^{+0.994}_{-0.994}$
pdf_Higgs_qq	$-4.49e-05^{+0.993}_{-0.993}$
pdf_Higgs_qq_ACCEPT	$-1e-05^{+0.993}_{-0.993}$
pdf_gg	$0.000262^{+0.993}_{-0.993}$
pdf_qq	$0.000293^{+0.994}_{-0.994}$

Table C.1.: Post-fit values of the systematic uncertainties for the likelihood fit in the Optimal Observable with SM signal expectation.

Nuisance parameter	postfit value (in σ unit)
ANA_EMB_ISOL_2012	$-0.0263^{+0.966}_{-0.966}$
ANA_EMB_MFS_2012	$-0.148^{+0.996}_{-0.996}$
ANA_LL12_Fake_ggf	$0.0964^{+0.956}_{-0.956}$
ANA_LL12_Fake_ggf_SH	$0.663^{+0.769}_{-0.769}$
ANA_LL12_Top_ggf	$0.0141^{+0.989}_{-0.989}$
ANA_LL12_Zll_ggf	$-0.000151^{+0.994}_{-0.994}$
ANA_LL12_Zll_vbf_DETAJJ	$-0.0119^{+0.994}_{-0.994}$
ANA_LL12_Ztt_ggf	$-0.0454^{+0.993}_{-0.993}$
BCH_LL12_ggf	$0.000609^{+0.993}_{-0.993}$
BR_WW	$-9.38e-05^{+0.993}_{-0.993}$
BR_tautau	$2.51e-05^{+0.994}_{-0.994}$
BTag_B10_2012	$0.262^{+0.894}_{-0.894}$
BTag_B1_2012	-0.0155^{+1}_{-1}
BTag_B2_2012	$0.00572^{+0.993}_{-0.993}$
BTag_B3_2012	$-0.00107^{+0.994}_{-0.994}$
BTag_B4_2012	$-0.00397^{+0.993}_{-0.993}$
BTag_B5_2012	$0.00163^{+0.993}_{-0.993}$
BTag_B6_2012	$0.0174^{+0.992}_{-0.992}$
BTag_B7_2012	$-0.0338^{+0.992}_{-0.992}$
BTag_B8_2012	$-0.023^{+0.992}_{-0.992}$
BTag_B9_2012	$0.137^{+0.957}_{-0.957}$
BTag_C1_2012	$-0.00267^{+0.994}_{-0.994}$
BTag_C2_2012	$-0.000195^{+0.993}_{-0.993}$
BTag_C3_2012	$-0.000481^{+0.993}_{-0.993}$
BTag_C4_2012	$-0.00106^{+0.993}_{-0.993}$
BTag_L10_2012	$0.000342^{+0.993}_{-0.993}$
BTag_L11_2012	$0.00125^{+0.993}_{-0.993}$
BTag_L12_2012	$-0.00235^{+0.993}_{-0.993}$
BTag_L1_2012	$7.96e-07^{+0.993}_{-0.993}$
BTag_L4_2012	$-3.72e-06^{+0.993}_{-0.993}$
BTag_L5_2012	$5.36e-06^{+0.993}_{-0.993}$
BTag_L6_2012	$9.02e-07^{+0.993}_{-0.993}$
BTag_L7_2012	$0.000835^{+0.993}_{-0.993}$
BTag_L8_2012	$-4.77e-06^{+0.993}_{-0.993}$
BTag_L9_2012	$0.000873^{+0.993}_{-0.993}$
BTag_T2_2012	$-5.09e-07^{+0.993}_{-0.993}$
BTag_T3_2012	$0.00036^{+0.993}_{-0.993}$
BTag_T4_2012	$0.000791^{+0.993}_{-0.993}$
EL_EFF	$0.0063^{+0.993}_{-0.993}$
EL_RES	$-0.0429^{+1.12}_{-1.12}$
EL_SCALE	$-0.0788^{+0.96}_{-0.96}$
JER	$0.00571^{+0.928}_{-0.928}$
JES_1112_Detector1	$-0.0808^{+0.844}_{-0.844}$

Nuisance parameter	postfit value (in σ unit)
JES_1112_Modelling1	$0.0705^{+0.895}_{-0.895}$
JES_2012_Detector2	$-0.173^{+1.01}_{-1.01}$
JES_2012_Detector3	$-0.159^{+0.976}_{-0.976}$
JES_2012_Eta_StatMethod	$0.1^{+0.844}_{-0.844}$
JES_2012_Mixed1	$-0.214^{+1.01}_{-1.01}$
JES_2012_Mixed2	$0.0316^{+0.956}_{-0.956}$
JES_2012_Modelling2	$-0.0761^{+0.878}_{-0.878}$
JES_2012_Modelling3	$-0.148^{+1.04}_{-1.04}$
JES_2012_Modelling4	$0.107^{+0.97}_{-0.97}$
JES_2012_PilePt	$0.104^{+1.05}_{-1.05}$
JES_2012_PileRho_TAU_GG	$8.02e-05^{+0.993}_{-0.993}$
JES_2012_PileRho_TAU_QG	$0.299^{+0.956}_{-0.956}$
JES_2012_PileRho_TAU_QQ	$6.26e-05^{+0.993}_{-0.993}$
JES_2012_Statistical1	$-0.178^{+1.04}_{-1.04}$
JES_2012_Statistical2	$0.064^{+1.02}_{-1.02}$
JES_2012_Statistical3	$-0.127^{+0.996}_{-0.996}$
JES_Eta_Modelling_LL	$-0.0116^{+1.43}_{-1.43}$
JES_FlavComp_TAU_G	$-0.0926^{+1.07}_{-1.07}$
JES_FlavComp_TAU_Q	$-0.000513^{+0.994}_{-0.994}$
JES_FlavResp	$-0.0197^{+0.957}_{-0.957}$
JES_Flavb	-0.145^{+1}_{-1}
JES_Mu	$-0.043^{+0.952}_{-0.952}$
JES_NPV	$0.0237^{+0.945}_{-0.945}$
JVF_2012	$0.00741^{+0.95}_{-0.95}$
LUMI_2012	$0.00976^{+0.993}_{-0.993}$
MET_RESOSOFT_2012	$0.122^{+0.895}_{-0.895}$
MET_SCALESOFT_2012	$-0.16^{+0.932}_{-0.932}$
MUID_RES	$-0.166^{+1.05}_{-1.05}$
MUMS_RES	$-0.157^{+0.953}_{-0.953}$
MU_EFF_2012	$-0.0113^{+0.994}_{-0.994}$
MU_EFF_2012_Emb	$0.00125^{+0.993}_{-0.993}$
MU_SCALE	$-0.103^{+0.92}_{-0.92}$
Matching_ACCEPT	$-1.23e-05^{+0.993}_{-0.993}$
TRIG_LL12_SF	$-0.00287^{+0.992}_{-0.992}$
UE_gg	$-6.48e-05^{+0.994}_{-0.994}$
UE_qq	$-1.29e-06^{+0.993}_{-0.993}$
NLO_EW_Higgs	$-2.57e-06^{+0.993}_{-0.993}$
QCDscale_VH	$-4.27e-05^{+0.993}_{-0.993}$
QCDscale_VV	$0.000345^{+0.993}_{-0.993}$
QCDscale_ggH_m12	$0.000389^{+0.997}_{-0.997}$
QCDscale_qqH	$-3.21e-06^{+0.993}_{-0.993}$
pdf_Higgs_gg	$0.00012^{+0.994}_{-0.994}$
pdf_Higgs_gg_ACCEPT	$2.65e-05^{+0.994}_{-0.994}$
pdf_Higgs_qq	$-2.55e-05^{+0.993}_{-0.993}$
pdf_Higgs_qq_ACCEPT	$-1.01e-05^{+0.993}_{-0.993}$
pdf_gg	$0.0245^{+0.986}_{-0.986}$
pdf_qq	$0.000726^{+0.994}_{-0.994}$

Table C.2.: Post-fit values of the systematic uncertainties for the likelihood fit in $\Delta\Phi_{jj}^{sign}$ with SM signal expectation.

D Nuisance Parameter Pulls

In the following the impact of systematic uncertainties on the fitted signal strength μ for the fit in the Optimal Observable and $\Delta\Phi_{jj}^{sign}$, as discussed inSection 10.4, are shown.

Fig. D.1: Fit in the Optimal Observable with SM ($\cos(\alpha) = 1$) signal expectation by using Asimov data with $\mu = 1$ and $\cos(\alpha) = 1$ in the signal region and real data in the control regions.

Fig. D.2: Fit in the Optimal Observable with SM ($\cos(\alpha) = 1$) signal expectation by using real data in the signal and control regions.

Fig. D.3: Fit in the Optimal Observable with $\cos(\alpha) = 0.50$ signal expectation by using real data in the signal and control regions.

Fig. D.4: Fit in $\Delta\Phi_{jj}^{sign}$ with SM ($\cos(\alpha) = 1$) signal expectation by using Asimov data with $\mu = 1$ and $\cos(\alpha) = 1$ in the signal region and real data in the control regions.

Fig. D.5: Fit in $\Delta\Phi_{jj}^{sign}$ with SM ($\cos(\alpha) = 1$) signal expectation by using real data in the signal and control regions.

Fig. D.6: Fit in $\Delta\Phi_{jj}^{sign}$ with $\cos(\alpha) = -0.30$ signal expectation by using real data in the signal and control regions.

Fig. D.7: Fit in the Optimal Observable binning B with SM ($\cos(\alpha) = 1$) signal expectation by using Asimov data with $\mu = 1$ and $\cos(\alpha) = 1$ in the signal region and real data in the control regions.

Fig. D.8: Fit in the Optimal Observable binning Bwith SM ($\cos(\alpha) = 1$) signal expectation by using real data in the signal and control regions.

In the following a brief description of the highest ranked nuisance parameters with the largest impact on the fitted signal strength μ for the fit in the Optimal Observable and $\Delta\Phi_{jj}^{sign}$, as discussed in Section 10.4, is given. A detailed description of the various systematic uncertainties can be found in Ref. [104].

QCDScale_ggH_m12: Theoretical uncertainty on the gluon-fusion production cross section due to the choice of renormalization and factorization scale.

stat_ggfHJ_highbdt_bin_i: Statistical uncertainty on the background model in bin i of the Optimal Observable/$\Delta\Phi_{jj}^{sign}$ distribution in the signal region.

ANA_LL12_Ztt_ggf: Uncertainty on the $Z \to \tau\tau$ background component due to differences in the normalization of same lepton flavour and different lepton flavour final states.

ANA_EMB_MFS_2012: Uncertainty on the $Z \to \tau\tau$ background component due cell energy subtraction in the embedding procedure.

ANA_EMB_ISO_2012: Uncertainty on the $Z \to \tau\tau$ background component due to muon isolation criteria in the embedding procedure.

JES_2012_Eta_StatMethod: Jet energy scale (JES) uncertainty on the statistical component of the intercalibration in different detector pseudorapidity regions.

JES_NPV: Jet energy scale (JES) uncertainty due to the pile-up parametrized in terms of the number of primary vertices (NPV).

JES_2012_Modelling: Jet energy scale (JES) uncertainty due to modelling uncertainties in the calibration procedure.

JES_FlavComp_TAUG: Jet energy scale (JES) uncertainty due to the different detector response for quark-initiated and gluon-initiated jets.

pdf_Higgs_gg: Theoretical uncertainty on the parton distribution functions (pdf) for Higgs-boson production with gluon initial states.

norm_LL12_Ztt(Zll,Top)_ggf: Free floating normalization factor of the $Z \to \tau\tau(Z/\gamma^* \to ll$, top-quark) background component.

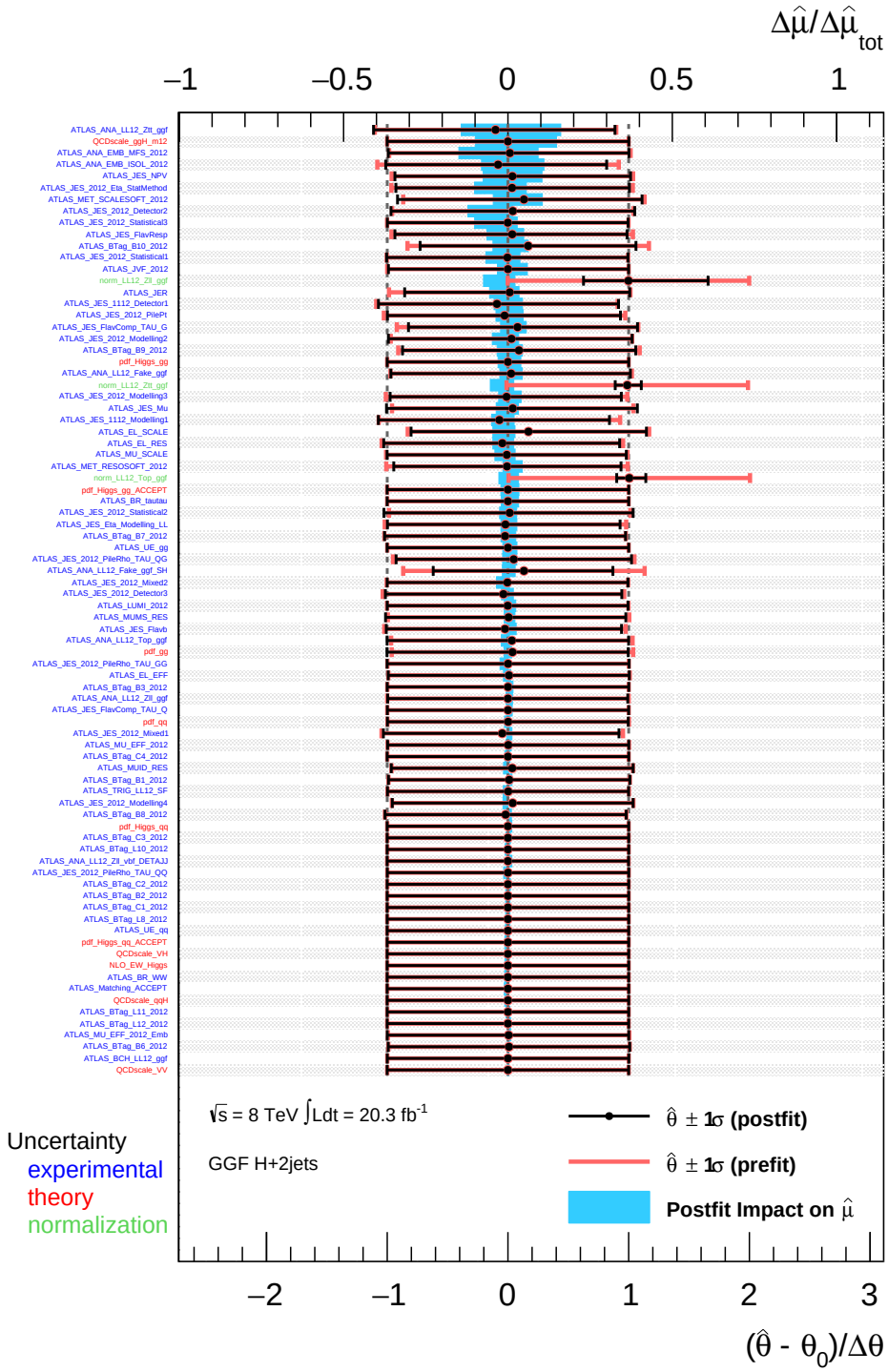

Figure D.1.: Impact of systematic uncertainties on the fitted signal strength μ for the fit in the Optimal Observable with SM signal expectation. Here, Asimov data with $\mu = 1$ and $\cos(\alpha) = 1$ are used in the signal region, while the control regions contain real data. The systematic uncertainties are listed in decreasing order of their impact on $\hat{\mu}$ on the y-axis. The blue boxes show the variation $\Delta\hat{\mu}$ with respect to the total error or $\Delta\hat{\mu}_{tot}$ when the corresponding nuisance parameter is fixed to its post-fit value $\hat{\theta}$ shifted by one standard deviation $\hat{\sigma}_{\hat{\theta}}$ upwards or downwards. The red line referring to the bottom x-axis show the pre-fit uncertainty of the nuisance parameters. The filled black circles also referring to the bottom x-axis show the deviation of the fitted parameters $\hat{\theta}$ from their nominal value θ_0 normalized to the nominal uncertainty $\Delta\theta$.

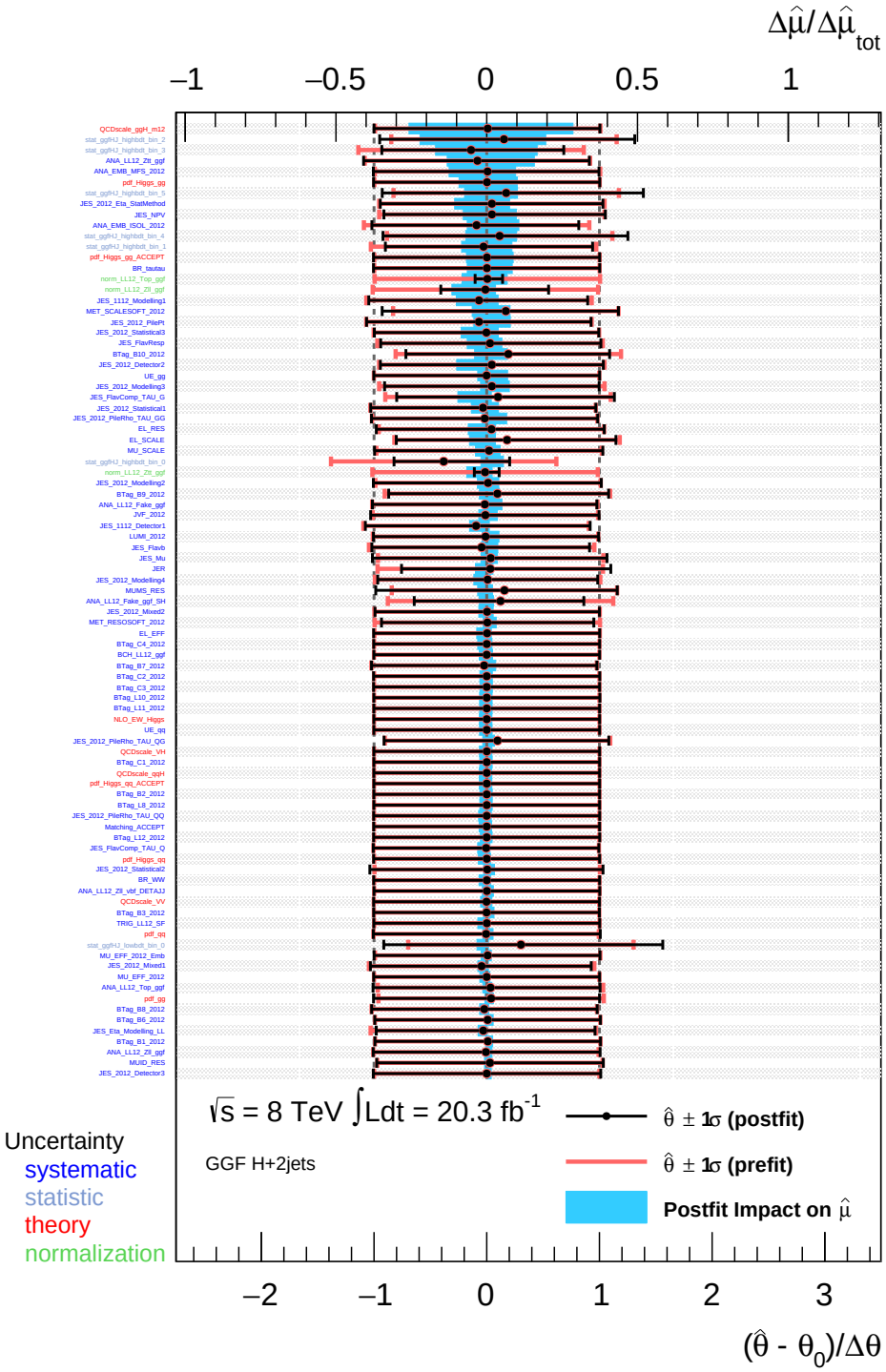

Figure D.2.: Impact of systematic uncertainties on the fitted signal strength μ for the fit in the Optimal Observable with SM signal expectation. The systematic uncertainties are listed in decreasing order of their impact on $\hat{\mu}$ on the y-axis. The blue boxes show the variation $\Delta\hat{\mu}$ with respect to the total error or $\Delta\hat{\mu}_{tot}$ when the corresponding nuisance parameter is fixed to its post-fit value $\hat{\theta}$ shifted by one standard deviation $\hat{\sigma}_{\hat{\theta}}$ upwards or downwards. The red line referring to the bottom x-axis show the pre-fit uncertainty of the nuisance parameters. The filled black circles also referring to the bottom x-axis show the deviation of the fitted parameters $\hat{\theta}$ from their nominal value θ_0 normalized to the nominal uncertainty $\Delta\theta$.

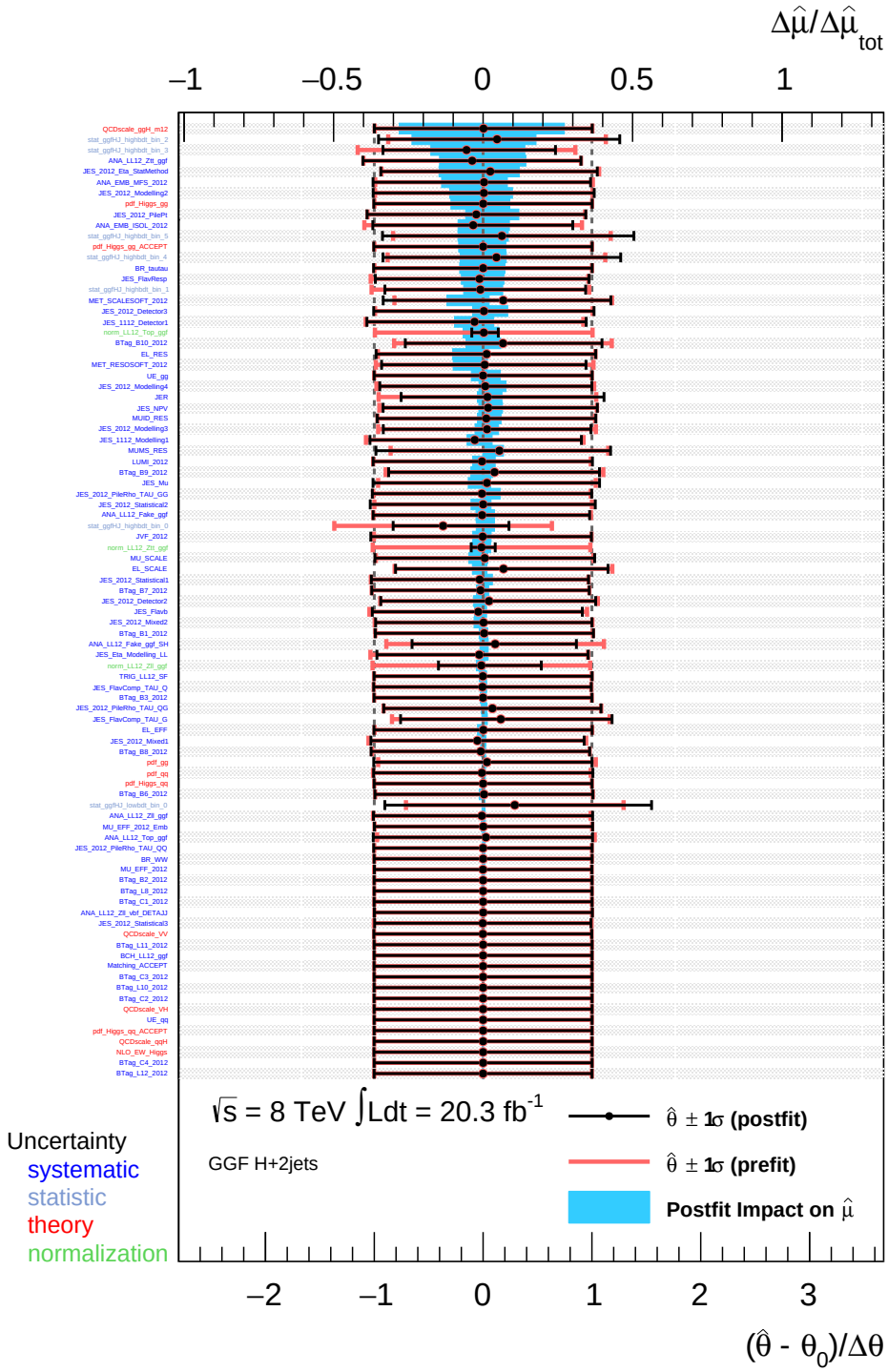

Figure D.3.: Impact of systematic uncertainties on the fitted signal strength μ for the fit in the Optimal Observable with $\cos(\alpha = 0.50)$ signal expectation. The systematic uncertainties are listed in decreasing order of their impact on $\hat{\mu}$ on the y-axis. The blue boxes show the variation $\Delta\hat{\mu}$ with respect to the total error or $\Delta\hat{\mu}_{tot}$ when the corresponding nuisance parameter is fixed to its post-fit value $\hat{\theta}$ shifted by one standard deviation $\hat{\sigma}_{\hat{\theta}}$ upwards or downwards. The red line referring to the bottom x-axis show the pre-fit uncertainty of the nuisance parameters. The filled black circles also referring to the bottom x-axis show the deviation of the fitted parameters $\hat{\theta}$ from their nominal value θ_0 normalized to the nominal uncertainty $\Delta\theta$.

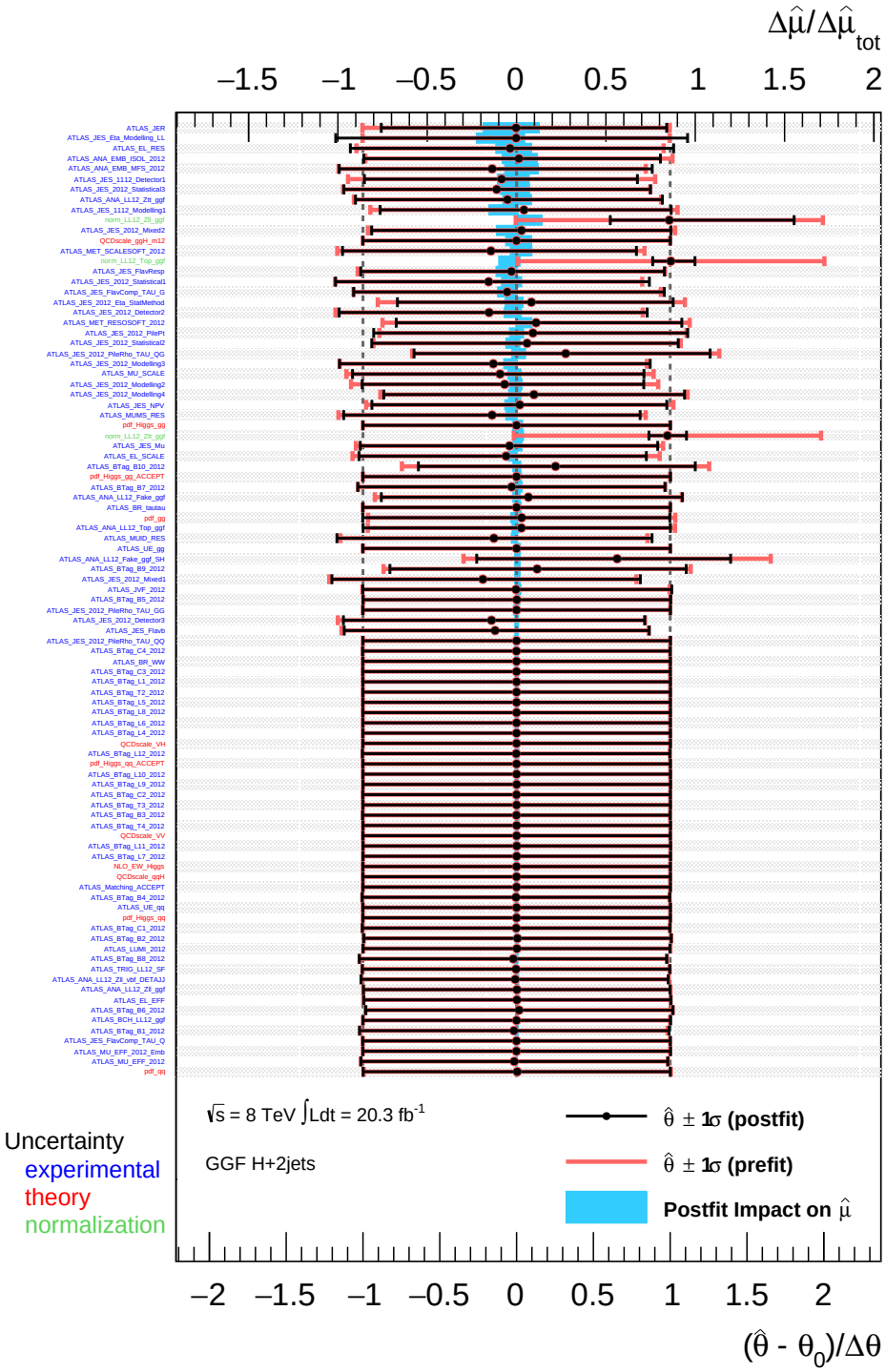

Figure D.4.: Impact of systematic uncertainties on the fitted signal strength μ for the fit in $\Delta\Phi_{jj}^{sign}$ with SM signal expectation. Here, Asimov data with $\mu = 1$ and $\cos(\alpha) = 1$ are used in the signal region, while the control regions contain real data.The systematic uncertainties are listed in decreasing order of their impact on $\hat{\mu}$ on the y-axis. The blue boxes show the variation $\Delta\hat{\mu}$ with respect to the total error or $\Delta\hat{\mu}_{tot}$ when the corresponding nuisance parameter is fixed to its post-fit value $\hat{\theta}$ shifted by one standard deviation $\hat{\sigma}_{\hat{\theta}}$ upwards or downwards. The red line referring to the bottom x-axis show the pre-fit uncertainty of the nuisance parameters. The filled black circles also referring to the bottom x-axis show the deviation of the fitted parameters $\hat{\theta}$ from their nominal value θ_0 normalized to the nominal uncertainty $\Delta\theta$.

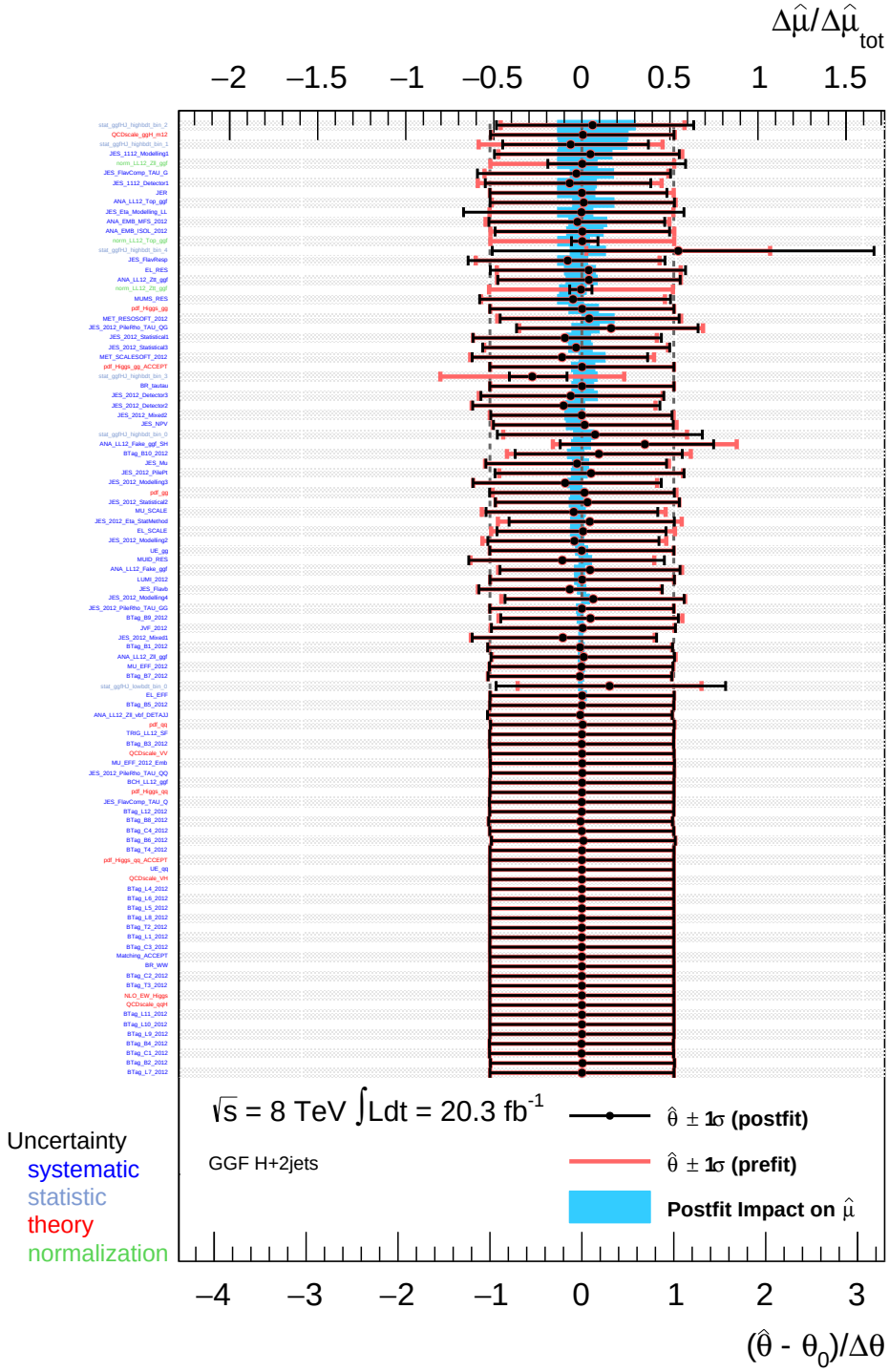

Figure D.5.: Impact of systematic uncertainties on the fitted signal strength μ for the fit in $\Delta\Phi_{jj}^{sign}$with SM signal expectation. The systematic uncertainties are listed in decreasing order of their impact on $\hat{\mu}$ on the y-axis. The blue boxes show the variation $\Delta\hat{\mu}$ with respect to the total error or $\Delta\hat{\mu}_{tot}$ when the corresponding nuisance parameter is fixed to its post-fit value $\hat{\theta}$ shifted by one standard deviation $\hat{\sigma}_{\hat{\theta}}$ upwards or downwards. The red line referring to the bottom x-axis show the pre-fit uncertainty of the nuisance parameters. The filled black circles also referring to the bottom x-axis show the deviation of the fitted parameters $\hat{\theta}$ from their nominal value θ_0 normalized to the nominal uncertainty $\Delta\theta$.

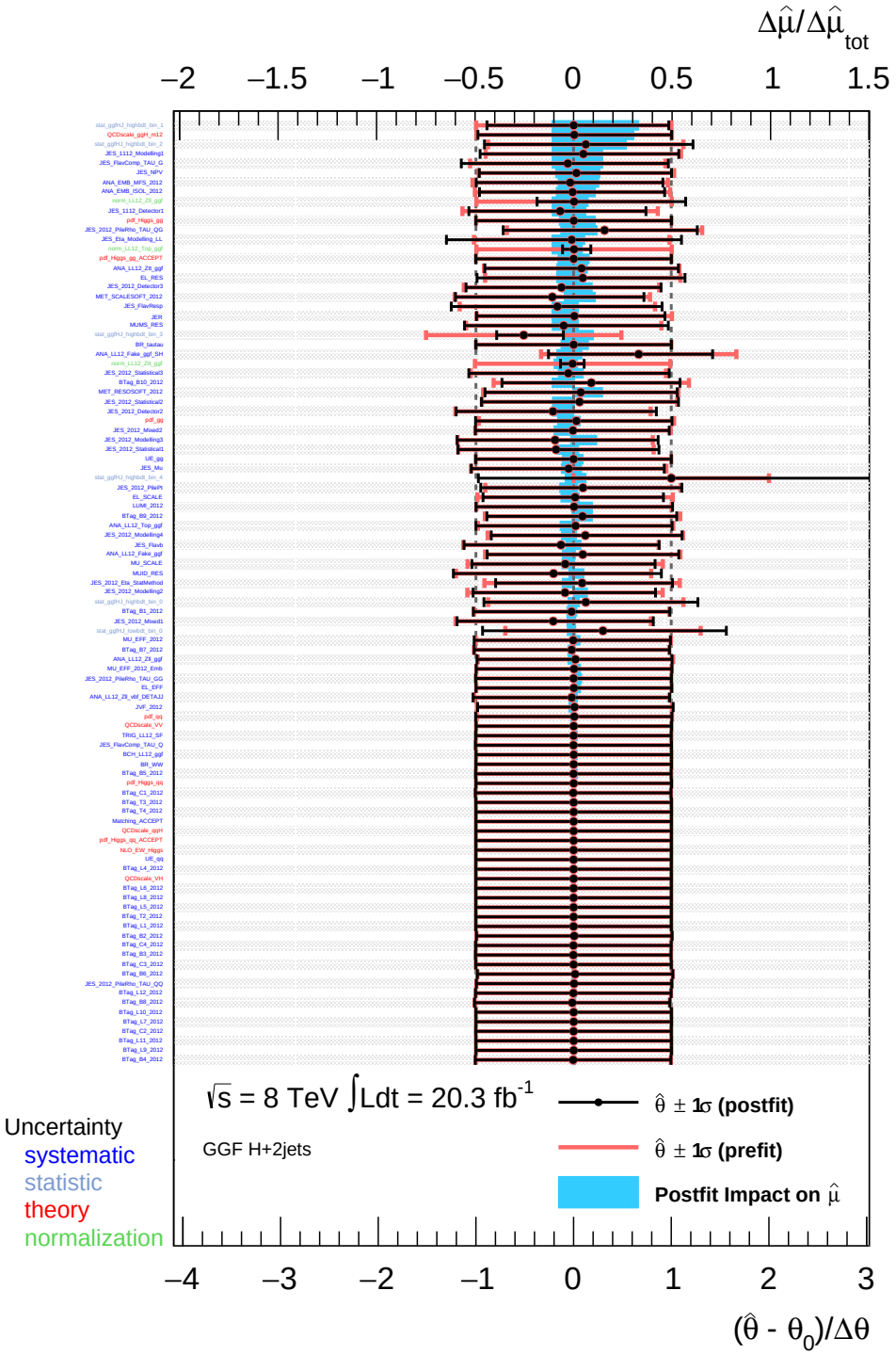

Figure D.6.: Impact of systematic uncertainties on the fitted signal strength μ for the fit in $\Delta\Phi_{jj}^{sign}$with $\cos(\alpha) = -0.30$ signal expectation. The systematic uncertainties are listed in decreasing order of their impact on $\hat{\mu}$ on the y-axis. The blue boxes show the variation $\Delta\hat{\mu}$ with respect to the total error or $\Delta\hat{\mu}_{tot}$ when the corresponding nuisance parameter is fixed to its post-fit value $\hat{\theta}$ shifted by one standard deviation $\hat{\sigma}_{\hat{\theta}}$ upwards or downwards. The red line referring to the bottom x-axis show the pre-fit uncertainty of the nuisance parameters. The filled black circles also referring to the bottom x-axis show the deviation of the fitted parameters $\hat{\theta}$ from their nominal value θ_0 normalized to the nominal uncertainty $\Delta\theta$.

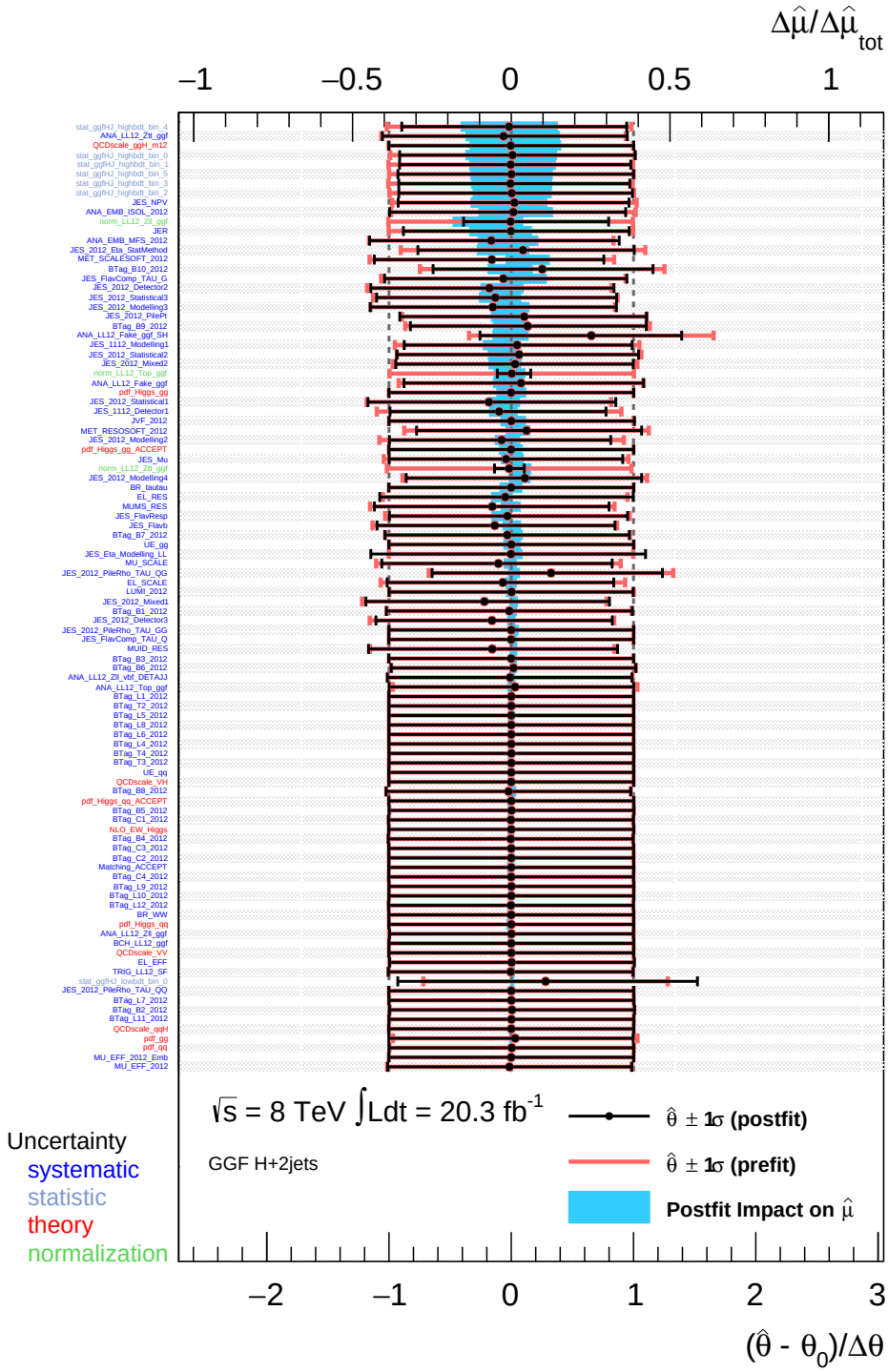

Figure D.7.: Impact of systematic uncertainties on the fitted signal strength μ for the fit in the Optimal Observable binning B with SM signal expectation. Here, Asimov data with $\mu = 1$ and $\cos(\alpha) = 1$ are used in the signal region, while the control regions contain real data. The systematic uncertainties are listed in decreasing order of their impact on $\hat{\mu}$ on the y-axis. The blue boxes show the variation $\Delta\hat{\mu}$ with respect to the total error or $\Delta\hat{\mu}_{tot}$ when the corresponding nuisance parameter is fixed to its post-fit value $\hat{\theta}$ shifted by one standard deviation $\hat{\sigma}_{\hat{\theta}}$ upwards or downwards. The red line referring to the bottom x-axis show the pre-fit uncertainty of the nuisance parameters. The filled black circles also referring to the bottom x-axis show the deviation of the fitted parameters $\hat{\theta}$ from their nominal value θ_0 normalized to the nominal uncertainty $\Delta\theta$.

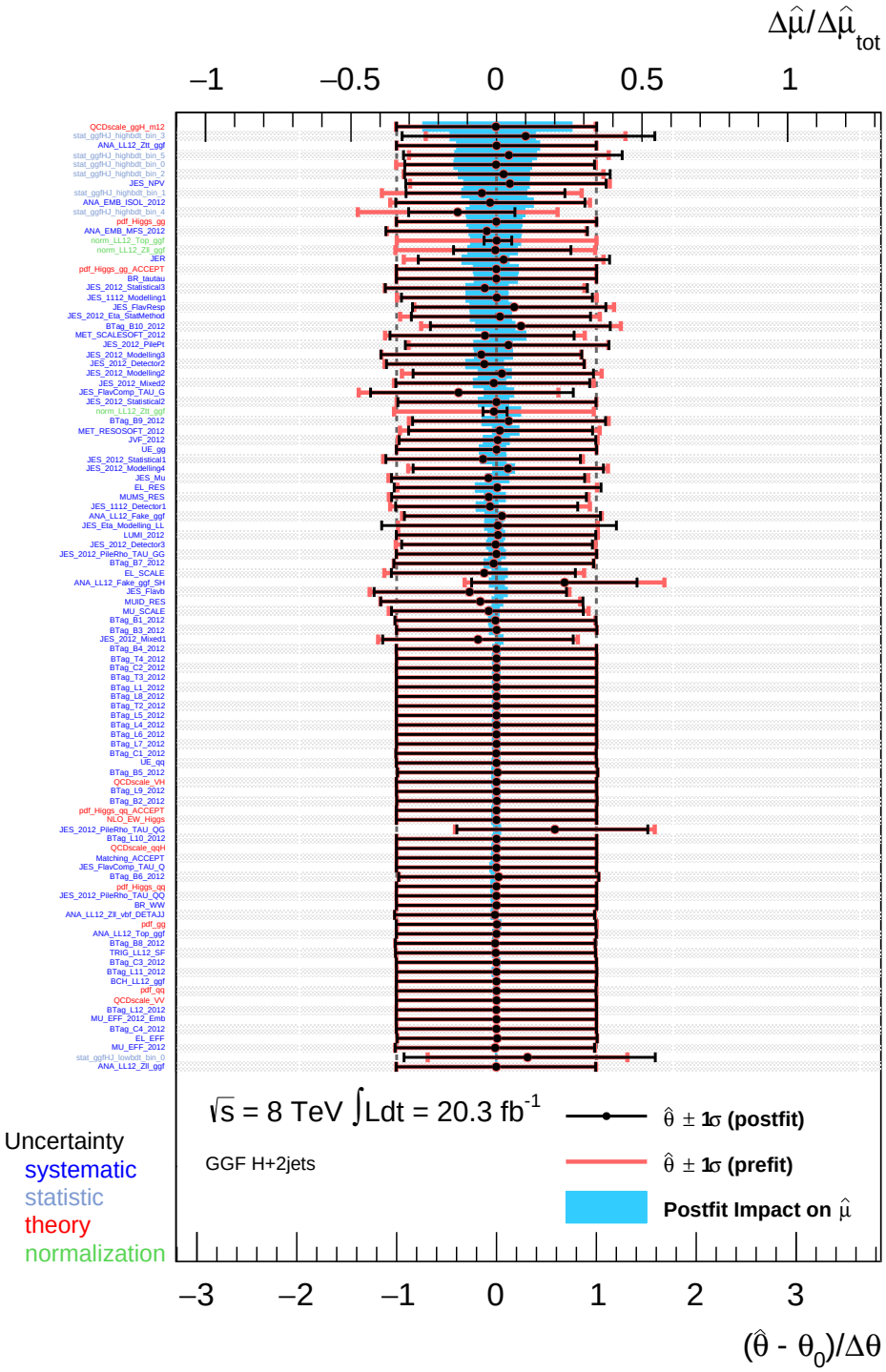

Figure D.8.: Impact of systematic uncertainties on the fitted signal strength μ for the fit in the Optimal Observable binning B with SM signal expectation.The systematic uncertainties are listed in decreasing order of their impact on $\hat{\mu}$ on the y-axis. The blue boxes show the variation $\Delta\hat{\mu}$ with respect to the total error or $\Delta\hat{\mu}_{tot}$ when the corresponding nuisance parameter is fixed to its post-fit value $\hat{\theta}$ shifted by one standard deviation $\hat{\sigma}_{\hat{\theta}}$ upwards or downwards. The red line referring to the bottom x-axis show the pre-fit uncertainty of the nuisance parameters. The filled black circles also referring to the bottom x-axis show the deviation of the fitted parameters $\hat{\theta}$ from their nominal value θ_0 normalized to the nominal uncertainty $\Delta\theta$.

Bibliography

[1] UA1 Collaboration, *Experimental Observation of Lepton Pairs of Invariant Mass around* $95\,\mathrm{GeV}/c^2$ *at the CERN SPS Collider*, Phys.Lett. **B126** (1983) 398.

[2] UA2 Collaboration, *Evidence for* $Z^0 \to e^+e^-$ *at the CERN* $\bar{p}p$ *Collider*, Phys.Lett. **B129** (1983) 130.

[3] UA2 Collaboration, *Observation of Single Isolated Electrons of High Transverse Momentum in Events with Missing Transverse Energy at the CERN* $\bar{p}p$ *Collider*, Phys.Lett. **B122** (1983) 476.

[4] P. W. Higgs, *Broken Symmetries and the Masses of Gauge Bosons*, Phys.Rev.Lett. **13** (1964) 508.

[5] P. W. Higgs, *Spontaneous Symmetry Breakdown without Massless Bosons*, Phys.Rev. **145** (1966) 1156.

[6] F. Englert and R. Brout, *Broken Symmetry and the Mass of Gauge Vector Mesons*, Phys.Rev.Lett. **13** (1964) 321.

[7] G. Guralnik, C. Hagen, and T. Kibble, *Global Conservation Laws and Massless Particles*, Phys.Rev.Lett. **13** (1964) 585.

[8] T. Kibble, *Symmetry breaking in nonAbelian gauge theories*, Phys.Rev. **155** (1967) 1554.

[9] ATLAS Collaboration, *Observation of a new particle in the search for the Standard Model Higgs boson with the ATLAS detector at the LHC*, Phys. Lett. **B716** (2012) , `arXiv:1207.7214 [hep-ex]`.

[10] CMS Collaboration, *Observation of a new boson at a mass of 125 GeV with the CMS experiment at the LHC*, Phys. Lett. **B716** (2012) , `arXiv:1207.7235 [hep-ex]`.

[11] ATLAS Collaboration and CMS Collaboration, *Combined Measurement of the Higgs Boson Mass in pp Collisions at* $\sqrt{s} = 7$ *and 8 TeV with the ATLAS and CMS Experiments*, Phys. Rev. Lett. **114** (2015) 191803, `arXiv:1503.07589 [hep-ex]`.

[12] A. D. Sakharov, *Violation of CP Invariance, c Asymmetry, and Baryon Asymmetry of the Universe*, Pisma Zh. Eksp. Teor. Fiz. **5** (1967) 32–35.

[13] N. Cabibbo, *Unitary Symmetry and Leptonic Decays*, Phys. Rev. Lett. **10** (1963) 531–533.

[14] M. Kobayashi and T. Maskawa, *CP Violation in the Renormalizable Theory of Weak Interaction*, Prog. Theor. Phys. **49** (1973) 652–657.

[15] ATLAS Collaboration, *Study of the spin and parity of the Higgs boson in diboson decays with the ATLAS detector*, Eur. Phys. J. **C75** no. 10, (2015) 476, arXiv:1506.05669 [hep-ex].

[16] ATLAS Collaboration, *Determination of spin and parity of the Higgs boson in the $WW^* \to e\nu\mu\nu$ decay channel with the ATLAS detector*, Eur. Phys. J. **C75** no. 5, (2015) 231, arXiv:1503.03643 [hep-ex].

[17] UA1 Collaboration, *Experimental Observation of Isolated Large Transverse Energy Electrons with Associated Missing Energy at $\sqrt{s}$ =540 GeV*, Phys.Lett. **B122** (1983) 103.

[18] CDF Collaboration, *Observation of Top Quark Production in $\overline{p}p$ Collisions with the Collider Detector at Fermilab*, Phys. Rev. Lett. **74** (Apr, 1995) 2626–2631.

[19] F. Halzen and A. D. Martin, *Quarks and Leptons: An Introductory Course in Modern Particle Physics*. Wiley, 2008.

[20] M. E. Peskin and D. V. Schroeder, *An Introduction to Quantum Field Theory*. Westview Press, 1995.

[21] D. Griffith, *Introduction to Elementary Particles*. Wiley, 1984.

[22] Particle Data Group, K. A. Olive *et al.*, *Review of Particle Physics*, Chin. Phys. **C38** (2014) 090001.

[23] G. V. Chibisov, *Astrophysical upper limits on the photon rest mass*, Soviet Physics Uspekhi **19** no. 7, (1976) 624.

[24] V. V. Ezhela, S. B. Lugovsky, and O. V. Zenin, *Hadronic part of the muon g-2 estimated on the sigma**2003(tot)(e+ e- —> hadrons) evaluated data compilation*, arXiv:hep-ph/0312114 [hep-ph].

[25] P. Schmuser, *Feynman-Graphen und Eichtheorien fuer Experimentalphysiker*. Springer Berlin Heidelberg, 1995.

[26] D. J. Gross and F. Wilczek, *Ultraviolet Behavior of Nonabelian Gauge Theories*, Phys. Rev. Lett. **30** (1973) 1343–1346.

[27] H. D. Politzer, *Reliable Perturbative Results for Strong Interactions?*, Phys. Rev. Lett. **30** (Jun, 1973) 1346–1349.

[28] T. D. Lee and C. N. Yang, *Question of Parity Conservation in Weak Interactions*, Phys. Rev. **104** (Oct, 1956) 254–258.

[29] C. S. Wu, E. Ambler, R. W. Hayward, D. D. Hoppes, and R. P. Hudson, *Experimental Test of Parity Conservation in Beta Decay*, Phys. Rev. **105** (Feb, 1957) 1413–1415.

[30] S. L. Glashow, *Partial Symmetries of Weak Interactions*, Nucl. Phys. **22** (1961) 579–588.

[31] S. Weinberg, *A Model of Leptons*, Phys. Rev. Lett. **19** (Nov, 1967) 1264–1266.

[32] A. Salam and J. Ward, *Weak and electromagnetic interactions*, Il Nuovo Cimento (1955-1965) **11** no. 4, (1959) 568–577.

[33] K. Nishijima, *Charge of Independence Theory of V Particles*, Progress of Theoretical Physics **13** (1955) 285–304.

[34] M. Gell-Mann, *The interpretation of the new particles as displaced charge multiplets*, Il Nuovo Cimento (1955-1965) **4** no. 2, (1956) 848–866.

[35] Z. Maki, M. Nakagawa, and S. Sakata, *Remarks on the Unified Model of Elementary Particles*, Progress of Theoretical Physics **28** (Nov., 1962) 870–880.

[36] B. Pontecorvo, *Neutrino Experiments and the Problem of Conservation of Leptonic Charge*, Sov. Phys. JETP **26** (1968) 984–988, [Zh. Eksp. Teor. Fiz.53,1717(1967)].

[37] K2K Collaboration, *Measurement of Neutrino Oscillation by the K2K Experiment*, Phys. Rev. **D74** (2006) 072003, arXiv:hep-ex/0606032 [hep-ex].

[38] CMS Collaboration, *The Discovery of the Higgs Boson with the CMS Detector and its Implications for Supersymmetry and Cosmology* in *Time and Matter 2013 (TAM2013) Venice, Italy*. 2013. arXiv:1309.0721 [hep-ph].

[39] Y. Nambu, *Quasi-Particles and Gauge Invariance in the Theory of Superconductivity*, Phys. Rev. **117** (Feb, 1960) 648–663.

[40] J. Goldstone, *Field theories with Superconductor solutions*, Il Nuovo Cimento (1955-1965) **19** no. 1, (1961) 154–164.

[41] ATLAS Collaboration, *ATLAS Twiki*, https://twiki.cern.ch/twiki/bin/view/AtlasPublic/StandardModelPublicResults.

[42] B. W. Lee, C. Quigg, and H. B. Thacker, *Weak interactions at very high energies: The role of the Higgs-boson mass*, Phys. Rev. D **16** (Sep, 1977) 1519–1531.

[43] J. Ellis, *Outstanding questions: physics beyond the Standard Model*, Philosophical Transactions of the Royal Society of London A: Mathematical, Physical and Engineering Sciences **370** no. 1961, (2012) 818–830.

[44] T. Hambye and K. Riesselmann, *Matching conditions and Higgs mass upper bounds revisited*, Phys. Rev. **D55** (1997) 7255–7262, arXiv:hep-ph/9610272 [hep-ph].

[45] A. Djouadi, *The Anatomy of electro-weak symmetry breaking. I: The Higgs boson in the standard model*, Phys. Rept. **457** (2008) 1–216, arXiv:hep-ph/0503172 [hep-ph].

[46] G. Degrassi, S. Di Vita, J. Elias-Miro, J. R. Espinosa, G. F. Giudice, G. Isidori, and A. Strumia, *Higgs mass and vacuum stability in the Standard Model at NNLO*, JHEP **08** (2012) 098, arXiv:1205.6497 [hep-ph].

[47] J. Ellis, J. Espinosa, G. Giudice, A. Hoecker, and A. Riotto, *The probable fate of the Standard Model*, Physics Letters B **679** no. 4, (2009) 369 – 375.

[48] M. Baak, M. Goebel, J. Haller, A. Hoecker, D. Kennedy, R. Kogler, K. Moenig, M. Schott, and J. Stelzer, *The Electroweak Fit of the Standard Model after the Discovery of a New Boson at the LHC*, Eur. Phys. J. **C72** (2012) 2205, arXiv:1209.2716 [hep-ph].

[49] S. D. Drell and T.-M. Yan, *Partons and their applications at high energies*, Annals of Physics **66** no. 2, (1971) 578 – 623.

[50] T. Rias, http://en.wikipedia.org/wiki/Higgs_boson.

[51] LHC Higgs Cross Section Working Group, *Handbook of LHC Higgs Cross Sections: 3. Higgs Properties*, arXiv:1307.1347 [hep-ph].

[52] ATLAS Collaboration, *Measurement of the Higgs boson mass from the $H \to \gamma\gamma$ and $H \to ZZ^* \to 4\ell$ channels with the ATLAS detector using 25 fb^{-1} of pp collision data*, Phys. Rev. **D90** no. 5, (2014) 052004, arXiv:1406.3827 [hep-ex].

[53] CMS Collaboration, *Precise determination of the mass of the Higgs boson and tests of compatibility of its couplings with the standard model predictions using proton collisions at 7 and 8 TeV*, Eur. Phys. J. **C75** no. 5, (2015) 212, arXiv:1412.8662 [hep-ex].

[54] ATLAS Collaboration, *Measurements of the Higgs boson production and decay rates and coupling strengths using pp collision data at $\sqrt{s} = 7$ and 8 TeV in the ATLAS experiment*, arXiv:1507.04548 [hep-ex].

[55] CMS Collaboration, *Constraints on the spin-parity and anomalous HVV couplings of the Higgs boson in proton collisions at 7 and 8 TeV*, Phys. Rev. **D92** no. 1, (2015) 012004, arXiv:1411.3441 [hep-ex].

[56] P. Artoisenet *et al.*, *A framework for Higgs characterisation*, JHEP **11** (2013) 043, arXiv:1306.6464 [hep-ph].

[57] G. Klamke and D. Zeppenfeld, *Higgs plus two jet production via gluon fusion as a signal at the CERN LHC*, JHEP **04** (2007) 052, arXiv:hep-ph/0703202 [HEP-PH].

[58] J. Alwall, R. Frederix, S. Frixione, V. Hirschi, F. Maltoni, O. Mattelaer, H. S. Shao, T. Stelzer, P. Torrielli, and M. Zaro, *The automated computation of tree-level and next-to-leading order differential cross sections, and their matching to parton shower simulations*, JHEP **07** (2014) 079, arXiv:1405.0301 [hep-ph].

[59] D. Atwood and A. Soni, *Analysis for magnetic moment and electric dipole moment form-factors of the top quark via e+ e- —¿ t anti-t*, Phys. Rev. **D45** (1992) 2405–2413.

[60] M. Diehl and O. Nachtmann, *Optimal observables for the measurement of three gauge boson couplings in e+ e- —¿ W+ W-*, Z. Phys. **C62** (1994) 397–412.

[61] M. Diehl, O. Nachtmann, and F. Nagel, *Triple gauge couplings in polarized e- e+ —¿ W- W+ and their measurement using optimal observables*, Eur. Phys. J. **C27** (2003) 375–397, arXiv:hep-ph/0209229 [hep-ph].

[62] D. Atwood and A. Soni, *Analysis for magnetic moment and electric dipole moment form factors of the top quark via $e^+e^- \to t\bar{t}$*, Phys. Rev. D **45** (Apr, 1992) 2405–2413.

[63] M. Davier, L. Duflot, F. L. Diberder, and A. Roug, *The optimal method for the measurement of tau polarization*, Physics Letters B **306** no. 3, (1993) 411 – 417.

[64] OPAL Collaboration, *Search for CP violation in $Z^0 \to \tau^+\tau^-$ and an Upper Limit on the Weak Dipole Moment of the τ Lepton*, Zeitschrift fuer Physik C Particles and Fields **74** no. 3, (1997) 403–413.

[65] M. Schumacher, *Determination of the cp quantum numbers of the Higgs boson and test of cp invariance in the higgs-strahlung process at a future e+ e- linear collider.*

[66] A. Buckley, J. Ferrando, S. Lloyd, K. Nordstrm, B. Page, M. Rfenacht, M. Schnherr, and G. Watt, *LHAPDF6: parton density access in the LHC precision era*, Eur. Phys. J. **C75** no. 3, (2015) 132, arXiv:1412.7420 [hep-ph].

[67] H.-L. Lai, M. Guzzi, J. Huston, Z. Li, P. M. Nadolsky, J. Pumplin, and C. P. Yuan, *New parton distributions for collider physics*, Phys. Rev. **D82** (2010) 074024, arXiv:1007.2241 [hep-ph].

[68] J. M. Campbell, R. K. Ellis, R. Frederix, P. Nason, C. Oleari, and C. Williams, *NLO Higgs Boson Production Plus One and Two Jets Using the POWHEG BOX, MadGraph4 and MCFM*, JHEP **07** (2012) 092, arXiv:1202.5475 [hep-ph].

[69] P. Nason and C. Oleari, *NLO Higgs boson production via vector-boson fusion matched with shower in POWHEG*, JHEP **02** (2010) 037, arXiv:0911.5299 [hep-ph].

[70] T. Sjostrand, S. Mrenna, and P. Z. Skands, *A Brief Introduction to PYTHIA 8.1*, Comput. Phys. Commun. **178** (2008) 852–867, arXiv:0710.3820 [hep-ph].

[71] M. L. Mangano, M. Moretti, F. Piccinini, R. Pittau, and A. D. Polosa, *ALPGEN, a generator for hard multiparton processes in hadronic collisions*, JHEP **07** (2003) 001, arXiv:hep-ph/0206293 [hep-ph].

[72] S. Frixione and B. R. Webber, *Matching NLO QCD computations and parton shower simulations*, JHEP **06** (2002) 029, arXiv:hep-ph/0204244 [hep-ph].

[73] S. Frixione, P. Nason, and B. R. Webber, *Matching NLO QCD and parton showers in heavy flavor production*, JHEP **08** (2003) 007, arXiv:hep-ph/0305252 [hep-ph].

[74] S. Frixione, E. Laenen, P. Motylinski, B. R. Webber, and C. D. White, *Single-top hadroproduction in association with a W boson*, JHEP **07** (2008) 029, arXiv:0805.3067 [hep-ph].

[75] B. P. Kersevan and E. Richter-Was, *The Monte Carlo event generator AcerMC versions 2.0 to 3.8 with interfaces to PYTHIA 6.4, HERWIG 6.5 and ARIADNE 4.1*, Comput. Phys. Commun. **184** (2013) 919–985, arXiv:hep-ph/0405247 [hep-ph].

[76] S. Gieseke, D. Grellscheid, K. Hamilton, A. Ribon, P. Richardson, M. H. Seymour, P. Stephens, and B. R. Webber, *Herwig++ 2.0 Release Note*, arXiv:hep-ph/0609306 [hep-ph].

[77] J. M. Butterworth, J. R. Forshaw, and M. H. Seymour, *Multiparton interactions in photoproduction at HERA*, Z. Phys. **C72** (1996) 637–646, arXiv:hep-ph/9601371 [hep-ph].

[78] J. Pumplin, D. R. Stump, J. Huston, H. L. Lai, P. M. Nadolsky, and W. K. Tung, *New generation of parton distributions with uncertainties from global QCD analysis*, JHEP **07** (2002) 012, arXiv:hep-ph/0201195 [hep-ph].

[79] S. Agostinelli *et al.*, *GEANT4: A simulation toolkit*, Nucl. Instrum. Meth. **A506** (2003) 250.

[80] J. Alwall, M. Herquet, F. Maltoni, O. Mattelaer, and T. Stelzer, *MadGraph 5 : Going Beyond*, JHEP **06** (2011) 128, arXiv:1106.0522 [hep-ph].

[81] O. Bruning and P. Collier, *Building a behemoth*, Nature **448** (2007) 285.

[82] L. Evans and P. Bryant, *LHC Machine*, Journal of Instrumentation **3** no. 08, (2008) S08001.

[83] M. Hostettler and G. Papotti, *Luminosity Lifetime at the LHC in 2012 Proton Physics.*

[84] ATLAS, G. Aad *et al.*, *The ATLAS Experiment at the CERN Large Hadron Collider*, JINST **3** (2008) S08003.

[85] ATLAS Collaboration, *ATLAS Twiki*, `https://twiki.cern.ch/twiki/bin/view/AtlasPublic/TriggerOperationPublicResults`.

[86] ATLAS Collaboration, *ATLAS Twiki*, `https://twiki.cern.ch/twiki/bin/view/AtlasPublic/LuminosityPublicResults`.

[87] ATLAS Collaboration, *Performance of pile-up subtraction for jet shapes*, ATLAS-CONF-2013-085 (2013) .

[88] ATLAS Collaboration, *Performance of the ATLAS Inner Detector Track and Vertex Reconstruction in the High Pile-Up LHC Environment.*

[89] ATLAS Collaboration, *Electron and photon reconstruction and identification in ATLAS: expected performance at high energy and results at 900 GeV* Tech. Rep. ATLAS-CONF-2010-005, CERN, Geneva, Jun, 2010. `https://cds.cern.ch/record/1273197`.

[90] ATLAS Collaboration, *Electron efficiency measurements with the ATLAS detector using the 2012 LHC proton-proton collision data* Tech. Rep. ATLAS-CONF-2014-032, CERN, 2014. `https://cds.cern.ch/record/1706245`.

[91] R. Nicolaidou, L. Chevalier, S. Hassani, J. F. Laporte, E. L. Menedeu, and A. Ouraou, *Muon identification procedure for the ATLAS detector at the LHC using Muonboy reconstruction package and tests of its performance using cosmic rays and single beam data*, Journal of Physics: Conference Series **219** no. 3, (2010) 032052.

[92] ATLAS Collaboration, *Preliminary results on the muon reconstruction efficiency, momentum resolution, and momentum scale in ATLAS 2012 pp collision data.*

[93] M. Cacciari, G. P. Salam, and G. Soyez, *The anti-kt jet clustering algorithm*, Journal of High Energy Physics **2008** no. 04, (2008) 063.

[94] ATLAS Collaboration, *Determination of the jet energy scale and resolution at ATLAS using Z/γ–jet events in data at $\sqrt{s} = 8$ TeV.*

[95] ATLAS Collaboration, *Commissioning of the ATLAS high-performance b-tagging algorithms in the 7 TeV collision data* tech. rep., 2011.

[96] *Calibration of b-tagging using dileptonic top pair events in a combinatorial likelihood approach with the ATLAS experiment* Tech. Rep. ATLAS-CONF-2014-004, CERN, Geneva, Feb, 2014. `https://cds.cern.ch/record/1664335`.

[97] *Performance of Missing Transverse Momentum Reconstruction in ATLAS studied in Proton-Proton Collisions recorded in 2012 at 8 TeV* Tech. Rep. ATLAS-CONF-2013-082, CERN, Geneva, Aug, 2013. `https://cds.cern.ch/record/1570993`.

[98] ATLAS Collaboration, *Reconstruction, Energy Calibration, and Identification of Hadronically Decaying Tau Leptons* Tech. Rep. ATLAS-CONF-2011-077, CERN, Geneva, May, 2011. `https://cds.cern.ch/record/1353226`.

[99] G. Pasztor, R. White, F. Monticelli, M. Wielers, T. Kono, F. Zhang, F. Wang, and K. Behr, *Electron trigger performance in 2012 ATLAS data* Tech. Rep. ATL-COM-DAQ-2015-091, CERN, Geneva, Jul, 2015. https://cds.cern.ch/record/2032463.

[100] ATLAS Collaboration, *Performance of the ATLAS muon trigger in pp collisions at* $\sqrt{s} = 8$ *TeV*, Eur. Phys. J. **C75** no. 3, (2015) 120, arXiv:1408.3179 [hep-ex].

[101] ATLAS Collaboration, *Simulation of Pile-up in the ATLAS Experiment* Tech. Rep. 2, 2014. http://stacks.iop.org/1742-6596/513/i=2/a=022024.

[102] ATLAS Collaboration, *Expected Performance of the ATLAS Experiment - Detector, Trigger and Physics*, arXiv:0901.0512 [hep-ex].

[103] A. Elagin, P. Murat, A. Pranko, and A. Safonov, *A New Mass Reconstruction Technique for Resonances Decaying to di-tau*, Nucl. Instrum. Meth. **A654** (2011) 481–489, arXiv:1012.4686 [hep-ex].

[104] ATLAS Collaboration, *Evidence for the Higgs-boson Yukawa coupling to tau leptons with the ATLAS detector*, JHEP **04** (2015) 117, arXiv:1501.04943 [hep-ex].

[105] ATLAS Collaboration, *ATLAS Twiki*, https://twiki.cern.ch/twiki/bin/viewauth/AtlasProtected/HowToCleanJets2012.

[106] ATLAS Collaboration, *ATLAS Twiki*, https://twiki.cern.ch/twiki/bin/viewauth/AtlasProtected/HowToCleanJets2012/Hot_Tile_calorimeter_in_period_B.

[107] A. Hoecker *et al.*, *TMVA - Toolkit for Multivariate Data Analysis*, ArXiv Physics e-prints (2007) , physics/0703039.

[108] J. H. Friedman, *Greedy function approximation: A gradient boosting machine.*, Ann. Statist. **29** no. 5, (10, 2001) 1189–1232.

[109] J. H. Friedman, *Stochastic Gradient Boosting*, Comput. Stat. Data Anal. **38** no. 4, (Feb., 2002) 367–378.

[110] *TMVA Users Guide*, http://tmva.sourceforge.net/docu/TMVAUsersGuide.pdf.

[111] N. Smirnov, *Table for Estimating the Goodness of Fit of Empirical Distributions*, The Annals of Mathematical Statistics **19** (1948) .

[112] A. Kolmogorov, *Sulla Determinazione Empirica di una Legge di Distribuzione*, Giornale dell?Istituto Italiano degli Attuari **4** (1933) 83–91.

[113] ATLAS Collaboration, *Modelling* $Z \to \tau\tau$ *processes in ATLAS with* τ*-embedded* $Z \to \mu\mu$ *data*, arXiv:1506.05623 [hep-ex].

[114] S. Jadach, Z. Was, R. Decker, and J. H. Kuhn, *The tau decay library TAUOLA: Version 2.4*, Comput. Phys. Commun. **76** (1993) 361–380.

[115] N. Davidson, T. Przedzinski, and Z. Was, *PHOTOS Interface in C++: Technical and Physics Documentation*, arXiv:1011.0937 [hep-ph].

[116] ATLAS Collaboration, *Improved luminosity determination in pp collisions at sqrt(s) = 7 TeV using the ATLAS detector at the LHC*, Eur. Phys. J. **C73** no. 8, (2013) 2518, arXiv:1302.4393 [hep-ex].

[117] ATLAS Collaboration, *ATLAS Twiki*, https://twiki.cern.ch/twiki/bin/viewauth/AtlasProtected/ApplyJetResolutionSmearing.

[118] ATLAS Collaboration, *ATLAS Twiki*, https://twiki.cern.ch/twiki/bin/view/AtlasProtected/EGammaCalibrationGEO20.

[119] ATLAS Collaboration, *ATLAS Twiki*, https://twiki.cern.ch/twiki/bin/viewauth/AtlasProtected/MCPAnalysisGuidelinesData2012.

[120] R. J. Barlow, *Extended maximum likelihood*, Nucl. Instrum. Meth. **A297** (1990) 496–506.

[121] ROOT Collaboration, *HistFactory: A tool for creating statistical models for use with RooFit and RooStats* Tech. Rep. CERN-OPEN-2012-016, New York U., New York, Jan, 2012. https://cds.cern.ch/record/1456844.

[122] L. Moneta, K. Cranmer, G. Schott, and W. Verkerke, *The RooStats project* in *Proceedings of the 13th International Workshop on Advanced Computing and Analysis Techniques in Physics Research*, p. 57. 2010. arXiv:1009.1003 [physics.data-an].

[123] W. Verkerke and D. Kirkby, *The RooFit toolkit for data modeling*, physics/0306116.

[124] G. Cowan, *Statistical Data Analysis*. Oxford University Press, Oxford, 1998.

[125] R. Brun and F. Rademakers, *ROOT: An object oriented data analysis framework*, Nucl. Instrum. Meth. **A389** (1997) 81–86.

[126] G. Cowan, K. Cranmer, E. Gross, and O. Vitells, *Asymptotic formulae for likelihood-based tests of new physics*, European Physical Journal C **71** (Feb., 2011) 1554, arXiv:1007.1727 [physics.data-an].

Acknowledgements

Ich möchte mich an dieser Stelle ganz herzlich bei allen Leuten bedanken, die mich während der letzten Jahre begleitet und unterstützt haben. Da mein Studium mit dieser Masterarbeit nun endet, beschränke ich mich hier auf all jene, die für deren Entstehung von besondere Bedeutung waren.

Ich bedanke mich bei Prof. Dr. Markus Schumacher für die Bereitstellung des Arbeitsthemas und für die sehr gute Betreuung während des letzten Jahres. Wo immer Probleme aufgetaucht sind hast du dir Zeit genommen und mir die Möglichkeit gegeben, viel über Teilchenphysik zu lernen.
Ein großer Dank geht auch an meinem Betreuer Dr. Elias Coniavitis, der mich während des letztes Jahres trotz der Entfernung zwischen Freiburg und Genf sehr gut betreute und immer Zeit für mich gefunden hat.
Ich möchte mich außerdem bei der gesamten Arbeitsgruppe für das angenehme Arbeitsklima und die Hilfsbereitschaft jedes Einzelnen bedanken. Hierbei geht ein großer Dank an Christian Schillo, der viel von seiner knappen Zeit geopfert hat, um mir bei kleinen und großen Problemen jeglicher Art zu helfen. Vielen Dank auch an Prof. Dr. Stan Lai und Dr. Michael Böhler, die jederzeit für Fragen und Anregungen zur Verfügung standen.

Meine Eltern und meine Familie haben mich während des gesamten Studiums begleitet und unterstützt. Auch wenn es nicht immer einfach war, ihr standet jederzeit hinter mir und habt mir Kraft gegeben. Dafür möchte ich euch von ganzem Herzen danken! Ohne euch, hätte ich das nicht geschafft.

Zum Schluss richtet sich mein Dank an Daniel. Für deine Hilfe, deine Zuversicht und dass du jederzeit für mich da bist! Danke!

Erklärung der Selbstständigkeit

Hiermit versichere ich, die eingereichte Masterarbeit selbstständig verfasst und keine anderen als die von mir angegebenen Quellen und Hilfsmittel benutzt zu haben.
Wörtlich oder sinngemäß aus anderen Werken übernommene Inhalte wurden entsprechend den anerkannten Regeln wissenschaftlichen Arbeitens (lege artis) kenntlich gemacht.
Ich erkläre weiterhin, dass die eingereichte Masterarbeit weder vollständig noch in wesentlichen Teilen Gegenstand eines anderen Prüfungsverfahrens war oder ist.

Freiburg, den _____ _____

Alena Lösle